Uncertainties in Digital Elevation Models: Evaluation and Effects on Landform and Soil Type Classification

Inaugural-Dissertation

zur

Erlangung des Doktorgrades

der Mathematisch-Naturwissenschaftlichen Fakultät

der Universität zu Köln

vorgelegt von

Tanja Kramm

aus Langenfeld

Köln 2022

Berichterstatter: Prof. Dr. Georg Bareth

Prof. Dr. Karl Schneider

Tag der mündlichen Prüfung: 28.10.2022

Abstract

Digital elevation models (DEMs) are a widely used source for the digital representation of the Earth's surface in a wide range of scientific, industrial and military applications. Since many processes on Earth are influenced by the shape of the relief, a variety of different applications rely on accurate information about the topography. For instance, DEMs are used for the prediction of geohazards, climate modelling, or planning-relevant issues, such as the identification of suitable locations for renewable energies. Nowadays, DEMs can be acquired with a high geometric resolution and over large areas using various remote sensing techniques, such as photogrammetry, RADAR, or laser scanning (LiDAR). However, they are subject to uncertainties and may contain erroneous representations of the terrain. The quality and accuracy of the topographic representation in the DEM is crucial, as the use of an inaccurate dataset can negatively affect further results, such as the underestimation of landslide hazards due to a too flat representation of relief in the elevation model. Therefore, it is important for users to gain more knowledge about the accuracy of a terrain model to better assess the negative consequences of DEM uncertainties on further analysis results of a certain research application. A proper assessment of whether the purchase or acquisition of a highly accurate DEM is necessary or the use of an already existing and freely available DEM is sufficient to achieve accurate results is of great qualitative and economic importance.

In this context, the first part of this thesis focuses on extending knowledge about the behaviour and presence of uncertainties in DEMs concerning terrain and land cover. Thus, the first two studies of this dissertation provide a comprehensive vertical accuracy analysis of twelve DEMs acquired from space with spatial resolutions ranging from 5 m to 90 m. The accuracy of these DEMs was investigated in two different regions of the world that are substantially different in terms of relief and land cover. The first study was conducted in the hyperarid Chilean Atacama Desert in northern Chile, with very sparse land cover and high elevation differences. The second case study was conducted in a mid-latitude region, the Rur catchment in the western part of Germany. This area has a predominantly flat to hilly terrain with relatively diverse and dense vegetation and land cover. The DEMs in both studies were evaluated with particular attention to the influence of relief and land cover on vertical accuracy. The change of error due to changing slope and land cover was quantified to determine an average loss of accuracy as a function of slope for each DEM. Additionally, these values were used to derive relief-adjusted error values for different land cover classes.

The second part of this dissertation addresses the consequences that different spatial resolutions and accuracies in DEMs have on specific applications. These implications were examined in two exemplary case studies. In a geomorphometric case study, several DEMs were used to classify landforms by different approaches. The results were subsequently compared and the accuracy of the classification results with different DEMs was analysed. The second case study is settled within the field of digital soil mapping. Various soil types were predicted with machine learning algorithms (random forest and artificial neural networks) using numerous relief parameters derived from DEMs of different spatial resolutions. Subsequently, the influence of high and low resolution DEMs with the respectively derived land surface parameters on the prediction results was evaluated.

The results on the vertical accuracy show that uncertainties in DEMs can have diverse reasons. Besides the spatial resolution, the acquisition technique and the degree of improvements made to the dataset significantly impact the occurrence of errors in a DEM. Furthermore, the relief and physical objects on

the surface play a major role for uncertainties in DEMs. Overall, the results in steeper areas show that the loss of vertical accuracy is two to three times higher for a 90 m DEM than for DEMs of higher spatial resolutions. While very high resolution DEMs of 12 m spatial resolution or higher only lose about 1 m accuracy per 10° increase in slope steepness, 30 m DEMs lose about 2 m on average, and 90 m DEMs lose more than 3 m up to 6 m accuracy. However, the results also show significant differences for DEMs of identical spatial resolution depending on relief and land cover. With regard to different land cover classes, it can be stated that mid-latitude forested and water areas cause uncertainties in DEMs of about 6 m on average. Other tested land cover classes produced minor errors of about 1 – 2 m on average.

The results of the second part of this contribution prove that a careful selection of an appropriate DEM is more crucial for certain applications than for others. The choice of different DEMs greatly impacted the landform classification results. Results from medium resolution DEMs (30 m) achieved up to 30 % lower overall accuracies than results from high resolution DEMs with a spatial resolution of 5 m. In contrast to the landform classification results, the predicted soil types in the second case study showed only minor accuracy differences of less than 2 % between the usage of a spatial high resolution DEM (15 m) and a low resolution 90 m DEM. Finally, the results of these two case studies were compared and discussed with other results from the literature in other application areas. A summary and assessment of the current state of knowledge about the impact of a particular chosen terrain model on the results of different applications was made.

In summary, the vertical accuracy measures obtained for each DEM are a first attempt to determine individual error values for each DEM that can be interpreted independently of relief and land cover and can be better applied to other regions. This may help users in the future to better estimate the accuracy of a tested DEM in a particular landscape. The consequences of elevation model selection on further results are highly dependent on the topic of the study and the study area's level of detail. The current state of knowledge on the impact of uncertainties in DEMs on various applications could be established. However, the results of this work can be seen as a first step and more work is needed in the future to extend the knowledge of the effects of DEM uncertainties on further topics that have not been investigated to date.

Zusammenfassung

Digitale Geländemodelle (engl. digital elevation models, DEMs) werden häufig genutzt, um eine digitale Darstellung und Repräsentation der Erdoberfläche in zahlreichen Bereichen der Wissenschaft, Industrie und im Militär zu erhalten. Da viele Prozesse auf der Erde von der Form des Reliefs beeinflusst werden, sind eine Vielzahl unterschiedlicher Anwendungen auf genaue topografische Informationen angewiesen. DEMs werden beispielsweise genutzt für die Vorhersage von Georisiken, Klimamodellierungen, oder planungsrelevante Fragestellungen wie die Ermittlung geeigneter Standorte für erneuerbare Energien. Digitale Geländemodelle können heutzutage durch verschiedene Fernerkundungstechniken, wie Photogrammmetrie, RADAR, oder Laserscanning (LiDAR), mit hoher geometrischer Auflösung und über große Gebiete erstellt werden. Dennoch sind sie mit Unsicherheiten behaftet und können fehlerhafte Darstellungen des Geländes enthalten. Die Qualität und Genauigkeit der abgebildeten Topografie ist jedoch von entscheidender Bedeutung. Die Nutzung eines fehlerbehafteten Datensatzes kann negative Auswirkungen auf weiterführende Ergebnisse haben, wie beispielsweise die Unterschätzung von Hangrutschungsgefahren durch ein zu flach dargestelltes Relief im Geländemodell. Es ist daher wichtig, genaue Kenntnisse über die Qualität eines verwendeten Geländemodells in einem bestimmten Gebiet zu besitzen, um negative Konsequenzen auf weiterführende Ergebnisse verschiedenster Forschungsanwendungen besser abschätzen zu können. Eine angemessene Beurteilung darüber, ob der Erwerb eines hochgenauen DEMs notwendig ist, oder die Verwendung eines bereits vorhandenen und frei verfügbaren DEMs zur Erzielung hinreichend genauer Ergebnisse ausreicht, ist von qualitativer und ökonomischer Wichtigkeit.

Im ersten Teil dieser Arbeit steht die Erweiterung des Wissens über das Auftreten von Unsicherheiten in DEMs in Bezug auf Gelände und Landbedeckung im Vordergrund. Die ersten beiden Studien dieser Dissertation liefern hierzu eine umfassende Analyse der vertikalen Genauigkeit von zwölf aus dem Weltraum aufgenommenen DEMs, welche eine geometrische Auflösung zwischen 5 m und 90 m besitzen. Die Genauigkeit dieser DEMs wurde in zwei unterschiedlichen Regionen der Welt untersucht, die sich in Bezug auf Relief und Landbedeckung stark unterscheiden. Die erste Studie erfolgte in der hyperariden chilenischen Atacama-Wüste im Norden Chiles, mit kaum vorhandener Landbedeckung und sehr großen Höhenunterschieden im Relief. Die zweite Fallstudie wurde in einer Region der mittleren Breiten durchgeführt, dem Rur-Einzugsgebiet im westlichen Teil Deutschlands. Dieses Gebiet besitzt ein überwiegend flaches bis hügeliges Gelände mit vielfältiger Vegetation und Landbedeckung. Die Auswertung beider Studien erfolgte mit besonderem Augenmerk auf den Einfluss von Relief und Landbedeckung auf die vertikale Genauigkeit der DEMs. Es wurde die Änderung des Fehlers durch wechselnde Hangneigungen und Landbedeckungen quantifiziert, um für jedes DEM einen durchschnittlichen Genauigkeitsverlust in Abhängigkeit zur Hangneigung zu ermitteln. Zusätzlich wurden diese Werte zur Ableitung von reliefbereinigten Fehlerwerten für verschiedene Landbedeckungsklassen verwendet.

Der zweite Teil dieser Dissertation befasste sich mit den Folgen, die unterschiedliche räumliche Auflösungen und Genauigkeiten in DEMs auf bestimmte Anwendungen haben können. Diese Auswirkungen wurden beispielhaft anhand von zwei verschiedenen Fallstudien untersucht. In einer geomorphometrischen Fallstudie wurden verschiedene Geländemodelle verwendet, um Landformen mit unterschiedlichen Methodiken zu klassifizieren. Die Ergebnisse wurden im Anschluss verglichen und die Genauigkeit der Klassifikationsergebnisse, hergestellt durch die Nutzung unterschiedlicher DEMs, analysiert. Die zweite Fallstudie ist im Bereich der digitalen Bodenkartierung angesiedelt. Es

wurden unter der Verwendung von zahlreichen Reliefparametern, abgeleitet von DEMs unterschiedlicher Auflösung, verschiedene Bodentypen mit Hilfe von Algorithmen des maschinellen Lernens (Random Forest und künstliche neuronale Netze) vorhergesagt. Anschließend wurde der Einfluss von hoch- und geringauflösenden DEMs mit den jeweils daraus abgeleiteten Landoberflächenparametern auf die Vorhersageergebnisse evaluiert.

Die Ergebnisse aus der Analyse der vertikalen Genauigkeit zeigen, dass Unsicherheiten in DEMs sehr vielfältige Ursachen besitzen können. Nicht nur die räumliche Auflösung, sondern auch die Aufnahmetechnik und der Grad der vorgenommenen Verbesserungen am DEM haben einen wesentlichen Einfluss auf das Vorkommen von Fehlern in einem DEM. Darüber hinaus haben das Relief und das Vorkommen von Objekten auf der Oberfläche einen erheblichen Einfluss auf die Genauigkeit von DEMs. Insgesamt zeigen die Ergebnisse in steileren Regionen, dass der Genauigkeitsverlust bei einem 90 m DEM zwei- bis dreimal so hoch ist im Vergleich zu DEMs höherer räumlicher Auflösung. Während sehr hoch aufgelöste DEMs mit einer geometrischen Auflösung von 12 m oder höher nur ca. 1 m Genauigkeitsverlust pro 10° steigender Hangneigung aufweisen, sinkt die Genauigkeit bei 30 m DEMs im Durchschnitt um etwa 2 m und bei 90 m DEMs um mehr als 3 m bis hin zu 6 m. Die Ergebnisse zeigen darüber hinaus für DEMs gleicher Auflösung deutliche Unterschiede in der Genauigkeit in Abhängigkeit von Relief und Landbedeckung. In Bezug auf unterschiedliche Landbedeckungsklassen ist feststellbar, dass Wald- und Wasserflächen in den mittleren Breiten Unsicherheiten von durchschnittlich 6 m in DEMs verursachen, andere Landbedeckungsklassen lediglich einen Fehler von nur 1 – 2 m im Durchschnitt.

Die Ergebnisse des zweiten Teils dieser Arbeit zeigen, dass die sorgfältige Auswahl eines geeigneten DEMs für bestimmte Anwendungen wichtiger ist als für andere. Die Wahl des DEMs hatte einen sehr großen Einfluss auf die Ergebnisse der Landformklassifikation. Geländemodelle mit mittlerer Auflösung (30 m) erzielten eine bis zu 30 % niedrigere Gesamtgenauigkeit als hochauflösende DEMs mit einer geometrischen Auflösung von 5 m. Im Gegensatz zu den Ergebnissen der Landformklassifikationen, zeigten die vorhergesagten Bodentypen in der zweiten Studie einen nur geringen Genauigkeitsunterschied von weniger als 2 % zwischen der Nutzung eines räumlich hoch aufgelösten DEMs (15 m) und eines niedrig aufgelösten 90 m DEMs. Abschließend wurden die Ergebnisse dieser beiden Fallstudien mit weiteren Ergebnissen aus der Literatur in anderen Anwendungsgebieten verglichen und diskutiert. Es erfolgte eine Zusammenfassung und Einschätzung des aktuellen Wissensstandes über die Auswirkungen, die die Wahl eines bestimmten Geländemodelles auf die Ergebnisse verschiedener Anwendungen hat.

Zusammenfassend lässt sich festhalten, dass die erzielten vertikalen Genauigkeitsmaße der einzelnen getesteten DEMs einen ersten Versuch darstellen, individuelle Fehlerwerte für jedes DEM zu ermitteln, die unabhängig von Relief und Landbedeckung interpretierbar sind und eine bessere Übertragbarkeit auf andere Regionen zulassen. Dies könnte Anwendern zukünftig helfen, die Genauigkeit eines getesteten DEMs in einer bestimmten Landschaft besser einschätzen zu können. Die Folgen der Geländemodellwahl auf weiterführende Ergebnisse hängt stark von Ziel und Inhalt der Studie und dem Detailgrad des Untersuchungsgebiets ab. Es konnte der aktuelle Wissensstand über die Auswirkungen von Unsicherheiten in Geländemodellen auf verschiedene Anwendungen aufgezeigt werden. Allerdings sind die vorliegenden Ergebnisse nur ein erster Schritt in diese Richtung und es sind weitere zukünftige Arbeiten notwendig, um dieses Wissen auf weitere und bisher nicht untersuchte Themen zu erweitern.

Acknowledgements

Now, as I am writing the last lines of this dissertation, it is the time to express my gratefulness to all those who have supported me over the last years and contributed to the successful completion of this contribution.

My special thanks go to Dr. Dirk Hoffmeister for his outstanding support of my work throughout the years. I thank him for guiding me the way through the scientific jungle and the fruitful ideas, valuable comments and motivation he gave to me. Without his support, this dissertation would probably never have been written.

I am also very grateful to my supervisor Prof. Dr. Georg Bareth for giving me the opportunity to work in his GIS & Remote Sensing working group and on this dissertation project. I particularly thank him for his continuous support and for giving me the freedom to work on so many totally different topics from geomorphometry to research data management.

I also express my thanks to Prof. Dr. Karl Schneider for his willingness to act as the co-examiner of this dissertation. Furthermore, I thank Prof. Dr. Ines Neundorf and Dr. Andreas Bolten for being members of the disputation committee.

I gratefully acknowledge the financial support of the German Research Foundation (DFG). A lot of data has been used in this dissertation that was acquired within the framework of the following DFG-funded research projects:

- SFB/TR32: “Patterns in Soil-Vegetation-Atmosphere Systems: Monitoring, Modelling and Data Assimilation”.
- CRC 1211: “Earth - Evolution at the Dry Limit”.
- “Remote sensing methods as a base for landform and soil maps of the Iranian loess plateau”.

Furthermore, I am grateful for the funding of the DFG project CRC/TRR228 “Future Rural Africa: Future-making and social-ecological transformation” that helped a lot to finance my position during the last years.

Many thanks also go to my colleagues of the GIS & Remote Sensing research group for good collaborations and a very nice working atmosphere. I particularly thank my former colleague Dr. Constanze Curdt who gave me the opportunity to immerse myself in the field of research data management and helped me a lot with different kinds of tasks through the years.

Moreover, I am deeply grateful to everyone who reviewed and proofread the manuscript and gave valuable comments for improvement.

Most importantly, I warmly thank my wonderful family for their constant love and caring support throughout my entire life.

Table of Contents

List of Figures

List of Tables

List of Abbreviations

ALOS	Advanced Land Observing Satellite
ALS	Airborne laser scanning
ANN	Artificial neural networks
ASTER	Advanced Spaceborne Thermal Emission and Reflection Radiometer
CCD	Charge-coupled device
DEM	Digital elevation model
DGPS	Differential Global Positioning System
DLR	German Aerospace Center
DSM	Digital surface model
DTM	Digital terrain model
ECP	Elevation control point
EDM	Electronic Distance Measurements
EGM96	Earth Gravitational Model 1996
EPSG	European Petroleum Survey Group
ESA	European Space Agency
GCP	Ground control point
GDEM	Global digital elevation model
GIS	Geographical Information System
GNSS	Global Navigation Satellite Systems
GPS	Global Positioning System
GSD	Ground sampling distance
ICESat	Ice, Cloud, and land Elevation Satellite
IDW	Inverse distance weighting
InSAR	Interferometric synthetic aperture radar
JAXA	Japan Aerospace Exploration Agency
LiDAR	Light detection and ranging
ML	Machine learning
MSL	Mean sea level
NASA	National Aeronautics and Space Administration
NMAD	Normalized median absolute deviation
NOAA	National Oceanic and Atmospheric Administration
OA	Overall accuracy
OBIA	Object-based image analysis
PA	Producer's accuracy
RADAR	Radio detection and ranging
RF	Random forest
RMSE	Root mean square error
RPC	Rational polynomial coefficient
RTK	Real time kinematic
SAR	Synthetic aperture radar
SPOT	Satellite Pour l'Observation de la Terre
SRTM	Shuttle Radar Topography Mission
TIN	Triangulated irregular network
TLS	Terrestrial laser scanning
TOF	Time-of-flight
TPI	Topographic position index
TRI	Terrain ruggedness index
TWI	Topographic wetness index
UA	User's accuracy
UAV	Unmanned aerial vehicle
UTM	Universal Transverse Mercator
WGS84	World Geodetic System 1984

1 Introduction

1.1 Preface

The relief is a key driver for a multitude of processes that occur on Earth. It affects the formation of soils, influences climatic conditions of humidity, wind and temperature as well as the presence or absence of certain species of flora and fauna (Franklin, 1995; Franklin, 2020; McBratney et al., 2003). In addition, different topographical forms and slopes influence gravity driven processes of hydrology, geomorphology and geology, such as landslides as well as erosion and accumulation processes (Hawker et al., 2018; Kirkby and Chorley, 1967; Pandey et al., 2016). Accurate information about the topography helps to describe and understand these processes and is therefore important for many scientific, commercial, industrial and even military applications (Mesa-Mingorance et al., 2017; Tarquini and Nannipieri, 2017). The importance of relief for current planning-relevant issues, such as the siting of transmission towers in telecommunications or of wind turbines to produce renewable energy, has increased significantly in recent decades (Chias and Abad, 2013; Murgatroyd et al., 2021; Shi and Xue, 2016). Furthermore, digital height information is used in a great variety of geohazard risk management purposes, such as hydrological modelling to predict water flow and determine flooding risks (Bajabaa et al., 2014; Callaghan and Wickert, 2019; Hoch et al., 2017) or for the prediction of landslide risks and slope instabilities (Baharvand et al., 2020; Iwahashi et al., 2021; Liu et al., 2021; Sturzenegger et al., 2021). Hence, numerous applications usually rely on digital height information of an appropriate accuracy and spatial resolution to represent the topography of an area.

Nowadays, using height information from digital sources is an established method to represent the Earth's relief. Digital elevation datasets, such as digital elevation models (DEM) or triangulated irregular networks (TINs), directly provide the height component of the surface. Based on digital height information, a multitude of land surface parameters can be derived by a DEM that provide additional information, such as terrain steepness and direction, roughness, moisture or visual exposure (Olaya, 2009). A vastly increasing and sophisticated range of datasets and techniques for topographic analysis, modelling and visualization has been established during the last decades. In former times, surveying the world was conducted by the use of traditional terrestrial instruments, which was a time consuming and laborious process. Nowadays, with photogrammetry, RADAR (InSAR) and laser scanning (LiDAR), three methods have been developed that enable large-scale surveying of elevation information with remote sensing techniques (Maune and Nayegandhi, 2018; Wilson, 2018). In particular, the RADAR based Shuttle Radar Topography Mission (SRTM) in February 2000 was an important step forward in the development of nearly globally available elevation data of remarkable spatial resolution. Additionally, satellite-based acquisition methods gained popularity as an efficient way of large-scale terrain mapping of high resolution.

Except for the pole-near areas, almost the entire surface of our planet has been mapped many times with varying accuracy, resolution and by different sensors. Significant improvements in DEM quality and resolution have been achieved over the past decades (Farr et al., 2007; Gesch et al., 2012; Hodgson and Bresnahan, 2004; Tachikawa et al., 2011). However, according to Ariza-Lopez et al. (2018) and Polidori and El Hage (2020), the acquisition and processing of data is still subject to various limitations and uncertainties. More knowledge should be developed on how the error behaviour as well as the spatial resolution of DEMs impacts the results of different research applications. The selection of an appropriate DEM is crucial for the outcome of many analyses and applications. According to a survey

carried out by Ariza-Lopez et al. (2018), over 85 % of participants, who use DEMs, state that a poor quality of the DEM product has a medium to high negative impact on their results. They also reveal that there is little knowledge among scientists on the relationship between DEM quality and results for their use case scenarios and the resulting economic consequences. For instance, results of Kaminski (2020) show in the context of landslide susceptibility prediction that a DEM of poor quality can cause misconceptions, which may have fatal consequences in the estimation of risks. For several scientific modelling purposes, a low spatial resolution can lead to uncertainties in prediction results. Likewise, the usage of different DEMs for the prediction of movements of past people at archaeological sites results in considerably different catchment sizes or travelling paths (Becker et al., 2017; Lewis, 2021). The results show that significant variations are observable in the calculated routings and prehistoric catchment sizes that can be potentially reached within a certain time.

These examples reveal that a poor quality of a DEM can cause serious issues on the results of further applications. In order to make the best possible estimation about the accuracy of certain application results, knowledge about the quality of input data is of great importance. Hence, much work has already been done to evaluate the accuracy of DEMs for different scientific applications, scales and landscapes. Mesa-Mingorance and Ariza-Lopez (2020) stated that more than 170 scientific documents have been published during the last 30 years that focus on the accuracy assessment of DEMs. However, most of them compared only a limited number of DEMs and mostly only for one specific region or scale, but the accuracy of a DEM depends on a multitude of factors such as the relief and land cover as well as the acquisition platform and spatial resolution. These factors make it difficult to transfer the results of a local study into other regions as acquisition parameters and the landscape characteristics may be completely different between two sites (Polidori and El Hage, 2020). Furthermore, all these accuracy factors can lead to an accumulated error which has an impact on subsequent analysis tasks where these DEMs are used. This means, the output of an analysis process is affected by the accuracy of the topographic input data. Therefore, it is of great importance to gain more knowledge about the quality of digital elevation datasets and the implication of its quality on further analysis tasks (Ariza-Lopez et al., 2018; Guth et al., 2021; Polidori and El Hage, 2020). However, the impact of DEM quality on other applications is diverse and needs to be considered separately for each task. Thus, there is still a lack of knowledge about which applications really require highly accurate DEMs of high spatial resolution.

1.2 Research objectives and study aims

This contribution is settled on the need of accurate elevation information in numerous applications and has two overall research objectives. The first part of this thesis aims to provide an encompassing vertical accuracy assessment of a multitude of DEMs with a spatial resolution between 5 m and 90 m. These DEMs are derived from many different sources, such as the SRTM mission, the TanDEM-X WorldDEM™ data or from stereo-photogrammetric imagery. Subsequently to this analysis of DEM accuracy, the second part of this contribution focuses on the impact of accuracy and spatial resolution of a DEM on further geoscientific applications. It is examined for the applications of digital soil mapping and landform classification how the results of these applications are affected by DEMs of different sources and spatial resolutions.

Part one of this contribution aims to gain more information about the vertical error behavior of DEMs caused by different slopes and land cover. Overall, this part contributes to existing research by providing accuracy values for a multitude of different DEMs and enhancing the analyses by regarding error values in connection with different slopes, landforms and land cover. For this purpose, the studies of vertical accuracy assessment were conducted in two different study sites to gain a comprehensive overview. One study was settled within the hyperarid Chilean Atacama Desert, the other in the typical mid-latitude landscape of the Rur catchment in Germany. The goal is to not only mention the differences in accuracy between various topography settings, but rather quantify the expectable error values of DEMs in relation to landscape and topography. Thus, a relief-dependent error is established, which enables the possibility to estimate the uncertainty of every tested DEM in all terrain slopes. Additionally, the influence of relief unbiased land cover classes on the accuracy of DEMs has been calculated. These accuracy values can help a user to predict the accuracy of a DEM on a certain study area for a given application. Overall, the contribution finds an answer to the following questions regarding the accuracy of a DEM:

- How accurate are different DEMs in certain relief and land cover situations?
- What is the most accurate DEM in which area?
- How much is the accuracy of a DEM influenced by spatial resolution, different acquisition techniques as well as relief and land cover?
- How much differences in quality consist between DEMs of local and global coverage?

In a second step, this contribution investigates the influence that the quality of DEMs and their derived parameters have on the analysis results of further applications. It was evaluated how much the results of a certain application are affected by DEMs of different sources and spatial resolution. For this purpose, two practical studies have been conducted within this contribution. It was exemplarily examined for the applications of digital soil mapping and landform classification, how much the results depend on the choice of an appropriate DEM. Additionally, further literature on this topic has been reviewed for other applications to overall obtain an answer to the following questions:

- How important is the right choice of a certain DEM for a particular application?
- How much are the analysis results of this application influenced by DEMs of a certain spatial resolution or a particular source?
- When is it advantageous to use a more accurate and expensive DEM over the freely available ones?

1.3 Study outline

To evaluate different DEMs and their effects on further applications, a general introduction about the basic principles of DEMs is given in chapter 2. This includes the definition of different digital elevation data types and structures as well as the description of different acquisition techniques to gain DEM data. Furthermore, this chapter introduces the different fields of scientific applications where DEMs are a widely used source for their analysis. Additionally, potential sources of errors in DEMs and common methods of accuracy assessment of DEMs are presented. Finally, chapter 2 ends with a brief introduction to the three study areas of this contribution.

The subsequent chapters 3 to 5 contain a comprehensive vertical accuracy assessment of a large number of different spaceborne DEMs. An overview of the DEMs used in the individual chapters is provided in Table 1-1. The assessment was conducted in two regions of the world that are rather contrastive in their terrain and land cover. The first research study has been performed in the hyperarid region of the Atacama Desert in Chile with large elevation differences and very sparse vegetation and settlement areas (chapter 3). Subsequently, chapter 4 provides an additional assessment of further newly released DEMs in the same study area to extend the results of chapter 3. In chapter 5, a second study has been carried out focusing on a vertical accuracy assessment of DEMs in the mid-latitude Rur catchment area in Germany. As this area is vastly different to the Atacama Desert, these results help to provide a more representative overview of the strengths and weaknesses of the individual DEMs.

Table 1-1: Overview about the different elevation datasets that were used and analysed in the different chapters of this contribution.

DEM	Spatial resolution	Acquisition source	Chapter 3	4	5	6	7
ALOS W3D	30 m	Stereo imagery	x		x		
ASTER GDEM	30 m	Stereo imagery	x		x	x	
Copernicus DEM	30 m	X-band RADAR		x	x		
Copernicus DEM	90 m	X-band RADAR		x	x		
DGM1	1 m	Airborne laser scanning					x
EU-DEM	25 m	C-band RADAR/Stereo imagery			x		
NASADEM	30 m	C-band RADAR		x	x		
Pléiades DEMs	5 m	Stereo imagery	x			x	
SPOT DEMs	5 m	Stereo imagery	x				
SRTM	30 m	C-band RADAR	x		x	x	
SRTM	90 m	C-band RADAR	x		x		
TanDEM-X	12 m	X-band RADAR	x				
TanDEM-X	90 m	X-band RADAR	x		x		x

The second part of this contribution contains two different case studies where DEMs and derived land surface parameters are necessary and crucial sources. Both studies are conducted to achieve more information about the influence that the choice of different DEMs has on the results of this application. Chapter 6 contains different input DEMs and compares the classification results of landforms with different classification approaches. The study in chapter 7 contains the prediction of different soil types with two different machine learning algorithms. DEMs and derived environmental parameters are key drivers in soil development and thus in the area of digital soil mapping (McBratney et al., 2003). By using two different DEMs and derived parameters in this approach, the influence on the prediction results for this approach is analysed.

In chapter 8, the results of the previously presented studies are discussed and interpreted concerning the objectives that have been presented in chapter 1.2. In the first part of the discussion, the gained results of the vertical accuracy assessment in chapters 3 to 5 are discussed and interpreted for all tested DEMs. The results are analysed with regard to the influence that environmental factors of relief and landscape have on the accuracy of DEMs from different acquisition sources. Furthermore, relief- and land cover adjusted accuracy values are derived. The second part of the discussion disputes the importance that the selection of a certain DEM of different source and spatial resolution has on the results of different applications. Thus, the results of the two studies of this contribution and additional findings from other studies on this topic are discussed here. Finally, a conclusion and a brief outlook is given in chapter 9.

2 Background

2.1 Digital elevation data types and structure

The relief can be generally understood as the boundary between the lithosphere/pedosphere and the atmosphere/hydrosphere (Dikau and Schmidt, 1999). Thus, it is the shape of the ground surface and represents the height differences over a predefined area. A digital elevation dataset is the numerical storage of this 3D terrain information. It is a digital representation of the Earth's relief and reflects its elevations in all various forms. To date, several terms have been established for digital elevation datasets and their definitions have to be clarified first, because they are sometimes used confusingly in literature.

The term digital elevation model is mostly used as a generic term for digital topographic datasets in all different forms (Guth et al., 2021). It normally depicts bare-earth elevations but may also include vegetation or manmade objects, depending on the acquisition technique. It also normally implies the water surface of lakes and rivers and does not reflect the ground below (Maune and Nayegandhi, 2018). Additionally, two nominal surfaces can be considered by elevation models with the digital surface model (DSM) and the digital terrain model (DTM). The difference between both definitions is illustrated in Figure 2-1. The DSM represents all elevations including surface objects, such as vegetation and buildings (Guth et al., 2021; Maune and Nayegandhi, 2018). In contrast, a DTM encompasses only bare-earth elevations without any natural or artificial objects that are located on top of the ground (Guth et al., 2021; Maune and Nayegandhi, 2018). The earliest definition of a DTM was given by Miller and Laflamme (1958) as "a statistical representation of the continuous surface of the ground by a large number of selected points with known XYZ coordinates in an arbitrary coordinate field". In the current contribution, the term DEM is used as a synonym of DSM as all investigated DEMs of this thesis cover the Earth's surface as a surface model.

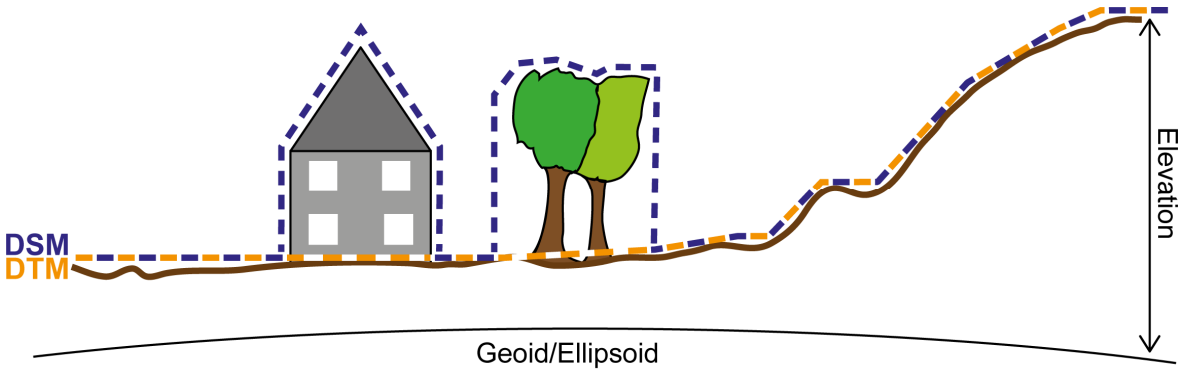

Figure 2-1: Illustration of the differences between digital surface model (DSM) and digital terrain model (DTM).

DEMs usually exist either as a 3D or as a 2.5D dataset. DEMs can be understood as 3D when their elevation data was directly measured or generated from the source and each 2D position can be represented by multiple points of different height information (Lenk and Heipke, 2002). In contrast, 2.5D DEMs are originally 2D data sets whose locations subsequently received only single elevation information (Lenk, 2001; Lenk and Heipke, 2002). These 2.5D DEMs are commonly used in GIS software as a raster dataset to represent the Earth's surface.

Digital elevation data can be represented and stored in different forms (Figure 2-2). The most frequently used structure is the storage of elevations as a regular grid. Over 90 % of all users who work

with digital elevation data use this data type for their analysis (Ariza-Lopez et al., 2018). Raster DEMs store elevation information in a series of rows and columns as a regular matrix of uniform grid width. The major advantage of raster DEMs is the possibility to relatively easy and fast handle the data for further applications and processing due to the simple and regular data structure (Hengl and Evans, 2009; Maune and Nayegandhi, 2018; Moore et al., 1991). A disadvantage of this storage technique is the inability to store points and lines of characteristic surface changes. This often leads to an under-representation of complex relief. Raster datasets are often generated by interpolating point-based elevation information to the regular grid structure of a desired spatial resolution. Several different interpolation methods exist, such as the Inverse Distance Weighted (IDW) interpolation, the Natural Neighbour interpolation or geostatistical approaches (Mitas and Mitasova, 1999).

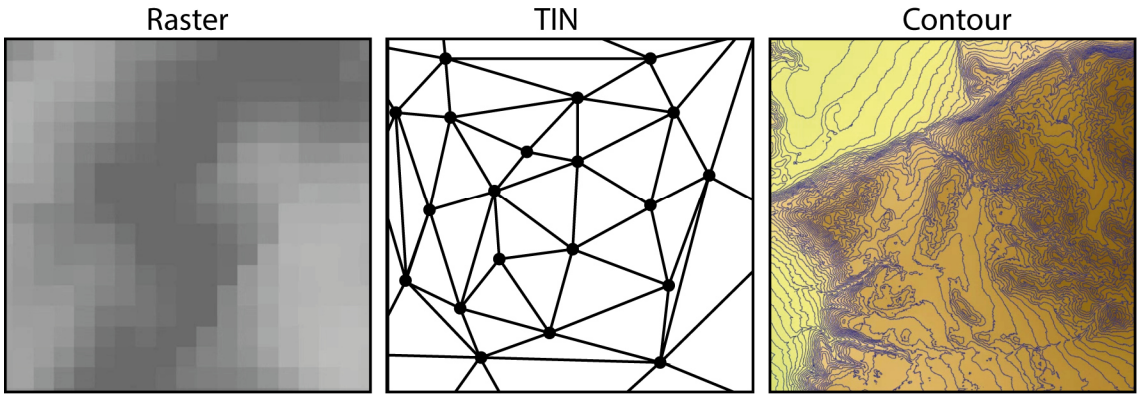

Figure 2-2: Illustration of different digital elevation data types.

Another common form of digital terrain representation is the vector-based surface by triangulated irregular networks. TINs consist of irregularly spaced 3D points that were connected to non-overlapping triangles (Moore and Hutchinson, 1991). These data points store the topological relationship between neighbouring triangles (Kumler, 1994; Maune and Nayegandhi, 2018). In comparison to raster datasets, TINs can better reflect surface changes as the density of triangles can vary depending on the complexity of terrain (Moore and Hutchinson, 1991). A major disadvantage of TINs is the greater difficulty to handle the data due to their more complex data structure.

As a third form of illustration, topography can also be represented by contour lines. These are 2D elevation isolines, with each line representing equal heights. They are well suitable for visual human interpretations, but have weaknesses in computational analyses. Contours are usually used in maps to illustrate the relief and show the steepness of slopes to support the visualization of specific regional relief characterizations and specific landforms (Carrara et al., 1997; Moore et al., 1991; Wilson, 2018).

2.2 Horizontal and vertical datum

To define the 3D position of an object on the Earth's surface by means of coordinates, it is necessary to know its datum in horizontal and vertical direction. The datum can be seen as a defined starting point of an abstract coordinate system that determines its connection to the Earth. The Earth's shape can be seen as a three-dimensional 'potato' that cannot be described exactly neither mathematically nor physically. This leads to some difficulties when the exact location of a point feature has to be determined. A model is needed that, on the one hand, 'fits' the shape of the Earth as accurately as possible, but on the other hand, is also mathematically calculable. Due to the existence of different

global, regional, national and local datums, the same position on the planet can have many different geographic coordinates. Therefore, it is important to know to which reference system the measured point is located. For individual identification, all datums are ideally assigned to a unique European Petroleum Survey Group (EPSG) code.

The horizontal datum is used to determine a specific position on the Earth's surface in coordinate systems. It can be defined in terms of geographic coordinate systems (i.e., latitude and longitude) or plane coordinate systems, such as UTM. Height measurements in a vertical direction can be seen as the vertical distance from a reference level surface (Guth et al., 2021; Hengl and Evans, 2009). These were defined by a vertical datum that represents a surface of zero height. Several types of reference surfaces have been established. The most traditional is the definition of height above mean sea level (MSL). This method has been practiced over several centuries and defines the mean surface of a large water body as a natural reference for elevations (Maune and Nayegandhi, 2018). However, water is usually not a static object and is affected by varying tides, waves and atmospheric impacts. Therefore, the datum is defined as the arithmetic mean of hourly sea level heights over a period of about 19 years (Maune and Nayegandhi, 2018). As the effects of local gravity are not considered, the altitude of MSL varies around the world. Transferring the MSL heights over land surface can be a cumbersome process by generating a high-precision levelling network (Kahmen, 2006).

Due to the previously mentioned difficulties of measuring sea level, the geoid has been established as another reference surface. The geoid is defined by the gravity field of the Earth. Considering the water of a sea as a freely moving mass, which is subjected only to the gravitational force composed of gravity and centrifugal force, then the surface of the oceans can be seen as a level surface of the gravity potential (Kahmen, 2006; Maune and Nayegandhi, 2018). Its equipotential surface in the gravitational field approximates the mean sea level as best as possible. This idealized sea level can be imagined to be continued under the continents so that it forms a closed surface, the geoid (Dietrich, 2021). Due to the irregular distribution of mass density in the Earth's body, the geoid cannot be described by an algebraic surface equation. It must be determined by terrestrial or satellite geodesy measurement methods (Kahmen, 2006; Maune and Nayegandhi, 2018).

Another definable reference surface is based on the mathematical model of ellipsoids. These so-called rotational ellipsoids are the most accurate mathematical description of the Earth's surface, as they consider the polar flattening of the globe (Maune and Nayegandhi, 2018). The center of such an ellipsoid can coincide with the center of gravity of the Earth (geocentric rotation ellipsoid) which is usually used for global observations. However, there are also ellipsoids which are displaced in their position from the center of the Earth to obtain higher accuracies for certain parts of the Earth's surface. These local coordinate systems can only describe a particular section of the globe with sufficient accuracy and are unsuitable for other locations (Dietrich, 2021). Thus, unlike the geoid, which has a unique definition, a large number of different ellipsoids exist for different parts of the world. The schematic difference between a reference geoid and ellipsoid is depicted in Figure 2-3.

To date, hundreds of horizontal and vertical datums were established for local and global coverage (Maune and Nayegandhi, 2018). For users of geospatial datasets, the datum is of high importance, as the difference between different datums can exceed tens of meters. This may cause problems in their practical use and interpretation, resulting in large errors. For example, the undulation between the geoid and the World Geodetic System 1984 (WGS84) ellipsoid can be up to 100 m depending on the location on Earth (Guth et al., 2021; Hengl and Evans, 2009). The undulation between different

reference ellipsoids can also be up to several meters (Kahmen, 2006). Therefore, it is important to transform different elevation datasets into the same datum before usage.

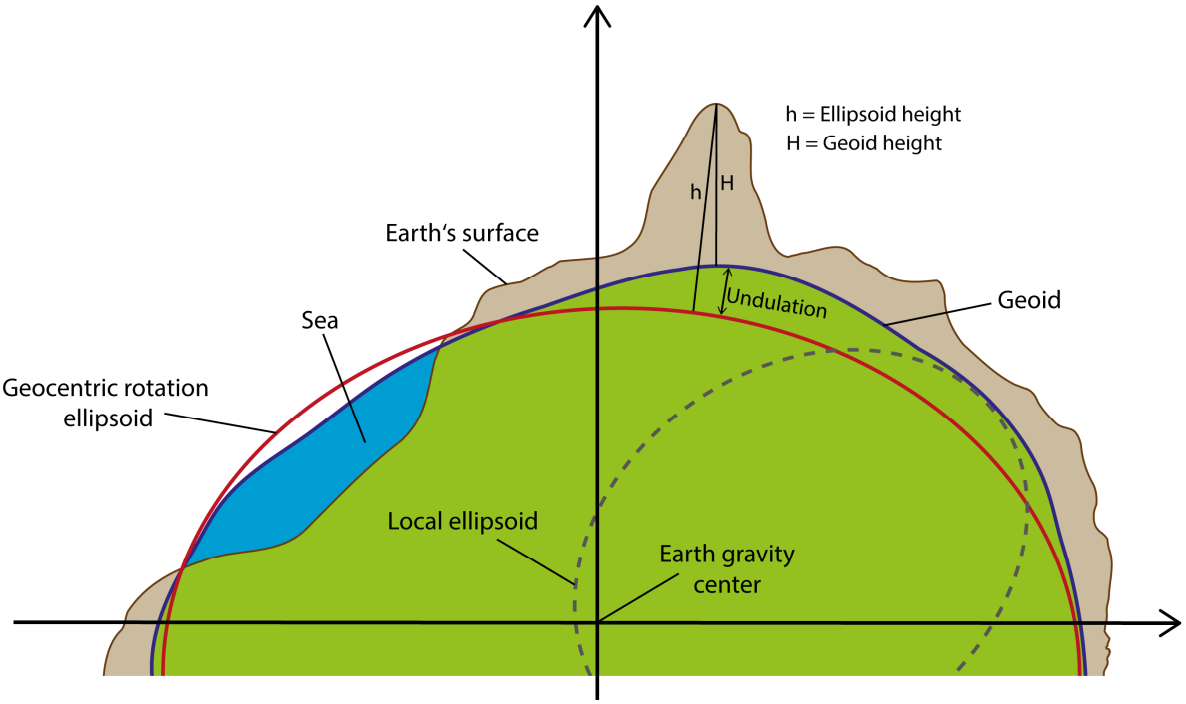

Figure 2-3: Schematic illustration of the differences between geoid, ellipsoid and local ellipsoid. The geoid approximates a (hypothetical) global mean sea level that represents the equipotential gravitational surface of the Earth. An ellipsoid is the approximation of the geoid by the mathematical model of ellipsoids.

2.3 Acquisition techniques

Many different remote sensing techniques have been evolved in the last decades that can be used to acquire elevation data. The most common methods will be described in the following sections. All methods are suitable for the acquisition of 3D surface data from a terrestrial, airborne and spaceborne position. In general, two different types of sensors can be distinguished for acquisition, active and passive sensors. Active sensors have their own source of light or signal for measurement, actively send the source of illumination to the ground and measure the reflected backscatter. In contrast, passive sensors do not streamline any source of emission signal on their own. They use the reflected or absorbed and re-emitted energy of the target location.

2.3.1 Photogrammetry

Photogrammetry is a remote sensing technique that enables the reconstruction of the position and shape of objects from imagery (Kraus, 2004). The pioneering work of Albrecht Meydenbauer in gathering 3D objects from photographical data and the introduction of stereo-photogrammetry by Carl Pulfrich in 1901 (Naturwissenschaftliche Abtheilung, 1901) made it possible to obtain the 3D position of a specific point from two or more overlapping images. The photogrammetric generation of elevation data can be done with imagery from terrestrial, airborne (including UAVs) or spaceborne platforms. It is a passive remote sensing technique that does not directly emit any kind of energy source for

measurement and only detects reflected or absorbed and re-emitted energy (Albertz, 2009). Hence, photogrammetric acquisition requires for its functionality naturally occurring energy, which is usually only available during daytime when corresponding parts of the Earth are illuminated by the sun.

The principle of photogrammetry is illustrated in Figure 2-4 and bases on the mathematical model of triangulation, where the same point in space is targeted from at least two different positions (Lillesand et al., 2015). In practice, the imaging geometry at the time of acquisition must be restored. This can be done according to the rules of central projection by following the collinearity condition (Kraus, 2004; Lillesand et al., 2015). Thereby, each image defines a direction to the real object point P for an imaged point P' together with the projection center O of the respective camera (Kraus, 2004). Knowing the position and orientation of the camera in space at the time of image recording (external orientation) as well as the geometry of the image layer inside the camera (internal orientation) allows to determine every ray in space. The internal orientation is usually determined during a camera calibration of the projection center position in relation to the sensor or is provided by the manufacturer. The external orientation is often determined by using the Global Positioning System (GPS), Global Navigation Satellite Systems (GNSS) and inertial navigation systems (Albertz, 2009; Kraus, 2004). Satellite systems are usually providing orbital, geometric and radiometric parameters by GNSS positions and star cameras as metadata information together with their imagery (Jacobsen, 2017; Maune and Nayegandhi, 2018).

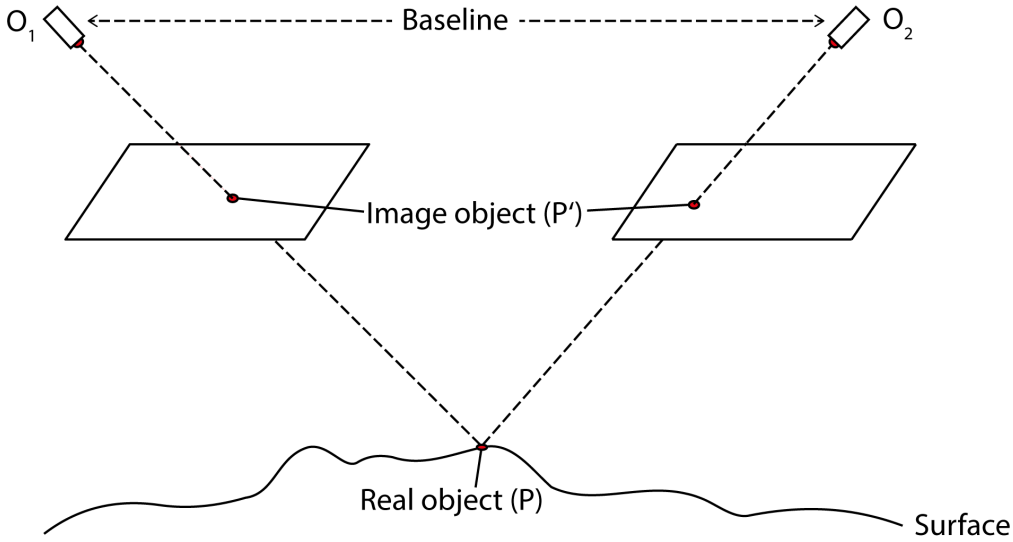

Figure 2-4: Basic geometric principle of stereo photogrammetry for the acquisition of 3D terrain information.

With the knowledge of these parameters, 3D information can be extracted by using the equation of collinearity. As input for the triangulation, ground control points (GCPs) and tie-points are measured on the overlapping imagery. In a first step, the relative orientation of two images can be defined by measuring identical points (tie-points) in two overlapping images and calculating the 3D coordinates of the depicted point in a local coordinate system. To date, many software packages provide automated tie-point measurement techniques where image operators were used to identify well-defined tie-point candidates in the overlap areas on each image. These match the appropriate candidate points between images by using the approximate image orientations and image correlation. In contrast to a time-consuming manual definition of tie-points, this method generates a large number of tie-points and builds a highly accurate triangulation as a solid geometry between both images (Maune and Nayegandhi, 2018).

With the relative orientation, the mutual spatial position of the ray bundles of image pairs is reconstructed. This means, all corresponding (homologous) projection rays intersect and form a spatial (stereo) model that is similar to the terrain in a mathematical sense. Thus, it has the same shape, but the scale is still random and it has an oblique position in space. Therefore, in a second step, the stereo model must be brought to the desired scale and the correct position in space by the absolute orientation. This must be done with surveyed and photo-identifiable GCPs of high accuracy and known horizontal and vertical position. With these points, the system can be transformed with a Helmert transformation from the local image coordinate system into a global coordinate system (Kraus, 2004). Seven parameters are necessary to transform a 3D point from one coordinate system to another. Three shifting parameters to move the point in space in X, Y, Z direction, one scale parameter and three rotation angle parameters. The relationship between the x, y, z coordinates in the model system and the X, Y, Z coordinates in the global coordinate system can be expressed by the following formula:

$$\begin{pmatrix} X \\ Y \\ Z \end{pmatrix} = \begin{pmatrix} X_U \\ Y_U \\ Z_U \end{pmatrix} + m \cdot R \cdot \begin{pmatrix} x \\ y \\ z \end{pmatrix} \tag{2-1}$$

Where:

m = scale parameter
R = Rotation matrix
$\begin{pmatrix} X_U \\ Y_U \\ Z_U \end{pmatrix}$ = Undulation parameters between both coordinate systems

In the past, the extraction of elevation information was primarily focused on producing topographic information from aerial stereo imagery that was digitized from analogue cameras (Jensen, 1995). With the increase of available digital (ortho)image products from airborne or spaceborne sensors, as well as the presence of GIS and other applications which utilize digital terrain data over the last decades, elevation information as raster datasets is the most common product (Maune and Nayegandhi, 2018). The civil photogrammetry from stereo satellite imagery started in 1986 with images from the SPOT-1 satellite. Satellite images have the advantage over aerial images that they can be generated without bureaucratic obstacles and allow image acquisition even in countries with aerial image restrictions. However, for nationwide projects in developed countries, aerial imagery is still sometimes cheaper than satellite imagery (Jacobsen, 2017).

A major disadvantage of elevation generation by photogrammetric principles is that only the 'visible' surface can be captured by imagery. Thus, DEMs derived by stereo-photogrammetry are always DSMs containing buildings, trees and other objects above the ground. As the imagery includes tree canopies, the DEM outcome is also often affected by seasonal effects, particularly in regions where trees are not covered by leaves during the whole year. Several atmospheric limitations are also evident. Cloud-free days with low haze conditions and no more than 10 % of cloud coverage are required, which decreases the flexibility in obtaining suitable scenes. Furthermore, long shadows on the imagery should be avoided by appropriate sun angles during the acquisition time (Maune and Nayegandhi, 2018). Photogrammetric DEMs often also have a higher risk for artefacts, such as spikes or pits in places where two points from the stereo-imagery were incorrectly matched. Another disadvantage is that this method requires highly accurate GCPs for georeferencing that may be not available or hard to obtain. Furthermore, it must be considered that the generation and processing of DEMs from imagery can

require considerable hardware and software resources, depending on the image resolution and size of the area.

2.3.2 RADAR/InSAR

The radio detection and ranging (RADAR) technique is an active remote sensing method and operates with microwave pulses of 1 to 100 cm wavelength that were transmitted to the surface and reflected (Albertz, 2009; Lillesand et al., 2015). A major advantage of RADAR technology over optical imagery is the independency from natural energy sources as microwaves are capable to penetrate the atmosphere under almost all conditions. This enables the collection of data by night and day, as well as under cloudy, foggy or hazy conditions (Lillesand et al., 2015).

The basic measuring principle consists of a combined transmitter/receiver that is aligned downward in a way to constantly emit microwaves in an oblique direction perpendicular to the direction of flight (across-track). At a certain point in time, the front of the wave reaches the ground and is partially reflected (Figure 2-5). Finally, a certain portion of the reflected signal reaches the antenna of the receiver and is registered there as a signal. Since the area being radiated by microwaves moves over the terrain, the reflection signals from a narrow strip of terrain can be captured one after the other and line-based recorded as an image. The forward motion of the flying object then produces a complete line-by-line image (Albertz, 2009; Lillesand et al., 2015).

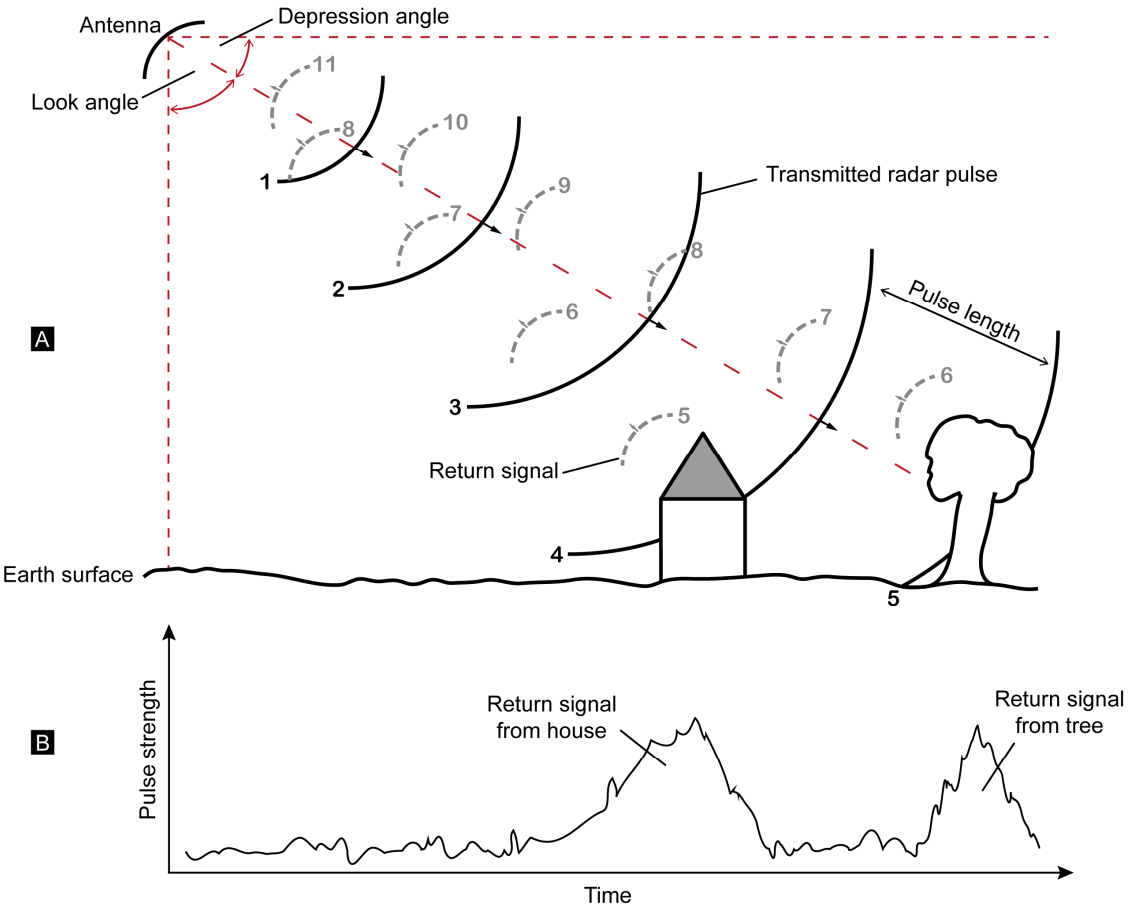

Figure 2-5: Operation principle of RADAR acquisition. A: Schematic illustration of one emitted RADAR pulse and its location over time. B: Received signal from the emitted RADAR pulse. (modified after Lillesand et al. (2015)).

However, the spatial resolution of real aperture systems decreases by increasing altitudes due to diverging antenna beam angles. Thus, RADAR systems of this type only produce high resolution ground measurements by flying at low altitudes and are not applicable for spaceborne measurements (Albertz, 2009; Lillesand et al., 2015). To reach higher spatial resolutions at high altitudes by satellite systems, Synthetic Aperture Radar (SAR) systems are usually used. The principle of the synthetic aperture is to replace the single ground record of a large antenna with many recordings of a small, moving antenna along-track (Figure 2-6). In the course of this movement, each object in the target area is numerously targeted at a varying angle of view and recorded accordingly as long as the target is within the pattern of the antenna (Lillesand et al., 2015). With exact knowledge of the antenna position, the aperture of a large antenna can be synthesized from the intensities and phases of the received synthetic RADAR echoes. The distance that the platform travelled during the time of recording the target determines the synthetic antenna size. The result is a high spatial resolution in the direction of antenna motion. This leads to the same effect as if one very long antenna of several km lengths would have been used. Thus, the resolution in flight direction becomes distance independent.

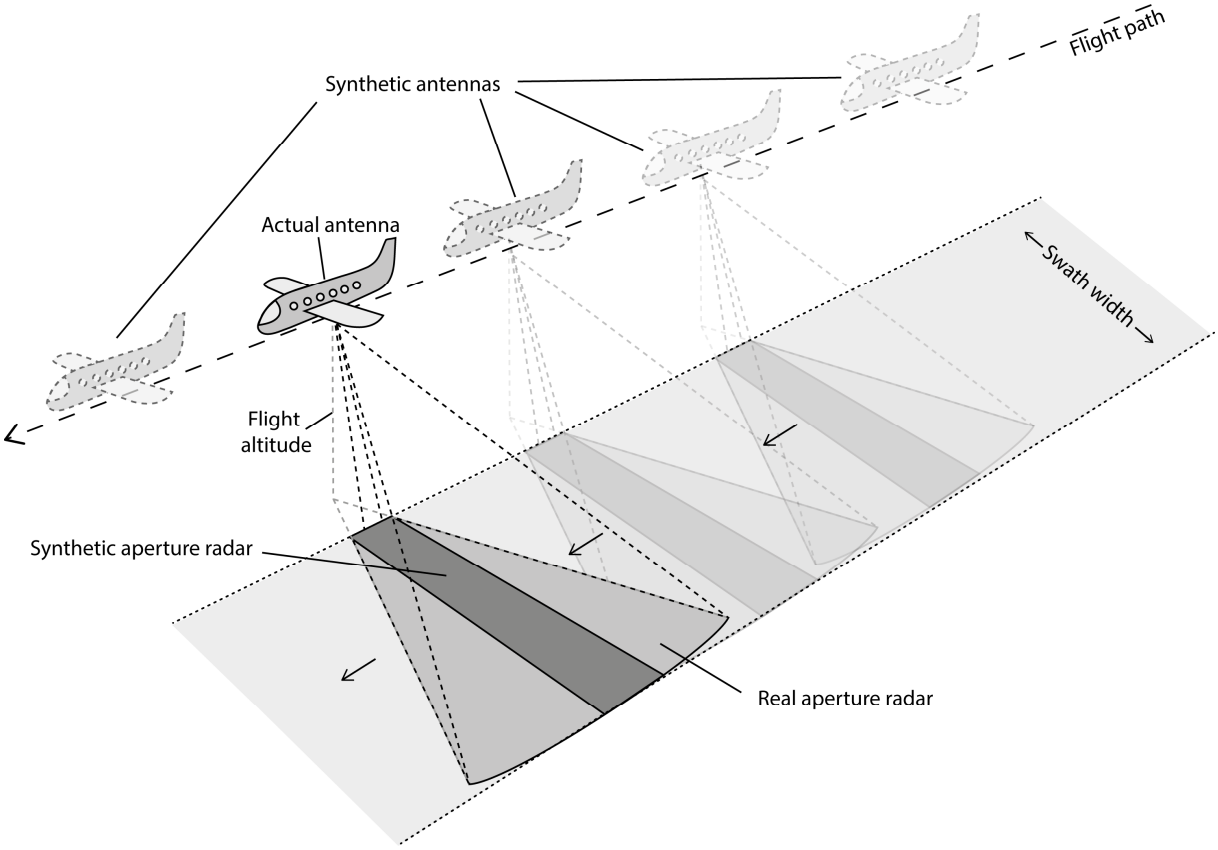

Figure 2-6: Simplified principle of a synthetic aperture radar system. The along path motion of the airborne or spaceborne RADAR sensor is used to record the same point from different positions and perspectives. The resulting coherent variations in the signal can be processed to achieve a higher azimuth resolution.

RADAR imagery only captures 2D information on its own. To derive 3D information, the terrain coverage from two different positions is necessary. This technique is called Interferometric Synthetic Aperture Radar (InSAR). The InSAR principle assumes that the reflected radiation of the terrain is received by two antennas arranged next to each other. Due to the different path lengths to the sensors, phase differences occur from which information about the topography of the terrain can be derived (Lillesand et al., 2015). In higher operation altitudes, this system requires longer baselines between

both sensors to achieve sufficient phase differences (Albertz, 2009). In practice, there are two different approaches to realize an InSAR surface measurement from spaceborne carrier systems, single-pass interferometry and repeat-pass interferometry (Figure 2-7) (Lillesand et al., 2015).

With the single-pass interferometry, observations are made at the same time from two different antennas in two different positions. This has been successfully conducted in the Shuttle Radar Topography Mission in February 2000, where the second antenna was installed on an extended mast of 60 m length on the operating spaceship (Figure 2-7 C). This construction enabled the simultaneous recording of terrain from 233 km altitude and was the first spaceborne single-pass InSAR system (Bamler, 1999). Another example is the constellation of the TerraSAR-X and TanDEM-X satellites, which can simultaneously record the surface from two different positions (Figure 2-7 B) (Krieger et al., 2007).

Another option for interferometric ground coverage is the repeat-pass interferometry where the baseline is realized by flying over the same area on two slightly different trajectories (Figure 2-7 A). This procedure has the major disadvantage of time decorrelation as both acquisitions do typically have a temporal baseline from minutes up to many days. For instance, the satellite RADARSAT has a temporal baseline of 24 days (Maune and Nayegandhi, 2018). Due to the time passed between the two overflights, the atmospheric conditions may significantly differ and affect the recorded results (Albertz, 2009).

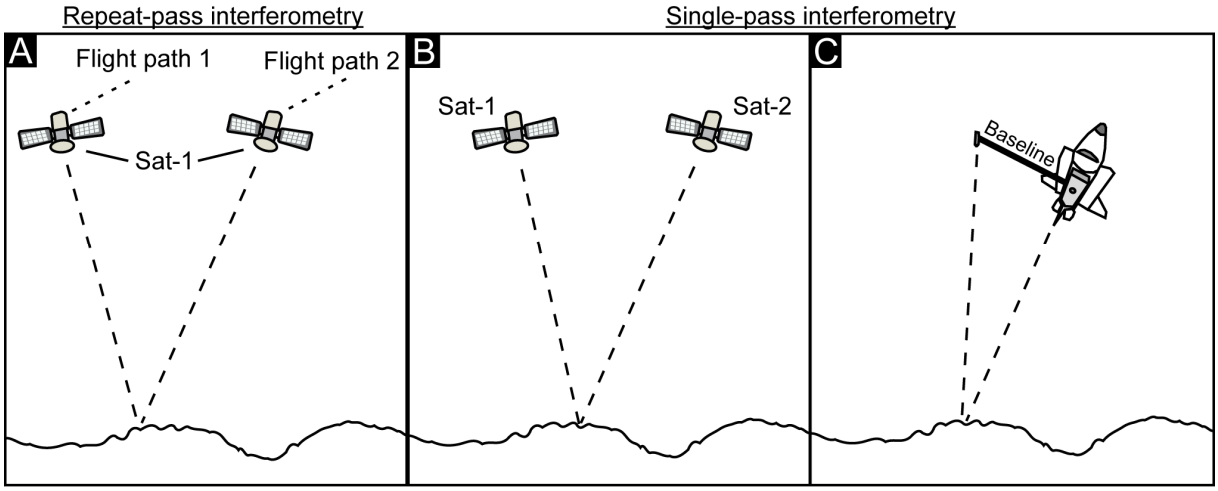

Figure 2-7: Illustration of different acquisition strategies. A: Repeat-pass interferometry with one satellite that covers the same area from different trajectories. B: Single-pass interferometry with two satellites that cover the same area simultaneously from different positions. C: Single-pass interferometry from one platform where the baseline between both acquisition perspectives is realized by an installed antenna on the spaceship.

Nowadays, satellite-based SAR-Systems can reach spatial resolutions of 1 m or higher and their positional accuracy is usually higher than optical remote sensing techniques (Bamler and Eineder, 2017). Several factors affect how a surface is represented in a RADAR image. The roughness of the surface significantly influences the backscattered signal. If the roughness is low, then almost all wavelengths will be mirrored and only very little signal is scattered back to the receiving sensor (Albertz, 2009; Lillesand et al., 2015). This results in a very dark area in the RADAR image. However, these reflections can also bounce off from other objects and be redirected to the receiver, where a stronger signal is measured afterwards. Rougher surfaces scatter back the incoming beams in many directions, resulting in a higher proportion of the signal being reflected back to the receiving sensor (Albertz, 2009; Lillesand et al., 2015). Thus, these surfaces usually have a brighter signature on the

RADAR image. Besides the roughness, also the electrical properties of a surface have an impact on the reflection signal of RADAR beams. The dielectric constant determines the amount of energy that is reflected or absorbed by the surface (Maune and Nayegandhi, 2018). For instance, water has a 10 times higher dielectric constant than dry soils (Lillesand et al., 2015). This enables the differentiation of wet and dry soils in the top layer in RADAR images, particularly for longer wavelengths with a higher penetration depth.

Modern spaceborne systems typically use wavelengths of approximately 3 cm (X-band), 6 cm (C-band), 10 cm (S-band) and 25 cm (L-band) (Bamler and Eineder, 2017). Many natural surfaces have a roughness structure that is well distinguishable in these wavelengths in SAR imagery. Wavelengths smaller than one centimeter are not feasible for satellite remote sensing as they are significantly affected by atmospheric conditions due to their inability to penetrate small water droplets (Jutzi et al., 2017). However, wavelengths from X-band to L-band also have different penetration depths, which influences the recorded signal depending on the structure of the surface being observed (Figure 2-8). In general, shorter wavelengths of X-band and C-band are better for the detection of crop and tree canopies as these wavelengths are predominantly backscattered by the leaves and do not penetrate the underlying soil. In contrast, longer wavelengths are better suitable for the recording of underlying objects, such as tree trunks or the ground soil (Lillesand et al., 2015). Repeat-pass systems usually use shorter wavelengths as these are less affected by temporal decorrelations, particularly in vegetated areas (Maune and Nayegandhi, 2018).

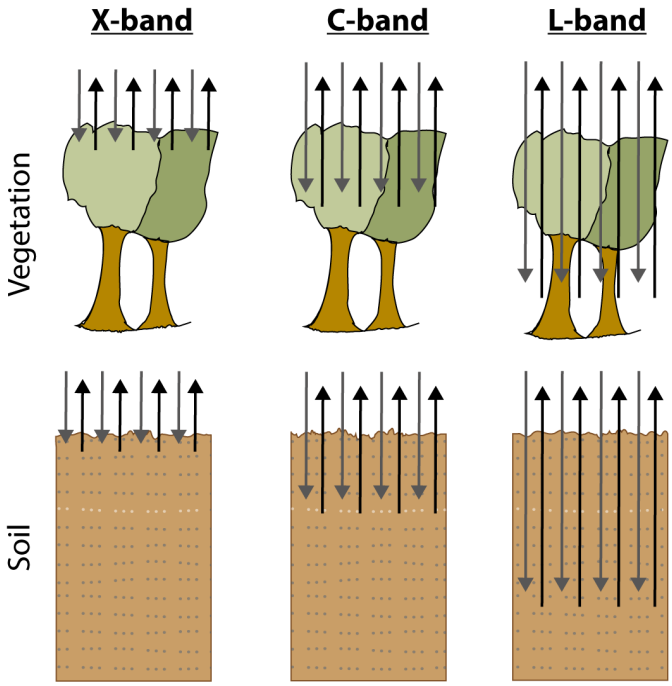

Figure 2-8: Schematic illustration of different penetration depths of X-band, C-band and L-band wavelengths.

2.3.3 Laser scanning/LiDAR

The method of laser scanning is another kind of active remote sensing technique that is commonly used for a point-based generation of 3D terrain data. The principle, also known as light detection and ranging (LiDAR), operates in a similar way to a microwave RADAR, but in a different range of the electromagnetic spectrum. Most modern airborne laser scanners operate within wavelengths of the

near-infrared spectrum (750 nm to 1.5 µm) (Lillesand et al., 2015). LiDAR systems use short pulses of laser light sent as a narrow beam to the ground and measure the return time of the signal that is backscattered from a target surface to the sensor (Renslow, 2012). The distance R from sensor to target can be calculated by the formula 2-2, knowing the speed of light c as well as the pulse emission time t_E and the arrival time t_A of the returned pulse signal.

$$R = \frac{t_A - t_E}{2} \cdot c \tag{2-2}$$

With this principle, known as time-of-flight (TOF), the distances between the ground and the sensor are calculated. TOF measurements can be used in the range of one meter to several kilometers (Jutzi et al., 2017). Another common acquisition method is the measurement of phase shifts between the emitted and the returned signal. These systems emit a constant laser beam of one or multiple phases. Although this measurement principle has the capability to achieve higher accuracies over short measurement distances, it has weaknesses over longer distances due to ambiguity problems (Beraldin et al., 2010; Jutzi et al., 2017). It is not possible to derive the absolute distance information, as different wavelength peaks cannot be counted and related to each other. Thus, a signal is only unambiguously identifiable within the range of the half wavelength. To avoid this problem, multiple waveforms of different frequencies can be used. Nevertheless, for airborne or even spaceborne LiDAR measurement, this system is usually not sufficient and only very rarely used (Beraldin et al., 2010).

A large number of individual 3D points can be acquired with LiDAR measurement methods, which in their entirety can geometrically describe the observed surface. The absolute position of each point in space can be determined with additional GPS/INS systems that accurately measure the sensor location and its angular orientation with respect to the observed ground. Overall, all measured points result in a point cloud determining the observed surface. For coarser resolutions of terrain mapping, 0.5 to 2 points per m² are used. For a more detailed mapping, particularly in more complex areas, at least 10 to 50 points per m² are required (Lillesand et al., 2015). Modern laser scanning systems can capture five or more returns per pulse. Point clouds do usually provide surface models including objects, such as trees or buildings. This allows not only the measurement of features, such as a tree canopy and bare ground, but also multiple returns of transmitted pulses from surfaces in between if there are sufficient gaps in the canopy (Danson et al., 2007; Koch et al., 2006; Liu et al., 2013). In comparison to Photogrammetry and RADAR, LiDAR is probably the most accurate technology to measure ground elevation through vegetation. Due to shorter wavelengths and a narrower beam angle, compared to RADAR, LiDAR can pass smaller gaps within the canopies without the entire signal being reflected from the canopy (Neuenschwander and Magruder, 2019).

While terrestrial laser scanning (TLS) and airborne laser scanning have become popular methods for acquiring highly accurate areal terrain information, the acquisition of data with LiDAR from space is relatively rare. To date, only six LiDAR missions have been carried out from a spaceborne platform with the objectives of atmospheric observation of clouds, aerosols and clean air wind speed (CALIPSO, CATS and Aeolus), the observation of forests (GEDI) and the measurements of ice-cap volumes (Ice, Cloud, and land Elevation Satellite (ICESat) 1 and 2) (Hancock et al., 2021; Neuenschwander and Pitts, 2019; Schutz et al., 2005; Smith et al., 2019; Zwally et al., 2002). The point-based elevations measured by the ICESat-1 and 2 satellites provide vertical accuracies of several decimeters, which is higher than those of other spaceborne products (Duong et al., 2009; Fricker et al., 2005). However, a downside of spaceborne LiDAR is that an own energy source is required for the illumination of the surface. Since

relatively high energy is necessary to illuminate every point that has to be measured first, it limits the area that can be covered. Thus, LiDAR from space is only capable to cover the surface very sparsely on a narrow track compared to other acquisition techniques (Figure 2-9). To date, LiDAR technique from space is not able to produce seamless elevation data and is not suitable for a continuous DEM generation. However, the measured elevation points of ICESat are often used as reference material to improve the accuracy of other spaceborne generated DEMs (Yue et al., 2017).

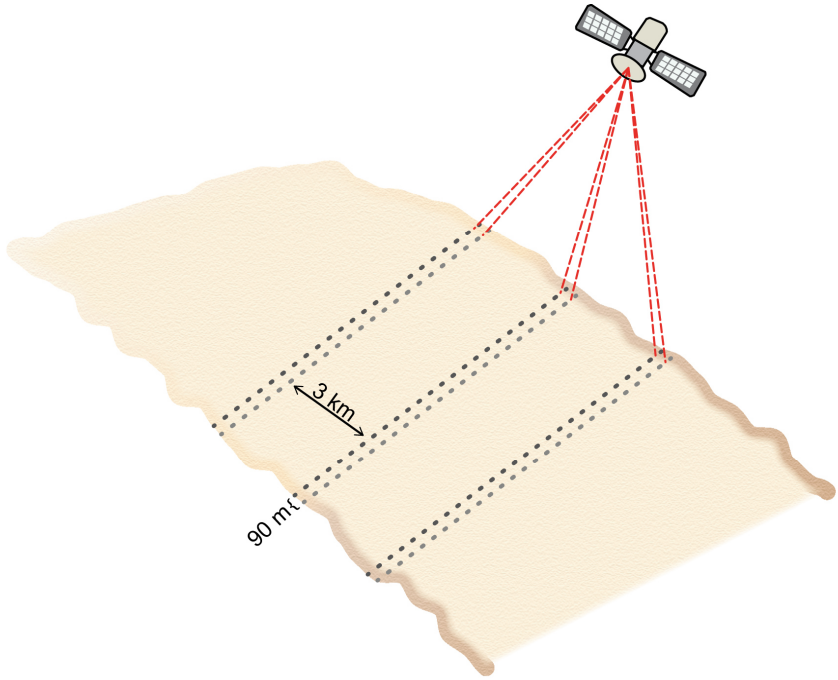

Figure 2-9: Sampling geometry of the ICESat-2 satellite with a 3x2 beam pattern.

2.3.4 Conventional topographical surveys

Ground-based surveying techniques can be carried out by measurement instruments that require a line-of-sight so that the entire area to be surveyed is visible through the instrument. These conventional methods have been used since more than 3000 years and are the most traditional way to capture elevation information from the ground. They are based on measurements of horizontal and vertical angles between points as well as the distances between the points and their relative elevations (Kahmen, 2006; Nelson et al., 2009). The surveys were conducted with theodolites and precise levelling. Theodolites survey horizontal and vertical angles to a target and enable the calculation of positions by trigonometric principles (Kahmen, 2006; Nelson et al., 2009). Additionally, differential level instruments are commonly used to determine relative elevation differences between two points. The instrument consists of a telescope rotating around a vertical axis, in which a horizontal target line can be generated that determines the differences in height between two points. By using level rods at specific points, the deviations above and below this exact levelling line can be determined from the horizontal line-of-sight (Ghilani and Wolf, 2015; Kahmen, 2006).

Nowadays, mostly digital electronic devices are used for the measurement of 3D points. Total station instruments combine a digital theodolite with an integrated electronic distance measurement (EDM) using a laser or infrared beam. These instruments can measure both angles and distances simultaneously and transmit the results to a built-in computer in real-time (Ghilani and Wolf, 2015).

Point measurement with total stations is based on open or closed polygon traverses where from each traverse station a set of characteristic points is targeted (Florinsky, 2016; Kahmen, 2006). With this measurement method, it is possible to achieve elevation information with an accuracy of less than 1 cm. However, the method is time consuming and requires a lot of effort and experience by the surveyor (Nelson et al., 2009).

Static or kinematic GPS or Differential Global Positioning System (DGPS) measurements are a faster way to obtain elevation information by creating large-scale 3D points with the usage of the global positioning satellite system and GPS receivers mounted on a vehicle or moved by an operator (Florinsky, 2016; Ghilani and Wolf, 2015). With a good constellation of satellites, vertical accuracies of 1 – 2 m can be achieved by DGPS measurements (Nelson et al., 2009). Nevertheless, an area-wide terrain survey with these conventional survey methods is very cumbersome and only feasible for very small areas.

2.3.5 Terrestrial vs. airborne vs. spaceborne acquisition techniques

As already mentioned before, the acquisition of terrain data can be obtained by terrestrial observations or by measurements from airborne or spaceborne platforms. The selection of the most suitable platform depends on several factors, such as the purpose of the study, accuracy requirements, scale and size of the area, type of terrain, costs, available equipment and time (Ghilani and Wolf, 2015). All three platform systems have their advantages and disadvantages regarding the area that can be covered and the spatial resolution of the ground that can be measured by different acquisition platforms. Figure 2-10 gives an overview about the differences of acquisition platforms regarding the scale and spatial resolution that they are able to capture.

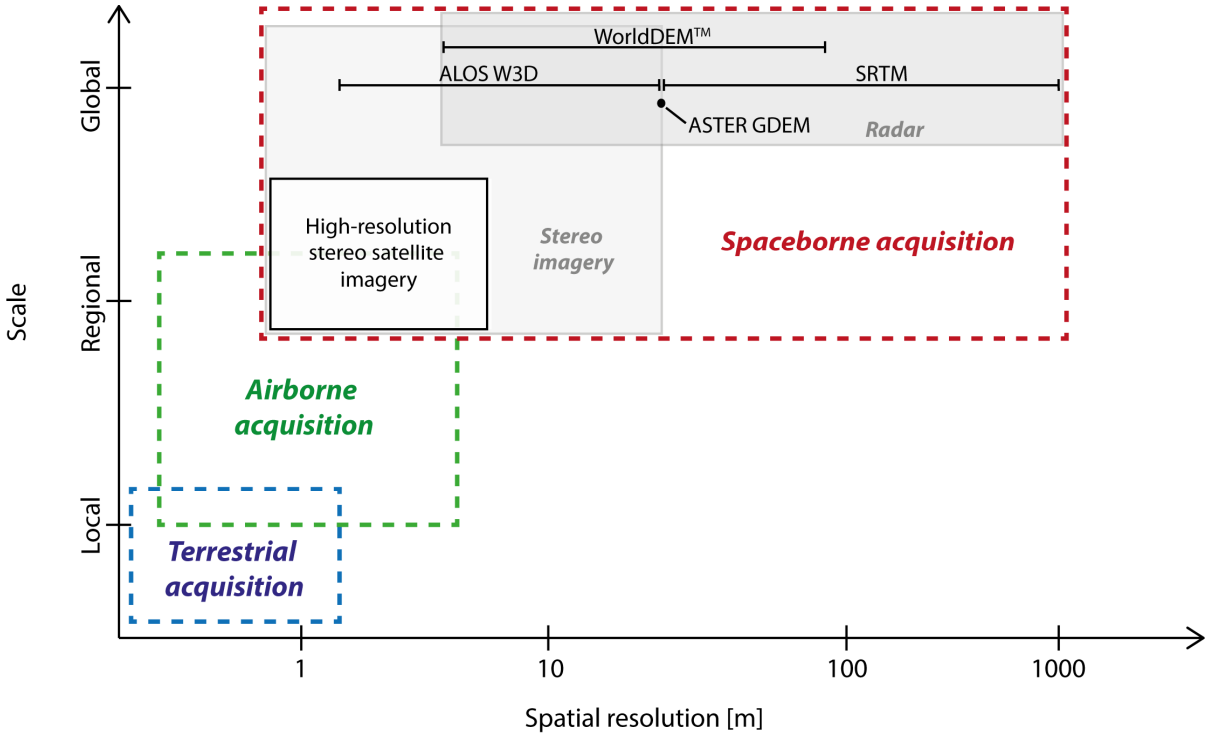

Figure 2-10: Schematic illustration of different DEM acquisition platforms in terms of their acquisition capability.

DEMs generated from a terrestrial based platform can achieve accuracies of a few mm to cm which is by far the most accurate way to capture ground elevation (Ghilani and Wolf, 2015; Nelson et al., 2009). However, these methods are usually only capable to survey a limited area of up to a few kilometers as these methods are time consuming, require a lot of effort and expensive equipment. Thus, capturing larger areas is often too expensive in comparison to airborne or spaceborne alternatives. Furthermore, the physical accessibility of terrain can often be an issue due to difficult terrain conditions or visiting restrictions. Terrestrial surveying methods are therefore often only used if these high accuracy standards are required in very large-scale analyses. However, the acquisition of 3D surface information with TLS has been established as a common method in applications that requires a very high accuracy, such as the monitoring of morphological surface movements (Day et al., 2013; Hoffmeister et al., 2020), modelling of small-scale roughness of agricultural soils (Aguilar et al., 2009), the characterization of river morphology (Heritage and Milan, 2009; Resop et al., 2012), the documentation of archaeological sites (Hoffmeister et al., 2016b; Marin-Buzon et al., 2021; Perez-Alvarez et al., 2020), or plant height monitoring (Guo et al., 2019; Hoffmeister et al., 2016a; Tilly et al., 2014). Furthermore, it is a common method for engineering tasks, such as control measurements to detect damage or deformation of infrastructural objects (Erdelyi et al., 2020; Qiu and Cheng, 2017; Wu et al., 2022), or for the construction of 3D models from buildings and objects (Gardzinska, 2021; Wu et al., 2022).

Since the first attempts in 1840, aerial photos have been a widely used source for the generation of topographical information (Lillesand et al., 2015). Generating DEMs from airborne platforms, mainly from stereo-imagery but also with LiDAR technique, is a practical solution to accurately cover much larger areas than with terrestrial acquisition methods. Airplanes are the most common platform for airborne measurements as they provide a good performance in terms of high spatial resolution and accuracy. Furthermore, they are relatively flexible in operation and can cover much larger areas than it is possible from the ground. However, flying and maintaining an aircraft produces considerable costs. Additionally, the circumstances where data can be obtained are not optimal as atmospheric conditions, such as clouds, fog or turbulences can affect the measurements (Jacobsen, 2012; Lillesand et al., 2015).

In recent years, also the use of UAVs has largely increased and established as an alternative to manned aircrafts or terrestrial acquisition methods. With their ability to rapidly cover the Earth from low altitudes, their products are able to reach resolutions of a few centimeters and can compete terrestrial measurement methods (Ajayi and Ajulo, 2021; Coveney and Roberts, 2017; Leitao et al., 2016). In particular, low-cost UAVs have become a valuable alternative to terrestrial methods due to lower costs and higher agility by producing datasets of similar accuracies (Bareth et al., 2016; Hoffmeister et al., 2020; Kim et al., 2019; Tsunetaka et al., 2020; Yurtseven, 2019).

Additionally, the use of spaceborne platforms to acquire DEMs has vastly increased over the last decades. One of the major advantages of spaceborne platforms is the ability to rapidly cover large areas up to the entire globe. This leads to a relatively cost-effective acquisition of huge areas in a rapid timely manner. Thus, spaceborne platforms are the only possibility to generate DEMs of global coverage with revisit times of a few days. With the increasing quality of spaceborne image camera systems that are nowadays capable to produce images with a ground sampling distance of a few decimeters, they can compete with aerial imagery for DEMs of regional coverage (Hobi and Ginzler, 2012; Jacobsen, 2012).

Satellites operate at altitudes of 500 to 800 km with large speeds and require large telescopes to produce high resolution imagery. Thus, for a long time, the biggest downside of satellite-based systems was the inability to produce high resolution data compared to ground-based or airborne platforms. The first attempts of producing global DEMs were made in 1988 with the ETOPO5 DEM. This dataset was created by the National Oceanic and Atmospheric Administration (NOAA) and depicted the topography of land and submarine surfaces with a spatial resolution of 5 minutes (NOAA, 1988). Several others followed with the GTOPO30 (Gesch et al., 1999; USGS, 1996) and Altimeter Corrected Elevations (ACE) DEM (Berry et al., 2002).

However, these DEMs all had spatial resolutions of more than 30" (≈ 1 km at the Equator) which is only applicable for very small-scale analyses but not sufficient for applications of larger scales. The first global DEM product with a significantly higher spatial resolution was the SRTM, which was firstly released in 2003 with a spatial resolution of 1" (≈ 30 m) (Rabus et al., 2003). Over the last years, the supply of freely distributed DEMs with a spatial resolution of 3" and 1" has largely increased. An overview of all so far publicly available DEMs with nearly global coverage and a spatial resolution of 3" or higher is provided in Table 2-1.

In addition to the presented DEMs of Table 2-1, several other DEM products of much higher resolutions exist but were only commercially distributed. These have an even higher spatial resolution of up to 1 m. For example, several WorldDEM™ products exist that were extracted from the acquired X-band RADAR data of TerraSAR-X/TanDEM-X satellites between 2011 and 2015 (Rizzoli et al., 2017; Wessel et al., 2018). They were distributed as 1" (≈ 30 m) and 0.4" (≈ 12 m) DEM products by the DLR and Airbus DS (German Aerospace Center (DLR), 2018a; German Aerospace Center (DLR), 2018b). Most recently, Airbus has additionally released the WorldDEM™ Neo elevation model that contains additional data from both satellites and has a spatial resolution of 0.15" (≈ 5 m) (Airbus Defence and Space, 2021). Furthermore, several very high resolution DEMs from stereo satellite imagery exist, such as the ALOS W3D products from JAXA in the spatial resolutions of 0.075" (2.5 m) and 0.15" (≈ 5 m) (Takaku et al., 2018). Also, from Airbus DS several GEO Elevation products with spatial resolutions from 1 m to 30 m exist that were processed from SPOT or Pléiades imagery (Airbus Defense and Space, 2015).

Table 2-1: Comparison of publicly available medium spatial resolution DEMs of global coverage regarding their acquisition time and source, as well as release information about their first and current available version.

Platform	DEM product	Producer	Acquisition time	Resolution	Primary source	First release	Most recent version	Latest release	Reference
SRTM	SRTM-1	NASA	02/2000	1" (≈ 30 m)	C-band RADAR	2003	Version 3	2015	Farr et al. (2007); NASA Shuttle Radar Topography Mission (SRTM) (2013); Rabus et al. (2003)
	SRTM-3	NASA/CGIAR-CSI		3" (≈ 90 m)	C-band RADAR	2003	Version 4.1	08/2008	Jarvis et al. (2008)
	NASADEM	NASA		1" (≈ 30 m)	C-band RADAR	02/2020	Version 1	-	Crippen et al. (2016); NASA JPL (2020)
ASTER	ASTER GDEM	NASA/METI	2000-2013	1" (≈ 30 m)	Stereo imagery	2009	Version 3	2016	Abrams et al. (2010); Abrams and Crippen (2019); Tachikawa et al. (2011)
SRTM-3 DEM v.2.1/ALOS W3D 30 m	MERIT	University of Tokyo	2000-2011	3" (≈ 90 m)	C-band RADAR/Stereo imagery	05/2017	Version 1.0.3	10/2018	Yamazaki et al. (2017)
ALOS	ALOS W3D	JAXA	2006-2011	1" (≈ 30 m)	Stereo imagery	2016	Version 3.2	03/2021	Tadono et al. (2009); Takaku et al. (2014); Takaku et al. (2018)
TerraSAR-X/TanDEM-X	TanDEM-X WorldDEM™	DLR/Airbus DS	2011-2015	3" (≈ 90 m)	X-band RADAR	2018	Version 1	-	German Aerospace Center (DLR) (2018)
	Copernicus DEM	ESA/Airbus		1" (≈ 30 m)	X-band RADAR/12m TanDEM-X WorldDEM™	2019	Version 3.0	2020/2021	Airbus Defence and Space (2020a)
	Copernicus DEM	ESA/Airbus		3" (≈ 90 m)	X-band RADAR/12m TanDEM-X WorldDEM™	12/2019	Version 1	2020/2021	

2.4 Land surface parameters

Biotic and abiotic factors, such as climate, soil components, vegetation distribution or other dynamic hydrological, geomorphological and biological processes are mainly influenced by spatial heterogeneity (Moore et al., 1991; Stein and Kreft, 2015). A key component to characterize this complexity is the relief by creating corresponding land surface parameters, such as slope or aspect. digital elevation models offer an efficient way to automatically extract distinct terrain features to provide more detailed information about characteristics and variations of topography. Besides using the 'pure' elevation from a DEM, numerous other land surface parameters can be extracted that help to understand the landscape properties of a study region. Overall, more than 100 of those land surface parameters exist that can be calculated from a DEM (Wilson, 2018). To mention all of them would go beyond the scope of this contribution. Therefore, only the most important and commonly used parameters are listed in Table 2-2. A more detailed overview of available parameters can be found in Wilson (2018) as well as Olaya (2009).

Land surface parameters can be categorized into two categories. The first category includes all primary land surface parameters that can be directly derived from the DEM without further knowledge or the use of additional datasets (Wilson and Gallant, 2000a). Typical parameters are slope, aspect and curvature that can be calculated from the first and second derivatives of a gridded elevation dataset (Evans, 1972; Shary, 1995; Zevenbergen and Thorne, 1987). A visual example of these surface parameters is given in Figure 2-11. The surface parameter slope specifies the steepness at each cell of a raster surface and can be calculated in degree or percent. It is of great importance for hydrological or geomorphological analysis as it directly affects the gravity-induced flow of water and other surface material (Wilson and Gallant, 2000b).

Table 2-2: Description of most common land surface parameters that can be derived from DEMs.

Parameter	Description	Source
Elevation	Surface heights.	
Slope	Slope gradient from a raster cell.	Evans (1972); Zevenbergen and Thorne (1987)
Aspect	Calculated downward direction of each surface cell.	Zevenbergen and Thorne (1987)
Curvature	Downslope (profile) and along-slope (plan) curvature of the raster surface.	Dikau (1989); Evans (1972); Shary (1995); Zevenbergen and Thorne (1987)
Terrain ruggedness index	Calculation of terrain complexity by the average elevation change in a user defined area.	Riley et al. (1999)
Topographic openness	Maximum vision angle from a point on the land surface in a user defined radius.	Yokoyama et al. (2002)
Flow direction	Direction of water flow.	Jenson and Domingue (1988); Tarboton et al. (1991)
Flow accumulation	Amount of water that flows through the cell.	Jenson and Domingue (1988); Tarboton et al. (1991)
Topographic wetness index	Calculation of saturation zones.	Beven and Kirkby (1979)
Watershed areas	Contributing drainage area based on flow algorithm.	
Solar radiation	Calculation of the potential solar radiation over a certain time period reaching the surface.	Kumar et al. (1997)
Hillshade	A shaded relief considering a user defined illumination source angle.	

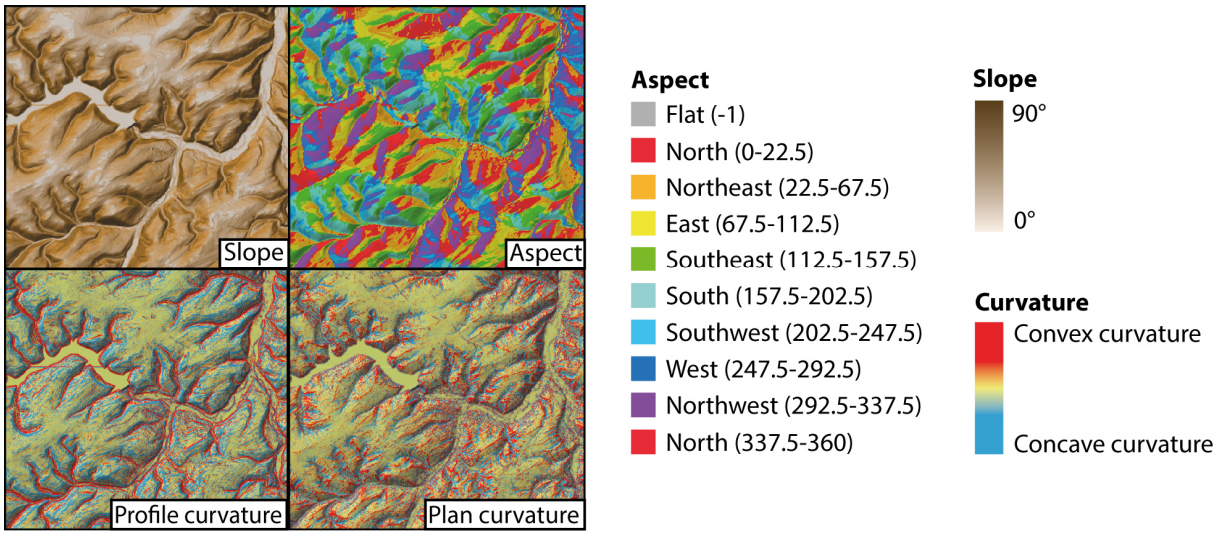

Figure 2-11: Exemplary illustration of the derived primary land-surface parameters slope, aspect, profile and plan curvature.

The parameter aspect determines the direction of the slope in degrees from 0 (true north) to 360 (true north again) in a full circle (Wilson and Gallant, 2000a). Flat areas without slope direction usually receive the value -1. Curvature is a collection of several surface parameter types used to describe the shape of a surface. Whereas slope and aspect are based on the first derivative, the curvature is based on the second derivative to distinguish convex (positive curvature) and concave (negative curvature) surfaces (Olaya, 2009). The most common curvatures are the vertical (profile) and horizontal (plan) curvature (Zevenbergen and Thorne, 1987). Figure 2-12 shows nine surface shapes classified by Dikau (1989) depending on their plan and profile curvature. They divided a sloped landscape into convex, straight and concave curvatures in horizontal and vertical direction to characterize distinct landform elements.

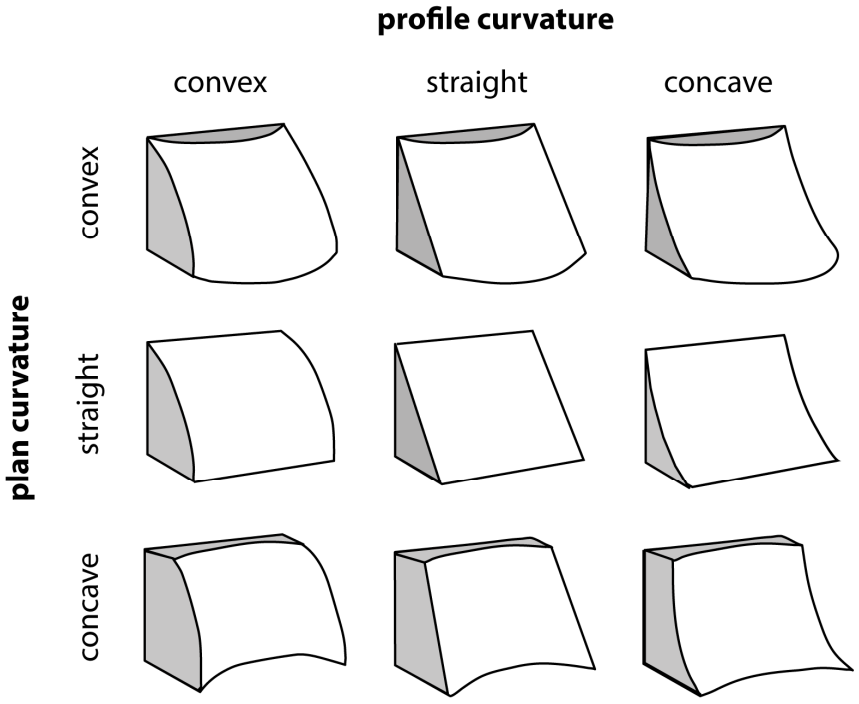

Figure 2-12: Classification of form elements based on profile and plan curvature (modified after Dikau (1989)).

Another example of a primary land surface parameter is the terrain roughness which also exists in many different types of calculations from the DEM (Olaya, 2009; Wilson and Gallant, 2000b). A famous parameter to determine surface roughness is the terrain ruggedness index (TRI). It quantifies the roughness of terrain and is a morphometric measure for the complexity of land surface (Riley et al., 1999). A primary land surface parameter in a hydrological context is the flow direction that describes the routing of draining water streams (Jenson and Domingue, 1988). Following the flow direction, also the flow accumulation can be calculated as the potential runoff flowing through a certain point and determines the upstream area that drains into the considered raster cell (Jenson, 1991; Tarboton et al., 1991; Wilson and Gallant, 2000a). These parameters help to identify river networks and to define watershed catchment areas where all water accumulated in this area drains to a single outflow point. They are mainly used in hydrological studies, for example, to predict the water flow in rainfall events and to identify potential flooding zones (Tarboton et al., 1991; Wilson, 2018).

The second category of land surface parameters includes derived terrain parameters from the DEM by the additional usage of two or more of the previously mentioned primary surface parameters or other additional input sources for calculation (Wilson, 2018). These are called secondary terrain parameters. The most popular one is the topographic wetness index (TWI), which is calculated by additionally using slope and flow direction. The TWI describes the spatial distribution of saturated zones for runoff generation as a function of upslope contributing area and slope (Beven and Kirkby, 1979). The TWI is largely used in studies of hydrological processes (Saleem et al., 2019). Another example of a secondary land surface parameter is the topographic radiation to calculate the solar insolation over a defined time period for a certain point at the Earth's surface (Kumar et al., 1997). This parameter helps to estimate meteorological processes, such as surface and air temperature, heat fluxes or wind by identifying shadowed areas and zones gaining high solar energy. It can be used in biological studies, e.g. for the modelling of flora and fauna sites, as well as in hydrological applications, such as water balance studies (Jaroslav, 2013; Kumar et al., 1997).

2.5 Fields of applications for DEMs and derived land surface parameters

DEMs are a valuable source for modelling and mapping tasks in numerous scientific disciplines, since the topography is a significant factor that influences many natural processes. Thus, numerous applications use elevation datasets in their GIS and remote sensing environment for analysis and modelling purposes. The most common use cases of DEMs are settled within scientific hydrological purposes and environmental tasks in the topics of disaster assessment, biodiversity as well as geomorphology and geology, ecology, soil science and agriculture (Ariza-Lopez et al., 2018; Mesa-Mingorance et al., 2017; Sofia, 2020; Tarquini and Nannipieri, 2017). These topics will be further explained in detail in the following paragraphs by stating several examples from literature where DEMs have been used.

Many geomorphologic studies focus on the description and categorization of the Earth's surface. The automated classification of landforms has been an increasing task that incorporates considerations of surface texture, pattern and context. In former times, landforms have been traditionally identified by the interpretation of aerial photos, but with the increasing availability of high resolution DEMs the (semi-)automatic extraction of terrain features has become an active research field. Thus, several approaches for the delineation of landforms from DEMs have been developed over time (Dikau et al.,

1995; Dragut and Blaschke, 2006; Jasiewicz and Stepinski, 2013; MacMillan et al., 2000; Marques et al., 2018; Weiss, 2001). Furthermore, several studies focused on the extraction of distinct landforms (Cuthbertson et al., 2021; d'Oleire-Oltmanns et al., 2013; Smith et al., 2006) or the classification of terrain for a specific landscape (Dekavalla and Argialas, 2017; Kuhni and Pfiffner, 2001; Schneevoigt et al., 2008; Zhao et al., 2017; Zhu et al., 2018). Overall, more than 100 studies are available to date that focused on the classification of landforms and the systematic categorization of terrain features. Furthermore, the modelling of land surface changes and the role of surface processes in terrain evolution has been done by using DEMs and topographic parameters (Bishop et al., 2003; Li et al., 2021).

In addition, the prediction of landslide hazards has become an important application in the field of geomorphology, where the usage of DEMs has a long tradition (Zhong et al., 2020). According to Kakavas and Nikolakopoulos (2021), more than 200 studies are available that have focused on the analysis of rockfalls and landslides. As the source areas and downslope paths of landslides mainly depend on topography, many applications have assessed slope instability as well as the risk and extent of potential hazards (Chudy et al., 2019; Gawrysiak and Kociuba, 2020; Iwahashi et al., 2021; Liu et al., 2021; Niculita, 2016; Nugraha et al., 2015; Rashid et al., 2020; Stumpf et al., 2014; Sturzenegger et al., 2021; Valentine and Kalnins, 2016; Xu et al., 2020). DEMs have also been widely used to investigate tectonic structures and mapping folds for volcanic or seismic activities (Abolins and Ogden, 2021; Baize et al., 2020; Dirscherl and Rossi, 2018; Gomez, 2018; Gottwald et al., 2021; Khan, 2019).

Since the flow of water highly depends on topography, elevation information is essential to model and determine water flow and possible inundation areas in flood events. Thus, many studies exist that used DEMs for their hydrological analysis. They have focused on the delineation of drainage networks (Hanief and Laursen, 2019; Liu and Zhang, 2011; Schwanghart et al., 2013) and watersheds from DEMs (Li et al., 2019; Liu et al., 2020a; Seyler et al., 2009; Wu and Lane, 2017) as well as the identification and evaluation of groundwater zones (Ardakani et al., 2020; Arya et al., 2020; Kadhem and Zubari, 2020; Maity and Mandal, 2019; Mishra and Singh, 2019). Additionally, much work has been done in the field of flood modelling and the creation of flood hazard maps (Bajabaa et al., 2014; Callaghan and Wickert, 2019; Dingle et al., 2020; Fleischmann et al., 2020; Pena et al., 2021).

In the field of soil science, topographic information is a valuable parameter for the prediction of soil types and soil genesis that has been widely used in numerous studies. Many soil-related studies based on the SCORPAN approach of McBratney et al. (2003) that lists all environmental factors responsible for soil genesis. These factors are an enhancement of Jenny's (1941) statement that the occurrence of different soils depends on climatic properties (c), organisms (o), relief (r), parental material (p), age (a) and the spatial position (n). To cover the factor (r), the usage of DEM and derived topographic variables as input variables for model predictions is a common method in the literature. Thus, numerous studies have used DEMs in the field of soil science to automatically predict different soil types (Adhikari et al., 2014; Brungard et al., 2015; Dornik et al., 2018; Gruber et al., 2019; Mansuy et al., 2014; Massawe et al., 2018; Ngunjiri et al., 2019; Taghizadeh-Mehrjardi et al., 2019) or distinct properties such as soil organic carbon or soil organic matter (Devine et al., 2020; Drouin et al., 2011; Grimm et al., 2008; Lamichhane et al., 2019; Piccini et al., 2020; Piccini et al., 2014; Qin et al., 2012; Zhang et al., 2012; Zhong and Xu, 2009).

DEMs and derived topographic parameters are also used in climatic and meteorological studies to adjust meteorological measurements with local topography. They are utilized to interpolate values

from weather stations over larger areas as well as input parameters for climatic modelling and meteorological predictions (Bianchi et al., 2016; Lloyd, 2005; Otgonbayar et al., 2019; Park et al., 2019; Thornton et al., 1997). Another common application is the detection of glacier changes over time by measuring the thickness of the ice layer with DEMs produced at different dates (Berthier et al., 2014; Gharehchahi et al., 2020; Jabbar et al., 2020; Ke et al., 2019; Larsen et al., 2007; Paul et al., 2007; Paul et al., 2020; Rieg et al., 2018; Semakova and Semakov, 2017; Zhang et al., 2020a; Zhang et al., 2020b; Zhang et al., 2018; Zheng et al., 2018).

Furthermore, vegetation directly depends on environmental conditions and several ecological studies have used land surface parameters to predict the occurrence of vegetation and plant species as well as the presence or absence of specific plants over very short distances (Cruzan et al., 2016; Gottfried et al., 1998; Kakembo et al., 2007; Leempoel et al., 2015; Nilsen et al., 1999; Pradervand et al., 2014; Steven et al., 2007). Derivatives of elevation data have also been used to classify the distribution of tree species in forests (Chaves et al., 2018; Mohtashamian et al., 2017; Tracz et al., 2019) and for wildfire management (Brown et al., 2016; Kushla and Ripple, 1997; Rim et al., 2018; Tufekcioglu et al., 2017). Furthermore, DEMs are an important source for the identification of suitable land for agroforestry (Ahmad et al., 2019; Ahmad et al., 2018b; Jarasiunas, 2016) and the analysis of wildlife and habitats of animals (Ahmad et al., 2018a; Aini et al., 2015; Aspinall and Veitch, 1993). Additionally, DEMs are used in many other applications, such as for the orthorectification of satellite images or the 3D visualization of objects (Aguilar et al., 2013; Casana and Cothren, 2008; Liu et al., 2007) as well as in several applications of archaeology, e.g. for the prediction of human travelling paths or the detection of archaeological features and sites (Becker et al., 2017; Casana and Cothren, 2008; De Clercq et al., 2016; Lewis, 2021; Stular et al., 2021).

2.6 Assessing the accuracy of DEMs

2.6.1 Error sources

How accurately the real surface is represented in a DEM is crucial for its reliability, since a DEM is always an abstraction and approximation of the ground surface. Thus, the assessment of its quality is an important step before using the DEM in any type of application. The vertical accuracy of a DEM is the main criterion to specify its quality. It is determined as the elevation difference between the heights of the DEM and the real surface. Before going more deeply into detail on how the accuracy of a DEM can be determined, a glance at the error sources should be thrown. According to the terminology from photogrammetry and surveying, three main sources of errors can occur during the acquisition and processing of measured data: blunders, systematic and random measurement errors (Fisher and Tate, 2006; Kahmen, 2006).

In principle, this system can be adapted to digital elevation models where these three error sources can also occur (Wise, 2000). Blunders usually result from an incorrect usage of the measuring device, defective devices or poor surveying conditions. They are usually visually recognizable as artefacts and outliers afterwards as they show a very large deviation from the other measured values (Reuter et al., 2009). Systematic measurement errors are expressed in a constant deviation of the measured value from the ‘true’ value in only one direction. They are usually caused by inaccuracies of the data acquisition equipment or the interpolation method (Hu et al., 2009). The systematic error can be determined afterwards by comparing the median elevation differences between the DEM and a more

accurate reference dataset (Höhle and Höhle, 2009). In contrast, random errors are caused by unpredictable occurring processes that cannot be determined afterwards. They lead to a scattering of the measured values around the mean value and thus affect the precision of the measurement series (Maune and Nayegandhi, 2018). Random errors are considered to be normally distributed and can be measured by calculating deviation measures of the elevation differences in comparison to a reference dataset.

However, evaluating how accurately a DEM reflects the real surface is complex and goes beyond the previously named error sources. It contains further aspects that need to be considered. As a geographic dataset, deviations in DEMs are often spatially autocorrelated and neighbouring points have similar errors (Amatulli et al., 2018; Fisher and Tate, 2006). Thus, it must be assumed that the random error of DEMs is not fully randomized and independent from the values of neighbouring cells. Rather, it has an autocorrelated component that depends on local behaviours such as the morphometric characteristics of terrain or land cover (Polidori and El Hage, 2020). Overall, finding an answer to the question of how accurate and reliable a DEM is for a specific application is rather complex. The accuracy of a DEM depends on the method of acquisition and processing, the type of terrain and the spatial resolution.

In addition to statistical measures, the quality of a DEM also depends on how accurately the surface roughness, shape and certain terrain features are represented in the model, as well as the consistency of the measured elevations over the entire area (Florinsky, 2012; Purinton and Bookhagen, 2021; Reuter et al., 2009). The covered terrain itself with its varying surfaces, roughness or land cover can be determined as an important source for errors in the DEM and has to be considered during the evaluation process. Furthermore, relief influences the elevation measurements directly and indirectly in combination with the spatial resolution. The spatial resolution of the acquisition data is particularly important for raster datasets as a larger pixel size covers for each pixel a larger area with more elevation differences that the terrain model cannot depict (Figure 2-13). This effect increases in rougher terrain, whereas in flat landscapes a large pixel size is usually less problematic. Furthermore, DEMs with larger spatial resolutions depict the real surface in less detail and have a higher potential for larger errors (Fisher and Tate, 2006).

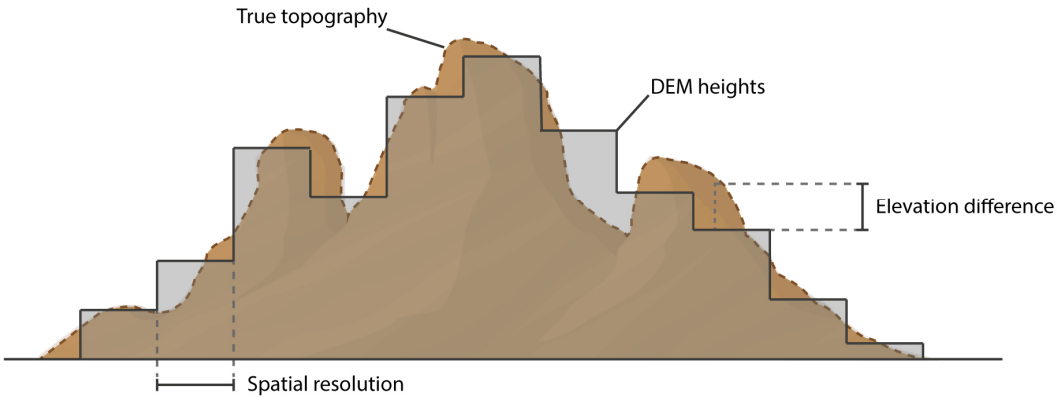

Figure 2-13: Illustration of elevation differences between a DEM and the true topography that are caused by spatial resolution. The effect of elevation difference is increased for steeper slopes and less significant in flat areas.

Spatial resolution is the main limiting factor for the identification of different terrain features and objects, since a coarser resolution captures fewer details of the terrain surface (Guth et al., 2021). If

the resolution is too coarse, small terrain features are not identifiable and cannot be extracted by terrain derivatives. This could lead to issues in further analyses when the detection of these features is crucial and necessary for further interpretations. For instance, several studies have shown that the overall slope values are decreasing in DEMs with coarser resolutions (Deng et al., 2007; Kienzle, 2004; Thompson et al., 2001; Vaze et al., 2010). This issue is of particular concern in applications that use the slope for landslide or erosion mapping, which may lead to an underestimation of risks.

In contrast, a too fine spatial resolution could overrepresent very small features, which could also lead to misleading results (Dikau, 1989). Several studies indicate that a higher spatial resolution does not always produce better results in certain applications (Cavazzi et al., 2013; Dai et al., 2019a; Keijsers et al., 2011; Mashimbye et al., 2019; Penizek et al., 2016; Sofia, 2020). For example, it has been shown that a coarser resolution could be beneficial in forested areas (Polidori and Simonetto, 2014). Moreover, Kienzle (2004) showed that in certain situations a coarser spatial DEM resolution can be advantageous for the extraction of surface parameters, in contrast to a finer resolution. Some research has been done to address this issue by using filtering techniques to reduce unwanted noise of too small topographic features (Clubb et al., 2014; Pelletier, 2013). Nevertheless, the scaling factor of the underlying research interest is important for the choice of the most suitable DEM with an appropriate spatial resolution.

DEM accuracy also depends on the acquisition method, since different sensors have different weaknesses and uncertainties that can be sources of elevation errors. The accuracy of conventional terrestrial surveys essentially depends on systematic instrumental errors, atmospheric refractions and errors made by the operator (Ghilani and Wolf, 2015; Kahmen, 2006). In the case of GPS-based measurements, the accuracy also depends on satellite geometry and biases of satellite and receiver clock (Ghilani and Wolf, 2015). The accuracy of DEMs generated from stereo imagery mainly depends on the camera resolution as well as the stability of airplane or satellite, camera distortion, atmospheric conditions and the image processing technique (Florinsky, 2012; Ghilani and Wolf, 2015; Kraus, 2004). For LiDAR derived DEMs, scan angle, flight speed, distance to the surface as well as the surface reflectivity and slope gradient of the terrain are sources for potential elevation errors (Brenner et al., 2007; Florinsky, 2012). RADAR based DEMs contain the error sources of weak baseline and inclination angle, receiver phase instabilities, atmospheric conditions as well as physical properties of the surface (Brenner et al., 2007; Bürgmann et al., 2000; Florinsky, 2012).

When assessing the quality of a DEM, primarily the vertical accuracy is meant and all previously mentioned error sources aim at the vertical accuracy of the DEM. However, the error of DEMs has also a horizontal dimension as a planimetric shift of elevation points influences the vertical accuracy as well. These shifts in horizontal direction can be caused by various factors during the data acquisition process, as well as during the processing of the data. For RADAR datasets, mainly atmospheric conditions, geometric distortions in shadowed or layover areas and signal discontinuities are responsible for horizontal inaccuracies of elevation data (Guan et al., 2020). For stereo imagery, the horizontal error mainly depends on the exterior and interior orientation parameters and can be compensated with highly accurate GCPs (Guan et al., 2020). Horizontal errors can affect significantly the vertical accuracy of DEMs. Especially in undulated areas with large elevation changes over short distances, a horizontal offset of elevation can have a great impact (American Society for Photogrammetry and Remote Sensing (ASPRS), 2004).

2.6.2 Quantitative accuracy assessment

A common method to assess the vertical accuracy of DEMs is the comparison with more accurate reference data using statistical measures. To achieve reliable results, a reference dataset should fulfil three requirements. It should be (1) independently surveyed, (2) at least three times more accurate than the evaluated DEM and (3) well distributed over the entire area to ensure representative results (Höhle and Höhle, 2009; Maune and Nayegandhi, 2018; Polidori and El Hage, 2020). The most common reference datasets used for the evaluation of DEMs are elevation data from GNSS, topographic maps, data from ground surveying or other DEM products (Mesa-Mingorance and Ariza-Lopez, 2020). According to Mesa-Mingorance and Ariza-Lopez (2020) almost 90 % of evaluations are conducted with point-based or grid-based datasets. Only minor evaluations were done with linear features, such as roads or runways (Becek, 2014; Becek et al., 2016).

Several common statistical measure formulas are listed in Table 2-3. Basic measures are the mean error and the standard deviation. The mean error provides the ability to compare the mean elevation of two datasets to detect systematic over- or underestimation of elevations (Fisher and Tate, 2006). The standard deviation gives an insight into the variability of the dataset and is a common measure for the random error of a dataset (Fisher and Tate, 2006; Höhle and Höhle, 2009). The most common statistical measure for the evaluation of DEM accuracy is the root mean square error (RMSE). It is an easy to calculate and reliable indicator for the vertical accuracy of DEMs. However, the RMSE assumes a normal distribution of errors, which is often not the case for DEMs due to filtering and interpolation errors. The presence of many outliers in the dataset can lead to a poor performance of the RMSE (Höhle and Höhle, 2009). To overcome this issue, the normalized median absolute deviation (NMAD) has been established as a more robust measure against outliers. This measure uses the median of all deviations instead of the mean, which is less sensitive to unbiased outliers (Höhle and Höhle, 2009).

Table 2-3: Common statistical accuracy measures for DEMs. In the table, Δh_i denotes the elevation difference between the assessed DEM and the reference DEM, n is the number of pixels and $m_{\Delta h}$ the median of all elevation differences.

Accuracy measure	Formula
Mean error	$ME = \frac{\sum_{i=1}^{n} \Delta h_i}{n}$
Standard deviation	$SD = \sqrt{\frac{\sum_{i=1}^{n} (\Delta h_i - ME)^2}{(n-1)}}$
Root mean square error	$RMSE = \sqrt{\frac{\left(\sum_{i=1}^{n} (\Delta h_i)^2\right)}{n}}$
Normalized median absolute deviation	$NMAD = 1.4826 \times median(\lvert \Delta h_i - m_{\Delta h} \rvert)$

2.6.3 Visual accuracy assessment

Besides a statistical evaluation of DEM accuracy, a qualitative assessment on the reliability of represented land surface and relief in the DEM is important. Unlike the quantitative assessment, the visual evaluation usually does not have a formalized framework (Mesa-Mingorance and Ariza-Lopez,

2020). It is often the initial step in the evaluation process to identify major issues in the DEM. The visual evaluation is mostly done visually by reviewing the degree of realism of the relief. Typically, it quickly reveals major issues in the DEM and identifies problematic sites. However, it depends on the experience of the person who conducts the visual control, as this is an intuitive evaluation approach based on human experience without quantitative GCPs.

DEMs can be visually reviewed in several different ways. A common method is the visual inspection of a hillshade derived from the DEM (Maune and Nayegandhi, 2018; Polidori and El Hage, 2020). A hillshade is a computed shaded relief created by a hypothetical illumination source at a specific position that illuminates the shapes of the landscape. It depends on the relative orientation of the cells to the light source. This technique provides a realistic view of the terrain similar to our view on landscapes in reality. Hillshades are particularly helpful for the identification of spikes and artefacts that cause unrealistic shapes or unwanted noise in the DEM (Figure 2-14) (Arrell et al., 2008; Polidori and El Hage, 2020).

The 2D perspective of a hillshade sometimes suffers from being limited to a single illumination source. This leads to features that are not visible to the viewer if they are hidden in the shadowed parts or parallel to the light source (Maune and Nayegandhi, 2018; Novak and Ostir, 2021). Therefore, it can be beneficial to calculate several hillshades with illumination sources from different perspectives. Another possibility to avoid this issue is the creation of a 3D model from the DEM that can be inspected in a software program. This allows the reviewer to rotate the data and view it from different perspectives. Some issues may be more apparent from additional perspectives than only from the 2D 'bird's eye' view (Maune and Nayegandhi, 2018).

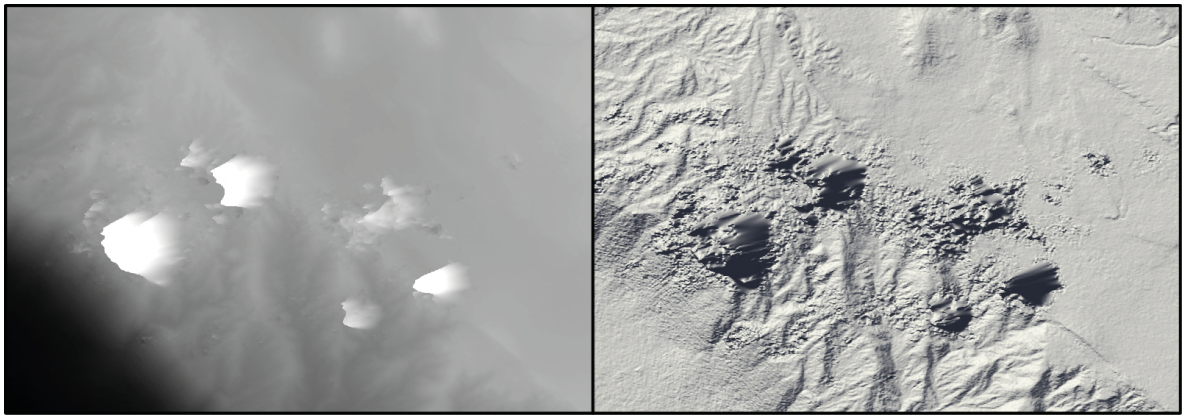

Figure 2-14: Example of artefacts in the DEM (left image) and hillshade (right image).

2.7 Study areas

The studies of this contribution have been conducted in three study areas at totally different places in the world. The areas are the Atacama Desert in northern Chile, the Rur catchment in western Germany and the Iranian Loess Plateau located in the northeast of Iran (Figure 2-15). In order to obtain representative results on the accuracy of DEMs, it is necessary to test their suitability in different landscapes in terms of land cover and terrain roughness. Hence, the accuracy assessment of the DEMs was performed in two study areas that have completely different landscape characteristics.

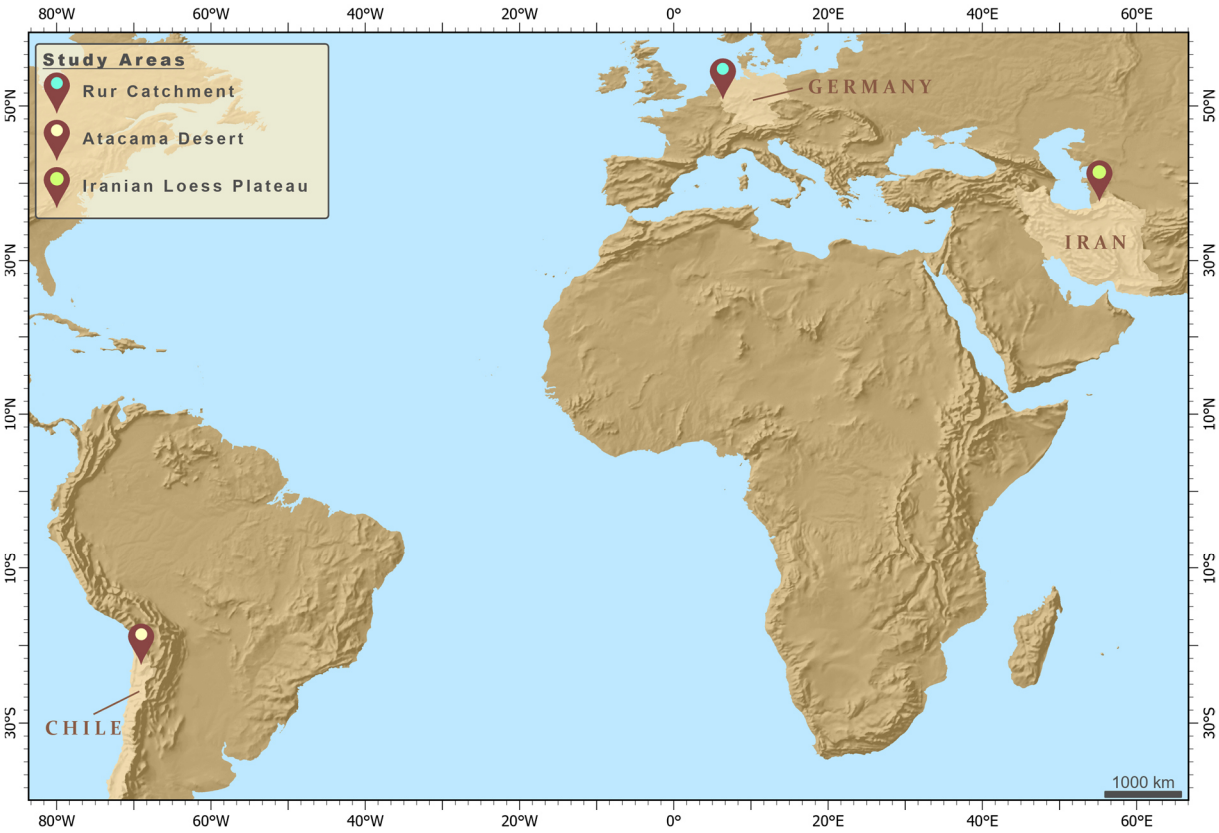

Figure 2-15: Geographic location of the three study areas of this contribution.

The analyses in chapters 3 and 4 have been conducted in one of the driest areas on Earth. The Atacama Desert is located in the administrative areas of Tarapacá and Antofagasta in the northern part of Chile. A detailed introduction to this study area is given in section 3.2. It consists of large elevation changes from the Pacific coast to the high Andes, resulting in a relatively high average slope steepness. The landscape offers a great variety of different relief types from broad and flat areas to very steep and dissected zones. A cross-section of the morphodynamical zonation of the area is illustrated in Figure 2-16, showing schematically the elevation differences from the Pacific Ocean in the west to the high Andes in the eastern part of the area. The area is characterized by very sparse vegetation and the absence of any land cover objects in most parts of the area. An impression of the landscape is given in Figure 2-17.

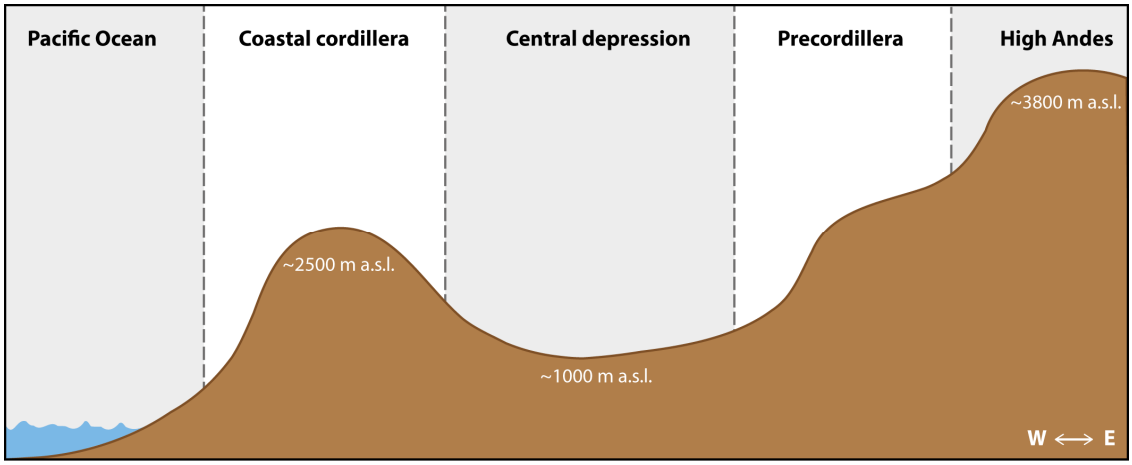

Figure 2-16: Schematic cross-section of the physiographic landscape units of the Atacama Desert.

Figure 2-17: Landscape of the Chilean Atacama Desert (Picture taken by Dirk Hoffmeister).

As a second study area for the vertical accuracy assessment of DEMs, the Rur catchment was chosen (chapter 5). This study site is mainly located in western Germany in the German Federal State of North-Rhine Westphalia. The location of the study area and its landscape properties is described in detail in section 5.2. It can be described as a typical mid-latitude landscape that is highly different to the hyperarid Atacama Desert. The Rur catchment consists of a very diverse land cover with a mixture of forested, urban and agricultural areas. The region has mostly flat landscapes in the northern part and moderately shaped terrain in the southern part of the catchment. The overall steepness of the Rur catchment is lower than in the Atacama Desert study area in Chile. While the Chilean study area has an average slope of 4.6°, the average slope of the Rur catchment is significantly lower with 2.1°. Since the Rur catchment additionally has a very heterogeneous soil type structure, the analysis of the digital soil mapping application in chapter 7 was also carried out in this area. A more detailed description of the occurring soils is provided in section 7.2. Figure 2-18 exemplary illustrates the landscape of the northern and southern parts of the Rur catchment.

Figure 2-18: Landscape of the Rur catchment. A: panoramic view of the northern part of the catchment with mostly flat and rural landscape. B: landscape of the southern part of the catchment with predominantly undulated and forested areas.

The analysis on the application of landform classifications from DEMs in chapter 6 was carried out in two small areas situated in the Iranian Loess Plateau. Both areas are located about 15 km apart and have a size of 100 km² each. The Loess Plateau is located in the province Golestan in the northeast of Iran near the state border of Turkmenistan. The area mainly consists of deposited quaternary sediments. In addition to the deposition of marine and fluvial sediments, mainly loess was deposited there during the last glacial cold periods (Ehlers, 1980; Frechen et al., 2009). Loess is a homogeneous and mostly unstratified light yellowish sediment, which was mostly formed and aeolian deposited during the Quaternary glacial (Pécsi and Richter, 1996). After the deposition of loess sediments, the landscape of the Iranian loess plateau was mainly formed by extensive erosion processes during the Holocene that have led to the development of a very small-scale differentiated relief (Kehl, 2010). Nowadays, the western part of the study area consists of a hilly landscape, which is dissected by a large number of narrow v-shaped valleys with steep slopes. The eastern part of the study area has a flatter relief characteristic with several valleys of different widths cut into the relief. A detailed overview of the study areas is provided in section 6.2. The characteristics of the landscape is illustrated in Figure 2-19.

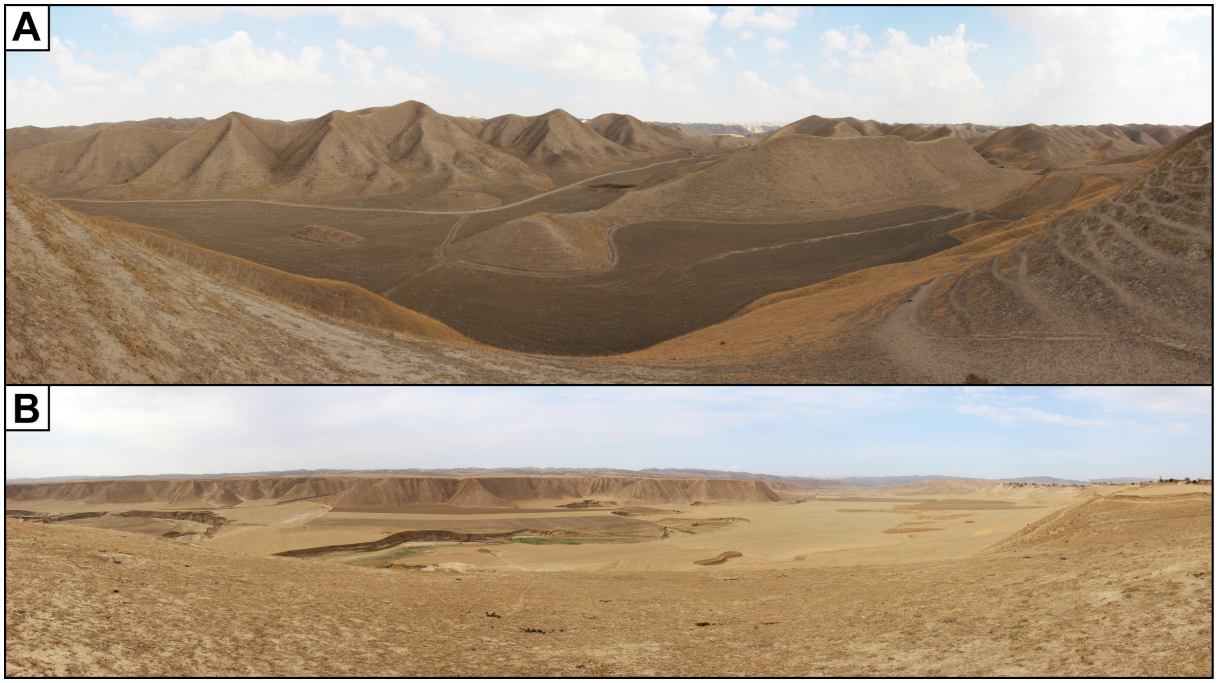

Figure 2-19: Landscape of the Iranian Loess Plateau. A: western study area with a multitude of hills and narrow valley incisions. B: eastern study area with a more levelled relief and broader incised valleys cut into the landscape (Pictures taken by Dirk Hoffmeister).

3 A relief dependent evaluation of digital elevation models on different scales for northern Chile

TANJA KRAMM[1], DIRK HOFFMEISTER[1]

Published in: ISPRS International Journal of Geo-Information, 2019, **8** (10), 430.

DOI: 10.3390/ijgi8100430

Formatting and orthography of the manuscript is adapted to the dissertation style.

[1]GIS and Remote Sensing, Institute of Geography, University of Cologne, Albertus Magnus Platz, 50923 Köln, Germany.

Abstract: Many geoscientific computations are directly influenced by the resolution and accuracy of digital elevation models (DEMs). Therefore, knowledge about the accuracy of DEMs is essential to avoid misleading results. In this study, a comprehensive evaluation of the vertical accuracy of globally available DEMs from Advanced Spaceborne Thermal Emission and Reflection Radiometer (ASTER), Shuttle Radar Topography Mission (SRTM), Advanced Land Observing Satellite (ALOS) World 3D and TanDEM-X WorldDEM™ was conducted for a large region in northern Chile. Additionally, several very high resolution DEM datasets were derived from Satellite Pour l'Observation de la Terre (SPOT) 6/7 and Pléiades stereo satellite imagery for smaller areas. All datasets were evaluated with three reference datasets, namely elevation points from both Ice, Cloud, and land Elevation (ICESat) satellites as well as very accurate high resolution elevation data derived by unmanned aerial vehicle (UAV)-based photogrammetry and terrestrial laser scanning (TLS). The accuracy was also evaluated with regard to the existing relief by relating the accuracy results to slope, terrain ruggedness index (TRI) and topographic position index (TPI). For all datasets with global availability, the highest overall accuracies are reached by TanDEM-X WorldDEM™ and the lowest by ASTER Global DEM (GDEM). On the local scale, Pléiades DEMs showed a slightly higher accuracy as SPOT imagery. Generally, accuracy highly depends on topography and the error is rising up to four times for high resolution DEMs and up to eight times for low resolution DEMs in steeply sloped terrain compared to flat landscapes.

Keywords: accuracy assessment; digital terrain model; stereo satellite imagery; topography; terrestrial laser scanning; topographic position index; terrain ruggedness index; unmanned aerial vehicles

3.1 Introduction

Relief plays a main role for numerous geomorphological, climatic, hydrologic and ecologic processes. Therefore, a detailed understanding of the prevailing terrain conditions is essential (Wilson, 2012). Nowadays, geomorphometric relief information is available by digital elevation models (DEMs), which provide a 2.5D digital representation of the Earth's relief using regularly spaced elevation data.

The first digital elevation datasets with a global coverage were DEMs from the Shuttle Radar Topography Mission (SRTM) and the Advanced Spaceborne Thermal Emission and Reflection Radiometer (ASTER) with a resolution of 30 m, which have revolutionized the use of DEMs (Farr et al., 2007; Tachikawa et al., 2011). While analyses in former times only were possible for small areas, these DEMs enabled the possibility of analysing larger surface areas up to almost the whole Earth. In recent years, the Advanced Land Observing Satellite (ALOS) World 3D as a third global DEM with a ground

sampling distance (GSD) of 30 m was made publicly available (Tadono et al., 2014; Takaku et al., 2014). The most recent dataset with global coverage is the TanDEM-X WorldDEM™ dataset with a GSD of 12 m, which is expected to be the new standard in geometric resolution and accuracy (Krieger et al., 2007; Rizzoli et al., 2017). However, all of these DEMs usually are less accurate and capture less terrain details due to lower GSD in comparison to very high resolution elevation models derived by stereo satellite imagery. These datasets normally have a higher GSD and vertical accuracy. However, they are often not suitable for larger areas due to high costs and time-consuming processing. Therefore, these are only usable for large scale analyses.

Elevation models generally enable the possibility of a quantitative characterization of relief and are used by geomorphometry as a multifaceted interdisciplinary subject in a multitude of different scientific fields (Sofia et al., 2016). Hence, DEMs are widely used sources in numerous geospatial studies for the terrain-based identification of environmental features. Many studies about landform distribution analyses (Dragut and Blaschke, 2006; Huang et al., 2018; Kramm et al., 2017; Mokarram et al., 2015; Newman et al., 2018b), geomorphology (Bishop et al., 2012) and the human impact on geomorphology (Tarolli and Sofia, 2016) were conducted. Furthermore, in the field of hydrology DEMs are required for stream network analysis (Drisya and Kumar, 2016; Schwanghart et al., 2013) and groundwater flow modelling (Rossman et al., 2018). Terrain features derived by DEMs are also used as a predictor for digital soil mapping (Guo et al., 2019; Kalambukattu et al., 2018; Marques et al., 2018). Additionally, DEMs are crucial for ecological analysis, such as vegetation and plant distribution research (Kellndorfer et al., 2004; Leempoel et al., 2015; Moudry et al., 2018). Climatic issues, like the observation of glacier changes (Blaszczyk et al., 2019), sea-level rise (Gesch, 2018) or climatic modelling (Mmbando and Kleyer, 2018), are also fields of application where terrain information is needed.

All of these applications have raised increasing needs for accessible DEMs of higher resolution and accuracy. However, if the process or object of interest is spatially smaller than the GSD of the utilized elevation datasets, the risk of misleading results increases (Goodchild, 2011). Likewise, it is well known that the GSD of a digital elevation model directly influences derived terrain variables, such as slope or aspect. For instance, Kienzle (2004) showed that the mean slope can differ from 13.9 % on a 50 m grid to 8.8 % on a 250 m resolution DEM. This effect even increases for higher resolutions and steeper terrain. Zhang and Montgomery (1994) derived mean slope differences of up to 24 % between a 2 m and a 90 m DEM for the same area. Kramm et al. (2017) showed that the accuracy of detected landforms can range up to 30 % for the same algorithm and area by using DEMs in different resolutions. Likewise, also different DEMs with the same grid size result in significant differences in the delineated landforms.

Thus, the effects of scale and the impact of the DEMs GSD when deriving topographical features are well documented (Deng et al., 2007; Kim and Zheng, 2011; Smith et al., 2006; Sörensen and Seibert, 2007) and also the first techniques for multiscale analysis are available (Grohmann et al., 2011; Lindsay et al., 2015; Newman et al., 2018a). Furthermore, it is crucial to analyse the accuracy of DEMs in order to select the most suitable one regarding the aim, accuracy and scale of the study. Large-channel profiles over wide distances are easily possible to identify even with 90 m resolution data, landscapes on large scales require elevation data with 1 – 30 m GSD for a successful identification of individual hillslopes and ridges (Grieve et al., 2016a; Grieve et al., 2016b). However, a DEM with a higher GSD is not always advantageous, as elevation models with a very high resolution can depict too many details, which are not relevant for the study.

In recent years, numerous studies have investigated the accuracy of available DEMs. Much research was already done on the accuracy of SRTM and ASTER Global DEM to examine their performance in different situations and sites (Mukherjee et al., 2013; Rexer and Hirt, 2014; Satge et al., 2015; Suwandana et al., 2012b; Zhao et al., 2011). All of these investigations indicate that the expectable root mean square error (RMSE) for the ASTER GDEM is about 3 – 4 m in flat terrain and 7 – 8 m with up to 16 m (RMSE) in steeper relief. For the SRTM1 DEM, the results show an average error of 3 – 4 m in flat landscapes up to 7 – 8 m in mountainous areas. Additionally, the accuracy of the newer ALOS World 3D (Caglar et al., 2018) and the TanDEM-X WorldDEM™ (Altunel, 2019; Wessel et al., 2018; Zhang et al., 2019a) was assessed by comparing them with various reference datasets. Several studies directly compared the performance of different global elevation models in various geographical settings. The accuracy of the 30 m resolution DEMs from SRTM, ASTER Global DEM and ALOS W3D was assessed by many studies (Alganci et al., 2018; Florinsky et al., 2018; Hu et al., 2017; Jain et al., 2018; Li and Zhao, 2018; Yahaya and El Azzab, 2019). They indicate a slightly higher accuracy of ALOS W3D in comparison to SRTM and ASTER GDEM. The result showed an average error of 2 – 3 m (RMSE) in flat terrain and 6 – 7 m (RMSE) in steeper sloped landscapes for the ALOS W3D. However, less studies are available yet that compare the performance of the newly available TanDEM-X WorldDEM™ with other globally available DEMs. Some studies investigated the accuracy of TanDEM–X WorldDEM™ with elevation models from SRTM and ASTER Global DEM (Becek et al., 2016; Pipaud et al., 2015; Podgorski et al., 2019). Others compared the accuracy of SRTM, ASTER GDEM, ALOS World 3D and TanDEM-X WorldDEM™ for coastal relief settings (Gesch, 2018; Zhang et al., 2019b) or for relatively small areas (Grohmann, 2018; Purinton and Bookhagen, 2017). They all showed a relatively high performance of the TanDEM-X WorldDEM™, which is mostly superior to the accuracy of the 30 m global DEMs. The results indicate an average error of less than 3 m for the 12 m TanDEM-X WorldDEM™, but some recent studies also showed weaknesses of this DEM in very steep terrain (Podgorski et al., 2019).

Nevertheless, a comprehensive analysis of the accuracy of all four global DEMs over large areas is still missing. Furthermore, fewer studies evaluated the accuracy of DEMs on different scales and compared them to very high resolution elevation models derived by stereo satellite imagery. Alganci et al. (2018) included some local DEMs derived from Satellite Pour l'Observation de la Terre (SPOT) and Pléiades satellite imagery in their study of an urban area with anthropogenic landscape. Thus, an analysis of the performance of these DEMs in a landscape which is not anthropogenic influenced is still missing.

The goal of this study is to conduct a comprehensive accuracy assessment on the vertical accuracy of a multitude of different DEMs, both for a regional coverage and for local coverages. The regional coverage for the selected study area, the Atacama Desert in northern Chile, is given by datasets with nearly global coverage, namely the TanDEM-X WorldDEM™, ASTER Global DEM, ALOS World 3D and SRTM DEM. Local areas are covered by DEMs derived from stereo-satellite imagery recorded by SPOT 6/7 and Pléiades satellites with areas of 100 to 400 km². The accuracy assessment was performed with three control datasets, which are the light detection and ranging (LiDAR)-based elevation points from both Ice, Cloud, and land Elevation (ICESat) satellites and very accurate high resolution elevation data derived by unmanned aerial vehicle (UAV)-based photogrammetry as well as terrestrial laser scanning (TLS). The accuracy analysis is based on the root mean square error (RMSE) and normalized median absolute deviation (NMAD). Furthermore, fewer studies have systematically investigated the influence of different terrain conditions on the vertical accuracy of DEMs. Some work has been done to investigate the appropriateness of DEMs for delineating different landforms (Pipaud et al., 2015) and the relationship of DEM errors in correlation to various landform types and altitudes (Liu et al., 2019).

Additionally, the accuracy of DEMs for several small areas with plain, hilly and mountainous terrain (Hu et al., 2017) and with different slopes (Podgorski et al., 2019) was assessed. Nevertheless, more information about the impact of relief over larger areas on the vertical accuracy of DEMs is necessary. Thus, in this study the accuracy is addressed and evaluated with regard to the existing topography by linking terrain ruggedness index (TRI), topographic position index (TPI) and slope to error values, as the terrain has a direct influence on accuracy (Grohmann, 2015; Holmes et al., 2000; Mukherjee et al., 2013).

3.2 Study area

The study was conducted in the northern part of Chile (Figure 3-1). The area covers the Chilean part of the Atacama Desert, represented by the administrative regions of Tarapacá and Antofagasta. The region, which is one of the driest areas on Earth, is characterized by its hyperarid climate with less than 10 mm/year rainfall on average (Houston and Hartley, 2003) lying in the 'Arid Diagonal' of South America. This hyperaridity of the Atacama is caused by a combination of subtropical subsidence, coastal upwelling of the cold Humboldt current and rain-shadow effects of the high Andes (Hartley et al., 2005), which might have been established since the mid-Miocene or earlier (Dunai et al., 2005).

The relief shows large height differences from the coast of the Pacific to the mountains of the Andes with altitudes up to 6700 m above sea level. Furthermore, the study area consists of a diverse topography with steep, seaward cliffs and deeply incised canyons as well as large alluvial fans and volcanos in the mountain range of the Andes. Thus, the landscape offers a cross-section of different relief types from flat and broad landscapes to steep and dissected terrain with hardly any vegetation cover. The morphodynamic zonation of the Atacama from west to east is described by the coastal ranges with the coastal cordillera reaching up to 2500 m above sea level, the central depression at about 1000 m above sea level and the pre-Andean or western cordillera, as well as the Altiplano (≈ 3800 m above sea level). DEMs are for instance used for geomorphometric analysis of alluvial fans at the coastal range (Walk et al., 2020) as well as the geomorphometric characterization of the unique so-called zebra stone stripes, described as contour-parallel bands of dark gravels with contrasting bands of fine-grained soil (May et al., 2019).

3.3 Materials and methods

3.3.1 Global digital elevation models (GDEMs)

The accuracy of several DEMs with a global coverage was validated in this study that is described in the following sections. Except for the 12 m TanDEM-X WorldDEM™, all utilized DEMs are freely available. All of these DEMs were evaluated for an area of around 190,000 km^2 (Figure 3-1). To make the heights of all DEMs comparable, a conversion to the same vertical datum is essential. Therefore, in this study all elevation models were converted to the World Geodetic System 1984 (WGS84) ellipsoid as the vertical datum.

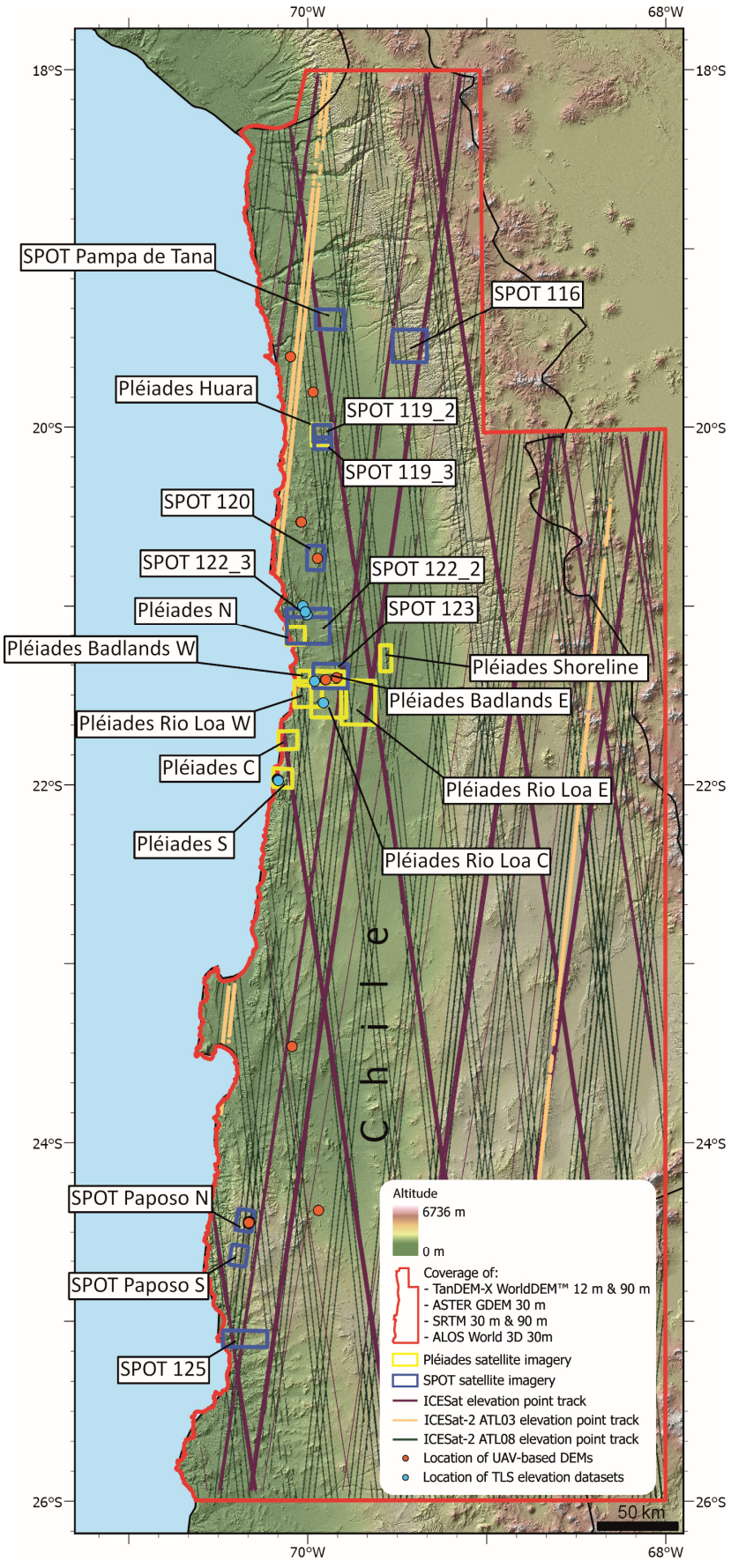

Figure 3-1: Overview map of the study area and locations of digital elevation models (DEMs) and ground truth data. Map is based on Shuttle Radar Topography Mission (SRTM) elevation data.

3.3.1.1 Advanced Spaceborne Thermal Emission and Reflection Radiometer (ASTER) GDEM

The ASTER Global DEM was produced by processing the entire optical imagery archive from the ASTER sensor onboard of National Aeronautics and Space Administration's (NASA) Earth Observing System Terra satellite, which was launched in December 1999 (Abrams et al., 2010; Tachikawa et al., 2011). The mission's aim was primarily to collect multispectral data of the Earth, but in addition to the multispectral bands, the ASTER sensor has a near infrared sensor that is inclined by 27.6° and enables stereoscopic recording according to the 'as-track' principle (Hirano et al., 2003).

A first version of this dataset was released for open access in June 2009 by the NASA and the Japanese Ministry of International Trade and Industry covering all land areas from 83°N to 83°S latitude. The second version was released in October 2011 with a GSD of 1 arc-second (≈ 30 m). It includes additional scenes from 2008 to 2011 and an improved water mask to achieve various improvements in the overall accuracy and to reduce artefacts mainly caused by cloud edges (Tachikawa et al., 2011). The last update was created by including even more Level 1-A ASTER scenes acquired between March 2000 and November 2013 and conducting a more effective cloud masking to reduce artefacts. Furthermore, voids were filled with additional data from SRTM1 and the Global Multi-resolution Terrain Elevation Data 2010 (GMTED2010) for most areas of the world. The average vertical accuracy of the ASTER GDEM Version 3 was estimated with a standard deviation of 12.1 m, which is 0.5 m superior to the prior version (Abrams and Crippen, 2019).

The utilized ASTER GDEM Version 3 in this contribution was originally referenced horizontally to the WGS84 and vertically to the Earth Gravitational Model 1996 (EGM96). Thus, the DEM was converted to WGS84 ellipsoid with a calculated raster of the undulation between EGM96 geoid and WGS84 ellipsoid for the whole region. The creation of the undulation raster was done with the software MSP GEOTRANS v.3.8. To do so, a net of points that were equally distributed over the whole area was created for which the undulation was calculated by the software. Subsequently, a raster was processed by interpolating the undulation points with Kriging algorithm. Finally, the heights of the undulation raster were added to the ASTER GDEM heights.

3.3.1.2 Advanced Land Observing Satellite (ALOS) World 3D

The ALOS was launched in 2006 by the Japan Aerospace Exploration Agency (JAXA). Onboard the satellite was the Panchromatic Remote-sensing Instrument for Stereo Mapping (PRISM) sensor that operated from 2006 to 2011 with the aim to generate global elevation data from along-track triplet stereoscopic panchromatic images with 2.5 m GSD (Tadono et al., 2009; Takaku et al., 2014). During the sensor´s operation time, approximately 6.5 million scenes, covering the entire globe, were produced that were used to generate a global DEM with a GSD of 5 m. To check data quality during the generation process, an automatic check by comparing the data with reference information of ICESat GLAH14 heights and SRTM as well as by visual human interpretations was conducted to achieve a target height accuracy of 5 m (Takaku et al., 2014). Besides the 5 m DEM that is only distributed commercially, JAXA released a freely available 1 arc-second (≈ 30 m) ALOS DEM for non-commercial purposes in 2016, which was produced by resampling the original 5 m version (Takaku and Tadono, 2017). The provided ALOS World 3D (W3D) dataset (version 1), which was used in this study, is already referenced to WGS84 horizontal and WGS84 ellipsoidal vertical datum. Therefore, no further georeferencing was necessary for this dataset.

3.3.1.3 Shuttle Radar Topography Mission (SRTM)

While the previously presented ASTER and ALOS DEMs were generated by passive remote sensing techniques, the SRTM recorded actively the Earth's surface in February 2000 with two synthetic aperture radar systems. A C-band system (5.6 cm, SIR-C), operated by NASA's Jet Propulsion Laboratory (JPL), and a X-band system (3.1 cm, X-SAR), controlled by the German Aerospace Centre (DLR) and the Agenzia Spaziale Italiana (ASI, Italy), scanned the Earth for 11 days with the aim to map its topography between latitudes 60°N and 60°S (Farr et al., 2007).

A first global DEM version of the C-band data was released by the USGS in 2003 with a GSD of 3 arc-seconds. Furthermore, a DEM with 1 arc-second resolution was made available, but at first only for the US. For the rest of the world, SRTM DEM data with 1 arc-second resolution followed in 2015. Since their initial release, the SRTM-1 and SRTM-3 datasets have been continuously improved in several versions. In 2003, the data was initially published unprocessed, i.e. they contained regions without data or with incorrect elevation information. Furthermore, any processing of coastlines and water bodies was missing, which took place in a revised second version. In a third revised version, regions without data were filled mainly with elevation data from ASTER GDEM2 (Rodríguez et al., 2005). For the SRTM-3 dataset, a 4th version was processed by the Consultative Group of International Agricultural Research-Consortium for Spatial Information (CGIAR-CSI), which used various interpolation techniques described by Reuter et al. (2007) and extra auxiliary DEM data for void filling.

The overall accuracy of the SRTM DEM is determined by Farr et al. (2007) with an absolute vertical height error of 6.2 m and a relative height error of 5.5 m for South America. The horizontal positional accuracy was assessed with an absolute geolocation error of 9.0 m. In this contribution, the SRTM-1 version 3 DEM with a GSD of 30 m and a SRTM-3 version 4.1 dataset with 90 m resolution were used. Both are referenced horizontally to WGS84 and vertically to the EGM96 geoid. The conversion to a vertical WGS84 datum was done analogous as described for the ASTER GDEM dataset.

3.3.1.4 TanDEM-X WorldDEM™

The TanDEM-X mission from 2010 to 2015 was launched as a public-private effort between the DLR and Airbus Defence and Space to produce a precise global DEM between the latitudes 90°N and 90°S with higher accuracy and resolution than the recently existing ones. The Earth was measured from two satellites (TerraSAR-X and TanDEM-X) in a controlled orbit with a baseline of 250 – 500 m with X-band RADAR interferometry (InSAR) (Rizzoli et al., 2017; Wessel, 2016). The TanDEM-X WorldDEM™, which is subsequently denoted as 'TanDEM-X', was produced in the original version with 0.4 arc-seconds (≈ 12 m) GSD as a commercial product of the TanDEM-X mission. The DEM heights were calibrated with heights of the ICESat GLA14 data product (Wessel et al., 2018). Furthermore, a 1 arc-second (≈ 30 m) version was generated from the unweighted mean values of the underlying 12 m pixels (Wessel, 2016). Additionally, a 3 arc-seconds (≈ 90 m) elevation model has been released by the DLR in 2018, which is free of charge for use in academic research. This DEM was also created by resampling the original 0.4 arc-second dataset.

The originally intended accuracy for the produced TanDEM-X DEM was an absolute error of less than 10 m in horizontal and vertical direction (Grohmann, 2018; Rizzoli et al., 2012; Wessel et al., 2018). Several studies showed that the DEM product reaches this goal (Rizzoli et al., 2017; Wessel et al., 2018).

However, they indicate that the accuracy is even higher than originally assumed. For the 90 m DEM, only few studies are available yet that investigated its accuracy, but they suppose a higher accuracy than the SRTM 90 m DEM (Altunel, 2019; Keys and Baade, 2019). In this study, the TanDEM-X DEM was used in two different resolutions of 12 m and 90 m. The horizontal datum for both DEMs is WGS84 and the heights were already referenced to WGS84 ellipsoid heights.

3.3.2 Local digital elevation models

In addition to the globally available elevation models with lower spatial resolution, 10 elevation models were derived from Pléiades satellite stereo imagery, seven DEMs from SPOT 6 and four from SPOT 7 satellite imagery. The DEMs are distributed over the whole area, depicted in Figure 3-1, and each DEM covers an area of about 100 – 400 km^2. These datasets were processed with the software PCI Geomatica 2018 OrthoEngine with automatic ground control point (GCP) and tie-point collection. For the GCP collection process, an additional orthorectified image was used to improve the accuracy of extracted GCPs. The orthorectified image was calculated with provided rational polynomial coefficients (RPCs) information and elevation data from the TanDEM-X 12 m DEM to reduce topographical distortions in the original satellite images. For each dataset, around 80 GCPs and 50 tie-points were extracted. The points were checked manually to receive a calculated residual error of less than 1 m (RMSE). All derived elevation models were resampled to 5 m during the generation process to avoid small artefacts in the DEM product.

3.3.2.1 Pléiades

The Pléiades system consists of a constellation of two satellites operated by the French Space Center (CNES) and ASTRIUM GEO-Information Services. The first satellite (Pléiades 1A) was brought into a sun-synchronous orbit on 16 December 2011. The second one (Pléiades 1B) followed on 2 December 2012 (Astrium GEO-Information Services, 2012). Both satellites are equipped with optoelectronic, charge-coupled device (CCD) scanners, which scan the Earth's surface transversely to the direction of flight and convert the measured radiation into a measurable electrical signal. It is recorded in a panchromatic channel and four multispectral channels, each with five line sensors (de Lussy et al., 2006; Gleyzes et al., 2012). The line sensors of the panchromatic sensor have a width of more than 6000 pixels and the multispectral sensors have a resolution of 1500 pixels. Thus, the satellite achieves a GSD of 0.5 m in the panchromatic channel and 2 m in the multispectral channels (Astrium GEO-Information Services, 2012). The Pléiades satellites thus belong to the satellite systems with a very high GSD. The positional accuracy is indicated with 8.5 m at nadir and 10.5 m within an angle of 30°. Due to the high agility of the satellites, the Pléiades system is able to acquire three or more nearly synchronous images of the same area (Poli et al., 2013; Rieg et al., 2018).

3.3.2.2 SPOT 6/7

The SPOT 6 satellite was launched in 2012 by EADS Astrium, SPOT 7 followed in 2014. Both satellites operate with high resolution pushbroom sensors and record images in one panchromatic channel and four multispectral channels. They are able to produce images with a GSD of 1.5 m in the panchromatic and of 6 m in the multispectral channels (ASTRIUM, 2013). They also have the capability of tri stereo

imaging. The expectable geolocation accuracy for SPOT image products with primary standard, which are also used in this study, is stated with a circular error of less than 10 m at the 90th percentile (ASTRIUM, 2013).

3.3.3 Ground truth elevation data

For a vertical accuracy assessment, highly accurate evaluation data is necessary that should be at least three times more accurate than the evaluated dataset (Maune and Nayegandhi, 2018). In this study, the evaluation check was conducted by comparing the DEM heights with several highly accurate elevation data, which are described in the following.

3.3.3.1 Ice, Cloud, and Land Elevation satellite (ICESat)

The primary goal of NASA's ICESat mission was to observe the cryosphere and to measure changes in the polar ice sheet mass balance (Schutz et al., 2005). One of the utilized instruments of the ICESat satellite is the Geoscience Laser Altimeter System (GLAS), which has a 1064 nm laser channel for surface altimetry measurements (Zwally et al., 2002). It operated between February 2003 and October 2009 and the surface elevation data was measured during two to three observation periods each year of about 1 month each. The laser footprints have 172 m spacing along-track and approximately 42 km cross-track spacing (Schutz et al., 2005; Zwally et al., 2002).

During its operation period, ICESat has acquired a huge database of raw and processed data organized in 15 data products. Of interest for this contribution is the 14th product ICESat/GLA14 data as this dataset contains highly accurate elevation data with a vertical accuracy of 0.1 m for flat locations and 1 m for undulated terrain (Duong et al., 2009; Schutz et al., 2005). Thus, several studies showed a successful vertical accuracy assessment over a broader regional extent with ICESat data (Huang et al., 2011; Zhao et al., 2017).

The originally provided ICESat/GLA14 land surface elevation data points were referenced to the Topex/Poseidon ellipsoid. To make them comparable with the elevation models of this study, a conversion to the WGS84 ellipsoid was conducted by using Equation (3-1) (Baghdadi et al., 2011).

$$h_{WGS84} = h_{Topex} - 0.707\,m \tag{3-1}$$

To detect outliers, e.g. from cloud reflections, all ICESat points with a height difference value greater than 60 m compared to the TanDEM-X heights were eliminated prior to the evaluation. Finally, a total number of around 450,000 points was used to evaluate the accuracy of the regional elevation models. Their locations are depicted in Figure 3-1. For the local elevation models, an average number of 500 elevation points was used for each scene. Scenes with less than 50 points were not evaluated in this study. Therefore, for 12 local DEMs no accuracy assessment with ICESat points was possible due to insufficient availability of elevation points.

3.3.3.2 ICESat-2

The Ice, Cloud, and land Elevation Satellite-2 (ICESat-2) was launched in September 2018 as the follow-on mission for ICESat (Markus et al., 2017; Neuenschwander and Pitts, 2019). It collects altimetry data from the Earth's surface with the Advanced Topographic Laser Altimeter System (ATLAS) instrument, which is a LiDAR system with a photon-level detection sensitivity. The outgoing single laser beam (532 nm) is split into three pairs of beams spaced approximately 3.3 km apart with a 90 m distance within the pairs. Furthermore, the laser emits a pulse signal every 0.7 m (Neuenschwander and Pitts, 2019). Therefore, it has a denser sampling and point coverage in comparison to its predecessor.

For accuracy assessment, the measured terrain heights of the ATL03 and ATL08 version 001 products were used in this study. The ATL03 product contains height information of all received photons with a point density of 0.7 m along each track. All heights of the ATL08 dataset are processed in fixed 100 m data points along-track that contain at least 50 signal photons. They include the best fit terrain elevation of each 100 m segment calculated by interpolating all photons within the segment. Only a few studies about the accuracy of these datasets are available yet. The terrain height accuracy of the ATL08 best fit dataset was denoted with a RMSE of 0.82 m for a large region in Finland (Neuenschwander and Magruder, 2019).

Prior to the accuracy assessment, all points in both datasets were eliminated that differ more than 30 m from TanDEM-X 12 m DEM heights. In this study a total of around 400,000 points were used from the ATL03 dataset and of around 650,000 points from the ATL08 dataset to evaluate the accuracy of the regional elevation models (Figure 3-1). For each local DEM, between 800 and 270,000 additional ATL03 points were used for evaluation. From the ATL08 dataset, an average number of 500 height points were used to evaluate each scene. The datasets were already provided with WGS84 horizontal and WGS84 ellipsoidal vertical datum. Therefore, no further georeferencing was required for this study.

3.3.3.3 Very High Resolution DEMs Derived by Unmanned Aerial Vehicle (UAV)

To evaluate the accuracy of the DEMs for large scale terrain, the height accuracy was compared to 19 elevation models derived with UAV-based photogrammetry with very high resolution. Figure 3-2 gives an overview about the covered terrain by these DEMs. They were achieved by imagery captured with two different systems. First, a 12 megapixel FC330 camera and a 20 mm full frame equivalent lens, fixed by a shock-absorbent gimbal on a rotary-wing quadrocopter (type: DJI Phantom 4), set to capture images every 10 secs. The camera was set to shutter speed priority (1/1000) with ISO-100. Second, an octocopter (type: Mikrokopter MK-Easy) with a 36.4 MP full-format Sony Alpha 7R with a Sony 28 mm lens (type: SEL28f20) was applied.

Flights at all sites were manually conducted between 10 am and 12 am local time on cloud-free days in a line-based pattern at two different heights, flying slower than 2.5 ms^{-1} to improve the accuracy of planimetry and altitude. Missions result in a high overlap of > 9 images per point. Subsequent image processing was conducted with AgiSoft Photoscan Professional (vers. 1.4.2). Images were mostly aligned using evenly distributed GCPs measured by real-time kinematic (RTK) positioning (type: Topcon GR5) and at 7 sites the direct Global Positioning System (GPS) measurements of the UAV recorded for each image were used. Processing in ultra-high quality for the dense point cloud generation resulted

in a GSD of 1 cm to 8 cm for the DEM and each scene covers an average area of about 0.04 km^2. Average errors range from 3 cm to 1.5 m for the datasets without GCPs in the horizontal direction and 3 cm to 1 m in the vertical direction. All data was exported in WGS84 UTM Zone 19S (EPSG: 32719). To evaluate the vertical accuracy of all DEMs, their GSD was up-sampled to the resolution of the UAV elevation models. Then, pixel-wise errors were derived by subtracting the heights of UAV derived DEMs from the other elevation models.

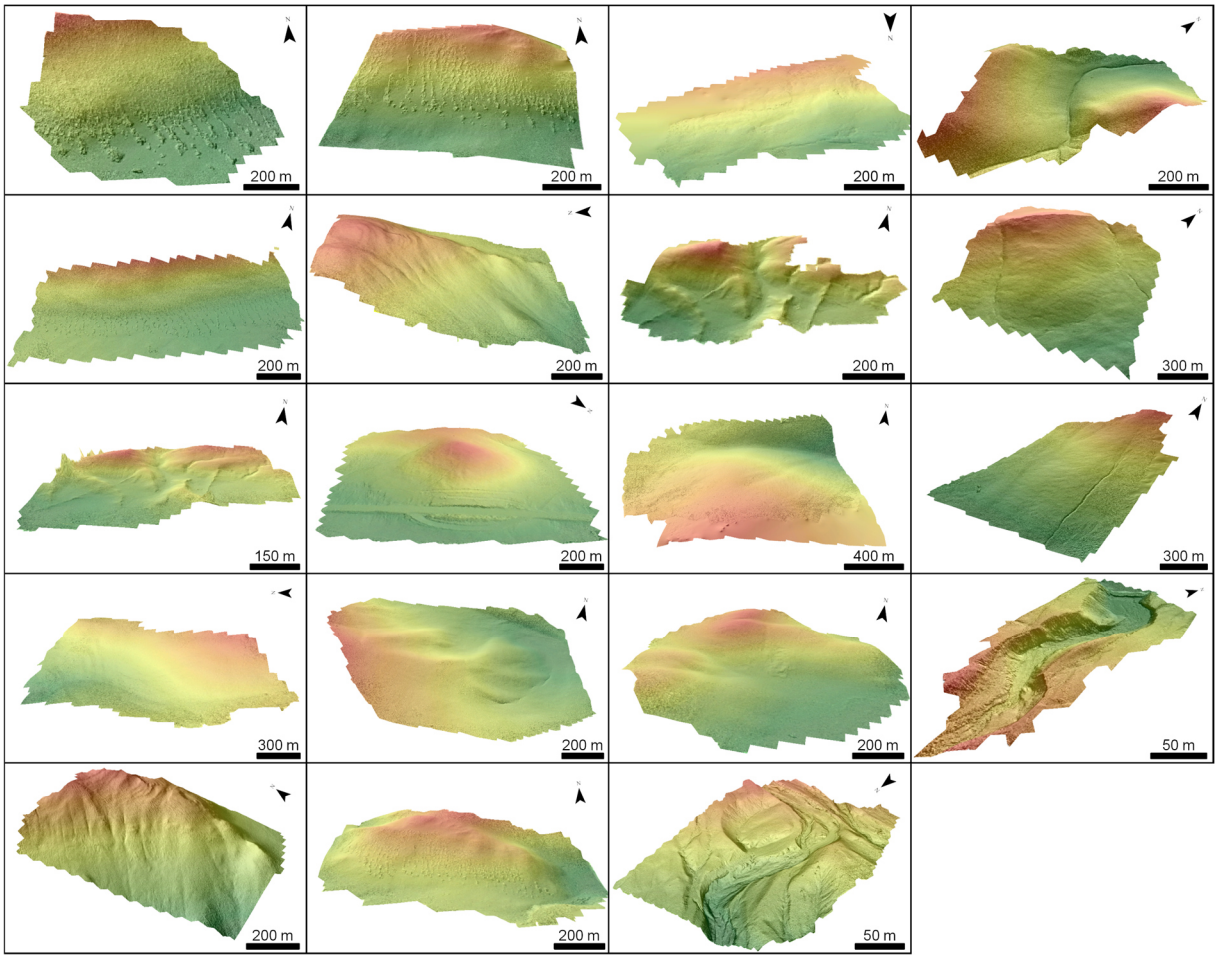

Figure 3-2: Perspective view of the covered relief of the 19 unmanned aerial vehicle (UAV) digital elevation models. Depicted relative altitudes of the raster datasets are from low (green) to high (red).

3.3.3.4 Terrestrial laser scanning

The topography at several areas (see Figure 3-1) was recorded by a terrestrial laser scanner (type: Riegl VZ-2000) in combination with the same RTK positioning system (type: Topcon GR5) for registration of the final point cloud. The derived raw point clouds were filtered and afterwards interpolated by inverse distance weighting to a raster dataset with a 50 cm cell size in ArcGIS Pro 2.2.4 (Environmental Systems Research Institute) for the estimation of the statistics comparable to the other analyses. The covered terrain of these raster datasets is depicted in Figure 3-3. In addition, subsampled point clouds with a similar mean point distance were compared with raster datasets in CloudCompare and analysed by the M3C2 algorithm in order to calculate detailed, reliable differences (Lague et al., 2013).

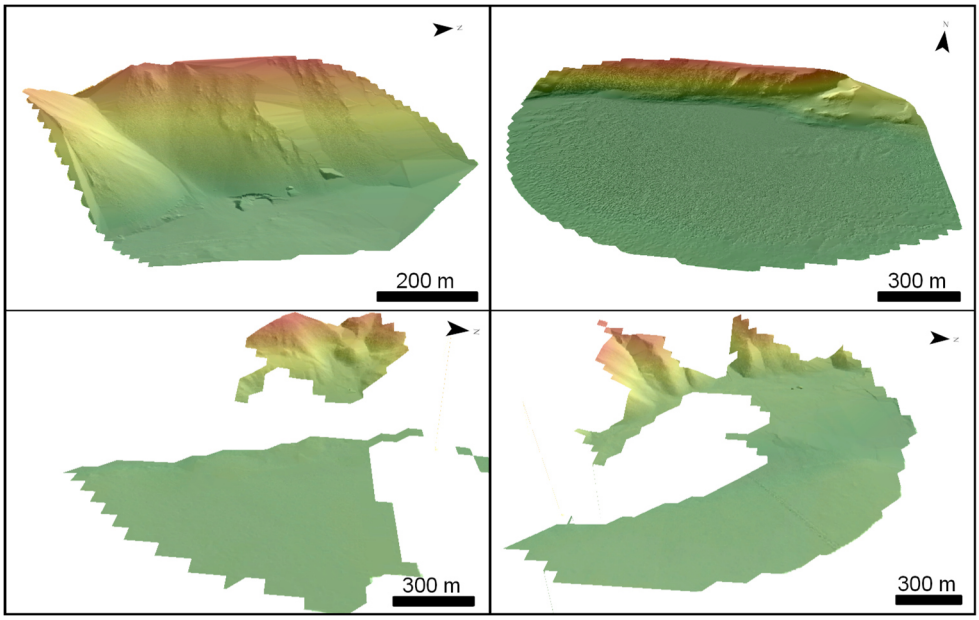

Figure 3-3: Perspective view of the covered relief of the four terrestrial laser scanning (TLS) derived elevation raster datasets. Depicted relative altitudes of the raster datasets are from low (green) to high (red).

3.3.4 Accuracy assessment

To assess the quality of the digital elevation models, the deviation of height differences was calculated against all previously presented datasets. At first, the root mean square error for all digital elevation models compared to each available ground truth dataset was calculated from height differences with the following equation:

$$RMSE = \sqrt{\frac{(\sum_{i=1}^{n}(\Delta h_i)^2)}{n}} \quad (3\text{-}2)$$

where

Δh_i= elevation difference between assessed DEM and reference DEM.
n = number of pixels.

Additionally, the normalized median absolute deviation was conducted as height differences tend to be not normal distributed and this is a more robust measure against outliers (Höhle and Höhle, 2009). The equation is:

$$NMAD = 1.4826 \times median(|\Delta h_i - m_{\Delta h}|) \quad (3\text{-}3)$$

where

Δh_i= elevation difference between assessed DEM and reference DEM.
$m_{\Delta h}$ = median of all elevation differences.

If error values are normally distributed, the NMAD is identical to the RMSE, otherwise the RMSE will be larger than the NMAD.

Accuracy values are only comparable if they can be related to the existing relief, since it is evident that different landscapes affect the accurateness of DEMs (Mukherjee et al., 2013). Therefore, a relief-adjusted evaluation of the ICESat heights was conducted by relating the accuracy of digital elevation models to specific terrain characteristics. In order to achieve this, several terrain parameters were calculated. First, the TRI was computed and divided into seven classes after Riley et al. (1999) from levelled surfaces to extremely rugged terrain. Second, the slope was calculated and classified into five classes from flat (<5°), gentle (5°–15°), moderate (15°–25°), steep (25°–35°) to extreme (>35°). Additionally, the TPI after Weiss (2001) was computed to assign the height errors to specific landforms. The number of classes was reduced to seven by combining the three ridge classes and two drainage classes into one class each. The TPI evaluation was only conducted for all global available datasets as the coverage region of the others was too small to gain enough evaluation data for all classes. All landforms and terrain features were derived over the whole region on the basis of the 12 m TanDEM-X elevation model (see Figure 3-4).

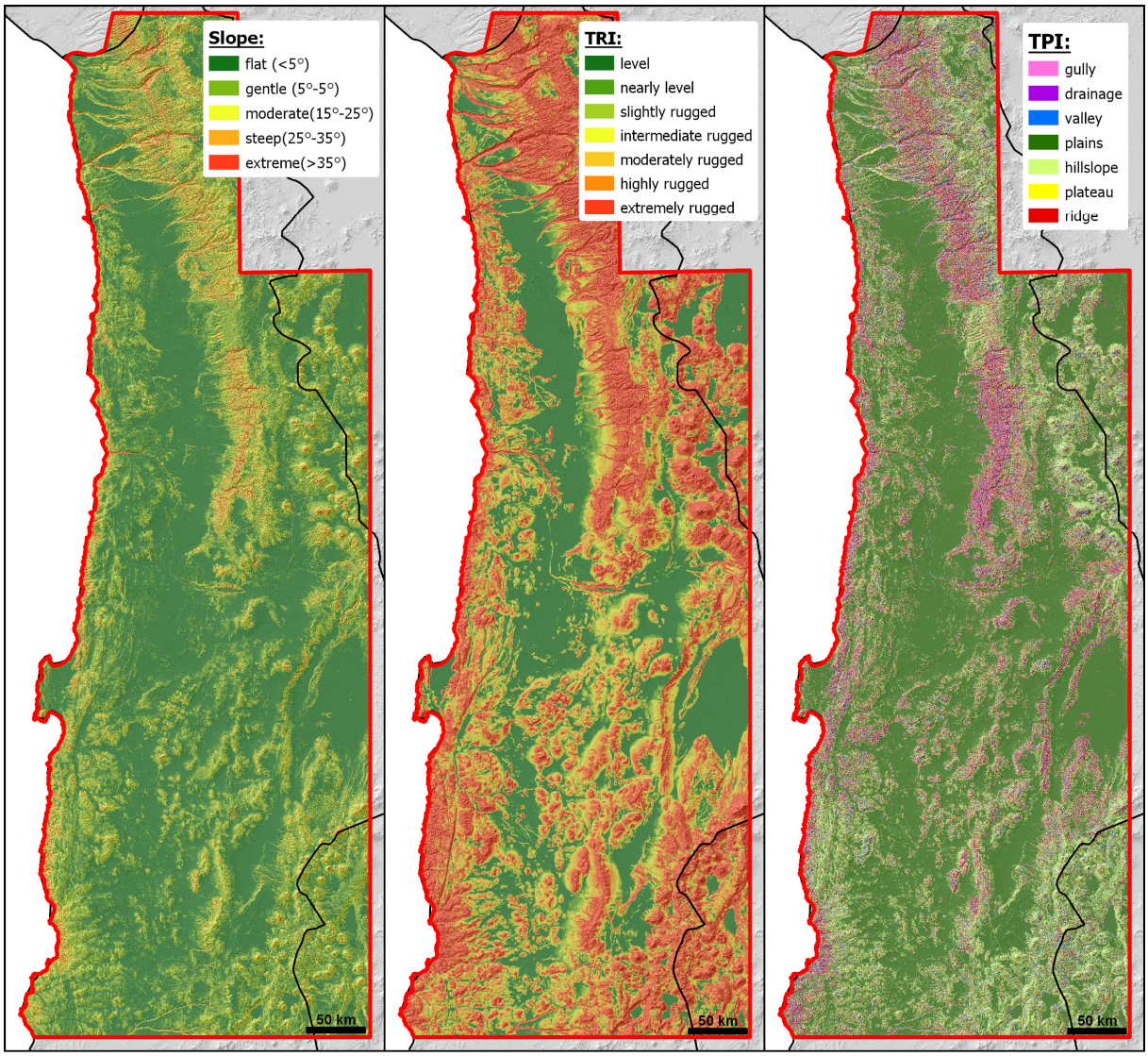

Figure 3-4: Spatial distribution of extracted terrain features slope, terrain ruggedness index (TRI) and topographic position index (TPI). Map is based on SRTM elevation data.

3.4 Results

3.4.1 Overall accuracies

All determined overall accuracies are presented in the Appendix Table 3-1 and Figure 3-5. Mostly, they show similar results for each dataset compared to all reference data. The ICESat-2 ATL08 dataset generally produced the highest error values for the DEMs in comparison to the other reference datasets. For the TanDEM-X 90 m and the SPOT 125 datasets in particular, a very high RMSE (13.9 m and 11.6 m) was calculated. Overall, for 17 DEMs the highest RMSE and for 21 DEMs the highest NMAD values were calculated with the ICESat-2 ATL08 dataset. For the UAV data, the lowest differences between RMSE and NMAD values can be observed for most datasets in comparison to all ICESat and TLS datasets. While the mean difference between RMSE and NMAD values is 0.4 m for the UAV dataset, it is more than 1.7 m for the other datasets. The highest differences between RMSE and NMAD can be observed for the TLS point cloud dataset with a mean difference of 4.8 m.

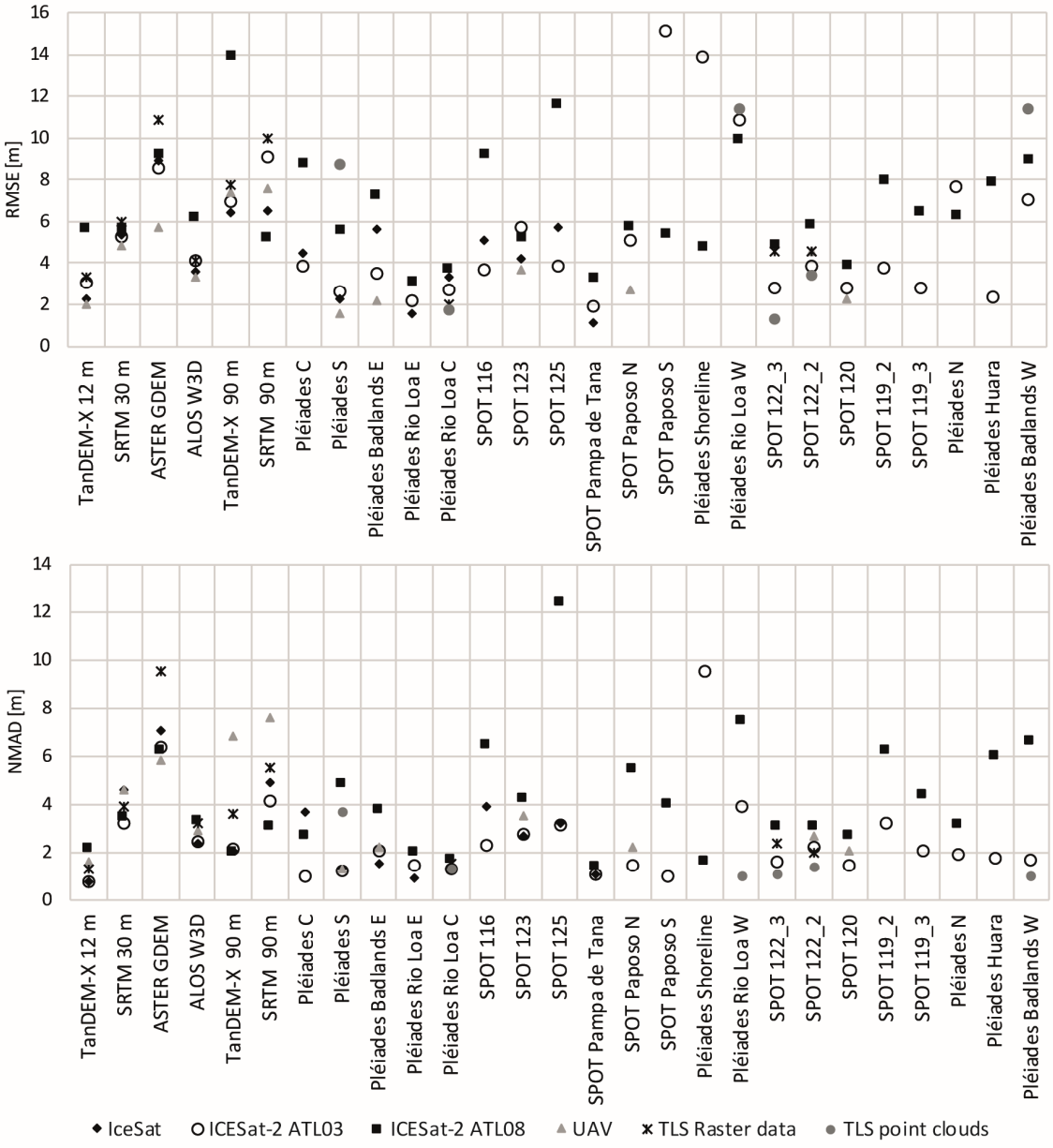

Figure 3-5: Comparison of all calculated overall accuracies for each digital elevation model.

For all global DEMs, the lowest RMSE and NMAD values are detectable for the TanDEM-X 12 m dataset. The highest RMSE of 5.7 m was calculated for TanDEM-X with the ICESat-2 ATL08 dataset, the lowest with the UAV dataset (2.0 m). The NMAD is generally lower with values between 0.8 m and 2.2 m. The calculated accuracy values for the ALOS W3D dataset are slightly higher with a RMSE between 3.3 m and 6.2 m and a NMAD between 2.4 m and 3.3 m. Thus, the ALOS W3D accuracies are higher in comparison to the other 30 m datasets.

The lowest accuracies were detected for the 30 m ASTER GDEM, which also tend to be lower than the calculated accuracies of both DEMs with 90 m GSD. The calculated RMSEs for the ASTER GDEM V3 are between 5.7 m and 10.9 m and the NMAD ranges between 5.8 m and 9.5 m. The smallest differences between RMSE and NMAD are detectable for the SRTM 30 m dataset, with a relatively small range between 4.8 m and 6.0 m (RMSE) and 3.2 m and 4.6 m (NMAD). In contrast, for the 90 m TanDEM-X it is noticeable that the discrepancy between the calculated RMSE and NMAD values are rather high, especially for all three ICESat datasets. The RMSE ranges between 6.4 m and 13.9 m, the calculated NMAD between 2.0 m and 6.8 m. Thus, the NMAD values are generally lower compared to the 90 m SRTM, which are between 3.0 m and 7.6 m. The calculated RMSEs of the SRTM 90 m dataset are on a similar level with values between 5.2 m and 10.1 m.

The results of the local scaled DEMs, derived by Pléiades and SPOT imagery, showed the highest overall accuracies for the SPOT-based Pampa de Tana scene with a RMSE between 1.1 m and 3.3 m. The calculated NMAD values for this dataset range between 1.1 m and 1.4 m. For the majority of the local DEMs, the calculated RMSE ranges between 2.0 m and 4.0 m and the NMAD between 1.0 m and 3.0 m. Relatively high RMSE values were calculated for the Pléiades Rio Loa W (9.9 – 11.4 m) and Badlands W (7.1 – 11.4 m) datasets. The SPOT Paposo S (15.1 m) and Pléiades Shoreline (13.9 m) datasets also achieve very high RMSE values for the ICESat-2 ATL03 dataset. While for the Pléiades Shoreline dataset the NMAD is also very high with 9.6 m, it is extremely low (1.0 m) for the SPOT Paposo S DEM. Compared to the ICESat-2 ATL08 reference data, the results show for the SPOT 125 DEM the highest error values with 11.6 m (RMSE) and 12.3 m (NMAD). However, the error values for this dataset are significantly lower in comparison with the ICESat (RMSE: 5.7 m; NMAD: 3.2 m) and ICESAT-2 ATL03 (RMSE: 3.9 m; NMAD: 3.2 m) dataset. For the Pléiades S DEM, a relatively high RMSE error was measured with the TLS point cloud data (RMSE: 8.7 m), whereas it is generally lower for all other reference datasets.

3.4.2 Terrain dependent accuracies

The results depicted in Figure 3-6 show the RMSE and NMAD of all digital elevation models calculated with the ICESat reference dataset according to their terrain ruggedness index. The calculation of error values was conducted here only for corresponding datasets with at least 10 available elevation points for more than one class. All other datasets were not considered. The diagram shows for most elevation models only a minor increase of error from class ‘level’ to class ‘highly rugged’. Both DEMs with a 90 m GSD have a higher increase of uncertainty from class ‘intermediate rugged’ terrain to ‘extremely rugged’ terrain. For all elevation models, the biggest loss in accuracy is visible in the category ‘extremely rugged’. The 90 m TanDEM-X in particular shows a very high accuracy in levelled terrain, which is similar to the 12 m TanDEM-X, but in rough terrain the accuracy decreases more than for all other DEMs and is even lower than for the SRTM 90 m DEM in ‘extremely rugged’ terrain. The freely

available ALOS W3D dataset shows a better overall accuracy and terrain independency than the other 30 m DEMs. Lowest accuracies were detected for the 30 m ASTER GDEM. Only in category 'extremely rugged' the 90 m TanDEM-X and 90 m SRTM perform with similar error values.

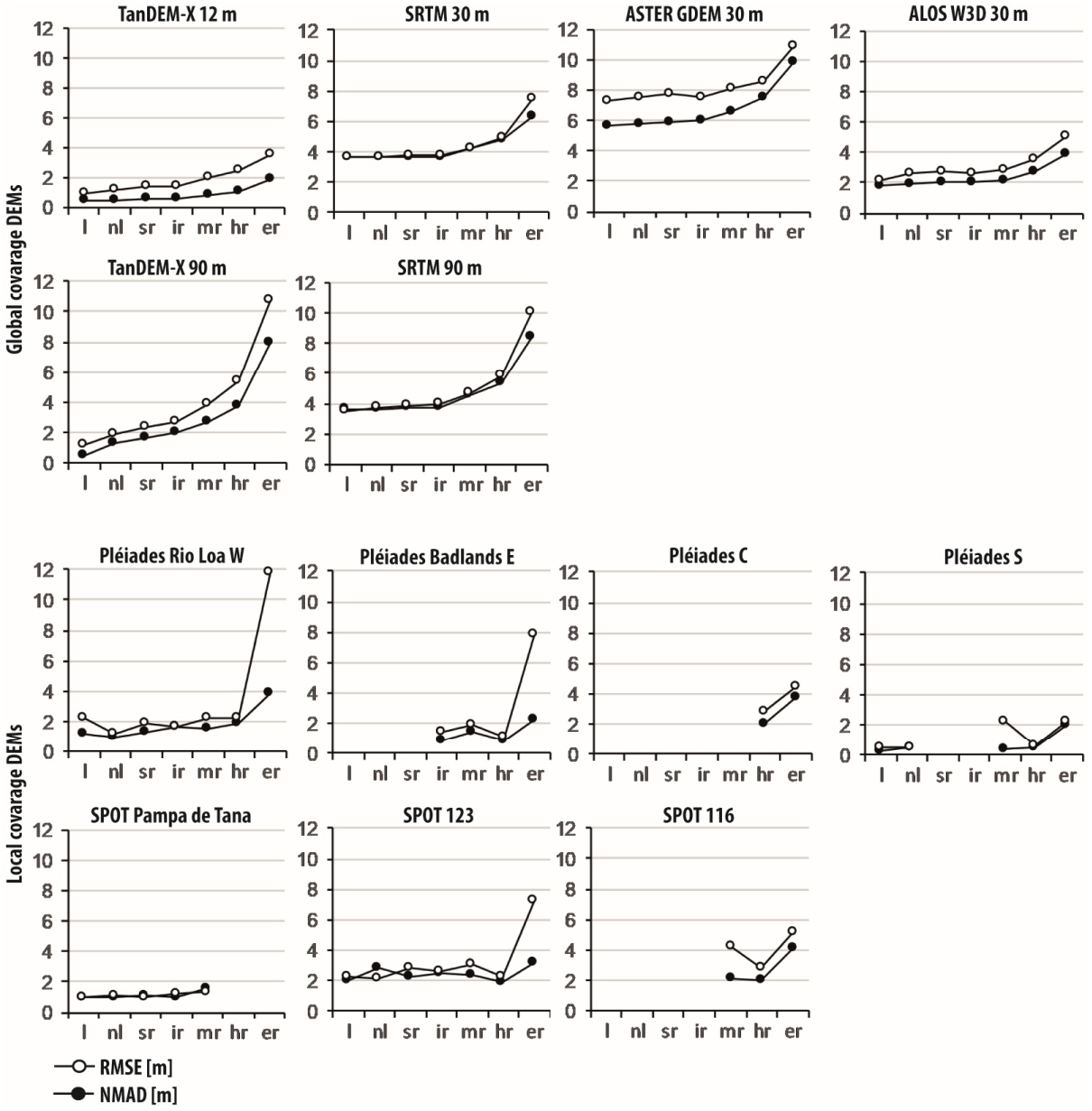

Figure 3-6: Calculated RMSE and NMAD of elevation differences according to the classified terrain ruggedness index from level to extremely rugged. Categorization of classes was conducted after Riley et al. (1999). Classes are level (l), nearly level (nl), slightly rugged (sr), intermediate rugged (ir), moderately rugged (mr), highly rugged (hr), extremely rugged (er).

The highest accuracies according to their terrain ruggedness were detected for the high resolution Pléiades S DEM in flat and rough terrain. For the Pléiades Rio Loa W and Pléiades Badlands E DEMs, a strong increase of RMSE is detectable in the category 'extremely rugged', whereas the RMSE is rather low for these DEMs in all other categories. Furthermore, the NMAD of these two elevation models in the highest category is also rather low and does not show such an increase in error.

Figure 3-7 shows the RMSE and NMAD of all elevation models according to their slope. All values were calculated against the ICESat reference dataset and only datasets with at least two classes with more than 10 reference points are considered here. Similar to the results of TRI classes, an increase in RMSE and NMAD values for steeper slopes is observable here. For DEMs with lower GSD, a stronger decrease in accuracy is detectable for rising slope gradients. Thus, the results show for the 90 m SRTM (RMSE: 20.6 m, NMAD 19.6 m) and the 90 m TanDEM-X (RMSE: 22.2 m, NMAD 21.0 m) the highest drop of accuracies in steep slope terrain.

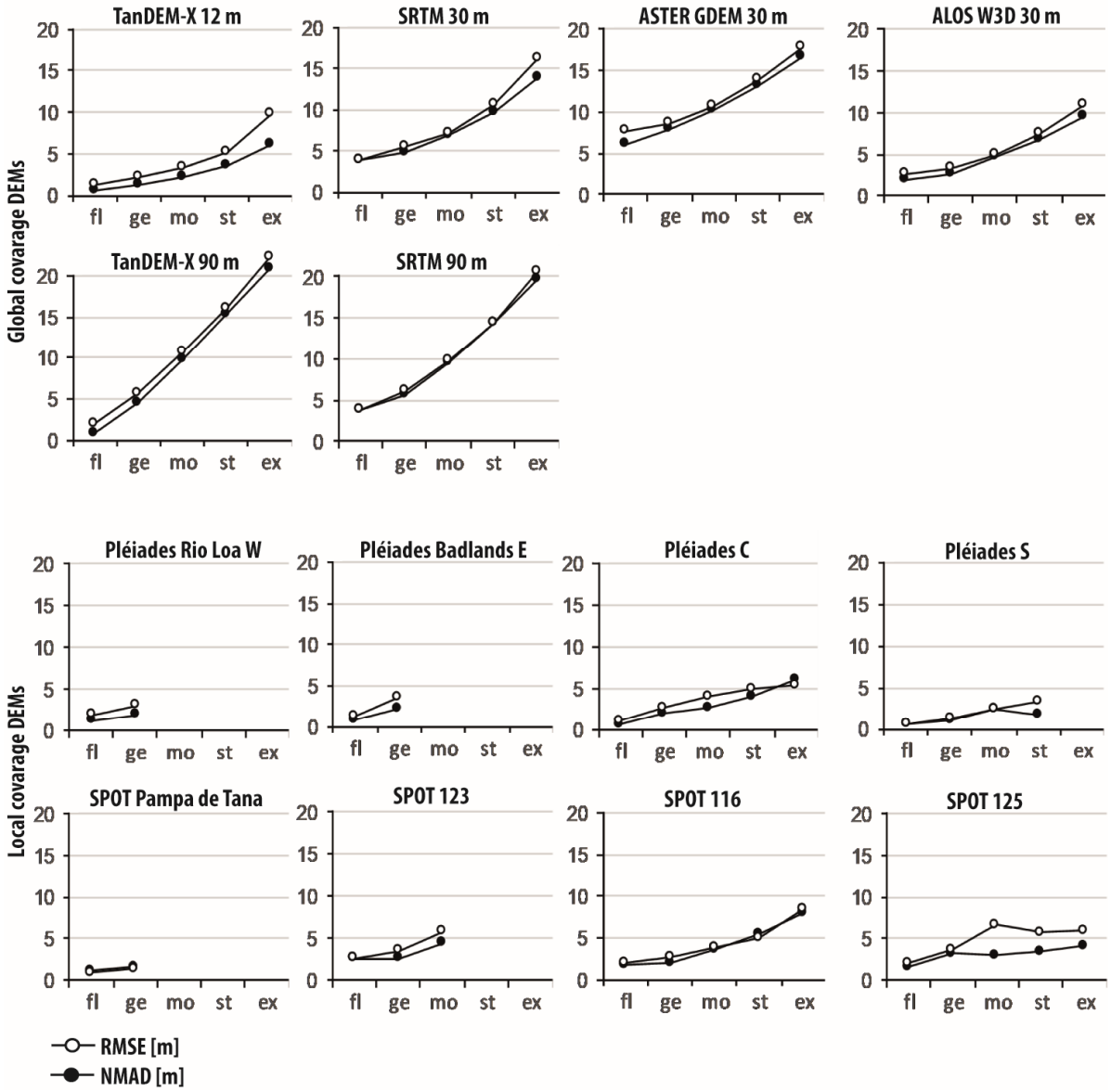

Figure 3-7: Calculated RMSE and NMAD of elevation differences according to the slope. Derived slope classes are flat (fl), gentle (ge), moderate (mo), steep (st) and extreme (ex).

Generally, the local DEMs derived from Pléiades and SPOT scenes achieved the highest accuracy values. Though, the diagram curves indicate a slightly higher accuracy for Pléiades datasets compared to SPOT scenes. For very steep slopes, only the TanDEM-X with a GSD of 12 m is able to achieve similar accuracy values (RMSE: 9.7 m, NMAD: 6.0 m) compared to the very high resolution DEMs, which have an average accuracy of RMSE 6.6 m and NMAD of 6.1 m here.

Figure 3-8 depicts the RMSE and NMAD for all global available DEMs according to their respective TPI landform class. The results show for all elevation models the lowest RMSE and NMAD values for the class 'plains'. All other classes achieved significantly lower accuracies. The highest error values were determined for the landform classes 'gully', 'drainage' and 'ridge'. The highest accuracies are calculated for the 12 m TanDEM-X, which also has the lowest error values for class 'plains' (RMSE: 1.0 m, NMAD: 1.1 m) and the highest RMSE for class 'drainage' with 5.0 m. For the NMAD calculation, the highest error values are determined for the classes 'gully' and 'drainage' with 2.4 m.

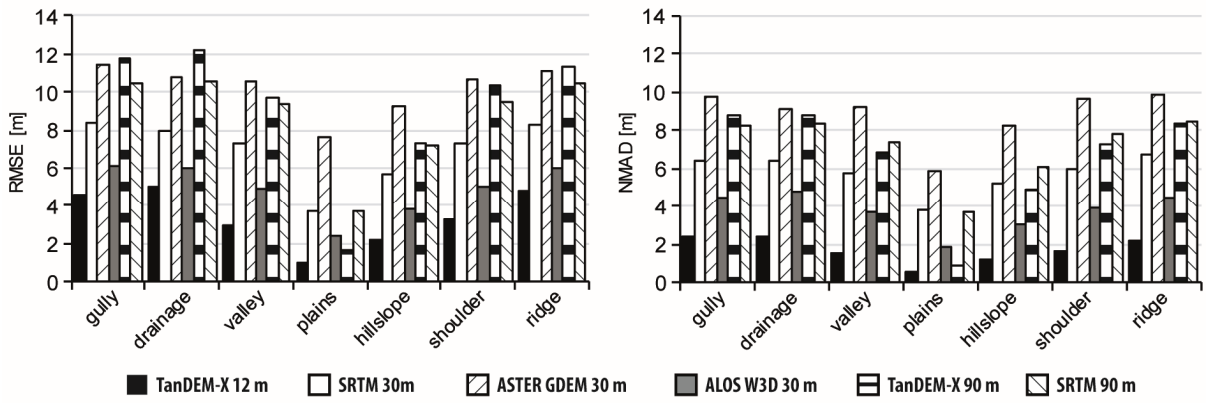

Figure 3-8: Calculated RMSE and NMAD of elevation differences according to topographic position index (TPI) classes classified with the 12 m TanDEM-X.

Again, in comparison to the other 30 m DEMs the ALOS W3D achieved higher accuracies between 2.4 m (RMSE) and 1.8 m (NMAD) for class 'plains' and 6.1 m (RMSE) and 4.8 m (NMAD) for the classes 'gully' and 'drainage'. The lowest accuracies are generally measured for the 30 m ASTER GDEM with values between 7.6 m (RMSE) and 5.9 m (NMAD) for class 'plains' and 11.4 m (RMSE) and 9.8 m (NMAD) for class 'gully'. Only the calculated RMSE for the 90 m TanDEM-X DEM was even higher for the classes 'gully', 'drainage' and 'ridge' with values of 11.7 m, 12.2 m and 11.3 m. The highest NMAD values are calculated for the ASTER GDEM in all classes. The biggest differences in accuracy are also observable here for the 90 m TanDEM-X elevation model. Whereas its error values are very low for class 'plains' (RMSE: 1.7 m, NMAD: 0.9 m), these rise significantly for all other classes.

3.4.3 Local scale evaluation

Figure 3-9 depicts the distribution of errors of each individual UAV scene. The results show for RMSE and NMAD that the deviations between the different UAV scenes rise for elevation models with coarser GSDs. Thus, the highest range is measured for the TanDEM-X 90 m elevation model with calculated RMSE values between 4.4 m and 11.2 m. NMAD values range from 2.8 m to 10.9 m. In contrast, the differences for the TanDEM-X 12 m DEM only range between 1.0 m and 4.6 m (RMSE) and 0.9 m and 3.0 m (NMAD). For the ALOS DEM, also relatively low variations are detectable with RMSEs from 2.1 m to 5.1 m and NMAD values from 1.6 m to 4.2 m. For the very high resolution Pléiades and SPOT scenes, varying differences are observable. Especially for SPOT Paposo N, the results show relatively large differences that are greater than the differences of TanDEM-X 12 m and ALOS W3D. For SPOT 120 and Pléiades S, almost no deviation of the results was measured.

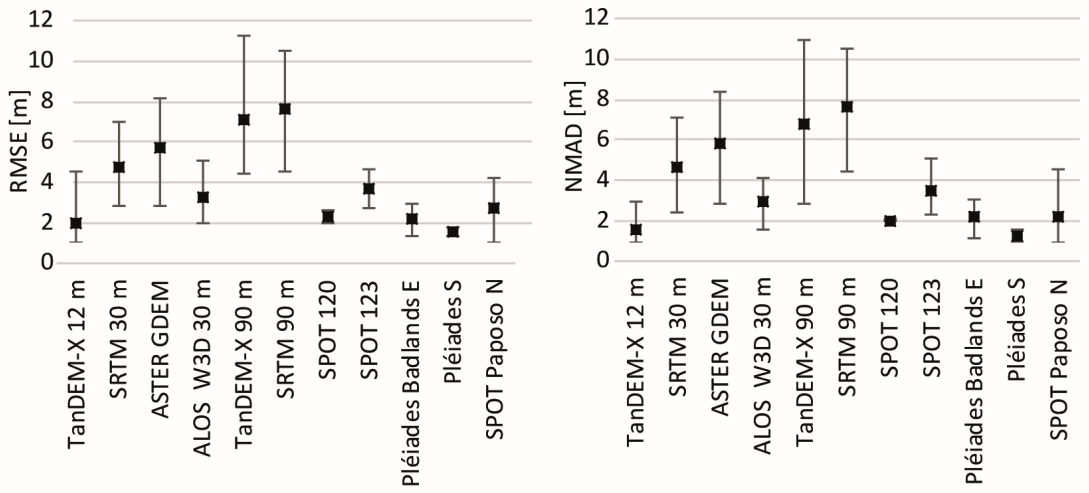

Figure 3-9: Distribution of calculated RMSE and NMAD of the individual UAV-derived reference datasets compared to elevation models.

A visual interpretation on a local scale shows that height differences are mainly affected by small scale landforms with large height differences at small areas. It is depicted in Figure 3-10 for two example sites that DEM heights in depressions tend to be higher than the heights of the reference elevation data. In contrast, the heights of ridges and summits tend to be lower in comparison to reference data. It can be observed that this effect is increased for the TanDEM-X 12 m DEM compared to the 5 m Pléiades S elevation model. All DEMs with a coarser GSD were not at all able to depict the sample canyons in a sufficient way.

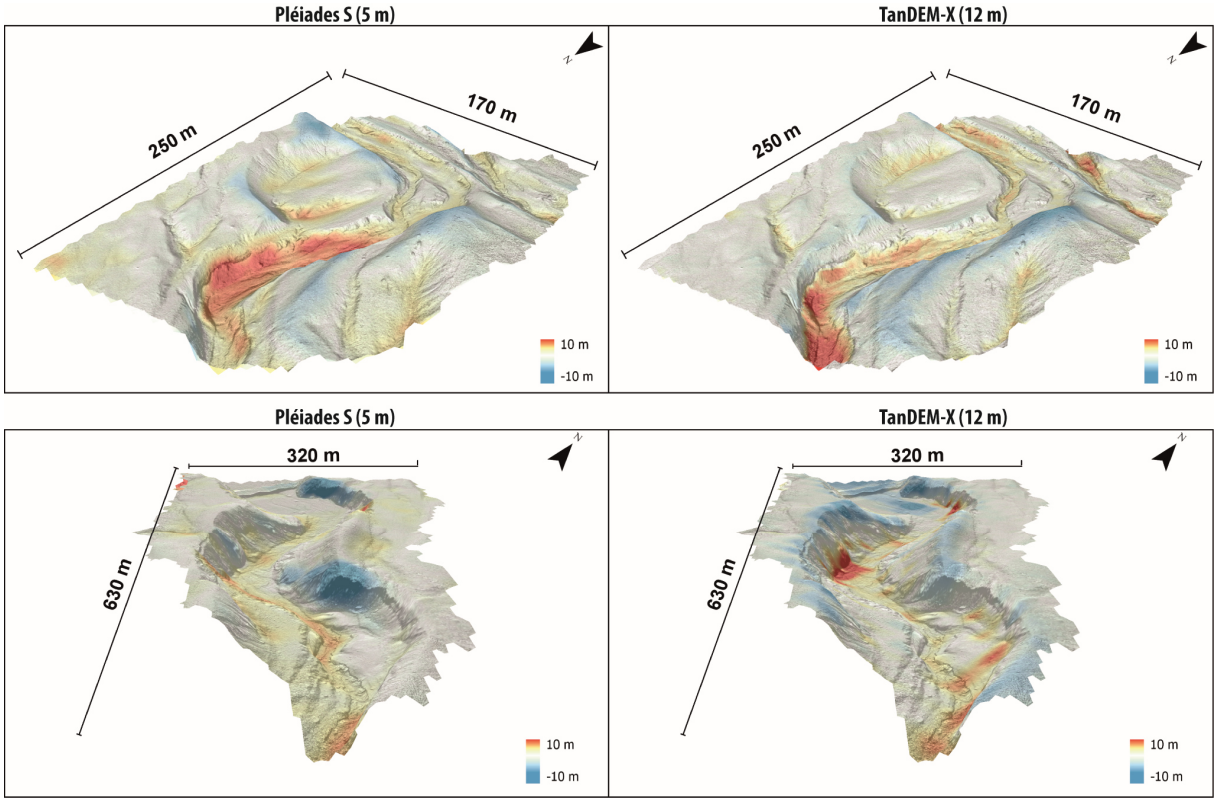

Figure 3-10: Spatial distribution of elevation differences of Pléiades S and TanDEM-X 12 m data compared to UAV reference data at two different sites. Pléiades satellite imagery data: © CNES (2016), Distribution Airbus DS. TanDEM-X WorldDEM™ data: © DLR (2017).

3.5 Discussion

The overall accuracies of the global DEMs are within the expected range when comparing them with findings from other studies. As the relief of the study area represents a cross-section of flat to very steep landscapes, the overall accuracies can be taken as an average error value over a broad landscape. Thus, the achieved overall accuracies are lower than those conducted by studies in mostly flat terrain (Becek et al., 2016; Caglar et al., 2018; Gesch, 2018; Zhang et al., 2019b). However, the results of these studies mostly fit well with the achieved results in flat landscapes. Likewise, the calculated overall accuracies in this study are generally higher than findings from many studies with predominantly undulated to very steep terrain conditions (Florinsky et al., 2018; Liu et al., 2019; Pipaud et al., 2015; Podgorski et al., 2019). Nevertheless, these results are also consistent with the calculated error values in very steep terrain.

Of all globally available elevation datasets, only the 12 m TanDEM-X was able to achieve similar accuracies in comparison to the local DEMs derived from Pléiades and SPOT imagery. Also, small-scale analyses show that this DEM is able to depict most terrain features compared to the other global DEMs. The results are generally consistent with the findings of other studies, which also showed that the accuracy of the new TanDEM-X generally outperforms the accuracy of ASTER GDEM and SRTM (Becek et al., 2016; Grohmann, 2018; Purinton and Bookhagen, 2017; Zhang et al., 2019b). Only the freely available ALOS W3D dataset was able to achieve similar results with only slightly lower overall accuracies. In comparison to all 30 m DEMs, the ALOS W3D seems to be superior compared to SRTM and ASTER. Therefore, similar findings from other studies can be agreed here (Alganci et al., 2018; Boulton and Stokes, 2018). It shows a good agreement with both evaluation scales and is more stable over all terrain types, slopes and landforms, only slightly worse than the TanDEM-X 12 m dataset. In mountainous areas with steep slopes in particular, the performance of ALOS W3D seems to be far superior compared to the other 30 m elevation models. This is probably caused by the fact that it is resampled from a higher resolution dataset and still more terrain features remain in the 30 m elevation data. Furthermore, optical imagery is often less affected by relief distortions due to usually small viewing angles. Nevertheless, the goal of 5 m vertical accuracy for ALOS W3D can only be reached here in flat to undulated terrain. In very steep terrain, the uncertainties are still higher.

Possibly, the high accuracy values of TanDEM-X and ALOS W3D compared to the ICESat dataset are affected by the fact that ICESat points were already used for quality assessments during the generation process of both elevation models (Gruber et al., 2012; Huber et al., 2009; Takaku et al., 2016). Thus, some correlation between these DEMs and the evaluation dataset cannot be excluded. However, the results of the evaluation with completely independent elevation data from UAV and TLS measurements produced similar results and a significant positive influence of ICESat data on the accuracy of both DEMs cannot be observed here.

The ASTER GDEM achieved the lowest overall accuracies in comparison to all global datasets. Furthermore, except for very steep terrain, its accuracies seem to be lower than the accuracies of both 90 m DEMs. Numerous studies showed that the previous 2nd version of the ASTER GDEM achieved the least accurate terrain representation compared to other freely available DEMs (Graf et al., 2018; Mouratidis and Ampatzidis, 2019; Rexer and Hirt, 2014; Suwandana et al., 2012a). Although a direct comparison of the latest two ASTER GDEM versions was not conducted here, the results indicate that also the last update of ASTER GDEM is not able to achieve the accuracies of the other global elevation datasets.

For all DEMs, a decrease in accuracy in rougher terrain compared to flat landscapes can be observed. This effect is particularly stronger for elevation models with coarser GSD, which have a higher decrease in accuracy compared to high resolution elevation models. For the 90 m TanDEM-X in particular, which is similarly accurate in flat terrain to the 12 m TanDEM-X elevation model, a very high drop in accuracy can be observed in rougher terrain with steep slopes. A similar trend was also observable for the SRTM 90 m DEM, but the decrease in accuracy is even higher for the 90 m TanDEM-X. This is in accordance with findings of Altunel (2019), who already noticed some overestimations of 90 m TanDEM-X for cliffy terrain and a high accuracy in flat areas. Generally, a comparison of the two 90 m elevation datasets leads to the conclusion that TanDEM-X is significantly more accurate in flat landscapes, but the SRTM 90 m still seems advantageous in steeper relief. Furthermore, the difference between the calculated RMSE and NMAD is conspicuously high for the TanDEM-X 90 m dataset. It can be assumed that more outliers exist in this DEM in its first version compared to the other global elevation models that were already revised several times. Nevertheless, the results lead to the conclusion that both DEMs with 90 m GSD are not suitable for accurate large-scale terrain analyses, especially in rough landscapes. Likewise, the results of the ASTER GDEM show that the accuracy of this DEM is already lower in flat landscapes than the accuracy of high resolution DEMs in rough terrain. Thus, for this DEM the results indicate a least suitability for geomorphometric analyses in this area.

The results for the local DEMs derived from stereo satellite imagery show a varying overall accuracy, which highly depends on the topography of each scene. Relating them to slope or TRI tends in most cases to lower error values for each terrain category compared to the globally available elevation models. Furthermore, the accuracies of Pléiades imagery seem to be slightly higher than images derived from SPOT imagery.

For most DEMs, similar accuracy values could be achieved by the different reference datasets. However, for some DEMs some anomalies could be detected. For example, the Pléiades S scene achieved relative low accuracies compared to the TLS point clouds, whereas the values were significantly lower for all other datasets. This is mainly caused by different locations of the reference datasets, even in this small area. While all ICESat datasets and the UAV data mostly cover flatter areas, the TLS data is situated on a hillside with relatively steep slopes. Therefore, it can be assumed that also for this DEM the error values are much higher in steeper areas compared to flatter landscapes. Also, the relatively high error values for the Pléiades Rio Loa W and Pléiades Badlands W DEMs can be explained by very steep relief conditions. Both scenes and the evaluation data cover the Rio Loa canyon, which is extremely steep at this point with average slope angles of more than 30°. This steepness possibly produces more outliers that are represented in the RMSE values, whereas the NMAD values are much lower.

In contrast, the large differences in the overall accuracy results from the Pléiades Shoreline DEM with the ICESat-2 ATL03 and ATL 08 reference data cannot be explained here by the relief, as both point datasets cover the same track. Therefore, it can be supposed that these differences are originated in the reference dataset. A similar contradiction is also evident in the results of the SPOT Paposo S DEM. Indeed, in contrast to the results of the Pléiades Shoreline DEM, there is also a large difference between the ICESat-2 ATL03 RMSE and NMAD. While the RMSE is with 15.1 m very high, the NMAD is extremely low with 1.0 m. This possibly indicates that a great number of outliers exists in the ICESat-2 ATL03 dataset at this location.

It is conspicuous that for most DEMs the highest values were calculated by the ICESat-2 ATL08 dataset, which are often not in line with the error values calculated with other datasets. It can be assumed that the interpolated ATL08 heights are probably less suitable for DEM accuracy assessment. Thus, it is likely that the calculated values by the ATL08 dataset at this early stage overestimate the error of the DEMs. In contrast, the ICESat-2 ATL03 mostly fit well with the results from the other reference datasets.

The TLS raster data produced higher error values than the point clouds from TLS measurements. This is possibly caused by the height interpolations of some areas that were not covered during the measurement process. During the generation process, it was not completely possible to exclude all of these areas and some small areas with probably lower accuracy remained for the evaluation process. A comparison of elevation differences on a local scale shows that the heights of small incised canyons are overestimated at the bottom and underestimated at upper elevations. The results reveal that even for the very high resolution DEMs a minor decrease in the deepness of such a canyon is detectable. This lack of deepness rises with coarser resolutions.

3.6 Conclusion

In this contribution, the accuracy of a multitude of digital elevation models was evaluated against various reference datasets. Furthermore, the influence of terrain on the accuracy of these DEMs was analysed by relating the accuracy values to several extracted terrain features and landforms on a regional scale. The results reveal that the rougher and steeper the landscape, the higher resolutions are necessary to depict the landscape in an accurate way. For instance, the 90 m TanDEM-X elevation model showed eight times higher RMSE error values in terrain with steep slopes (25° – 35°) compared to landscapes with flat slopes (0° – 5°). Thus, an average rise of about 5 m RMSE per 10° slope can be assumed for this DEM. In contrast, for the 12 m TanDEM-X the increase of error in steep terrain (25° – 35°) is only four times as high as in flat landscapes with slopes less than 5° and an average rise of 1.5 m RMSE per 10° slope can be supposed here. The results of the very high resolution DEMs from Pléiades and SPOT satellites reveal that the RMSE error is increasing by about 1 m per 10° slope. Therefore, an increase of error by about three times in terrain with steep slopes compared to flat landscapes could be expected for these DEMs. Hence, for analyses in flatter landscapes, a 30 m or 90 m DEM could possibly be sufficient. If the relief is steeper, only high resolution DEMs show satisfying accuracies. This applies for a regional coverage, but even more for analyses on a local scale with smaller landforms. Furthermore, the presented results are valid for regions with almost no vegetation cover. It cannot be stated here how the accuracies of different DEMs are affected by vegetation and to which degree an increase of error is probably detectable in densely vegetated areas.

The results of this study point out that of all globally available datasets only the TanDEM-X 12 m and partly the 30 m ALOS World 3D are able to depict the landscape in the same accuracy as very high resolution DEMs with a GSD of 5 m. Thus, it can be assumed that the 12 m TanDEM-X data are suitable not only for global scale analyses, but also has a sufficient accuracy for local scale analysis in flat to moderately sloped landscapes. Only in landscapes with very steep terrain they seem to be less accurate than DEMs derived by Pléiades and SPOT imagery. All other freely worldwide available elevation models were not able to achieve promising accuracies here and seem less suitable for delineating small terrain features on large scales. Furthermore, it can be concluded that most reference datasets from

different sources produced coherent values. Only the ICESat-2 ATL08 dataset seems to significantly underestimate the accuracy, especially of the local-scaled DEMs.

Author Contributions: Methodology, Formal Analysis, Visualization, T.K.; Conceptualization, Supervision, Funding Acquisition, D.H.; Validation, Data Curation, Writing - Original Draft Preparation, Writing-Review and Editing, T.K. and D.H.

Funding: This research was funded by the Deutsche Forschungsgemeinschaft (DFG, German Research Foundation)-Project number 268236062-SFB 1211.

Acknowledgments: The TanDEM-X WorldDEM™ data is provided by a DLR Science grant, 2017. Pléiades satellite imagery data: ©CNES (2014–2016), distributed by Airbus DS. SPOT 6 and 7 imagery data: ©Airbus DS (2013–2017). We thank both anonymous reviewers for improving the contribution.

Conflicts of Interest: The authors declare no conflict of interest.

3.7 Appendix

Table 3-1: Overall accuracies of all digital elevation models compared to the reference point datasets of Ice, Cloud, and Land Elevation Satellite (ICESat), ICESat-2 ATL03, ICESat-2 ATL08 and terrestrial laser scanning (TLS) point clouds as well as raster datasets derived from unmanned aerial vehicle (UAV)-based photogrammetry and TLS datasets. Listed are the spatial resolution (Res.), the calculated root mean square error (RMSE), the normalized median absolute deviation (NMAD) and the total number of applied points or raster for each DEM.

		ICESat			ICESat-2 ATL03			ICESat-2 ATL08			UAV DEMs			TLS raster data			TLS point clouds		
DEM	**Res.**	**RMSE [m]**	**NMAD [m]**	**No. points**	**RMSE [m]**	**NMAD [m]**	**No. points**	**RMSE [m]**	**NMAD [m]**	**No. points**	**RMSE [m]**	**NMAD [m]**	**No. raster**	**RMSE [m]**	**NMAD [m]**	**No. raster**	**RMSE [m]**	**NMAD [m]**	**No. points**
TanDEM-X	12 m	2.3	0.8	453434	3.1	0.8	392333	5.7	2.2	643926	2.0	1.6	19	3.3	1.3	4	-	-	-
SRTM	30 m	5.4	4.6	453434	5.3	3.2	392333	5.7	3.5	643926	4.8	4.6	19	6.0	3.9	4	-	-	-
ASTER GDEM	30 m	8.9	7.1	453434	8.6	6.4	392333	9.2	6.2	643926	5.7	5.8	19	10.9	9.5	4	-	-	-
ALOS W3D	30 m	3.6	2.4	447372	4.1	2.4	392043	6.2	3.3	636761	3.3	2.9	19	4.1	3.2	4	-	-	-
TanDEM -X	90 m	6.4	2.1	453434	7.0	2.1	392333	13.9	2.0	643926	7.4	6.8	19	7.8	3.6	4	-	-	-
SRTM	90 m	6.5	4.9	453434	9.1	4.1	392333	5.2	3.0	643926	7.6	7.6	19	10.0	5.5	4	-	-	-
Pléiades C	5 m	4.5	3.7	629	3.9	1.0	11796	8.8	2.7	67	-	-	-	-	-	-	-	-	-
Pléiades S	5 m	2.3	1.3	273	2.6	1.2	9852	5.6	4.8	154	1.6	1.3	2	-	-	-	8.7	3.6	1004405
Pléiades Badlands E	5 m	5.6	1.5	158	3.5	2.1	12131	7.3	3.8	244	2.2	2.2	4	-	-	-	-	-	-
Pléiades Rio Loa E	5 m	1.6	0.9	634	2.2	1.4	271078	3.1	2.0	1819	-	-	-	-	-	-	-	-	-
Pléiades Rio Loa C	5 m	3.3	1.4	475	2.7	1.3	124934	3.7	1.7	1057	-	-	-	2.0	1.5	1	1.7	1.2	242730
SPOT 116	5 m	5.1	3.9	1293	3.7	2.3	55427	9.2	6.5	614	-	-	-	-	-	-	-	-	-
SPOT 123	5 m	4.2	2.7	424	5.7	2.8	34806	5.2	4.2	648	3.7	3.5	4	-	-	-	-	-	-
SPOT 125	5 m	5.7	3.2	958	3.9	3.2	75149	11.6	12.3	388	-	-	-	-	-	-	-	-	-
SPOT Pampa de Tana	5 m	1.1	1.1	445	1.9	1.1	67805	3.3	1.4	417	-	-	-	-	-	-	-	-	-
SPOT Paposo N	5 m	-	-	-	5.1	1.5	143298	5.8	5.4	951	2.7	2.2	4	-	-	-	-	-	-
SPOT Paposo S	5 m	-	-	-	15.1	1.0	2235	5.4	4.0	695	-	-	-	-	-	-	-	-	-
Pléiades Shoreline	5 m	-	-	-	13.9	9.6	177271	4.8	1.6	294	-	-	-	-	-	-	-	-	-
Pléiades Rio Loa W	5 m	-	-	-	10.9	3.9	4793	9.9	7.5	407	-	-	-	-	-	-	11.4	0.9	880609
SPOT 122_3	5 m	-	-	-	2.8	1.6	26349	4.9	3.0	220	-	-	-	4.6	2.4	1	1.3	1.0	230017
SPOT 122_2	5 m	-	-	-	3.9	2.2	68967	5.9	3.1	449	4.6	2.7	1	4.6	2.0	1	3.4	1.3	347589
SPOT 120	5 m	-	-	-	2.8	1.4	66810	3.9	2.7	281	2.3	2.1	2	-	-	-	-	-	-
SPOT 119_2	5 m	-	-	-	3.8	3.2	77527	8.0	6.2	599	-	-	-	-	-	-	-	-	-
SPOT 119_3	5 m	-	-	-	2.8	2.0	52071	6.5	4.4	456	-	-	-	-	-	-	-	-	-
Pléiades N	5 m	-	-	-	7.7	1.9	2551	6.3	3.1	200	-	-	-	-	-	-	-	-	-
Pléiades Huara	5 m	-	-	-	2.4	1.7	73224	7.9	6.0	572	-	-	-	-	-	-	-	-	-
Pléiades Badlands W	5 m	-	-	-	7.1	1.7	839	9.0	6.6	63	-	-	-	-	-	-	11.4	0.9	880609

3.8 References

Abrams, M., Bailey, B., Tsu, H., Hato, M., 2010. The ASTER Global DEM. Photogrammetric Engineering and Remote Sensing, 76 (4), 344-348.

Abrams, M., Crippen, R., 2019. ASTER GDEM V3 (ASTER Global DEM).

Alganci, U., Besol, B., Sertel, E., 2018. Accuracy Assessment of Different Digital Surface Models. ISPRS International Journal of Geo-Information, 7 (3), 114. doi: 10.3390/ijgi7030114.

Altunel, A.O., 2019. Evaluation of TanDEM-X 90 m Digital Elevation Model. International Journal of Remote Sensing, 40 (7), 2841-2854. doi: 10.1080/01431161.2019.1585593.

Astrium GEO-Information Services, 2012. Pléiades Imagery User Guide V 2.0. Astrium Services.

Astrium GEO-Information Services, 2013. SPOT 6 & SPOT 7 Imagery User Guide. Astrium Services.

Baghdadi, N., Lemarquand, N., Abdallah, H., Bailly, J.S., 2011. The Relevance of GLAS/ICESat Elevation Data for the Monitoring of River Networks. Remote Sensing, 3 (4), 708-720. doi: 10.3390/rs3040708.

Becek, K., Koppe, W., Kutoglu, S.H., 2016. Evaluation of Vertical Accuracy of the WorldDEM (TM) Using the Runway Method. Remote Sensing, 8 (11), 934. doi: 10.3390/rs8110934.

Bishop, M.P., James, L.A., Shroder, J.F., Walsh, S.J., 2012. Geospatial technologies and digital geomorphological mapping: Concepts, issues and research. Geomorphology, 137 (1), 5-26. doi: 10.1016/j.geomorph.2011.06.027.

Blaszczyk, M., Ignatiuk, D., Grabiec, M., Kolondra, L., Laska, M., Decaux, L., Jania, J., Berthier, E., Luks, B., Barzycka, B., Czapla, M., 2019. Quality Assessment and Glaciological Applications of Digital Elevation Models Derived from Space-Borne and Aerial Images over Two Tidewater Glaciers of Southern Spitsbergen. Remote Sensing, 11 (9), 1121. doi: 10.3390/rs11091121.

Boulton, S.J., Stokes, M., 2018. Which DEM is best for analyzing fluvial landscape development in mountainous terrains? Geomorphology, 310, 168-187. doi: 10.1016/j.geomorph.2018.03.002.

Caglar, B., Becek, K., Mekik, C., Ozendi, M., 2018. On the vertical accuracy of the ALOS world 3D-30m digital elevation model. Remote Sensing Letters, 9 (6), 607-615. doi: 10.1080/2150704x.2018.1453174.

De Lussy, F., Kubik, P., Greslou, D., Pascal, V., Gigord, P., P., C.J., 2006. Pleiades-HR Image System Products and Quality. Pleiades-HR Image System Products and Geometric Accuracy. Proceedings of the ISPRS Hannover Workshop, Hannover, Germany.

Deng, Y., Wilson, J.P., Bauer, B.O., 2007. DEM resolution dependencies of terrain attributes across a landscape. International Journal of Geographical Information Science, 21 (1-2), 187-213. doi: 10.1080/13658810600894364.

Dragut, L., Blaschke, T., 2006. Automated classification of landform elements using object-based image analysis. Geomorphology, 81 (3-4), 330-344. doi: 10.1016/j.geomorph.2006.04.013.

Drisya, J., Kumar, D.S., 2016. Comparison of digitally delineated stream networks from different spaceborne digital elevation models: A case study based on two watersheds in South India. Arabian Journal of Geosciences, 9 (18), 710. doi: 10.1007/s12517-016-2726-x.

Dunai, T.J., Lopez, G.A.G., Juez-Larre, J., 2005. Oligocene-Miocene age of aridity in the Atacama Desert revealed by exposure dating of erosion-sensitive landforms. Geology, 33 (4), 321-324. doi: 10.1130/G21184.1.

Duong, H., Lindenbergh, R., Pfeifer, N., Vosselman, G., 2009. ICESat Full-Waveform Altimetry Compared to Airborne Laser Scanning Altimetry Over The Netherlands. IEEE Transactions on Geoscience and Remote Sensing, 47 (10), 3365-3378. doi: 10.1109/Tgrs.2009.2021468.

Farr, T.G., Rosen, P.A., Caro, E., Crippen, R., Duren, R., Hensley, S., Kobrick, M., Paller, M., Rodríguez, E., Roth, L., Seal, D., Shaffer, S., Shimada, J., Umland, J., Werner, M., Oskin, M., Burbank, D., Alsdorf, D., 2007. The shuttle radar topography mission. Reviews of Geophysics, 45 (2). doi: 10.1029/2005rg000183.

Florinsky, I., Skrypitsyna, T., Luschikova, O., 2018. Comparative accuracy of the AW3D30 DSM, ASTER GDEM, and SRTM1 DEM: A case study on the Zaoksky testing ground, Central European Russia. Remote Sensing Letters, 9 (7), 706-714. doi: 10.1080/2150704x.2018.1468098.

Gesch, D.B., 2018. Best Practices for Elevation-Based Assessments of Sea-Level Rise and Coastal Flooding Exposure. Frontiers in Earth Science, 6, 230. doi: 10.3389/feart.2018.00230.

Gleyzes, M.A., Perret, L., Kubik, P., 2012. Pleiades System Architecture and Main Performances, International Archives of the Photogrammetry, Remote Sensing and Spatial Information Sciences. XXII ISPRS Congress, Australia, Melbourne, 537-542. doi: 10.5194/isprsarchives-XXXIX-B1-537-2012.

Goodchild, M.F., 2011. Scale in GIS: An overview. Geomorphology, 130 (1-2), 5-9. doi: 10.1016/j.geomorph.2010.10.004.

Graf, L., Moreno-de-las-Heras, M., Ruiz, M., Calsamiglia, A., Garcia-Comendador, J., Fortesa, J., Lopez-Tarazon, J.A., Estrany, J., 2018. Accuracy Assessment of Digital Terrain Model Dataset Sources for Hydrogeomorphological Modelling in Small Mediterranean Catchments. Remote Sensing, 10 (12), 2014. doi: 10.3390/rs10122014.

Grieve, S.W.D., Mudd, S.M., Hurst, M.D., Milodowski, D.T., 2016a. A nondimensional framework for exploring the relief structure of landscapes. Earth Surface Dynamics, 4 (2), 309-325. doi: 10.5194/esurf-4-309-2016.

Grieve, S.W.D., Mudd, S.M., Milodowski, D.T., Clubb, F.J., Furbish, D.J., 2016b. How does grid-resolution modulate the topographic expression of geomorphic processes? Earth Surface Dynamics, 4 (3), 627-653. doi: 10.5194/esurf-4-627-2016.

Grohmann, C.H., 2015. Effects of spatial resolution on slope and aspect derivation for regional-scale analysis. Computers & Geosciences, 77, 111-117. doi: 10.1016/j.cageo.2015.02.003.

Grohmann, C.H., 2018. Evaluation of TanDEM-X DEMs on selected Brazilian sites: Comparison with SRTM, ASTER GDEM and ALOS AW3D30. Remote Sensing of Environment, 212, 121-133. doi: 10.1016/j.rse.2018.04.043.

Grohmann, C.H., Smith, M.J., Riccomini, C., 2011. Multiscale Analysis of Topographic Surface Roughness in the Midland Valley, Scotland. IEEE Transactions on Geoscience and Remote Sensing, 49 (4), 1200-1213. doi: 10.1109/Tgrs.2010.2053546.

Gruber, A., Wessel, B., Huber, M., Roth, A., 2012. Operational TanDEM-X DEM calibration and first validation results. ISPRS Journal of Photogrammetry and Remote Sensing, 73, 39-49. doi: 10.1016/j.isprsjprs.2012.06.002.

Guo, L., Shi, T.Z., Linderman, M., Chen, Y.Y., Zhang, H.T., Fu, P., 2019. Exploring the Influence of Spatial Resolution on the Digital Mapping of Soil Organic Carbon by Airborne Hyperspectral VNIR Imaging. Remote Sensing, 11 (9), 1032. doi: 10.3390/rs11091032.

Hartley, A.J., Chong, G., Houston, J., Mather, A.E., 2005. 150 million years of climatic stability: evidence from the Atacama Desert, northern Chile. Journal of the Geological Society, 162, 421-424. doi: 10.1144/0016-764904-071.

Hirano, A., Welch, R., Lang, H., 2003. Mapping from ASTER stereo image data: DEM validation and accuracy assessment. ISPRS Journal of Photogrammetry and Remote Sensing, 57 (5-6), 356-370. doi: 10.1016/S0924-2716(02)00164-8.

Höhle, J., Höhle, M., 2009. Accuracy assessment of digital elevation models by means of robust statistical methods. ISPRS Journal of Photogrammetry and Remote Sensing, 64 (4), 398-406. doi: 10.1016/j.isprsjprs.2009.02.003.

Holmes, K.W., Chadwick, O.A., Kyriakidis, P.C., 2000. Error in a USGS 30-meter digital elevation model and its impact on terrain modeling. Journal of Hydrology, 233 (1-4), 154-173. doi: 10.1016/S0022-1694(00)00229-8.

Houston, J., Hartley, A.J., 2003. The central andean west-slope rainshadow and its potential contribution to the origin of HYPER-ARIDITY in the Atacama desert. International Journal of Climatology, 23 (12), 1453-1464. doi: 10.1002/joc.938.

Hu, Z.H., Peng, J.W., Hou, Y.L., Shan, J., 2017. Evaluation of Recently Released Open Global Digital Elevation Models of Hubei, China. Remote Sensing, 9 (3), 262. doi: 10.3390/rs9030262.

Huang, L.C., Liu, L., Jiang, L.M., Zhang, T.J., 2018. Automatic Mapping of Thermokarst Landforms from Remote Sensing Images Using Deep Learning: A Case Study in the Northeastern Tibetan Plateau. Remote Sensing, 10 (12), 2067. doi: 10.3390/rs10122067.

Huang, X.D., Xie, H.J., Liang, T.G., Yi, D.H., 2011. Estimating vertical error of SRTM and map-based DEMs using ICESat altimetry data in the eastern Tibetan Plateau. International Journal of Remote Sensing, 32 (18), 5177-5196. doi: 10.1080/01431161.2010.495092.

Huber, M., Wessel, B., Kosmann, D., Felbier, A., Schwieger, V., Habermeyer, M., Wendleder, A., Roth, A., 2009. Ensuring globally the TanDEM-X height accuracy: Analysis of the reference data sets ICESat, SRTM and KGPS-tracks, Proceedings of the 2009 IEEE International Geoscience and Remote Sensing Symposium (IGARSS), Cape Town, South Africa, 12–17 July 2009, 769-772. doi: 10.1109/IGARSS.2009.5418204.

Jain, A.O., Thaker, T., Chaurasia, A., Patel, P., Singh, A.K., 2018. Vertical accuracy evaluation of SRTM-GL1, GDEM-V2, AW3D30 and CartoDEM-V3.1 of 30-m resolution with dual frequency GNSS for lower Tapi Basin India. Geocarto International, 33 (11), 1237-1256. doi: 10.1080/10106049.2017.1343392.

Kalambukattu, J.G., Kumar, S., Raj, R.A., 2018. Digital soil mapping in a Himalayan watershed using remote sensing and terrain parameters employing artificial neural network model. Environ Environmental Earth Sciences, 77 (5), 203. doi: 10.1007/s12665-018-7367-9.

Kellndorfer, J., Walker, W., Pierce, L., Dobson, C., Fites, J.A., Hunsaker, C., Vona, J., Clutter, M., 2004. Vegetation height estimation from shuttle radar topography mission and national elevation datasets. Remote Sensing of Environment, 93 (3), 339-358. doi: 10.1016/j.rse.2004.07.017.

Keys, L., Baade, J., 2019. Uncertainty in Catchment Delineations as a Result of Digital Elevation Model Choice. Hydrology, 6 (1), 13. doi: 10.3390/hydrology6010013.

Kienzle, S., 2004. The Effect of DEM Raster Resolution on First Order, Second Order and Compound Terrain Derivatives Transactions in GIS, 8 (1), 83-111. doi: 10.1111/j.1467-9671.2004.00169.x.

Kim, D., Zheng, Y.B., 2011. Scale-dependent predictability of DEM-based landform attributes for soil spatial variability in a coastal dune system. Geoderma, 164 (3-4), 181-194. doi: 10.1016/j.geoderma.2011.06.002.

Kramm, T., Hoffmeister, D., Curdt, C., Maleki, S., Khormali, F., Kehl, M., 2017. Accuracy Assessment of Landform Classification Approaches on Different Spatial Scales for the Iranian Loess Plateau. ISPRS International Journal of Geo-Information, 6 (11), 366. doi:10.3390/ijgi6110366.

Krieger, G., Moreira, A., Fiedler, H., Hajnsek, I., Werner, M., Younis, M., Zink, M., 2007. TanDEM-X: A satellite formation for high-resolution SAR interferometry. IEEE Transactions on Geoscience and Remote Sensing, 45 (11), 3317-3341. doi: 10.1109/Tgrs.2007.900693.

Lague, D., Brodu, N., Leroux, J., 2013. Accurate 3D comparison of complex topography with terrestrial laser scanner: Application to the Rangitikei canyon (N-Z). ISPRS Journal of Photogrammetry and Remote Sensing, 82, 10-26. doi: 10.1016/j.isprsjprs.2013.04.009.

Leempoel, K., Parisod, C., Geiser, C., Daprà, L., Vittoz, P., Joost, S., 2015. Very high-resolution digital elevation models: are multi-scale derived variables ecologically relevant? Methods in Ecology and Evolution, 6 (12), 1373-1383. doi: 10.1111/2041-210x.12427.

Li, H., Zhao, J.Y., 2018. Evaluation of the Newly Released Worldwide AW3D30 DEM Over Typical Landforms of China Using Two Global DEMs and ICESat/GLAS Data. Ieee Journal of Selected Topics in Applied Earth Observations and Remote Sensing, 11 (11), 4430-4440. doi: 10.1109/Jstars.2018.2874361.

Lindsay, J.B., Cockburn, J.M.H., Russell, H.A.J., 2015. An integral image approach to performing multi-scale topographic position analysis. Geomorphology, 245, 51-61. doi: 10.1016/j.geomorph.2015.05.025.

Liu, K., Song, C.Q., Ke, L.H., Jiang, L., Pan, Y.Y., Ma, R.H., 2019. Global open-access DEM performances in Earth's most rugged region High Mountain Asia: A multi-level assessment. Geomorphology, 338, 16-26. doi: 10.1016/j.geomorph.2019.04.012.

Markus, T., Neumann, T., Martino, A., Abdalati, W., Brunt, K., Csatho, B., Farrell, S., Fricker, H., Gardner, A., Harding, D., Jasinski, M., Kwok, R., Magruder, L., Lubin, D., Luthcke, S., Morison, J., Nelson, R., Neuenschwander, A., Palm, S., Popescu, S., Shum, C.K., Schutz, B.E., Smith, B., Yang, Y.K., Zwally, J., 2017. The Ice, Cloud, and land Elevation Satellite-2 (ICESat-2): Science requirements, concept, and implementation. Remote Sensing of Environment, 190, 260-273. doi: 10.1016/j.rse.2016.12.029.

Marques, K.P.P., Dematte, J.A.M., Miller, B.A., Lepsch, I.F., 2018. Geomorphometric segmentation of complex slope elements for detailed digital soil mapping in southeast Brazil. Geoderma Regional, 14, e00175. doi: 10.1016/j.geodrs.2018.e00175.

Maune, D.F., Nayegandhi, A., 2018. Digital elevation model technologies and applications: the DEM users manual. American Society for Photogrammetry and Remote Sensing, Bethesda, Md, USA.

May, S.M., Hoffmeister, D., Wolf, D., Bubenzer, O., 2019. Zebra stripes in the Atacama Desert revisited – Granular fingering as a mechanism for zebra stripe formation? Geomorphology, 344, 46-59. doi: 10.1016/j.geomorph.2019.07.014.

Mmbando, G.A., Kleyer, M., 2018. Mapping Precipitation, Temperature, and Evapotranspiration in the Mkomazi River Basin, Tanzania. Climate, 6 (3), 63. doi: 10.3390/cli6030063.

Mokarram, M., Seif, A., Sathyamoorthy, D., 2015. Landform classification via fuzzy classification of morphometric parameters computed from digital elevation models: case study on Zagros Mountains. Arabian Journal of Geosciences, 8 (7), 4921-4937. doi: 10.1007/s12517-014-1556-y.

Moudry, V., Lecours, V., Gdulova, K., Gabor, L., Moudra, L., Kropacek, J., Wild, J., 2018. On the use of global DEMs in ecological modelling and the accuracy of new bare-earth DEMs. Ecological Modelling, 383, 3-9. doi: 10.1016/j.ecolmodel.2018.05.006.

Mouratidis, A., Ampatzidis, D., 2019. European Digital Elevation Model Validation against Extensive Global Navigation Satellite Systems Data and Comparison with SRTM DEM and ASTER GDEM in Central Macedonia (Greece). ISPRS International Journal of Geo-Information, 8 (3), 108. doi: 10.3390/ijgi8030108.

Mukherjee, S., Joshi, P.K., Mukherjee, S., Ghosh, A., Garg, R.D., Mukhopadhyay, A., 2013. Evaluation of vertical accuracy of open source Digital Elevation Model (DEM). International Journal of Applied Earth Observation and Geoinformation, 21, 205-217. doi: 10.1016/j.jag.2012.09.004.

Neuenschwander, A., Pitts, K., 2019. The ATL08 land and vegetation product for the ICESat-2 Mission. Remote Sensing of Environment, 221, 247-259. doi: 10.1016/j.rse.2018.11.005.

Neuenschwander, L.A., Magruder, A.L., 2019. Canopy and Terrain Height Retrievals with ICESat-2: A First Look. Remote Sensing, 11 (14), 1721. doi: 10.3390/rs11141721.

Newman, D.R., Lindsay, J.B., Cockburn, J.M.H., 2018a. Evaluating metrics of local topographic position for multiscale geomorphometric analysis. Geomorphology, 312, 40-50. doi: 10.1016/j.geomorph.2018.04.003.

Newman, D.R., Lindsay, J.B., Cockburn, J.M.H., 2018b. Measuring Hyperscale Topographic Anisotropy as a Continuous Landscape Property. Geosciences, 8 (8), 278. doi: 10.3390/geosciences8080278.

Pipaud, I., Loibl, D., Lehmkuhl, F., 2015. Evaluation of TanDEM-X elevation data for geomorphological mapping and interpretation in high mountain environments - A case study from SE Tibet, China. Geomorphology, 246, 232-254. doi: 10.1016/j.geomorph.2015.06.025.

Podgorski, J., Kinnard, C., Petlicki, M., Urrutia, R., 2019. Performance Assessment of TanDEM-X DEM for Mountain Glacier Elevation Change Detection. Remote Sensing, 11 (2), 187. doi: 10.3390/rs11020187.

Poli, D., Remondino, F., Angiuli, E., Agugiaro, G., 2013. Evaluation of Pleiades-1A Triplet on Trento Testfield. International Archives of the Photogrammetry, Remote Sensing and Spatial Information Sciences , XL-1/W1, 287-292. doi: 10.5194/isprsarchives-XL-1-W1-287-2013.

Purinton, B., Bookhagen, B., 2017. Validation of digital elevation models (DEMs) and comparison of geomorphic metrics on the southern Central Andean Plateau. Earth Surface Dynamics, 5 (2), 211-237. doi: 10.5194/esurf-5-211-2017.

Reuter, H.I., Nelson, A., Jarvis, A., 2007. An evaluation of void-filling interpolation methods for SRTM data. International Journal of Geographical Information Science, 21 (9), 983-1008. doi: 10.1080/13658810601169899.

Rexer, M., Hirt, C., 2014. Comparison of free high resolution digital elevation data sets (ASTER GDEM2, SRTM v2.1/v4.1) and validation against accurate heights from the Australian National Gravity Database. Australian Journal of Earth Sciences, 61 (2), 213-226. doi: 10.1080/08120099.2014.884983.

Rieg, L., Klug, C., Nicholson, L., Sailer, R., 2018. Pleiades Tri-Stereo Data for Glacier InvestigationsExamples from the European Alps and the Khumbu Himal. Remote Sensing, 10 (10), 1563. doi: 10.3390/rs10101563.

Riley, S.J., DeGloria, S.D., Elliot, R., 1999. A terrain ruggedness index that quantifies topographic heterogeneity. Intermountain Journal of Sciences., 5 (1-4), 23-27.

Rizzoli, P., Bräutigam, B., Kraus, T., Martone, M., Krieger, G., 2012. Relative height error analysis of TanDEM-X elevation data. ISPRS Journal of Photogrammetry and Remote Sensing, 73, 30-38. doi: 10.1016/j.isprsjprs.2012.06.004.

Rizzoli, P., Martone, M., Gonzalez, C., Wecklich, C., Tridon, D.B., Bräutigam, B., Bachmann, M., Schulze, D., Fritz, T., Huber, M., Wessel, B., Krieger, G., Zink, M., Moreira, A., 2017. Generation and performance assessment of the global TanDEM-X digital elevation model. ISPRS Journal of Photogrammetry and Remote Sensing, 132, 119-139. doi: 10.1016/j.isprsjprs.2017.08.008.

Rodríguez, E., Morris, C.S., Belz, J.E., Chapin, E.C., Martin, J.M., Daffer, W., Hensley, S., 2005. An Assessment of the SRTM Topographic Products. Jet Propulsion Laboratory (JPL), Pasadena, CA, USA.

Rossman, N.R., Zlotnik, V.A., Rowe, C.M., 2018. An approach to hydrogeological modeling of a large system of groundwater-fed lakes and wetlands in the Nebraska Sand Hills, USA. Hydrogeology Journal, 26 (3), 881-897. doi: 10.1007/s10040-017-1691-0.

Satge, F., Bonnet, M.P., Timouk, F., Calmant, S., Pillco, R., Molina, J., Lavado-Casimiro, W., Arsen, A., Cretaux, J.F., Garnier, J., 2015. Accuracy assessment of SRTM v4 and ASTER GDEM v2 over the Altiplano watershed using ICESat/GLAS data. International Journal of Remote Sensing, 36 (2), 465-488. doi: 10.1080/01431161.2014.999166.

Schutz, B.E., Zwally, H.J., Shuman, C.A., Hancock, D., DiMarzio, J.P., 2005. Overview of the ICESat Mission. Geophysical Research Letters, 32, L21S01. doi: 10.1029/2005gl024009.

Schwanghart, W., Groom, G., Kuhn, N.J., Heckrath, G., 2013. Flow network derivation from a high resolution DEM in a low relief, agrarian landscape. Earth Surface Processes and Landforms, 38 (13), 1576-1586. doi: 10.1002/esp.3452.

Smith, M.P., Zhu, A.X., Burt, J.E., Stiles, C., 2006. The effects of DEM resolution and neighborhood size on digital soil survey. Geoderma, 137 (1-2), 58-69. doi: 10.1016/j.geoderma.2006.07.002.

Sofia, G., Hillier, J.K., Conway, S.J., 2016. Frontiers in Geomorphometry and Earth Surface Dynamics: possibilities, limitations and perspectives. Earth Surface Dynamics, 4 (3), 721-725. doi: 10.5194/esurf-4-721-2016.

Sörensen, R., Seibert, J., 2007. Effects of DEM resolution on the calculation of topographical indices: TWI and its components. Journal of Hydrology, 347 (1-2), 79-89. doi: 10.1016/j.jhydrol.2007.09.001.

Suwandana, E., Kawamura, K., Sakuno, Y., Kustiyanto, E., 2012a. Thematic information content assessment of the ASTER GDEM: a case study of watershed delineation in West Java, Indonesia. Remote Sensing Letters, 3 (5), 423-432. doi: 10.1080/01431161.2011.593580.

Suwandana, E., Kawamura, K., Sakuno, Y., Kustiyanto, E., Raharjo, B., 2012b. Evaluation of ASTER GDEM2 in Comparison with GDEM1, SRTM DEM and Topographic-Map-Derived DEM Using Inundation Area Analysis and RTK-dGPS Data. Remote Sensing, 4 (8), 2419-2431. doi: 10.3390/rs4082419.

Tachikawa, T., Kaku, M., Iwasaki, A., Gesch, D.B., Oimoen, M.J., Zhang, Z., Danielson, J.J., Krieger, T., Curtis, B., Haase, J., Abrams, M., Carabajal, C., 2011. ASTER Global Digital Elevation Model Version 2 - summary of validation results. NASA, Washington, DC, USA.

Tadono, T., Ishida, H., Oda, F., Naito, S., Minakawa, K., Iwamoto, H., 2014. Precise Global DEM Generation by ALOS PRISM. ISPRS Annals of the Photogrammetry, Remote Sensing and Spatial Information Sciences, II-4, 71-76. doi: 10.5194/isprsannals-II-4-71-2014.

Tadono, T., Shimada, M., Murakami, H., Takaku, J., 2009. Calibration of PRISM and AVNIR-2 Onboard ALOS "Daichi". IEEE Transactions on Geoscience and Remote Sensing, 47 (12), 4042-4050. doi: 10.1109/Tgrs.2009.2025270.

Takaku, J., Tadono, T., 2017. Quality updates of 'AW3D' global DSM generated from ALOS PRISM, Proceedings of the 2017 IEEE International Geoscience and Remote Sensing Symposium (IGARSS), Fort Worth, TX, USA, 23–28 July 2017, 5666-5669. doi: 10.1109/IGARSS.2017.8128293.

Takaku, J., Tadono, T., Tsutsui, K., 2014. Generation of High Resolution Global DSM from ALOS PRISM. International Archives of the Photogrammetry, Remote Sensing and Spatial Information Sciences, XL-4, 243-248. doi: 10.5194/isprsarchives-XL-4-243-2014.

Takaku, J., Tadono, T., Tsutsui, K., Ichikawa, M., 2016. Validation of 'AW3D' Global DSM generated from ALOS PRISM. In Proceedings of the XXIII ISPRS Congress, Prague, Czech Republic, 12–19 July 2016. doi: 10.5194/isprsannals-III-4-25-2016.

Tarolli, P., Sofia, G., 2016. Human topographic signatures and derived geomorphic processes across landscapes. Geomorphology, 255, 140-161. doi: 10.1016/j.geomorph.2015.12.007.

Walk, J., Stauch, G., Reyers, M., Vásquez, P., Sepúlveda, F.A., Bartz, M., Hoffmeister, D., Brückner, H., Lehmkuhl, F., 2020. Gradients in climate, geology, and topography affecting coastal alluvial fan morphodynamics in hyperarid regions – The Atacama perspective. Global and Planetary Change, 185, 102994. doi: 10.1016/j.gloplacha.2019.102994.

Weiss, A.D., 2001. Topographic Position and Landforms Analysis, ESRI Users Conference, San Diego, CA, USA.

Wessel, B., 2016. TanDEM-X Ground Segment – DEM Products Specification Document. EOC, Munich, Germany, 2016.

Wessel, B., Huber, M., Wohlfart, C., Marschalk, U., Kosmann, D., Roth, A., 2018. Accuracy assessment of the global TanDEM-X Digital Elevation Model with GPS data. ISPRS Journal of Photogrammetry and Remote Sensing, 139, 171-182. doi: 10.1016/j.isprsjprs.2018.02.017.

Wilson, J.P., 2012. Digital terrain modeling. Geomorphology, 137 (1), 107-121. doi: 10.1016/j.geomorph.2011.03.012.

Yahaya, S.I., El Azzab, D., 2019. Vertical accuracy assessment of global digital elevation models and validation of gravity database heights in Niger. International Journal of Remote Sensing, 40 (20), 7966-7985. doi: 10.1080/01431161.2019.1607982.

Zhang, K.Q., Gann, D., Ross, M., Biswas, H., Li, Y.P., Rhome, J., 2019a. Comparison of TanDEM-X DEM with LiDAR Data for Accuracy Assessment in a Coastal Urban Area. Remote Sensing, 11 (7), 876. doi: 10.3390/rs11070876.

Zhang, K.Q., Gann, D., Ross, M., Robertson, Q., Sarmiento, J., Santana, S., Rhome, J., Fritz, C., 2019b. Accuracy assessment of ASTER, SRTM, ALOS, and TDX DEMs for Hispaniola and implications for mapping vulnerability to coastal flooding. Remote Sensing of Environment ,225, 290-306. doi: 10.1016/j.rse.2019.02.028.

Zhang, W.H., Montgomery, D.R., 1994. Digital Elevation Model Grid Size, Landscape Representation, and Hydrologic Simulations. Water Resources Research, 30 (4), 1019-1028. doi: 10.1029/93WR03553.

Zhao, S.M., Cheng, W.M., Zhou, C.H., Chen, X., Zhang, S.F., Zhou, Z.P., Liu, H.J., Chai, H.X., 2011. Accuracy assessment of the ASTER GDEM and SRTM3 DEM: an example in the Loess Plateau and North China Plain of China. International Journal of Remote Sensing, 32 (23), 8081-8093. doi: 10.1080/01431161.2010.532176.

Zhao, S.M., Cheng, W.M., Zhou, C.H., Liu, H.J., Su, Q.M., Zhang, S.F., He, W.C., Wang, L., Wu, W.J., 2017. Using MLR to model the vertical error distribution of ASTER GDEM V2 data based on ICESat/GLA14 data in the Loess Plateau of China. Zeitschrift für Geomorphologie, 61, 9-26. doi: 10.1127/zfg_suppl/2016/0325.

Zwally, H.J., Schutz, B., Abdalati, W., Abshire, J., Bentley, C., Brenner, A., Bufton, J., Dezio, J., Hancock, D., Harding, D., Herring, T., Minster, B., Quinn, K., Palm, S., Spinhirne, J., Thomas, R., 2002. ICESat's laser measurements of polar ice, atmosphere, ocean, and land. Journal of Geodynamics, 34 (3-4), 405-445. doi: 10.1016/S0264-3707(02)00042-X.

4 Additional evaluation of newly released DEMs in northern Chile

As an extension to the analysis conducted in chapter 3, the accuracy of three additional DEMs was evaluated in this chapter. These DEMs are the 30 m NASADEM and the Copernicus DEM with a spatial resolution of 30 m and 90 m. All three elevation datasets were published after the completion of the study conducted in the previous chapter and are therefore considered separately here.

4.1 Materials and methods

The NASADEM can be considered the successor of the original SRTM DEM. It was mainly processed by the NASA and the National Geospatial-Intelligence Agency (NGA) using the original elevation data obtained from the Shuttle Radar Topography Mission in February 2000 (NASA JPL, 2020). It was created with newer processing techniques as well as additional datasets from ASTER GDEM, ICESat GLAS and PRISM data (Crippen et al., 2016). These datasets were used for ground control to achieve a higher overall accuracy and for void reduction to improve its overall quality. The NASADEM was released in early 2020 and is currently available in its first version, which was also used for this study.

The Copernicus DEM was processed from the WorldDEM™ data obtained during the TanDEM-X mission funded by the German Aerospace Centre (DLR) and Airbus Defence and Space (Airbus Defence and Space, 2020a). It is provided in two different spatial resolutions, 30 m and 90 m. The 30 m version was initially released in 2019 and updated in 2020. The most recent product is available in version 3, which was also used for evaluation in this chapter. The 90 m Copernicus DEM was released in late 2019 and has not received any updates to date. Both Copernicus DEMs were obtained from the Copernicus Planetary Data Access (PANDA) provided by the European Space Agency (ESA) (Airbus Defence and Space, 2020a). The estimated error was stated as 1.51 m for deserts and regions with less vegetation, comparable to the Chilean study area (Airbus Defence and Space, 2020b).

The accuracy assessment of the three previously mentioned DEMs was conducted in the identical manner as described in section 3.3 with the same control datasets. These datasets are the ICESat GLA14 elevation data from the first ICESat mission as well as the ATL03 and ATL08 elevation datasets from the follow-up ICESAT-2 satellite (see sections 3.3.3.1 and 3.3.3.2). In addition, the very high resolution DEMs derived by UAV and TLS presented in the previous chapters 3.3.3.3 and 3.3.3.4 were used for the evaluation of smaller areas.

For accuracy assessment, the overall accuracy in the Chilean study area was assessed, as previously described in section 3.3.4, by calculating the RMSE and NMAD for all three DEMs compared to all mentioned reference datasets. Furthermore, the accuracies calculated with the ICESat reference dataset were evaluated with regard to the relief. For this purpose, the errors were related to the terrain features of slope, TRI and TPI that were derived from the 12 m TanDEM-X elevation model and classified as described in section 3.3.4.

4.2 Results

The achieved overall accuracies obtained with all control data sets are listed in Table 4-1. For all DEMs, the assessment with most reference datasets produced similar results and only minor variations in

accuracy are observable. Only the RMSE for the TLS dataset is significantly higher for all DEM. The results show that the 30 m Copernicus DEM achieved the highest overall accuracies with all reference datasets, slightly higher than the NASADEM. The Copernicus DEM achieved a RMSE of 3.6 m for the ICESat and ICESat-2 ATL03 reference datasets. The calculated RMSE in comparison to the ICESat-2 ATL08 and UVA raster DEMs is similar with 3.0 m and 3.2 m. Only the RMSE achieved with the TLS dataset is significantly higher with 9.4 m. The calculated NMAD values for this DEM are all relatively low, ranging from 1.4 m with the ICESat-2 ATL03 dataset to 2.9 m with the ICESat-2 ATL08 dataset. The achieved accuracies for the NASADEM are slightly lower, being 3.2 m with the ICESat-2 ATL08 dataset, 4.4 m with the ICESat-2 ATL03 dataset, 4.5 m with the ICESat and UAV datasets and 10.3 m with the TLS dataset. The NMAD results are lowest with 2.7 m for the ICESat-2 ATL03 dataset and highest with 4.3 m for the UAV DEMs. The 90 m Copernicus DEM achieved significantly lower accuracies than both 30 m DEMs. The RMSE values of this DEM range from 4.0 m (ICESat-2 ATL08) to 7.6 m (ICESat). The NMAD values are between 2.9 m (ICESat-2 ATL03) and 4.6 m (UAV DEMs).

The achieved error values obtained as a function of slope are depicted in Figure 4-1. They show a mostly linear decrease in accuracy in steeper terrain for all three DEMs. However, the decrease is much larger for the 90 m Copernicus DEM than for the others. Although all DEMs have a similar accuracy in flat terrain, ranging between 2 m and 3 m, the achieved accuracy of the 90 m Copernicus DEM in extremely steep terrain is much lower. There, the 90 m Copernicus DEM has a RMSE of 26.9 m and a NMAD of 24.8 m. In contrast, the achieved error values of the 30 m Copernicus DEM (RMSE: 12.8 m, NMAD: 11.6 m) and NASADEM (RMSE: 15.1 m, NMAD: 12.4 m) are approximately half as high as those of the 90 m DEM. A comparison of the two 30 m DEMs shows a similar increase of errors for both. However, the NASADEM seems to contain more outliers as the difference between RMSE and NMAD increases on steeper slopes.

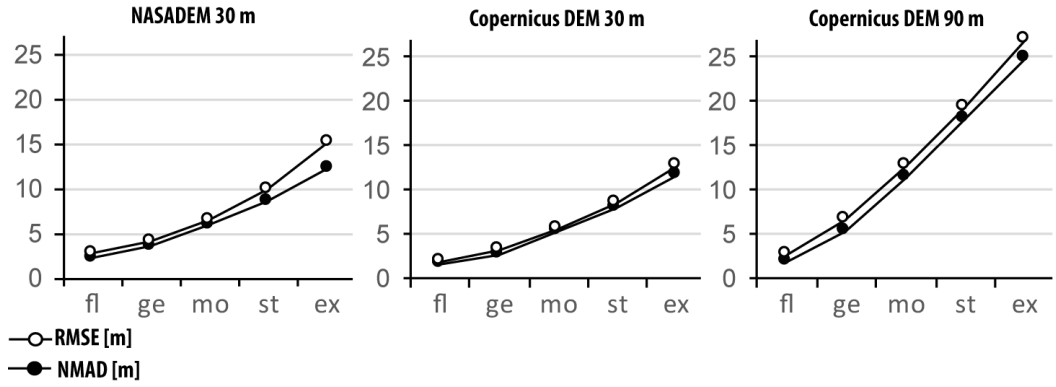

Figure 4-1: Calculated RMSE and NMAD of elevation differences according to the slope. Derived slope classes are flat (fl), gentle (ge), moderate (mo), steep (st) and extreme (ex).

The calculated error values compared to the TRI are shown in Figure 4-2. In flat terrain, an overall similar accuracy can be observed for all DEMs, slightly higher for both Copernicus DEMs (1.6 m to 1.8 m RMSE and NMAD) than for the NASADEM (2.4 m RMSE and 2.1 m NMAD). This error remains at a similar level and only slightly increases for both 30 m DEMs in medium to moderately rugged terrain. Only the 90 m Copernicus DEM shows a higher increase of error in medium rugged terrain and is here on a similar accuracy level to the NASADEM. In highly to extremely rugged terrain, all DEMs reveal a strong decrease in accuracy, which is by far the highest for the 90 m Copernicus DEM. While both 30 m DEMs achieved errors of less than 7 m, the 90 m Copernicus DEM achieved a significantly lower RMSE of about 12.7 m and NMAD of 9.2 m.

Table 4-1: Overall accuracies of all digital elevation models compared to the reference point datasets of Ice, Cloud, and Land Elevation Satellite (ICESat), ICESat-2 ATL03, ICESat-2 ATL08 and terrestrial laser scanning (TLS) point clouds as well as raster datasets derived from unmanned aerial vehicle (UAV)-based photogrammetry and TLS raster datasets. Listed are the spatial resolution (Res.), the calculated RMSE, the NMAD and the total number of applied points or raster for each DEM.

		ICESat			**ICESat-2 ATL03**			**ICESat-2 ATL08**			**UAV DEMs**			**TLS raster data**		
DEM	**Res.**	**RMSE [m]**	**NMAD [m]**	**No. points**	**RMSE [m]**	**NMAD [m]**	**No. points**	**RMSE [m]**	**NMAD [m]**	**No. points**	**RMSE [m]**	**NMAD [m]**	**No. raster**	**RMSE [m]**	**NMAD [m]**	**No. raster**
NASADEM	30 m	4.5	2.9	453434	4.4	2.7	392333	3.2	3.6	643926	4.5	4.3	19	10.3	4.2	4
Copernicus DEM	30 m	3.6	2.1	453434	3.6	1.4	392333	3.0	2.9	643926	3.2	2.6	19	9.4	1.8	4
Copernicus DEM	90 m	7.6	3.2	453434	7.1	2.9	392333	4.0	3.2	643926	5.2	4.6	19	10.2	3.8	4

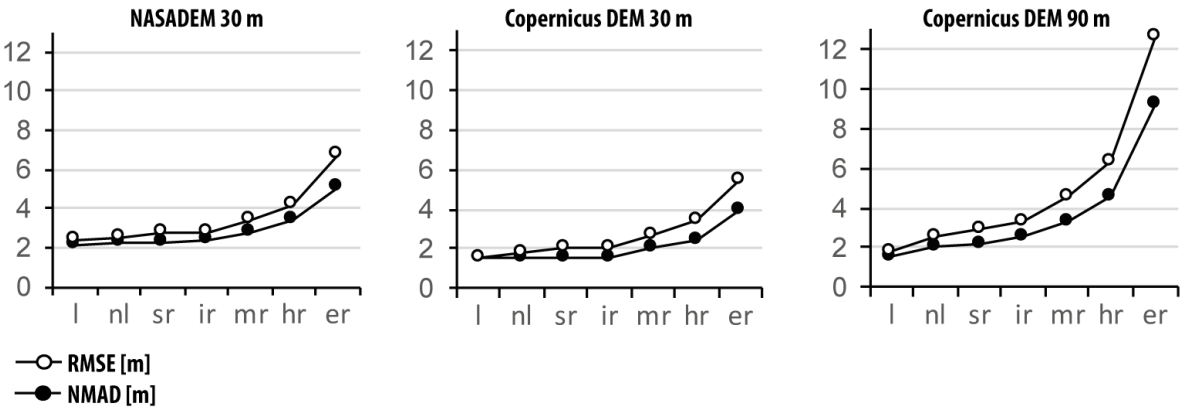

Figure 4-2: Calculated RMSE and NMAD of elevation differences according to the classified terrain ruggedness index from level to extremely rugged. Categorization of classes was conducted after Riley et al. (1999). Classes are level (l), nearly level (nl), slightly rugged (sr), intermediate (ir), moderately rugged (mr), highly rugged (hr), extremely rugged (ex).

Figure 4-3 compares the calculated error values of the three tested DEMs in comparison to their respective TPI landform classes that were derived from the 12 m TanDEM-X. All DEMs show by far the highest accuracies in plain terrain with an error of less than 2.7 m. Overall, the 30 m Copernicus DEM achieved the highest accuracies in all landform classes, followed by the NASADEM. The 90 m Copernicus DEM revealed a comparable accuracy to the NASADEM only in flat terrain. For all other landforms, its achieved accuracy is significantly lower compared to both 30 m DEMs. The overall lowest accuracies are observable for the landforms 'gully', 'ridge' and 'drainage' with RMSE accuracies of about 5 m to 6 m for the 30 m Copernicus DEMs, 8 m to 9 m for the NASADEM and 12 m to 16 m for the 90 m Copernicus DEM.

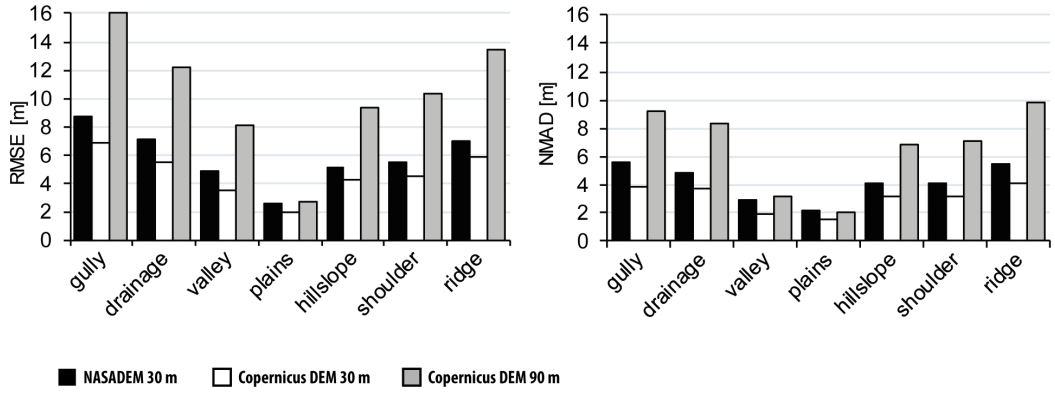

Figure 4-3: Calculated RMSE and NMAD of elevation differences according to topographic position index (TPI) classes.

4.3 Discussion

To compare the tested DEMs of this chapter with the previously tested global DEMs of chapter 3, the mean overall accuracy of all achieved RMSE and NMAD results was calculated. These mean overall accuracies of each DEM are presented in the ranking of Table 4-2. Overall, it shows that the 30 m Copernicus DEM achieved a comparable accuracy to the previously tested ALOS W3D. Comparing the accuracies of both DEMs according to slope shows that the observed accuracy of the 30 m Copernicus

DEM seems to be slightly higher in flat terrain and slightly worse in rough terrain compared to the ALOS W3D DEM. This confirms the results of Karlson et al. (2021), who also showed a slightly higher accuracy of the Copernicus DEM over the ALOS W3D DEM in an overall flatter study area than the Chilean Atacama Desert. They achieved an average RMSE of 2.44 m for their study area, which is comparable to the results of this study in mostly flat areas. In undulated areas, the assessed error values of this DEM in this chapter rise significantly up to more than 8 m. This mostly confirms results the of Marešová et al. (2021) who stated for three mountainous areas an average RMSE between about 7 m and 14 m for this DEM.

The NASADEM reveals a higher overall accuracy than its predecessor, the 30 m SRTM DEM. Thus, the new processing techniques and additional datasets used to create the DEM seem to have positively affected the quality of this DEM. Nevertheless, it does not reach the accuracy of the ALOS DEM and the 30 m Copernicus DEM in all landscape types of the study area. This is in accordance with findings from Uuemaa et al. (2020), who also showed a slightly higher accuracy of the NASADEM over the older SRTM DEM. Overall, the NASADEM accuracies obtained in this chapter are comparable to the findings of Carrera-Hernandez (2021) who achieved an overall RMSE of 5.2 m for the large and diverse area of the Mexican country.

In comparison to the other tested 90 m DEMs, the 90 m Copernicus DEM shows ambivalent results. It reveals a high accuracy in flat landscapes, which is slightly lower, but overall comparable to the 90 m TanDEM-X. Compared to the 90 m SRTM, its accuracy is considerably higher in flat terrain. In contrast, the loss of accuracy in hilly to steep terrain is highest for the 90 m Copernicus DEM and exceeds the observed decrease of the 90 m TanDEM-X. Thus, the 90 m Copernicus DEM showed the lowest overall accuracies in steep terrain of all investigated DEMs in this study area. This is in contradiction to the findings of Marešová et al. (2021) who showed a considerably higher accuracy of the 90 m Copernicus DEM compared to the 90 m TanDEM-X for three European mountainous regions. Nevertheless, it can be stated that both Copernicus DEMs mostly show a similar behavior in their error distribution concerning the relief as the TanDEM-X DEM. This is not surprising as both originally consist of the same WorldDEM™ data from the TanDEM-X mission.

Table 4-2: Ranking of the achieved mean overall accuracies of all RMSE and NMAD error measures for all global DEMs evaluated in chapters 3 and 4.

	RMSE			**NMAD**		
Rank	**Spatial resolution**	**DEM**	**Mean OA [m]**	**Spatial resolution**	**DEM**	**Mean OA [m]**
1	12 m	TanDEM-X	3.3	12 m	TanDEM-X	1.3
2	30 m	ALOS W3D	4.3	30 m	Copernicus DEM	2.2
3	30 m	Copernicus DEM	4.6	30 m	ALOS W3D	2.8
4	30 m	NASADEM	5.4	90 m	TanDEM-X	3.3
5	30 m	SRTM	5.4	30 m	NASADEM	3.5
6	90 m	Copernicus DEM	6.8	90 m	Copernicus DEM	3.5
7	90 m	SRTM	7.7	30 m	SRTM	4.0
8	90 m	TanDEM-X	8.5	90 m	SRTM	5.0
9	30 m	ASTER GDEM	8.7	30 m	ASTER GDEM	7.0

5 Comprehensive vertical accuracy analysis of freely available DEMs for different landscape types of the Rur catchment, Germany

TANJA KRAMM[1], DIRK HOFFMEISTER[1]

Published in: Geocarto International, 2021, In Press

DOI: 10.1080/10106049.2021.1984588

Formatting and orthography of the manuscript is adapted to the dissertation style.

[1]GIS and Remote Sensing, Institute of Geography, University of Cologne, Albertus Magnus Platz, 50923 Köln, Germany.

Abstract: This study evaluates the vertical accuracy of nine freely available digital elevation models (DEMs) with a medium spatial resolution for a typical mid-latitude flat to hilly landscape in the Rur catchment in Germany. All datasets were evaluated with two reference datasets, a 1 m DEM and a highly precise set of elevation control points. The accuracy was evaluated with regard to different slopes, landforms and land use. The results reveal in flat areas an average error of 2 – 4 m, which increases about two to three times in undulated terrain. Areas with dense tree cover show a mean error of 6 – 10 m. The highest accuracies were achieved by the SRTM DEM, followed by other DEMs that mainly implemented SRTM data. TanDEM-X and Copernicus DEM showed ambivalent results showing a higher ratio of existing errors in the elevation product for vegetation and water areas that prevent a higher overall accuracy of these DEMs.

Keywords: accuracy assessment; digital terrain model; topography; land use; slope

5.1 Introduction

Digital elevation models (DEMs) as a representation of the Earth's surface play a key role in many scientific disciplines. They enable the possibility of a quantitative characterization of relief by deriving terrain variables (e.g. slope, aspect, curvature, topographic wetness index), which are essential inputs in numerous environmental analyses (Wilson 2018). Thus, DEMs are widely used sources in numerous geospatial studies in the fields of geomorphology (Bishop et al., 2012; Ullmann et al., 2019; Walk et al., 2020), landform distribution analysis (Dragut and Blaschke, 2006; Huang et al., 2018; Kramm et al., 2017; Mokarram et al., 2015), hydrology (Drisya and Kumar, 2016; Fenta et al., 2015; Rossman et al., 2018; Schwanghart et al., 2013), digital soil mapping (Kalambukattu et al., 2018; Kramm and Hoffmeister, 2020; Marques et al., 2018), climatic modelling (Mmbando and Kleyer, 2018) or the evaluation of glacier changes (Berthier and Brun, 2019; Blaszczyk et al., 2019). In recent years, these applications have raised the need for DEMs that provide a highly accurate representation of the Earth's surface. As the outcome of these applications is often limited to the quality of available elevation models, it is crucial to gain an understanding of their accuracy in different landscapes with varying relief and land cover.

From 2003 onwards, many freely available digital elevation models with a nearly global coverage and a spatial resolution of about 30 m and 90 m have been released that are based on optical imagery or

synthetic aperture radar (SAR) interferometry. The first nearly global DEM was released as a product of the Shuttle Radar Topography Mission (SRTM) in 2003, followed by DEMs from the Advanced Spaceborne Thermal Emission and Reflection Radiometer (ASTER) from 2009 onwards, the Advanced Land Observing Satellite (ALOS) World 3D (first release in 2016) and the TanDEM-X WorldDEM™ (released in 2018). Furthermore, with the EU-DEM (firstly released in 2013), the Copernicus DEM (release: 2019) and the NASADEM (release: 2020), several reworked and improved DEMs from the previously mentioned sources have been released in recent years that offer the perspective of an even higher accuracy than the originally created elevation models.

A lot of research on the accuracy of many of these elevation models has already been done by numerous publications at different sites with varying relief and land cover. Several studies compared the vertical accuracy of SRTM and ASTER GDEM (Graf et al., 2018; Luana et al., 2015; Mukherjee et al., 2013; Pakoksung and Takagi, 2020; Rexer and Hirt, 2014; Satge et al., 2015; Thomas et al., 2014; Zhao et al., 2011) as well as the accuracy of the ALOS World 3D in comparison to SRTM and ASTER GDEM (Alganci et al., 2018; Hu et al., 2017; Li and Zhao, 2018; Liu et al., 2019; Yahaya and El Azzab, 2019; Yap et al., 2019). Furthermore, some studies evaluated the performance of the TanDEM-X WorldDEM™ in different resolutions on its own (Altunel, 2019; Baade and Schmullius, 2016; Gdulova et al., 2020) and in varying combinations with the three previously mentioned DEMs (Becek et al., 2016; Gonzalez-Moradas and Viveen, 2020; Nagaveni et al., 2019; Pandey et al., 2017; Tian et al., 2017). Several studies have conducted a comprehensive comparison of all four DEMs (Grohmann, 2018; Kramm and Hoffmeister, 2019; Kumar et al., 2020; Liu et al., 2020; Uuemaa et al., 2020; Vassilaki and Stamos, 2020; Zhang et al., 2019).

However, only a few studies are available yet that have investigated the newly available EU-DEM, NASADEM and Copernicus DEM. Mouratidis and Ampatzidis (2019) have evaluated both available versions of the EU-DEM against ASTER GDEM and SRTM DEM. Uuemaa et al. (2020) have tested the performance of the NASADEM at four different sites against a set of other DEMs. To date, no evaluation is available that has tested the newly available Copernicus DEM. Additionally, a comprehensive analysis that compares the accuracy of all of these DEMs in different relief and land cover settings is still missing. Therefore, this contribution has the aim to conduct an evaluation of the vertical accuracy of these previously mentioned and freely available DEMs with a medium spatial resolution between 25 m and 90 m. Furthermore, it is the aim to test whether the most recent and newly created DEMs are able to outperform the older ones.

The accuracy assessment was performed with two different reference datasets, a very accurate 1 m high resolution digital elevation model (DGM1) that was acquired by airborne laser scanning and a set of highly accurate elevation control points (ECPs). The study was conducted in the heterogeneous Rur catchment in Germany, which consists of two neighbouring but significantly different landscapes regarding their relief and land cover. As the area represents typical mid-latitude landscape types with varying agricultural crops, settlements with corresponding infrastructure as well as woods and pasture in hilly landscapes, this contribution has the aim of addressing the achieved accuracies with regard to these differences in topography and land cover. According to the Copernicus Global Land Cover Map from 2019 (Buchhorn et al., 2020), about 10 % of the global land surface is covered by cropland similar to the northern part of the Rur catchment. Further 10 % of the global surface is covered by mid-latitude evergreen needle-leave or tempered deciduous broad-leave forest as it can be found in the southern part of the study area. Therefore, the aim of this study is to produce representative error measures for

the different DEMs that can also be transferred to a relatively large area of the Earth. The comparison of accuracy in this study is based on the calculated statistical parameters of root mean square error (RMSE) and normalized median absolute deviation (NMAD). These error values are linked to slope and geomorphometric landform features as the terrain directly influences the accuracy (Grohmann, 2018; Holmes et al., 2000; Mukherjee et al., 2013). Furthermore, these errors are compared to different land use classes, which can also significantly influence the accuracy of a DEM (Alganci et al., 2018; Mouratidis and Ampatzidis, 2019; Uuemaa et al., 2020).

Overall, the aim of this contribution is to conduct an accuracy assessment of all previously mentioned openly accessible DEMs and to provide fully comparable quantitative error measures for each DEM in a study area with different mid-latitude landscapes. Thus, the errors are assessed against different types of land cover, relief types and steepness in two neighbouring but significantly different landscapes. To date, there is no study available that altogether compares all freely available global elevation models under the same conditions, which is essential to achieve a full comparability of the data. This contribution aims to precisely elaborate on which DEM provides the most accurate representation of the Earth's surface under which conditions and is most likely preferable for a mid-latitude landscape and different relief types. This knowledge should help further studies to choose the most suitable DEM for their research to achieve the most accurate results. Furthermore, general average accuracy values shall be determined from the results in relation to relief and land cover that can be expected for medium resolution DEMs and also in other but similar mid-latitude landscapes.

5.2 Study area

The study was conducted in the catchment of the river Rur, which is primarily situated in the German Federal State of North-Rhine Westphalia with small neighbouring parts in the Netherlands and Belgium. Here, mainly the German parts of the Rur catchment and very small neighbouring areas are considered. The location and landscape of the included area is presented in Figure 5-1. The landscape of the study area varies significantly from north to south and can be subdivided into two different major units with significantly different characteristics. Furthermore, the elevation declines from 740 m in the south to about 70 m in the northern part of the study area.

The northern part is situated in the fertile Germany-Belgium loess belt and is characterized by predominantly flat landscapes covered by Tertiary Pleistocene terrace deposits near the rivers Maas and Rur as well as aeolian loess deposits and dune sands (Bogena et al., 2018). The average altitude of this area lies at 100 m. The area is highly productive for agriculture (Korres et al., 2015) and widely used for crop growth, mainly winter wheat, winter barley, winter rapeseed, maize, potato and sugar beet (IT.NRW, 2012; Waldhoff et al., 2017). About 5 % of the area is covered by settlements (Bogena et al., 2018). A small area within the northern part has been left out from the study as it contains a brown coal open cast mine and neighbouring backfilled areas where the landscape and elevations have vastly changed during the last decades. This area has been excluded from the study as the evaluated DEMs were recorded in different time periods and their elevation data cover different stages of the brown coal mine.

The upland area in the southern part of the catchment is mainly covered by a hilly landscape with a low mountain range that consists of Paleozoic to Mesozoic solid rocks of the Rhenish Massif, with

alternating sequences of mudstones, siltstones, sandstones and greywackes (Bogena et al., 2018). The elevation ranges from 180 m to 740 m with elevation differences of up to 300 m between the valley bottom and surrounding ridges. The area consists of mostly forested areas, pasture and several water reservoirs (Bogena et al., 2018; Korres et al., 2015). The mean annual precipitation is considerably higher in the southern part with 1,400 mm compared to about 700 mm in the northern part of the catchment (Korres et al., 2015).

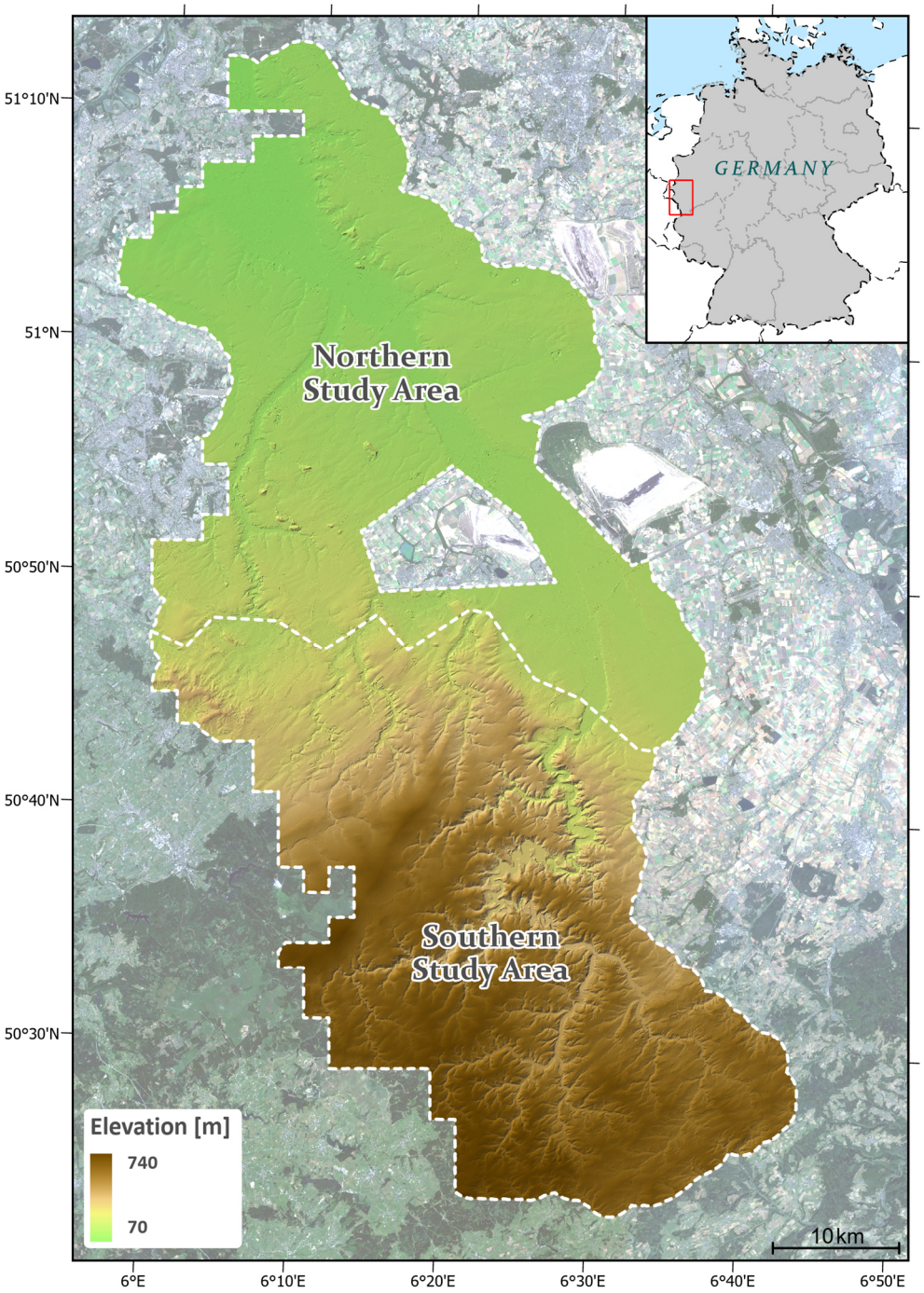

Figure 5-1: Hill-shaded relief and location overview map of the Rur catchment. Elevations are derived from the DGM1. A part within the northern study area has been excluded from the study as it contains a brown coal open cast mine and neighbouring backfilled areas where elevations have vastly changed during the last decades. The background image contains a cloud-free mosaic of Sentinel-2 images from 2017 to 2019 derived from Google Earth Engine.

5.3 Materials and methods

5.3.1 DEMs

The accuracy of nine freely available DEMs was evaluated in this study. All DEMs were assessed for an area of about 2,000 km^2. Further information about the origin, properties and expectable accuracies of all evaluated DEMs is briefly summarized in Table 5-1 and described in the following paragraphs. Additionally, the relationship of all DEMs to each other and their original data sources is illustrated in Figure 5-2.

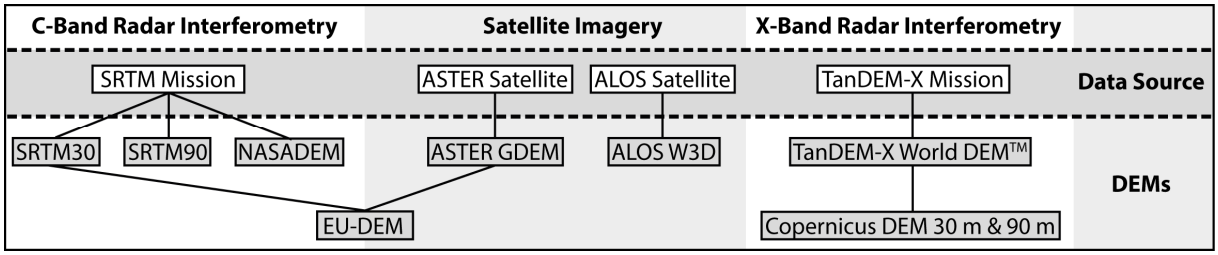

Figure 5-2: Relationship of all evaluated DEMs and their original data sources.

The most recent version of the ASTER GDEM was created by producing images from the ASTER sensor that were acquired until November 2013 (Abrams and Crippen, 2019). The ASTER sensor was started in December 1999 as part of the National Aeronautics and Space Administration's (NASA) Earth Observing System Terra satellite (Abrams et al., 2010; Tachikawa et al., 2011). The DEM includes several improvements such as water masks and filled voids with additional SRTM-1 data and Global Multi-resolution Terrain Elevation Data 2010 (GMTED2010).

Several DEMs used in this study were created from data obtained by the Shuttle Radar Topography Mission, which was a cooperation between NASA's Jet Propulsion Laboratory (JPL), the German Aerospace Centre (DLR) and the Agenzia Spaziale Italiana (ASI, Italy). A 1 arc-second resolution (≈ 30 m) SRTM DEM Version 3 and a 3 arc-seconds (≈ 90 m) SRTM-3 in its 4th version from the acquired C-band data will be assessed. Both were produced by the Consultative Group of International Agricultural Research-Consortium for Spatial Information (CGIAR-CSI) (Jarvis et al., 2008) and contain several improvements, such as coastlines and water bodies and additional elevation data from ASTER GDEM2 for void filling (Rodríguez et al., 2005). The 90 m version uses various interpolation techniques that are further explained in detail by Reuter et al. (2007). Additionally, the NASADEM is used as a renewed product of the original SRTM data. It has been produced as a collaboration between the NASA and the National Geospatial-Intelligence Agency (NGA) with additional participation of the DLR and the Italian space agency (NASA JPL, 2020). The DEM was created by reprocessing the original SRTM mission RADAR data and combining it with newer algorithms and datasets that were not available when the original SRTM DEM was processed. Furthermore, ASTER GDEM Version 2, ALOS W3D and ICESat GLAS datasets were additionally used to improve geolocation accuracy and to fill voids of no sufficient SRTM data (Crippen et al., 2016).

Table 5-1: Summary of specific properties of all evaluated DEMs.

	Acquisition method	Spatial resolution	Horizontal datum	Vertical datum	Estimated vertical accuracy	References
ASTER GDEM V3.0	Imagery acquired from the Earth Observing System Terra satellite	30 m	WGS84	EGM96	12.1 m	Abrams and Crippen (2019)
ALOS W3D V3.1	Imagery acquired from the ALOS satellite by Japan Aerospace Exploration Agency (JAXA)	30 m	WGS84	EGM96	5.0 m	Tadono et al. (2009); Takaku et al. (2014)
SRTM-1 V3.0	Shuttle Radar Topography Mission with two synthetic aperture radar systems (5.6 cm SIR-C and 3.1 cm X-SAR)	30 m	WGS84	WGS84 ellipsoid	6.2 m	Farr et al. (2007); Rodríguez et al. (2005)
SRTM-3 V4.1		90 m	WGS84	WGS84 ellipsoid	6.2 m	
NASADEM		30 m	WGS84	EGM96	< 6.2 m	Crippen et al. (2016); Gesch (2018)
EU-DEM V1.1	Fusion of SRTM Version 2 and ASTER GDEM Version 2.1	25 m	ETRS89	EVRF2000 with EGG08 geoid	7.0 m	European Environment Agency (EEA) (2014)
TanDEM-X	TanDEM-X mission with X-band RADAR interferometry (InSAR)	90 m	WGS84	WGS84 ellipsoid	< 10.0 m	Grohmann (2018); Rizzoli et al. (2012); Wessel et al. (2018)
Copernicus DEM	TanDEM-X mission with X-band RADAR interferometry (InSAR) and additional ICESat data	30 m	WGS84	EGM2008	< 4.0 m	Airbus Defence and Space (2020a), Airbus Defence and Space (2020b)
Copernicus DEM		90 m	WGS84	EGM2008	< 4.0 m	

The 30 m ALOS World 3D DEM was produced from 5 m resolution satellite imagery of the Panchromatic Remote-sensing Instrument for Stereo Mapping (PRISM) sensor on board of the ALOS satellite by the Japan Aerospace Exploration Agency (JAXA). The most recent version uses ICESat GLAH14 heights, elevations from SRTM and visual human interpretations, as well as additional supplementary data for void filling to improve the overall quality of the DEM (Earth Observation Research Center and Japan Aerospace Exploration Agency, 2021).

The EU-DEM is a hybrid digital surface model that was generated within the framework of the EU Copernicus program coordinated by the European Environment Agency (EEA). The original version was produced as a fusion of SRTM version 2 and ASTER GDEM version 2.1 elevation datasets using a weighted averaging approach for the whole European continent. The most recent version 1.1 (European Environment Agency (EEA), 2016) was improved by addressing geopositioning issues with SPOT 2011 imagery as well as the reduction of artefacts and the improvement of vertical accuracy by using additional ICESat data as a reference.

Three DEMs were used that originate from data of the TanDEM-X mission, which was launched as a public-private effort between the DLR and Airbus Defence and Space. From 2010 to 2015, the Earth was measured by two satellites (TerraSAR-X and TanDEM-X) in a controlled orbit with X-band RADAR interferometry (InSAR) between the latitudes 90°N and 90°S (Rizzoli et al., 2017; Wessel, 2016). Due to its shorter wavelength, the X-band RADAR is more affected by vegetation heights as it has a lower penetration depth than SRTMs C-band RADAR (Schlund et al., 2019; Solberg et al., 2018). One evaluated DEM is the freely available 3 arc-seconds (≈ 90 m) TanDEM-X, which was reprocessed from the 0.4 arc-second TanDEM-X version and calibrated with ICESat GLA14 elevation data (Wessel et al., 2018). The other two assessed DEMs were the Copernicus DEMs with a spatial resolution of 30 m (GLO-30) and 90 m (GLO-90) that also mainly base on the elevation data obtained from the TanDEM-X mission and were obtained from Copernicus Planetary Data Access (PANDA) (Airbus Defence and Space, 2020a).

5.3.2 Ground truth data

5.3.2.1 DGM1

The DGM1 is made available by the Regional Government of Cologne (Bezirksregierung Köln, 2017). It is produced from 3D measurement data acquired with airborne laser scanning. With a point density of at least four points per square meter, it is a very high resolution DEM that includes after filtering only the Earth's surface without vegetation and buildings (Arbeitsgemeinschaft der Vermessungsverwaltungen der Länder der Bundesrepublik Deutschland, 2017). The DGM1 is provided as a regular point grid with a point distance of 1 m. The data is updated frequently about every five years. For this contribution, a produced version of 2017 was used with acquisition dates in 2015 and 2016 for the landscape of the study area (Bezirksregierung Köln, 2017). The proposed vertical accuracy of the DGM1 is stated with 15 cm in flat to medium elevated landscapes and up to 30 cm in steep terrain, the horizontal accuracy can be expected with about 10 cm (Arbeitsgemeinschaft der Vermessungsverwaltungen der Länder der Bundesrepublik Deutschland, 2017). To compare the elevation of the DGM1 with the other DEM datasets, the provided point cloud was converted to a mean elevation raster dataset with a spatial resolution of 1 m. The accuracy of the reference raster was tested against the set of elevation control points introduced in the following section. It achieved

an accuracy of 0.97 m (RMSE) and 0.46 m (NMAD) for the area of this study and fulfils the requirement of a reference dataset to be at least three times more accurate than the evaluated DEMs (Höhle and Höhle, 2009; Maune, 2007).

5.3.2.2 Elevation control points

Highly precise elevation control points are used for several administrative surveying tasks as well as the determination of ground movement caused by mining or tectonic origin. For the area of this study, the ECPs are provided by the Regional Government of Cologne (Bezirksregierung Köln, 2020). They are determined by precision levelling in a highly accurate manner with a relative vertical accuracy of 1.5 mm. All points are frequently updated every two to six years, depending on the degree of ground motion. In this study, the heights of 4715 ECPs were compared with the elevations of all investigated digital elevation models. The location and distribution of the control points are depicted in Figure 5-3.

5.3.3 Preprocessing

To evaluate the elevation differences of all DEMs, it is necessary to convert them to the same horizontal and vertical datum. The WGS84 (EPSG: 4326) was used for all datasets as the horizontal datum. Thus, the EU-DEM, the DGM1 and the ECPs were transformed in ArcGIS Pro 2.5 from ETRS89 (EPSG: 25832) to WGS84 coordinates. All other datasets were already supplied in the WGS84 format. As most DEMs of this study originally have different vertical reference systems, they also had to be projected to the same vertical datum. For this study, the WGS84 ellipsoid was chosen as the vertical datum and all DEMs were converted to this datum in a first step.

The utilized ASTER GDEM, ALOS DEM and NASADEM were originally referenced to the Earth Gravitational Model 1996 (EGM96) (EPSG: 5773). To convert them to the WGS84 ellipsoid, a calculated raster of the undulation between EGM96 geoid and WGS84 ellipsoid for the entire area was calculated with the software MSP GEOTRANS v.3.8. A net of regularly distributed points was created and the undulation for these points was calculated by the software. Subsequently, the undulation points were interpolated with a Kriging algorithm to generate an undulation raster for the whole area. The elevations of the produced undulation raster were finally added to the three DEMs. The same procedure was conducted for both Copernicus DEMs that were originally referenced to the Earth Gravitational Model 2008 (EGM2008) (EPSG: 3855) vertical datum. The undulation between EGM2008 and WGS84 ellipsoid was also calculated with MSP GEOTRANS v.3.8 and finally added to the heights of the Copernicus DEM. The EU-DEM is referenced to the European vertical reference system EVRF2000 (EPSG: 5730) with EGG08 Geoid (EPSG: 4258). Both ground truth datasets are referenced to the DHHN2016 (EPSG: 7837), which is almost identical to the EVRF2000 with elevation differences of about 1 cm for the area of this study (Ihde et al., 2002). All three datasets were transformed to ellipsoidal heights by calculating the height differences between the reference systems with an online calculator tool (http://gibs.bkg.bund.de/geoid/gscomp.php?p=g) for a set of equally distributed points over the whole area. These points were subsequently interpolated to a raster and the elevation differences were added to the three datasets. The TanDEM-X DEM and the SRTM DEM were originally referenced with WGS84 ellipsoid and no projection was needed for these datasets.

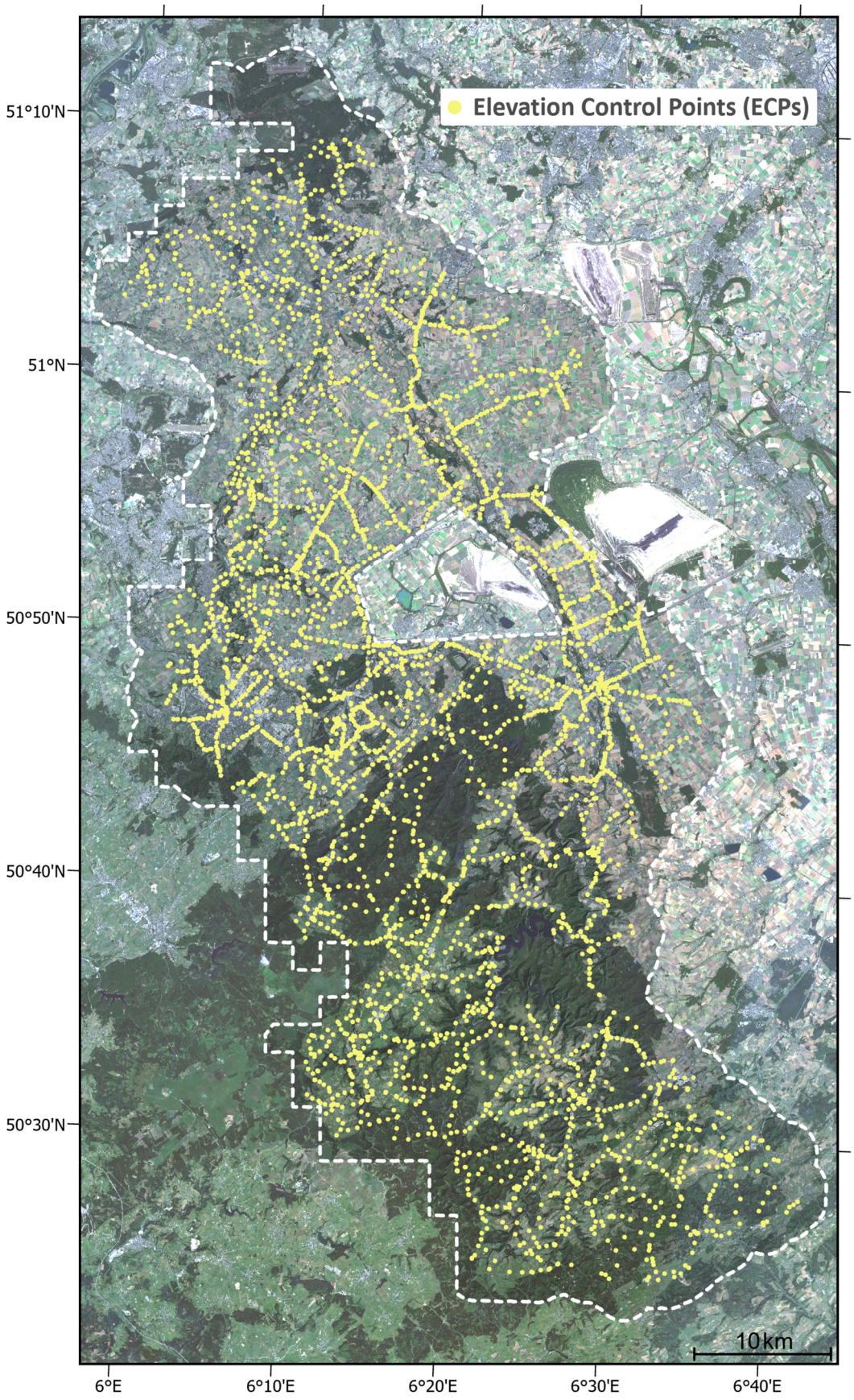

Figure 5-3: Spatial distribution of elevation control points (ECPs) in the Rur catchment. The background image contains a cloud-free mosaic of Sentinel-2 images from 2017 to 2019 derived from Google Earth Engine.

5.3.4 Accuracy assessment

The accuracy of each DEM was assessed by calculating the deviation of height differences against both reference datasets. For this purpose, the RMSE from the height differences between reference datasets and all DEMs was calculated with the following equation:

$$RMSE = \sqrt{\frac{\left(\sum_{i=1}^{n}(\Delta h_i)^2\right)}{n}} \tag{5-2}$$

where

Δh_i= elevation difference between assessed DEM and reference DEM.
n = number of pixels.

Furthermore, the NMAD was calculated, which is a more robust measure against outliers and has a higher tolerance against not normally distributed error values as it refers to the calculated median of the height differences (Höhle and Höhle, 2009). Thus, a not normal distribution generally leads to larger RMSE values compared to NMAD. It will be calculated with equation:

$$NMAD = 1.4826 \times median(|\Delta h_i - m_{\Delta h}|) \tag{5-3}$$

where

Δh_i= elevation difference between assessed DEM and reference DEM.
$m_{\Delta h}$ = median of all elevation differences.

The achieved accuracies are only completely interpretable if they can be related to the prevalent relief and land cover of the study area. Thus, the error values were evaluated against three datasets that represent the landscape and relief features of the study area. First, the slope was calculated in ArcGIS Pro from the DGM1 and classified into five classes of different slope angles from ‘flat’ (<5°), ‘gentle’ (5° – 15°), ‘moderate’ (15° – 25°), ‘steep’ (25° – 35°) to ‘extreme’ (>35°). Second, a geomorphometric map (GMK10) was utilized that consists of a combination of three different categories of DEM extracted morphometric relief parameters (Scilands GmbH, 2010). Category one contains bottom areas, summit areas and slopes. The second category includes convergent and divergent areas and category three divides flat and sloped areas from each other. For this contribution, the provided landform classes were reclassified into the four classes ‘Depression/Valley’, ‘Flat’, ‘Hillslope’ and ‘Ridge’. The GMK10 is originally provided with a spatial resolution of 10 m. Third, a land use classification of the study area from the year 2015 was used that was originally produced by Waldhoff and Lussem (2016). The original dataset contains 55 classes of different land use types, which were reclassified into the eight classes ‘Bare Ground/Grassland’, ‘Coniferous Trees’, ‘Deciduous Trees’, ‘Agriculture’, ‘Residential Area’, ‘Public/Commercial Area’, ‘Street/Railway’ and ‘Water’. Several remaining classes of small coverage that do not fit to these previously mentioned classes were classified into a class ‘Other’ which has not been considered for evaluation. The dataset was provided with a spatial resolution of 15 m. An evaluation of different crop types of this land use classification has shown an overall accuracy of about 97 % for these classes (Waldhoff et al., 2017). The spatial distribution of all extracted terrain and land cover features in the study area is depicted in Figure 5-4. The distribution of their classes in percent for both reference datasets in the entire area and the two subareas is presented in Table 5-2.

Table 5-2: Percentage distribution of the DGM1 and ECPs on classified features slope, land use classification and geomorphometric map (GMK10) for the entire study area and the northern and southern study area separately.

Class	Entire area [%]		Northern area [%]		Southern area [%]	
	DGM1	ECPs	DGM1	ECPs	DGM1	ECPs
Slope						
Flat	73.0	82.9	95.1	95.9	52.9	68.5
Gentle	19.9	12.9	4.3	4.0	34.0	22.6
Moderate	5.2	3.1	0.5	0.1	9.5	6.5
Steep	1.8	1.0	0.1	0.0	3.2	2.2
Extreme	0.1	0.1	0.0	0.0	0.3	0.1
Land Use Classification						
Agriculture	26.1	3.9	48.2	6.4	6.0	0.5
Bare Ground/Grassland	17.5	5.0	8.7	1.9	25.5	8.6
Coniferous Trees	11.9	8.2	6.5	6.8	16.9	9.9
Deciduous Trees	17.5	4.6	6.9	1.0	27.2	8.6
Water	0.9	0.3	0.6	0.1	1.1	0.4
Streets/Railways	5.9	39.7	7.9	45.8	4.2	33.3
Urban/Commercial Area	1.6	4.2	2.2	4.9	1.1	3.4
Residential Area	3.5	17.1	5.2	21.5	2.0	12.2
Other	14.9	17.0	13.8	11.6	16.0	23.1
GMK10						
Depression/Valley	17.8	26.3	31.2	37.9	5.5	13.5
Flat	32.8	33.1	59.2	52.5	8.7	11.6
Hillslope	26.0	17.7	6.3	6.4	44.0	30.3
Ridge	23.4	22.8	3.3	3.2	41.7	44.6

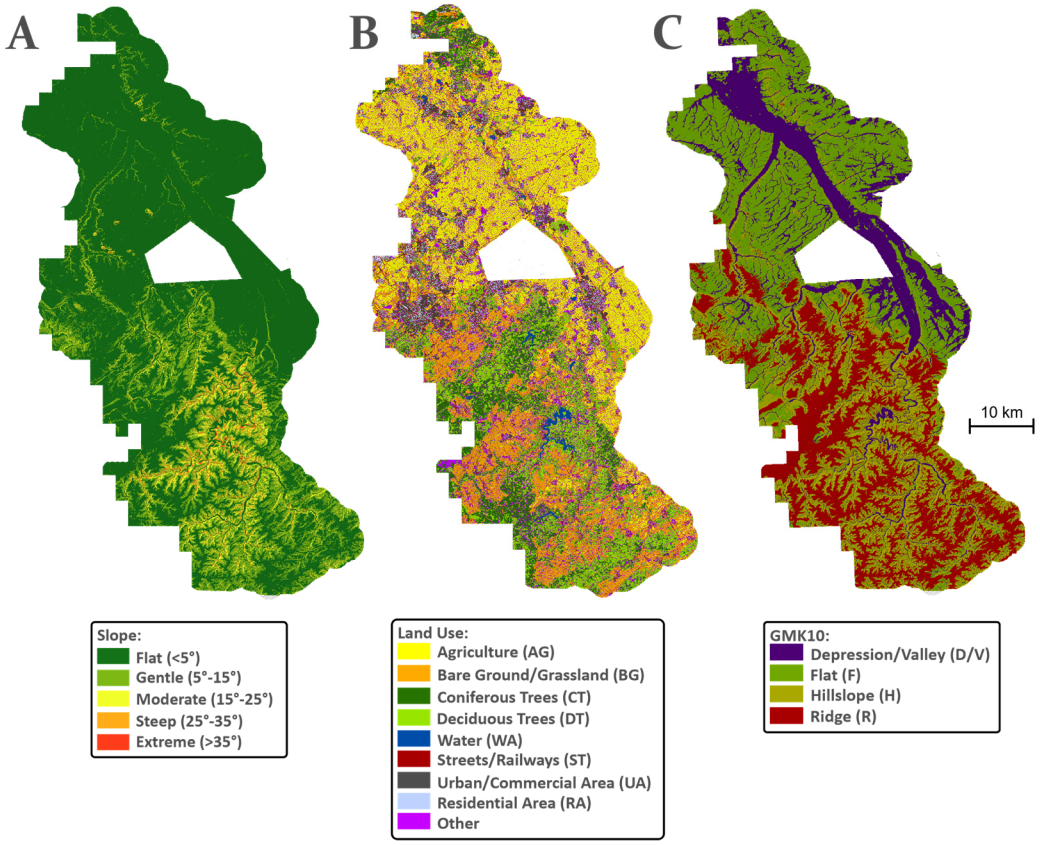

Figure 5-4: Spatial distribution of the extracted terrain and land use features (A) slope, (B) land use classification from 2015 and (C) the geomorphometric map (GMK10).

5.4 Results

5.4.1 Overall vertical accuracy

The achieved error measures conducted for the entire Rur catchment are shown in Figure 5-5. Depicted are the achieved RMSE and NMAD values for all DEMs in comparison to the DGM1 and the ECPs. For all DEMs, the derived error values are slightly higher with the DGM1 than with the ECPs. The results show the highest overall accuracies for the 30 m SRTM DEM with a RMSE of 5.6 m (DGM1) and 4.5 m (ECPs) as well as a NMAD of 3.3 m (DGM1) and 2.5 m (ECPs). In contrast, the lowest accuracies of all 30 m DEMs are detectable for the ASTER GDEM with RMSE values of 6.6 m (DGM1) and 6.9 m (ECPs). The NMAD is also considerably high for this DEM with 8.0 m compared to the DGM1 dataset and 5.6 m in comparison to the ECPs.

A comparison of all 90 m DEMs also shows the highest overall accuracies for the SRTM with a RMSE of 6.0 m (DGM1) and 5.5 m (ECPs) as well as a NMAD of 3.2 m (DGM1) and 2.7 m (ECPs). The 90 m TanDEM-X and Copernicus DEM achieved similar NMAD values, but considerably higher RMSEs that are about 2.5 m higher than those of the 90 m SRTM. For the 30 m Copernicus DEM, a relatively high difference is also observable in the results between the achieved RMSE and NMAD values. It achieved the overall highest NMAD measures (2.3 m with DGM1 and 2.4 m with ECPs), the calculated RMSEs are relatively low (7.1 m with DGM1 and 4.9 m with ECPs).

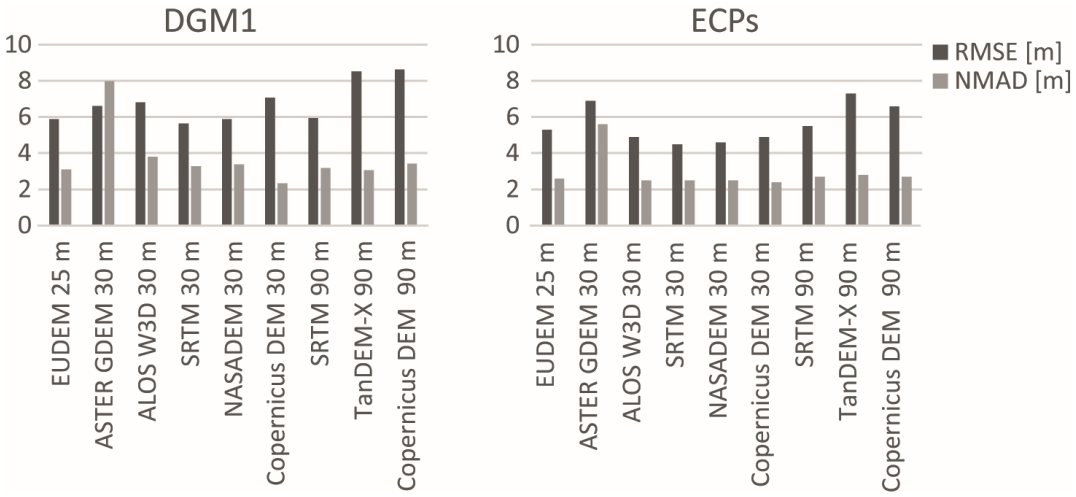

Figure 5-5: Calculated error values for the entire study area for each digital elevation model in comparison with both reference datasets, the DGM1 and the elevation control points (ECPs).

A comparison of the accuracies in both different areas of the Rur catchment reveals generally higher error values for the hillier landscapes in the south compared to the flatter north. All calculated error measures for both areas are presented in Figure 5-6. The error values are on a similar level for most DEMs in the northern part. Compared to the DGM1, the error of most evaluated DEMs ranges from 3.1 m to 4.2 m RMSE and 1.2 m to 1.9 m NMAD, whereas the EU-DEM achieved the overall highest accuracies. The ALOS W3D achieved slightly lower accuracies of 4.6 m (RMSE) and 2.3 m (NMAD) and the overall lowest accuracies were achieved by the ASTER GDEM with a RMSE of 6.1 m and NMAD of 5.0 m. The results with the ECPs show similar tendencies for this region. All DEMs achieved relatively similar error values that range from 2.4 m to 3.2 m (RMSE) and 1.8 m to 2.0 m (NMAD), except the ASTER GDEM. The ASTER GDEM achieved considerably higher error values of 5.2 m (RMSE) and 4.8 m (NMAD).

In the southern part of the Rur Catchment, most DEMs achieved a 3 m to 4 m lower accuracy compared to the north. The largest differences are detectable for the TanDEM-X DEM with about three times higher error values in this area with a RMSE of 12.0 m and a NMAD of 8.5 m in comparison to the DGM1. All other DEMs have considerably lower errors here that range from 6.5 m (RMSE) for the 30 m SRTM DEM to 9.4 m for the Copernicus 90 m DEM. The NMAD values of the other DEMs range from 5.2 m for the 30 m Copernicus DEM to 8.1 m for the ASTER GDEM. Likewise, the lowest RMSE was achieved for the 30 m SRTM with 5.7 m and the highest with 9.5 m for TanDEM-X in comparison with the ECPs. The lowest NMAD values could also be observed for the 30 m Copernicus DEM (3.0 m) and the highest for ASTER GDEM (6.5 m).

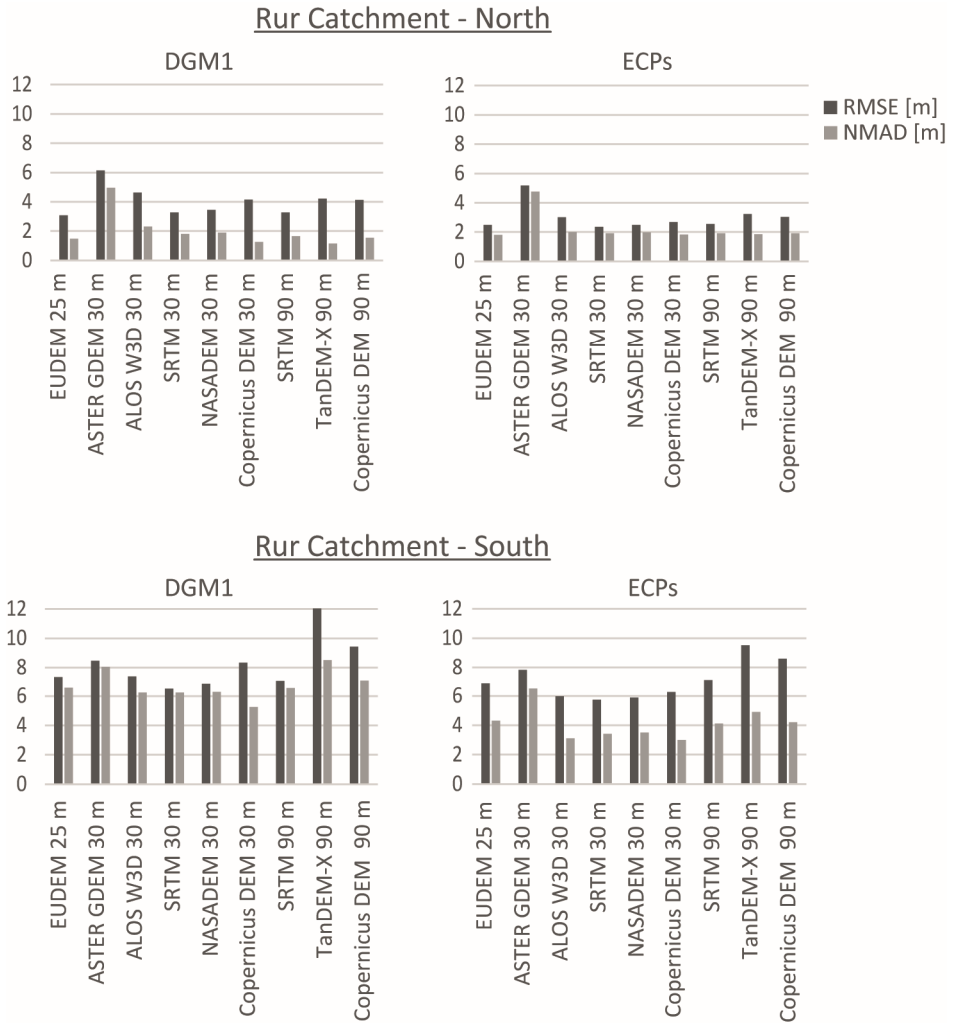

Figure 5-6: Calculated error values from the northern and southern part of the study area for each digital elevation model in comparison to both reference datasets, the DGM1 and the elevation control points (ECPs).

5.4.2 Land-use dependent accuracies

The derived errors of all evaluated DEMs according to various land use and land cover types are depicted in Figure 5-7. The results show that the highest error values are observable for forest landscapes, whereby the different tree types produced mostly very similar results. Only for the 90 m TanDEM-X and Copernicus DEM a higher RMSE was observable for class 'Deciduous Trees' compared to 'Coniferous Trees'. The highest accuracies in both classes are detectable for both SRTM DEMs with

error values of 6.0 m ('Coniferous Trees') and 5.8 m ('Deciduous Trees') RMSE for the 30 m elevation model and 5.9 m ('Coniferous Trees') and 6.1 ('Deciduous Trees') for the 90 m DEM. Likewise, these DEMs also achieved the lowest NMAD values with 6.4 m ('Coniferous Trees') and 6.0 m ('Deciduous Trees') for the 30 m SRTM and 6.1 m ('Coniferous Trees') and 5.8 m ('Deciduous Trees') for the 90 m version. In contrast, the 90 m TanDEM-X and Copernicus DEM achieved the overall lowest accuracies in forest regions. The TanDEM-X achieved errors of 10.4 m (RMSE) and 10.6 m (NMAD) for class 'Coniferous Trees' and 12.3 m (RMSE) and 10.2 m (NMAD) for class 'Deciduous Trees'. For the 90 m Copernicus DEM, error measures of 10.4 m (RMSE) and 10.5 m (NMAD) were calculated for class 'Coniferous Trees' and 12.5 m (RMSE) and 10.4 m (NMAD) for 'Deciduous Trees'.

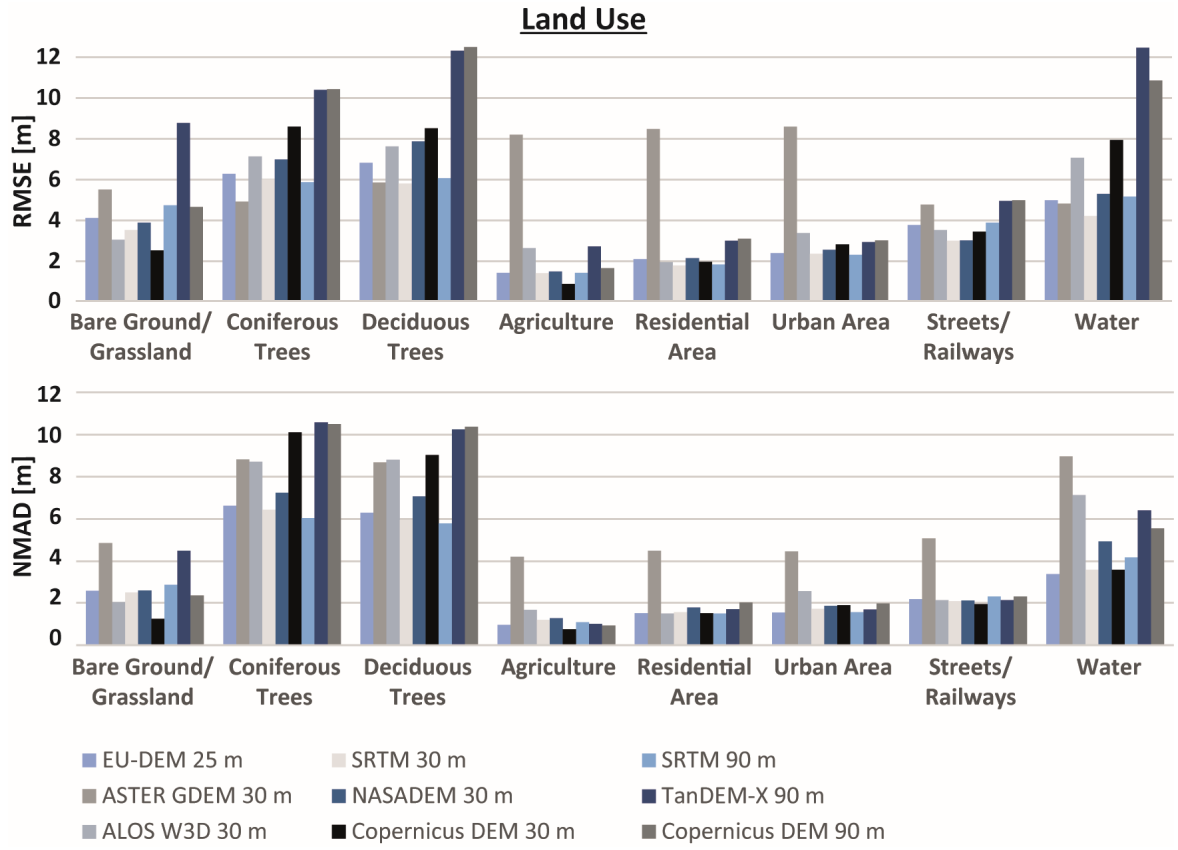

Figure 5-7: Calculated RMSE and NMAD of elevation differences according to different land use types.

The lowest error values were calculated for the land use classes 'Agriculture' and the urban classes 'Residential Area' and 'Public/Commercial Area'. For these three classes, all DEMs, except the ASTER GDEM, performed on a similar level and achieved average errors of less than 3 m. Only the ASTER GDEM showed considerably higher average RMSE and NMAD values for these classes between 4 m and 5 m. A considerable difference between both types of urban land cover classes could not be detected here. Similar effects are observable for the class 'Streets/Railways', where also the accuracy of the ASTER GDEM is considerably lower than for the other DEMs. The calculated RMSE results of most DEMs are slightly worse in this class compared to the three previously mentioned classes. A medium accuracy could be detected for the classes 'Bare Ground/ Grassland' and 'Water'. The lowest error values for class 'Bare Ground/Grassland' could be detected for the 30 m Copernicus DEM with 2.5 m (RMSE) and 1.2 m (NMAD). In contrast, the by far lowest RMSE for this class was calculated for the TanDEM-X with 8.8 m and NMAD for ASTER GDEM with 4.9 m. For water areas, the lowest errors were achieved by the NASADEM (4.2 m RMSE) and EU-DEM (3.4 m NMAD). In contrast, the RMSEs of

the 90 m TanDEM-X (12.4 m RMSE) and Copernicus DEM (10.8 m RMSE) are considerably higher compared to the other DEMs. The highest NMAD values were achieved by ASTER GDEM (9.0 m) and ALOS W3D (7.1 m).

5.4.3 Slope dependent accuracies

The derived error curves from different slope angles for all DEMs are presented in Figure 5-8. In flat terrain, most DEMs performed on a similar level and achieved RMSEs from 4 m to 6 m and NMAD values from 2 m to 3 m. Only the ASTER GDEM achieved a significantly higher NMAD with 5.5 m compared to the other elevation models. With increasing slope angles, the accuracy is decreasing significantly for all evaluated DEMs. However, the decrease in accuracy is different. The lowest error values on extremely steep slopes with slope angles of more than 35° were achieved for the 30 m SRTM with 8.9 m (RMSE) and 8.8 m (NMAD), followed by the ALOS DEM with only slightly higher errors. The results show the by far strongest increase of error for the TanDEM-X DEM. The error rises from 6.7 m (RMSE) and 2.6 m (NMAD) in flat landscapes up to 36.6 m (RMSE) and 35.0 m (NMAD) in extremely steep terrain. All other DEMs achieved an error of 20 m or less in extremely steep landscapes. The increase of error varies significantly for different DEMs. In particular, for the 30 m SRTM, ALOS DEM, Copernicus DEM and the 25 m EU-DEM a significant increase is only detectable from flat slopes to gentle slopes. For steeper slopes, the decrease in accuracy is only minor for these DEMs. In contrast, for the other DEMs a mostly linear decrease in accuracy is observable from flat to extremely steep slopes.

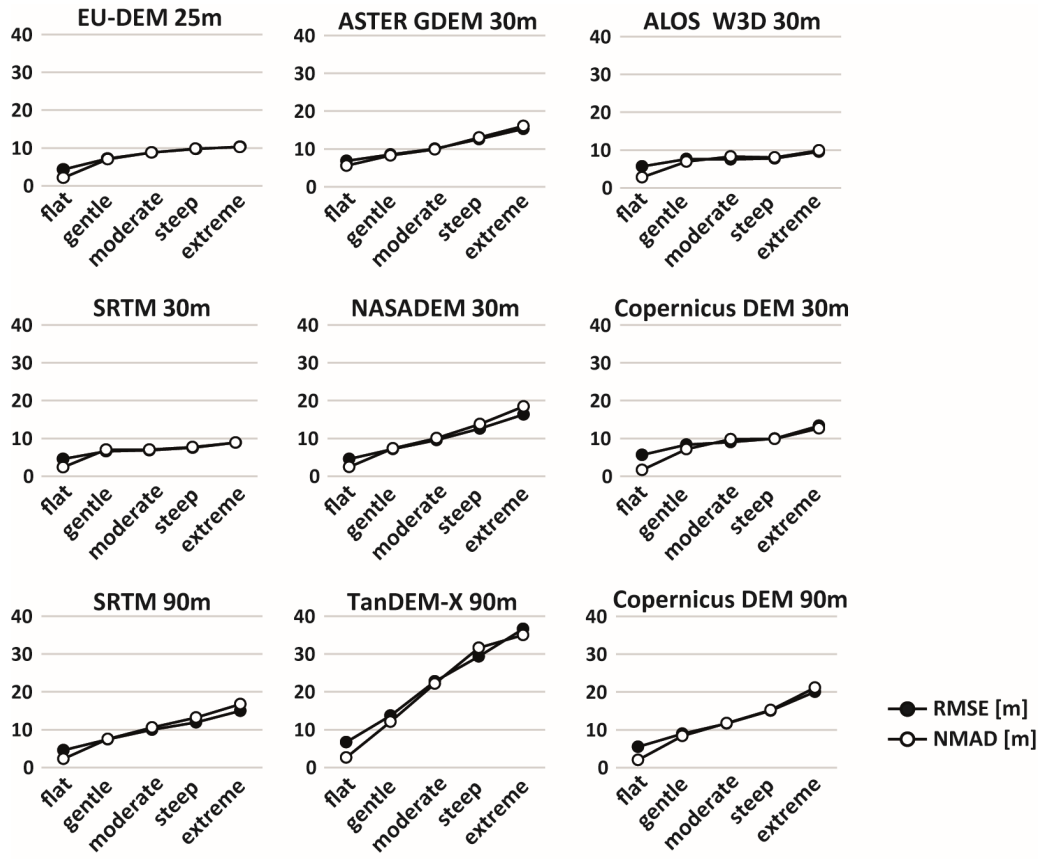

Figure 5-8: Calculated RMSE and NMAD of elevation differences according to slope. Derived slope classes are 'flat' (<5°), 'gentle' (5° – 15°), 'moderate' (15° – 25°), 'steep' (25° – 35°) and 'extreme' (>35°).

5.4.4 Landform dependent accuracies

The achieved errors of all DEMs in comparison to four different landforms are depicted in Figure 5-9. The results show that the highest accuracies were achieved in flat landscapes, followed by 'Depression/Valley' landforms. For both landforms, it is observable for all DEMs, except the ASTER GDEM, that the achieved NMAD values are significantly lower in comparison to the RMSEs. Most DEMs achieved a RMSE of 3 m to 5 m and a NMAD that ranges from 1 m to 2 m for landform class 'Flat'. For landform class 'Depression/ Valley' they achieved a RMSE from 4 m to 6 m and a NMAD from 1 m to 3 m. Only ASTER GDEM performed worse with errors of more than 6 m (RMSE) and 5 m (NMAD) for both landform classes. The other two investigated landforms, hillslopes and ridges, do not show such a difference between RMSE and NMAD. The overall lowest accuracies are observable for landform class 'Hillslope' with average errors of about 7 m for most DEMs. Only the ASTER GDEM and both Copernicus DEMs achieved higher errors of about 9 m and the TanDEM-X performed worst here with error values of 12.2 m (RMSE) and 10.6 m (NMAD). For landform class 'Ridge', medium average error measures of 5 m to 7 m RMSE and 4 m to 6 m NMAD are observable for most DEMs with a slightly worse performance of ASTER GDEM and TanDEM-X.

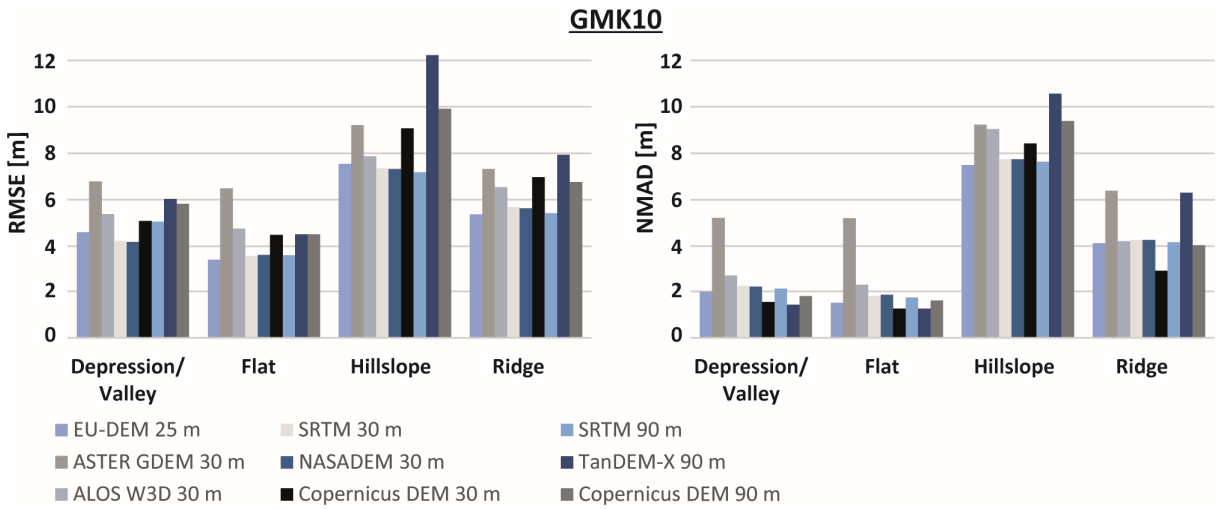

Figure 5-9: Calculated RMSE and NMAD of elevation differences according to the different classes of the geomorphometric map (GMK10).

5.4.5 Spatial distribution of elevation differences

The spatial distribution of elevation differences between the DGM1 and all evaluated DEMs is presented in Figure 5-10. It shows that the differences in elevation are mostly low in the northern part of the catchment for all DEMs. Only in the northernmost part, some larger differences are observable for areas that are covered by trees. Overall, the differences reveal that the ASTER GDEM consists of slightly lower heights compared to the reference DEM. For the other DEMs, this effect could not be detected. A considerably higher elevation difference is observable for many areas in the southern part of the Rur catchment. Thus, notably height deviations are mainly observable in parts with incised valleys and in the undulated transition area between the northern part and the southern part of the catchment, which is also mainly covered by forests. In particular, all 90 m DEMs reveal relatively high elevation differences in these areas. The observable height differences of the ALOS W3D and the 30 m Copernicus DEM are also slightly higher here than for the other DEMs.

Figure 5-10: Spatial distribution of elevation differences of all DEMs in comparison with the DGM1.

5.5 Discussion

The results clearly show for all DEMs that their accuracy is mainly influenced by different landscapes and land cover types. It is observable that the highest elevation differences exist for areas that are covered by deciduous or coniferous trees and have high slope angles. Thus, the northern predominantly flat area with mostly agricultural and some residential areas is represented in almost all DEMs far more accurate than the undulated southern area with extensive forest and grassland areas. Overall, the accuracy of most DEMs was considerably higher in urban areas than in areas with dense tree vegetation, whereas between different tree types and urban classes only minor differences could be observed. The lower accuracy of areas with trees is probably increased due to the fact that these areas are mainly situated in undulated areas with steeper relief, while urban areas are mainly located in the flatter northern part of the study area.

Both reference datasets produced predominantly comparable results for all DEMs with only slightly lower accuracies in comparison to the DGM1 than with the ECPs. As the ECPs are mostly situated near roads and pathways, they overall cover gentler relief than the mean relief of the DGM1, which causes the slightly superior accuracy of the tested DEMs in comparison with this dataset. The DGM1 covers the entire study area and the results in comparison with this reference dataset are probably more representative as it reflects the full terrain variability.

In comparison to existing landforms, also predominantly flat geomorphometric features such as mostly flat plains, depressions and the bottom parts of valleys achieved significantly higher accuracies than the landforms hillslope and ridge, which overall contain much more steepness. However, as the landform class ‘Depression/Valley’ contains two different types of valleys, with the broader river valleys in the north and narrower valleys in the south, the accuracy of this class might be overestimated. Due to the fact that the broader river valleys cover the majority area of this class, the expectable accuracy might be lower for the narrower valleys in the southern part.

The evaluation showed the best overall performances for the DEMs that originate from SRTM data. Thus, the 30 m SRTM achieved the highest accuracies in this study area. Previously conducted studies of this DEM showed an average error of 3 – 4 m in flat landscapes, which can increase up to 7 – 10 m in undulated terrain (Kramm and Hoffmeister, 2019; Mukherjee et al., 2013; Rexer and Hirt, 2014; Suwandana et al., 2012; Zhao et al., 2011). The results from this study indicate a slightly higher performance with an about 1 – 2 m higher accuracy of the DEM in steeper relief than it was observed in previous studies. However, they mostly fit well with other findings.

The 90 m SRTM also showed predominantly high accuracies in most situations, namely 2 – 4 m in flat terrain and about 7 – 15 m in areas with steeper relief and high tree density or water. This is also mostly in accordance with other studies that showed an average error of 3 – 6 m in flat terrain, which can rise up to 20 m in steep landscapes (Becek et al., 2016; Hu et al., 2017; Kramm and Hoffmeister, 2019; Liu et al., 2019; Liu et al., 2020; Nagaveni et al., 2019; Yahaya and El Azzab, 2019). Particularly in flat relief, almost no notabe differences between the 30 m SRTM and the 90 m DEM could be observed. Only in steeper terrain its accuracy dropped significantly and showed errors that were up to 8 m higher compared to the 30 m SRTM. However, even in steeper relief, the 90 m SRTM revealed a higher overall accuracy in this study than the other DEMs with a similar spatial resolution.

The NASADEM, as a successor of the SRTM DEM, did show mostly a similar performance as its predecessor. Results from Uuemaa et al. (2020) showed a slightly better performance of this DEM in comparison to the older SRTM version. They achieved a RMSE of 6.39 m for the NASADEM in a relatively flat rural Estonian landscape that is comparable to the Rur catchment in its land cover and relief. Thus, their results are in accordance with the findings of this study with an only slightly worse accuracy in the probably steeper southern part of the study area. In contrast, the observed results of the northern part are with 3.5 m RMSE higher than the results of Uuemaa et al. (2020), which is very likely caused by an overall flatter landscape. Nevertheless, a significant improvement in accuracy over the SRTM is not observable for the area of the Rur catchment. The NASADEM even showed slightly worse accuracies in very steep areas and forest landscapes compared to the original SRTM.

The EU-DEM, as a hybrid elevation model generated predominantly from SRTM and ASTER data sources, also reveals a good overall performance, which is mostly similar to the previously mentioned DEMs. Its slightly higher spatial resolution of 25 m seems not to have a recognizable impact on accuracy in comparison to others with a resolution of 30 m. Results of Mouratidis and Ampatzidis (2019) showed a slightly higher accuracy of the EU-DEM in vegetated areas compared to the 30 m ASTER and SRTM. They achieved an absolute elevation RMSE of 4.3 m for the EU-DEM, which is higher than the observed errors in the northern part of this study, but significantly lower than in the southern part. Overall, the EU-DEM produced ambivalent results. Whereas it achieved the overall highest accuracies in the northern part of the study area, it was about 1 m less accurate than the 30 m SRTM and NASADEM in the more undulated southern parts of the Rur catchment.

The lowest overall performance could be observed for the ASTER GDEM. Particularly in flat areas, this DEM revealed the by far highest inaccuracies of all DEMs. Only in very steep relief and forests the TanDEM-X and Copernicus DEMs produced higher errors. In most parts of the study area, the ASTER GDEM was the least accurate DEM, which was even more inaccurate than DEMs with a spatial resolution of 90 m. Overall, the results of this study confirm numerous other studies that showed an inferior performance of the ASTER GDEM compared to other freely available digital elevation models (Alganci et al., 2018; Becek et al., 2016; Graf et al., 2018; Hu et al., 2017; Kumar et al., 2020; Liu et al., 2019; Mouratidis and Ampatzidis, 2019; Pandey et al., 2017; Vassilaki and Stamos, 2020; Zhang et al., 2019). These studies already indicated an average RMSE for the ASTER GDEM of about 3 – 4 m in flat terrain and 7 – 8 m with up to 16 m RMSE in steeper relief. Thus, the results of this study in the southern part of the Rur catchment fit well with the undulated terrain results and showed a slightly lower accuracy in flat landscapes of about 5 – 6 m.

Ambivalent results are also observable for the ALOS DEM. Several existing studies reported a high accuracy of this DEM that is superior to the SRTM DEM in many cases (Alganci et al., 2018; Kumar et al., 2020; Liu et al., 2019; Yahaya and El Azzab, 2019). They showed an average RMSE of 2 – 3 m in flat landscapes and 6 – 7 m in steeper relief for the ALOS W3D, which fits mostly well with the findings from this study. In most parts of the Rur catchment, the ALOS DEMs showed similar accuracies compared to the 30 m SRTM. However, particularly in areas with dense vegetation and water the ALOS DEM produced about 2 m higher errors than the SRTM DEMs.

Several recent studies indicated a good performance of the 90 m TanDEM-X DEM, which seems to be superior to the 90 m SRTM DEM (Altunel, 2019; Keys and Baade, 2019; Kramm and Hoffmeister, 2019; Kumar et al., 2020). These studies indicate an average error of 1 – 4 m in flat terrain and about

10 – 12 m in undulated terrain, which can rise to more than 20 m in very steep relief. In this study, the accuracies in flat landscapes were similar to other studies. However, particularly in densely vegetated and undulated to steep terrain, the accuracy of this DEM was overall lower here than it was observed in other studies. In comparison to the 90 m SRTM, the achieved accuracy of the TanDEM-X was similar in the mostly flat northern part of the study area, but revealed considerably higher inaccuracies in the southern parts of the catchment. Thus, it can be concluded that the accuracy of TanDEM-X is much more affected by undulated to steep terrain with dense vegetation and reveals a by far higher decrease than the SRTM DEMs. The evaluation with land use classes also shows that this DEM performs disproportionately worse in areas with trees and water. As these densely vegetated areas are mostly situated in undulated relief with predominantly hillslope and ridge landforms, this DEM achieved the highest error values of all tested DEMs in the southern part of the study area. One reason could be that the available version of the TanDEM-X DEM is mostly uncorrected yet. In areas with a high density of trees and buildings, this leads to potentially higher errors compared to DEMs from SRTM or ALOS sources as these DEMs already exist in a higher product version with numerous improvements and fixes of erroneous heights. This is also indicated by the larger differences between the achieved NMAD and RMSE values for this DEM compared to others. It is likely that the TanDEM-X has basically a very high accuracy, but a disproportionately high number of existing outliers is still present for the investigated area of the Rur catchment. However, an increased loss of accuracy in steep terrain could also be observed in regions with less vegetation (Kramm and Hoffmeister, 2019; Podgorski et al., 2019). This leads to the conclusion that the accuracy of the 90 m TanDEM-X in its current form seems to be generally lower in undulated relief compared to the 90 m SRTM, but the presence of vegetation might increase this effect. In particular, as the penetration depth into vegetation for X-band RADAR is less deep than for C-band, this leads to higher elevations in forested areas (Schlund et al., 2019; Solberg et al., 2018; Weydahl et al., 2007).

As the newly released Copernicus DEM is also mainly generated from TanDEM-X WorldDEM™ data, it shows a mostly similar behaviour in its accuracies. In particular, the 90 m DEM has also considerably high errors over areas with trees and water and reveals similar weaknesses to the TanDEM-X. Nevertheless, the results show an overall higher performance of the Copernicus DEM, particularly in steep terrain, where it is up to two times more accurate than the 90 m TanDEM-X. This indicates that several improvements, which had been conducted to the Copernicus dataset, could increase the accuracy in comparison to the original WorldDEM™ product. However, its overall performance mostly did not reach the accuracy of the SRTM product here. The accuracy of the 30 m Copernicus DEM is considerably high in bare ground and predominantly flat agricultural areas and reveals potentially the highest accuracy in these regions of all DEMs. Nevertheless, the DEMs also contain several outliers, which is indicated by the considerably higher RMSEs compared to NMAD values.

It is observable in the results that all DEMs generated partly or completely from data of the Shuttle Radar Topography Mission in February 2000 show a higher accuracy in landscapes with dense vegetation compared to the DEMs from other resources. One reason could be a higher suitability of the C-band RADAR system compared to the X-band system that was used for data acquisition of the TanDEM-X mission as it has a higher penetration depth in densely vegetated areas. Furthermore, this effect is probably also influenced by the acquisition date of the mission in the mid-European winter season, when trees are mostly free of foliage and less dense. Thus, a scan of the ground heights is better possible than in other seasons where the ground is not visible due to dense vegetation.

5.6 Conclusion

This contribution evaluated the performance of nine freely available DEMs in the heterogeneous Rur catchment in order to establish expectable error values in relation to relief and land cover. Based on the results of this study, general accuracy values for these medium resolution DEMs in different types of landscape and relief can be stated. These expectable accuracies can be considered in further studies where these DEMs are utilized in comparable mid-latitude landscapes. In flat landscapes with a mean slope of less than 2°, an error of about 2 – 4 m can be expected. The accuracy of all DEMs dropped significantly in undulated terrain and is about two to three times lower in the southern part of the catchment with an average slope of about 5° compared to the northern part. Thus, according to the results of this study, an expectable average mean error of 6–8 m can be stated for a medium elevated terrain. The largest differences in the accuracy between the individual DEMs occur in areas that have slope angles steeper than 15°. An average error of 8 – 12 m must be expected for the DEMs in steep terrain. Likewise, for areas that are mainly covered by trees a mean error of 6 – 10 m is expectable. However, the observed differences between different tree types are only minor and do not have a significant impact on the accuracy. The same applies to varying types of urban land cover that also showed only minor differences in the achieved accuracy values for the evaluated DEMs. For these areas, an average error of 2 – 3 m can be stated.

Furthermore, we showed the strengths and weaknesses of each individual DEM in different situations. In flat terrain, almost all DEMs performed on a very similar level with only minor differences. Only the Aster DEM showed higher errors even in flat areas and is probably the worst choice for an accurate representation of the surface. Interestingly, the results mostly revealed a higher overall performance for the datasets that were created from data of the Shuttle Radar Topography Mission. Nevertheless, a superior performance of the NASADEM compared to the original SRTM DEM was not observable and both performed on a very similar level. The EU-DEM also showed a good performance, but slightly worse in undulated terrain than the original SRTM. The ALOS W3D DEM achieved a good overall performance, but however not superior to the SRTM derived DEM products.

Contrary to other findings, the DEMs from TanDEM-X WorldDEM™ data source could not achieve higher overall accuracies in this study area compared to the other DEMs. Particularly in steeper terrain and areas with dense land cover, this DEM reveals higher inaccuracies than the DEMs created with SRTM data. This is probably mainly caused by the portion of remaining outliers, which is higher than in other DEMs that have been corrected with several additional resources and where outliers mostly have been removed to date. Thus, although the basic accuracy of TanDEM-X is considerably high, additional work on this DEM is necessary for the region of this study to remove outliers. The achieved accuracy of the newly available Copernicus DEM is slightly superior to the original TanDEM-X. However, as this DEM is mainly based on the WorldDEM™ data, it also reveals a higher number of potential outliers than the other DEMs, in both the 30 m and 90 m version.

Acknowledgements

The authors gratefully acknowledge financial support by the CRC/TR32 ‘Patterns in Soil-Vegetation-Atmosphere Systems: Monitoring, Modelling, and Data Assimilation’ funded by the German Research Foundation (DFG).

Disclosure statement

The authors declare no conflict of interest.

Data availability statement

Data analysed in this study, which is openly available from third party resources according to corresponding licence conditions:

- ASTER GDEM V003 in Land Processes Distributed Active Archive Center (LP DAAC) at https://doi.org/10.5067/ASTER/ASTGTM.003.
- ALOS W3D from Earth Observation Research Center (EORC) Japan Aerospace Exploration Agency (JAXA) at https://www.eorc.jaxa.jp/ALOS/en/aw3d30/index.htm.
- SRTM V3 (30 m) in OpenTopography at https://doi.org/10.5069/G9445JDF.
- SRTM V4.1 (90 m) in CGIAR-CSI at http://srtm.csi.cgiar.org.
- TanDEM-X WorldDEM™ in DLR Earth Observation Center Geoservice at https://doi.org/10.15489/ju28hc7pui09.
- EU-DEM from Copernicus land services at https://land.copernicus.eu/imagery-in-situ/eu-dem/eu-dem-v1.1?tab=metadata.
- NASADEM in Land Processes Distributed Active Archive Center (LP DAAC) at https://doi.org/10.5067/MEaSUREs/NASADEM/NASADEM_HGT.001.
- Copernicus DEM in PANDA at https://panda.copernicus.eu.
- Digital Elevation Model (DGM1) of the Rur catchment in CRC/TR32 Database (TR32DB) at https://www.tr32db.uni-koeln.de/data.php?dataID=1690.
- Elevation Control Points in OpenGeodata.NRW at https://www.opengeodata.nrw.de/produkte/geobasis/rb/fd/hfp_pl_csv/.
- Enhanced land use classification of 2015 for the Rur catchment in CRC/TR32 Database (TR32DB) at https://doi.org/10.5880/TR32DB.19.

Data from third party sources with restricted access due to licence conditions:

- GMK10 Rur – Terrainfactors in CRC/TR32 Database (TR32DB) at https://www.tr32db.uni-koeln.de/data.php?dataID=196.

5.7 References

Abrams, M., Bailey, B., Tsu, H., Hato, M., 2010. The ASTER Global DEM. Photogrammetric Engineering and Remote Sensing, 76 (4), 344-348.

Abrams, M., Crippen, R., 2019. ASTER GDEM V3 (ASTER Global DEM).

Airbus Defence and Space, 2020a. Copernicus Digital Elevation Model - Product Handbook. Airbus Defense & Space. https://spacedata.copernicus.eu/documents/20126/0/GEO1988-CopernicusDEM-SPE-002_ProductHandbook_I1.00.pdf. 12.04.2021.

Airbus Defence and Space, 2020b. Copernicus Digital Elevation Model - Validation Report. Airbus Defense & Space. https://spacedata.copernicus.eu/documents/20126/0/GEO1988-CopernicusDEM-RP-001_ValidationReport_V1.0.pdf. 12.04.2021.

Alganci, U., Besol, B., Sertel, E., 2018. Accuracy Assessment of Different Digital Surface Models. ISPRS International Journal of Geo-Information, 7 (3), 114. doi: 10.3390/ijgi7030114.

Altunel, A.O., 2019. Evaluation of TanDEM-X 90 m Digital Elevation Model. International Journal of Remote Sensing, 40 (7), 2841-2854. doi: 10.1080/01431161.2019.1585593.

Arbeitsgemeinschaft der Vermessungsverwaltungen der Länder der Bundesrepublik Deutschland, 2017. Produkt- und Qualitätsstandard für Digitale Geländemodell - Version 3.0.

Baade, J., Schmullius, C., 2016. TanDEM-X IDEM precision and accuracy assessment based on a large assembly of differential GNSS measurements in Kruger National Park, South Africa. ISPRS Journal of Photogrammetry and Remote Sensing, 119, 496-508. doi: 10.1016/j.isprsjprs.2016.05.005.

Becek, K., Koppe, W., Kutoglu, S.H., 2016. Evaluation of Vertical Accuracy of the WorldDEM (TM) Using the Runway Method. Remote Sensing, 8 (11), 934. doi: 10.3390/rs8110934.

Berthier, E., Brun, F., 2019. Karakoram geodetic glacier mass balances between 2008 and 2016: persistence of the anomaly and influence of a large rock avalanche on Siachen Glacier. Journal of Glaciology, 65 (251), 494-507. doi: 10.1017/jog.2019.32.

Bezirksregierung Köln, 2017. Digital Elevation Model (DGM1) of the Rur Catchment, based on data from Bezirksregierung Köln [dataset]. CRC/TR32 Database (TR32DB). https://www.tr32db.uni-koeln.de/data.php?dataID=1690. 12.04.2021.

Bezirksregierung Köln, 2020. Festpunktdaten NW im amtlichen Festpunktinformationssystem (AFIS) [dataset]. Geobasis NRW. German. https://www.opengeodata.nrw.de/produkte/geobasis/rb/fd/hfp_pl_csv. 12.04.2021.

Bishop, M.P., James, L.A., Shroder, J.F., Walsh, S.J., 2012. Geospatial technologies and digital geomorphological mapping: Concepts, issues and research. Geomorphology, 137 (1), 5-26. doi: 10.1016/j.geomorph.2011.06.027.

Blaszczyk, M., Ignatiuk, D., Grabiec, M., Kolondra, L., Laska, M., Decaux, L., Jania, J., Berthier, E., Luks, B., Barzycka, B., Czapla, M., 2019. Quality Assessment and Glaciological Applications of Digital Elevation Models Derived from Space-Borne and Aerial Images over Two Tidewater Glaciers of Southern Spitsbergen. Remote Sensing, 11 (9), 1121. doi: 10.3390/rs11091121.

Bogena, H.R., Montzka, C., Huisman, J.A., Graf, A., Schmidt, M., Stockinger, M., von Hebel, C., Hendricks-Franssen, H.J., van der Kruk, J., Tappe, W., Baatz, R., Lucke, A., Bol, R., Groh, J., Putz, T., Jakobi, J., Kunkel, R., Sorg, J., Vereecken, H., 2018. The TERENO-Rur Hydrological Observatory: A Multiscale Multi-Compartment Research Platform for the Advancement of Hydrological Science. Vadose Zone Journal, 17 (1), 1-22. doi: 10.2136/vzj2018.03.0055.

Buchhorn, M., Smets, B., Bertels, L., De Roos, B., Lesiv, M., Tesendbazar, N.-E., Herold, M., Fritz, S., 2020. Copernicus Global Land Service: Land Cover 100m: collection 3: epoch 2019: Globe. 3.0.1 [dataset]. Zenodo. doi: 10.5281/zenodo.3939050.

Crippen, R., Buckley, S., Agram, P., Belz, E., Gurrola, E., Hensley, S., Kobrick, M., Lavalle, M., Martin, J., Neumann, M. Nguyen, Q., Rosen, P., Shimada, J., Simard, M., Tung, W., 2016. NASADEM Global Elevation Model: Methods and Progress. ISPRS - International Archives of the Photogrammetry, Remote Sensing and Spatial Information Sciences, XLI-B4, 125-128. doi: 10.5194/isprs-archives-XLI-B4-125-2016.

Dragut, L., Blaschke, T., 2006. Automated classification of landform elements using object-based image analysis. Geomorphology, 81 (3-4), 330-344. doi: 10.1016/j.geomorph.2006.04.013.

Drisya, J., Kumar, D.S., 2016. Comparison of digitally delineated stream networks from different spaceborne digital elevation models: A case study based on two watersheds in South India. Arabian Journal of Geosciences, 9 (18), 710. doi: 10.1007/s12517-016-2726-x.

Earth Observation Research Center, Japan Aerospace Exploration Agency, 2021. ALOS World 3D-30m (AW3D30) Version 3.2/3.1. https://www.eorc.jaxa.jp/ALOS/en/aw3d30/aw3d30v3.2_product_e_e1.2.pdf. 12.04.2021.

European Environment Agency (EEA), 2014. EU-DEM Statistical Validation. https://land.copernicus.eu/user-corner/technical-library/eu-dem-2013-report-on-the-results-of-the-statistical-validation. 12.04.2021.

European Environment Agency (EEA), 2016. European Digital Elevation Model (EU-DEM), version 1.1 [dataset]. https://land.copernicus.eu/imagery-in-situ/eu-dem/eu-dem-v1.1?tab=metadata. 12.04.2021.

Farr, T.G., Rosen, P.A., Caro, E., Crippen, R., Duren, R., Hensley, S., Kobrick, M., Paller, M., Rodríguez, E., Roth, L., Seal, D., Shaffer, S., Shimada, J., Umland, J., Werner, M., Oskin, M., Burbank, D., Alsdorf, D., 2007. The shuttle radar topography mission. Reviews of Geophysics, 45 (2). doi: 10.1029/2005rg000183.

Fenta, A.A., Kifle, A., Gebreyohannes, T., Hailu, G., 2015. Spatial analysis of groundwater potential using remote sensing and GIS-based multi-criteria evaluation in Raya Valley, northern Ethiopia. Hydrogeology Journal, 23 (1), 195-206. doi: 10.1007/s10040-014-1218-x.

Gdulová, K., Marešová, J., Moudrý, V., 2020. Accuracy assessment of the global TanDEM-X digital elevation model in a mountain environment. Remote Sensing of Environment, 241, 111724. doi: 10.1016/j.rse.2020.111724.

German Aerospace Center (DLR), 2018. TanDEM-X - Digital Elevation Model (DEM) - Global, 90m [dataset]. doi: 10.15489/ju28hc7pui09.

Gesch, D.B., 2018. Best Practices for Elevation-Based Assessments of Sea-Level Rise and Coastal Flooding Exposure. Frontiers in Earth Science, 6, 230. doi: 10.3389/feart.2018.00230.

Gonzalez-Moradas, M.D.R., Viveen, W., 2020. Evaluation of ASTER GDEM2, SRTMv3.0, ALOS AW3D30 and TanDEM-X DEMs for the Peruvian Andes against highly accurate GNSS ground control points and geomorphological-hydrological metrics. Remote Sensing of Environment, 237, 111509. doi: 10.1016/j.rse.2019.111509.

Graf, L., Moreno-de-las-Heras, M., Ruiz, M., Calsamiglia, A., Garcia-Comendador, J., Fortesa, J., Lopez-Tarazon, J.A., Estrany, J., 2018. Accuracy Assessment of Digital Terrain Model Dataset Sources for Hydrogeomorphological Modelling in Small Mediterranean Catchments. Remote Sensing, 10 (12), 2014. doi: 10.3390/rs10122014.

Grohmann, C.H., 2018. Evaluation of TanDEM-X DEMs on selected Brazilian sites: Comparison with SRTM, ASTER GDEM and ALOS AW3D30. Remote Sensing of Environment, 212, 121-133. doi: 10.1016/j.rse.2018.04.043.

Hirano, A., Welch, R., Lang, H., 2003. Mapping from ASTER stereo image data: DEM validation and accuracy assessment. ISPRS Journal of Photogrammetry and Remote Sensing, 57 (5-6), 356-370. doi: 10.1016/S0924-2716(02)00164-8.

Höhle, J., Höhle, M., 2009. Accuracy assessment of digital elevation models by means of robust statistical methods. ISPRS Journal of Photogrammetry and Remote Sensing, 64 (4), 398-406. doi: 10.1016/j.isprsjprs.2009.02.003.

Holmes, K.W., Chadwick, O.A., Kyriakidis, P.C., 2000. Error in a USGS 30-meter digital elevation model and its impact on terrain modeling. Journal of Hydrology, 233 (1-4), 154-173. doi: 10.1016/S0022-1694(00)00229-8.

Hu, Z.H., Peng, J.W., Hou, Y.L., Shan, J., 2017. Evaluation of Recently Released Open Global Digital Elevation Models of Hubei, China. Remote Sensing, 9 (3), 262. doi: 10.3390/rs9030262.

Huang, L.C., Liu, L., Jiang, L.M., Zhang, T.J., 2018. Automatic Mapping of Thermokarst Landforms from Remote Sensing Images Using Deep Learning: A Case Study in the Northeastern Tibetan Plateau. Remote Sensing, 10 (12), 2067. doi: 10.3390/rs10122067.

Ihde, J., Augath, W., Sacher, M., 2002. The Vertical Reference System for Europe. In: Drewes, H., Dodson, A.H., Fortes, L.P.S., Sánchez, L., Sandoval, P. Vertical Reference Systems, Berlin, Heidelberg. Springer Berlin Heidelberg, 345–350.

IT.NRW, 2012. Landwirtschaftszählung in Nordrhein-Westfalen 2010 – Gemeinde- und Kreisstatistik der landwirtschaftlichen Betriebe Betriebsgrößen, Bodennutzung, Viehhaltung, sozialökonomische Betriebstypen, betriebswirtschaftliche Ausrichtung, Arbeitskräfte. Information und Technik Nordrhein-Westfalen (Geschäftsbereich Statistik). Düsseldorf, Germany.

Jarvis, A., Reuter, H., Nelsen, A., Guevara, E., 2008. Hole-filled seamless SRTM data V4 [dataset]. International Centre for Tropical Agriculture (CIAT). http://srtm.csi.cgiar.org. 12.04.2021.

Kalambukattu, J.G., Kumar, S., Raj, R.A., 2018. Digital soil mapping in a Himalayan watershed using remote sensing and terrain parameters employing artificial neural network model. Environ Environmental Earth Sciences, 77 (5), 203. doi: 10.1007/s12665-018-7367-9.

Keys, L., Baade, J., 2019. Uncertainty in Catchment Delineations as a Result of Digital Elevation Model Choice. Hydrology, 6 (1), 13. doi: 10.3390/hydrology6010013.

Korres, W., Reichenau, T.G., Fiener, P., Koyama, C.N., Bogena, H.R., Comelissen, T., Baatz, R., Herbst, M., Diekkruger, B., Vereecken, H., Schneider, K., 2015. Spatio-temporal soil moisture patterns - A meta-analysis using plot to catchment scale data. Journal of Hydrology, 520, 326-341. doi: 10.1016/j.jhydrol.2014.11.042.

Kramm, T., Hoffmeister, D., 2019. A Relief Dependent Evaluation of Digital Elevation Models on Different Scales for Northern Chile. ISPRS International Journal of Geo-Information, 8 (10), 430. doi: 10.3390/ijgi8100430.

Kramm, T., Hoffmeister, D., 2020. Assessing the influence of environmental factors and datasets on soil type prediction with two machine learning algorithms in a heterogeneous area in the Rur catchment, Germany. Geoderma Regional, 22, e00316. doi: 10.1016/j.geodrs.2020.e00316.

Kramm, T., Hoffmeister, D., Curdt, C., Maleki, S., Khormali, F., Kehl, M., 2017. Accuracy Assessment of Landform Classification Approaches on Different Spatial Scales for the Iranian Loess Plateau. ISPRS International Journal of Geo-Information, 6 (11), 366. doi:10.3390/ijgi6110366.

Kumar, A., Negi, H.S., Kumar, K., Shekhar, C., 2020. Accuracy validation and bias assessment for various multi-sensor open-source DEMs in part of the Karakoram region. Remote Sensing Letters, 11 (10), 893-902. doi: 10.1080/2150704x.2020.1792001.

Li, H., Zhao, J.Y., 2018. Evaluation of the Newly Released Worldwide AW3D30 DEM Over Typical Landforms of China Using Two Global DEMs and ICESat/GLAS Data. Ieee Journal of Selected Topics in Applied Earth Observations and Remote Sensing, 11 (11), 4430-4440. doi: 10.1109/Jstars.2018.2874361.

Liu, K., Song, C.Q., Ke, L.H., Jiang, L., Pan, Y.Y., Ma, R.H., 2019. Global open-access DEM performances in Earth's most rugged region High Mountain Asia: A multi-level assessment. Geomorphology, 338, 16-26. doi: 10.1016/j.geomorph.2019.04.012.

Liu, Z.W., Zhu, J.J., Fu, H.Q., Zhou, C., Zuo, T.Y., 2020. Evaluation of the Vertical Accuracy of Open Global DEMs over Steep Terrain Regions Using ICESat Data: A Case Study over Hunan Province, China. Sensors, 20 (17), 4865. doi: 10.3390/s20174865.

Luana, S.P., Hou, X.Y., Wang, Y.T., 2015. Assessing the Accuracy of Srtm Dem and Aster Gdem Datasets for the Coastal Zone of Shandong Province, Eastern China. Polish Maritime Research, 22, 15-20. doi: 10.1515/pomr-2015-0026.

Marques, K.P.P., Dematte, J.A.M., Miller, B.A., Lepsch, I.F., 2018. Geomorphometric segmentation of complex slope elements for detailed digital soil mapping in southeast Brazil. Geoderma Regional, 14, e00175. doi: 10.1016/j.geodrs.2018.e00175.

Maune, D.F., Nayegandhi, A., 2018. Digital elevation model technologies and applications: the DEM users manual. American Society for Photogrammetry and Remote Sensing, Bethesda, Md, USA.

Mmbando, G.A., Kleyer, M., 2018. Mapping Precipitation, Temperature, and Evapotranspiration in the Mkomazi River Basin, Tanzania. Climate, 6 (3), 63. doi: 10.3390/cli6030063.

Mokarram, M., Seif, A., Sathyamoorthy, D., 2015. Landform classification via fuzzy classification of morphometric parameters computed from digital elevation models: case study on Zagros Mountains. Arabian Journal of Geosciences, 8 (7), 4921-4937. doi: 10.1007/s12517-014-1556-y.

Mouratidis, A., Ampatzidis, D., 2019. European Digital Elevation Model Validation against Extensive Global Navigation Satellite Systems Data and Comparison with SRTM DEM and ASTER GDEM in Central Macedonia (Greece). ISPRS International Journal of Geo-Information, 8 (3), 108. doi: 10.3390/ijgi8030108.

Mukherjee, S., Joshi, P.K., Mukherjee, S., Ghosh, A., Garg, R.D., Mukhopadhyay, A., 2013. Evaluation of vertical accuracy of open source Digital Elevation Model (DEM). International Journal of Applied Earth Observation and Geoinformation, 21, 205-217. doi: 10.1016/j.jag.2012.09.004.

Nagaveni, C., Kumar, K.P., Ravibabu, M.V., 2019. Evaluation of TanDEMx and SRTM DEM on watershed simulated runoff estimation. Journal of Earth System Science, 128 (1), 2. doi: 10.1007/s12040-018-1035-z.

NASA JPL, 2020. NASADEM Merged DEM Global 1 arc second V001 [dataset]. NASA EOSDIS Land Processes DAAC. doi: 10.5067/MEaSUREs/ NASADEM/NASADEM_HGT.001.

NASA Shuttle Radar Topography Mission (SRTM), 2013. Shuttle Radar Topography Mission (SRTM) Global [dataset]. OpenTopography. doi: 10.5069/ G9445JDF.

Pakoksung, K., Takagi, M., 2020. Assessment and comparison of Digital Elevation Model (DEM) products in varying topographic, land cover regions and its attribute: a case study in Shikoku Island Japan. Modeling Earth Systems and Environment, 7 (1), 465-484. doi: 10.1007/s40808-020-00891-x.

Pandey, P., Manickam, S., Bhattacharya, A., Ramanathan, A.L., Singh, G., Venkataraman, G., 2017. Qualitative and quantitative assessment of TanDEM-X DEM over western Himalayan glaciated terrain. Geocarto International, 32 (4), 442-454. doi: 10.1080/10106049.2016.1155655.

Podgorski, J., Kinnard, C., Petlicki, M., Urrutia, R., 2019. Performance Assessment of TanDEM-X DEM for Mountain Glacier Elevation Change Detection. Remote Sensing, 11 (2), 187. doi: 10.3390/rs11020187.

Reuter, H.I., Nelson, A., Jarvis, A., 2007. An evaluation of void-filling interpolation methods for SRTM data. International Journal of Geographical Information Science, 21 (9), 983-1008. doi: 10.1080/13658810601169899.

Rexer, M., Hirt, C., 2014. Comparison of free high resolution digital elevation data sets (ASTER GDEM2, SRTM v2.1/v4.1) and validation against accurate heights from the Australian National Gravity Database. Australian Journal of Earth Sciences, 61 (2), 213-226. doi: 10.1080/08120099.2014.884983.

Rizzoli, P., Bräutigam, B., Kraus, T., Martone, M., Krieger, G., 2012. Relative height error analysis of TanDEM-X elevation data. ISPRS Journal of Photogrammetry and Remote Sensing, 73, 30-38. doi: 10.1016/j.isprsjprs.2012.06.004.

Rizzoli, P., Martone, M., Gonzalez, C., Wecklich, C., Tridon, D.B., Bräutigam, B., Bachmann, M., Schulze, D., Fritz, T., Huber, M., Wessel, B., Krieger, G., Zink, M., Moreira, A., 2017. Generation and performance assessment of the global TanDEM-X digital elevation model. ISPRS Journal of Photogrammetry and Remote Sensing, 132, 119-139. doi: 10.1016/j.isprsjprs.2017.08.008.

Rodríguez, E., Morris, C.S., Belz, J.E., Chapin, E.C., Martin, J.M., Daffer, W., Hensley, S., 2005. An Assessment of the SRTM Topographic Products. Jet Propulsion Laboratory (JPL), Pasadena, CA, USA.

Rossman, N.R., Zlotnik, V.A., Rowe, C.M., 2018. An approach to hydrogeological modeling of a large system of groundwater-fed lakes and wetlands in the Nebraska Sand Hills, USA. Hydrogeology Journal, 26 (3), 881-897. doi: 10.1007/s10040-017-1691-0.

Satge, F., Bonnet, M.P., Timouk, F., Calmant, S., Pillco, R., Molina, J., Lavado-Casimiro, W., Arsen, A., Cretaux, J.F., Garnier, J., 2015. Accuracy assessment of SRTM v4 and ASTER GDEM v2 over the Altiplano watershed using ICESat/GLAS data. International Journal of Remote Sensing, 36 (2), 465-488. doi: 10.1080/01431161.2014.999166.

Schlund, M., Baron, D., Magdon, P., Erasmi, S., 2019. Canopy penetration depth estimation with TanDEM-X and its compensation in temperate forests. ISPRS Journal of Photogrammetry and Remote Sensing, 147, 232-241. doi: 10.1016/j.isprsjprs.2018.11.021.

Schwanghart, W., Groom, G., Kuhn, N.J., Heckrath, G., 2013. Flow network derivation from a high resolution DEM in a low relief, agrarian landscape. Earth Surface Processes and Landforms, 38 (13), 1576-1586. doi: 10.1002/esp.3452.

Scilands GmbH, 2010. GMK10 Rur – Terrainfactors [dataset]. CRC/TR32 Database (TR32DB). https://www.tr32db.uni-koeln.de/data.php?dataID=196. 12.04.2021.

Solberg, S., May, J., Bogren, W., Breidenbach, J., Torp, T., Gizachew, B., 2018. Interferometric SAR DEMs for Forest Change in Uganda 2000-2012. Remote Sensing, 10 (2), 228. doi: 10.3390/rs10020228.

Suwandana, E., Kawamura, K., Sakuno, Y., Kustiyanto, E., Raharjo, B., 2012. Evaluation of ASTER GDEM2 in Comparison with GDEM1, SRTM DEM and Topographic-Map-Derived DEM Using Inundation Area Analysis and RTK-dGPS Data. Remote Sensing, 4 (8), 2419-2431. doi: 10.3390/rs4082419.

Tachikawa, T., Kaku, M., Iwasaki, A., Gesch, D.B., Oimoen, M.J., Zhang, Z., Danielson, J.J., Krieger, T., Curtis, B., Haase, J., Abrams, M., Carabajal, C., 2011. ASTER Global Digital Elevation Model Version 2 - summary of validation results. NASA, Washington, DC, USA.

Tadono, T., Shimada, M., Murakami, H., Takaku, J., 2009. Calibration of PRISM and AVNIR-2 Onboard ALOS "Daichi". IEEE Transactions on Geoscience and Remote Sensing, 47 (12), 4042-4050. doi: 10.1109/Tgrs.2009.2025270.

Takaku, J., Tadono, T., 2017. Quality updates of 'AW3D' global DSM generated from ALOS PRISM, Proceedings of the 2017 IEEE International Geoscience and Remote Sensing Symposium (IGARSS), Fort Worth, TX, USA, 23–28 July 2017, 5666-5669. doi: 10.1109/IGARSS.2017.8128293.

Takaku, J., Tadono, T., Tsutsui, K., 2014. Generation of High Resolution Global DSM from ALOS PRISM. International Archives of the Photogrammetry, Remote Sensing and Spatial Information Sciences, XL-4, 243-248. doi: 10.5194/isprsarchives-XL-4-243-2014.

Thomas, J., Joseph, S., Thrivikramji, K.P., Arunkumar, K.S., 2014. Sensitivity of digital elevation models: The scenario from two tropical mountain river basins of the Western Ghats, India. Geoscience Frontiers, 5 (6), 893-909. doi: 10.1016/j.gsf.2013.12.008.

Tian, J.J., Schneider, T., Straub, C., Kugler, F., Reinartz, P., 2017. Exploring Digital Surface Models from Nine Different Sensors for Forest Monitoring and Change Detection. Remote Sensing, 9 (3), 287. doi: 10.3390/rs9030287.

Ullmann, T., Sauerbrey, J., Hoffmeister, D., May, S.M., Baumhauer, R., Bubenzer, O., 2019. Assessing Spatiotemporal Variations of Sentinel-1 InSAR Coherence at Different Time Scales over the Atacama Desert (Chile) between 2015 and 2018. Remote Sensing, 11 (24), 2960. doi: 10.3390/rs11242960.

Uuemaa, E., Ahi, S., Montibeller, B., Muru, M., Kmoch, A., 2020. Vertical Accuracy of Freely Available Global Digital Elevation Models (ASTER, AW3D30, MERIT, TanDEM-X, SRTM, and NASADEM). Remote Sensing, 12 (21), 3482. doi: 10.3390/rs12213482.

Vassilaki, D.I., Stamos, A.A., 2020. TanDEM-X DEM: Comparative performance review employing LIDAR data and DSMs. ISPRS Journal of Photogrammetry and Remote Sensing, 160, 33-50. doi: 10.1016/j.isprsjprs.2019.11.015.

Waldhoff, G., Lussem, U., 2016. Enhanced land use classification of 2015 for the Rur catchment – Update [dataset]. CRC/TR32 Database (TR32DB). doi: 10.5880/ TR32DB.19.

Waldhoff, G., Lussem, U., Bareth, G., 2017. Multi-Data Approach for remote sensing-based regional crop rotation mapping: A case study for the Rur catchment, Germany. International Journal of Applied Earth Observation and Geoinformation, 61, 55-69. doi: 10.1016/j.jag.2017.04.009.

Walk, J., Stauch, G., Reyers, M., Vásquez, P., Sepúlveda, F.A., Bartz, M., Hoffmeister, D., Brückner, H., Lehmkuhl, F., 2020. Gradients in climate, geology, and topography affecting coastal alluvial fan morphodynamics in hyperarid regions – The Atacama perspective. Global and Planetary Change, 185, 102994. doi: 10.1016/j.gloplacha.2019.102994.

Wessel, B., 2016. TanDEM-X Ground Segment – DEM Products Specification Document. EOC, Munich, Germany, 2016.

Wessel, B., Huber, M., Wohlfart, C., Marschalk, U., Kosmann, D., Roth, A., 2018. Accuracy assessment of the global TanDEM-X Digital Elevation Model with GPS data. ISPRS Journal of Photogrammetry and Remote Sensing, 139, 171-182. doi: 10.1016/j.isprsjprs.2018.02.017.

Weydahl, D.J., Sagstuen, J., Dick, O.B., Ronning, H., 2007. SRTM DEM accuracy assessment over vegetated areas in Norway. International Journal of Remote Sensing, 28 (16), 3513-3527. doi: 10.1080/01431160600993447.

Wilson, J.P., 2012. Digital terrain modeling. Geomorphology, 137 (1), 107-121. doi: 10.1016/j.geomorph.2011.03.012.

Yahaya, S.I., El Azzab, D., 2019. Vertical accuracy assessment of global digital elevation models and validation of gravity database heights in Niger. International Journal of Remote Sensing, 40 (20), 7966-7985. doi: 10.1080/01431161.2019.1607982.

Yap, L., Kande, L.H., Nouayou, R., Kamguia, J., Ngouh, N.A., Makuate, M.B., 2019. Vertical accuracy evaluation of freely available latest high-resolution (30 m) global digital elevation models over Cameroon (Central Africa) with GPS/leveling ground control points. International Journal of Digital Earth, 12 (5), 500-524. doi: 10.1080/17538947.2018.1458163.

Zhang, K.Q., Gann, D., Ross, M., Robertson, Q., Sarmiento, J., Santana, S., Rhome, J., Fritz, C., 2019. Accuracy assessment of ASTER, SRTM, ALOS, and TDX DEMs for Hispaniola and implications for mapping vulnerability to coastal flooding. Remote Sensing of Environment ,225, 290-306. doi: 10.1016/j.rse.2019.02.028.

Zhao, S.M., Cheng, W.M., Zhou, C.H., Chen, X., Zhang, S.F., Zhou, Z.P., Liu, H.J., Chai, H.X., 2011. Accuracy assessment of the ASTER GDEM and SRTM3 DEM: an example in the Loess Plateau and North China Plain of China. International Journal of Remote Sensing, 32 (23), 8081-8093. doi: 10.1080/01431161.2010.532176.

6 Accuracy assessment of landform classification approaches on different spatial scales for the Iranian Loess Plateau

TANJA KRAMM[1], DIRK HOFFMEISTER[1], CONSTANZE CURDT[1], SEDIGHEH MALEKI[2], FARHAD KHORMALI[2], MARTIN KEHL[1]

Published in: ISPRS International Journal of Geo-Information, 2017, **6** (11), 366.

DOI: 10.3390/ijgi6110366

Formatting and orthography of the manuscript is adapted to the dissertation style.

[1]GIS and Remote Sensing, Institute of Geography, University of Cologne, Albertus Magnus Platz, 50923 Köln, Germany.

[2]Department of Soil Sciences, Faculty of Water and Soil Engineering, Gorgan University of Agricultural Sciences and Natural Resources, Gorgan, 49138-15739 Iran.

Abstract: An accurate geomorphometric description of the Iranian loess plateau landscape will further enhance our understanding of recent and past geomorphological processes in this strongly dissected landscape. Therefore, four different input datasets for four landform classification methods were used in order to derive the most accurate results in comparison to ground-truth data from a geomorphological field survey. The input datasets in 5 m and 10 m pixel resolution were derived from Pléiades stereo satellite imagery and the 'Shuttle Radar Topography Mission' (SRTM) as well as 'Advanced Spaceborne Thermal Emission and Reflection Radiometer' (ASTER GDEM) datasets with a spatial resolution of 30 m were additionally applied. The four classification approaches tested with this data include the stepwise approach after Dikau, the geomorphons, the topographical position index (TPI) and the object-based approach. The results show that input datasets with higher spatial resolutions produced overall accuracies of greater than 70 % for the TPI and geomorphons and greater than 60 % for the other approaches. For the lower resolution datasets, only accuracies of about 40 % were derived, 20 – 30 % lower than for data derived from higher spatial resolutions. The results of the topographic position index and the geomorphons approach worked best for all selected input datasets.

Keywords: digital terrain models; landform classification; geomorphometry; stereo satellite imagery; ASTER GDEM; SRTM; loess

6.1 Introduction

The description of the Earth's surface by automatic classifications is important to derive insight into a landscape. Geomorphometry, as a quantitative analysis of landscape structures, is applied in several fields, such as hydrology, geomorphology, soil science, oceanography or civil engineering (Florinsky, 2012; Pike and Park, 1995). In practice, this valuable geomorphometric information can be used for map making, digital soil mapping (Behrens et al., 2014; Behrens et al., 2010; Bishop et al., 2012), hydrological simulations (Armstrong and Martz, 2003; Schwanghart et al., 2013) and risk potential analysis (Barka et al., 2011; Wood et al., 2011). Furthermore, this information is useful for the estimation of arable land as well as areas endangered by soil erosion. Likewise, the achieved information allows estimating past landscape evolution (Bishop et al., 2012).

To derive landform classifications, geomorphometric parameters, e.g. slope and curvature, of digital terrain models are used. These values are utilized for landform classification approaches in different ways and a multitude of different algorithms were developed for a systematic landform classification. Most of them are working with different terrain parameters and combinations of them to derive distinct landform types. For this purpose, most approaches use the assumption of landform types distinguishable by a comparison to the corresponding neighbouring elements. The first approaches for a digital landform classification were conducted by Pennock et al. (1987), who classified seven landform elements from the morphometric parameters slope, plan curvature and profile curvature. Dikau et al. (1995) digitalized the landform classification scheme of Hammond (Hammond, 1954; Hammond, 1964). Based on Hammond's work, he calculated three morphometric values for each cell with a surrounding moving window and grouped them into different categories. Finally, he combined them into five different landform types.

In the following decades, a large number of alternative and modified classification methods were presented. Brabyn (1998) modified the classification system of Hammond and Dikau. MacMillan et al. (2000) enhanced the classification scheme of Pennock et al. (1987) and were able to derive 15 different landform classes instead of seven. In addition, more complex decision tree-based approaches were tested to achieve a systematic landform classification (Iwahashi and Pike, 2007; Klingseisen et al., 2008). Furthermore, besides these numerous landform classification schemes with 'crisp, unambiguous boundaries' (Burrough et al., 2000), fuzzy classification methods were introduced (Burrough et al., 2000; Schmidt and Hewitt, 2004). To consider the problem that different landform types mostly vary strongly in their sizes, Weiss (2001) developed the topographic position index (TPI). The TPI measures relative height positions of a certain point compared to its surrounding area in two different window sizes, whereas other approaches mostly use only one size for calculation. Thus, this approach is more suitable for heterogeneous landscapes (De Reu et al., 2013). Another promising approach was conducted by Jasiewicz and Stepinski (2013). Their geomorphons approach creates ternary patterns as a set of possible morphological landscape types from elevation differences in a certain neighbourhood.

To take advantage of the segmentation technique over pixel-based classification methods, Dragut and Blaschke (2006) introduced a new object-based approach. Pixel-based approaches ignore contextual information and only consider values of individual pixels in the classification process. In contrast, object-based approaches use segmentation algorithms prior to the classification to partition the data into semantic objects that are much better able to divide the landscape in a comprehensible way. Therefore, object-based image analysis (OBIA) approaches became very popular in geomorphometry and the number of applied approaches increased in the last decade (d'Oleire-Oltmanns et al., 2013; Pedersen, 2016; Schneevoigt et al., 2008; van Asselen and Seijmonsbergen, 2006).

Recently, all developed approaches were applied to many different thematic fields and landscapes. They have also become essential for the mapping of natural landscapes at different scales. Besides classifications of terrestrial landscape (Dragut and Eisank, 2012) or undersea topography (Dekavalla and Argialas, 2017) on global scales, small scale distinct landforms such as gullies (d'Oleire-Oltmanns et al., 2013), drumlins or volcanoes (Camiz et al., 2017; Pedersen, 2016) were also classified. All these approaches show very promising results. However, a thorough evaluation and comparison of the landform classification schemes is missing. In addition, it is rarely shown how different scales and input datasets overall work with these approaches. The questions of accuracy and scaling arise in particular

for areas with stronger relief variation as such landscapes are more sensitive to changes in digital elevation model (DEM) resolutions (Deng et al., 2007). Generally, most experiences indicate that DEM pixel resolutions between 5 m and 30 m are most suitable for landform classifications (Kienzle, 2004; Zhang and Montgomery, 1994). Likewise, input terrain datasets in a higher spatial resolution are available, as satellites nowadays are enabled to record stereo-views of an area. This optical imagery for the derivation of DEMs now achieved a submeter pixel resolution, comparable to already available datasets derived by airborne laser scanning (LiDAR). Furthermore, a global DEM with a 12 m pixel resolution will be available from the TanDEM-X mission, which incorporated two RADAR satellites and is nearly finished (Zink et al., 2014).

In this contribution, the comparison of four different landform classification approaches was conducted by three different input datasets for a remote region, which is characterized by a strongly dissected relief, the Iranian loess plateau. The input datasets are the publicly available DEMs of the 'Shuttle Radar Topography Mission' (SRTM) and 'Advanced Spaceborne Thermal Emission and Reflection Radiometer' (ASTER) (30 m pixel resolution) and two digital elevation models derived from Pléiades stereo imagery aggregated to a 5 m and 10 m pixel resolution. Based on the presented approaches by Dikau et al. (1995), Weiss (2001), Jasiewicz and Stepinski (2013) as well as Dragut and Blaschke (2006), landforms were classified in four different ways for each digital elevation model. These methods were applied in two different study areas of the Iranian loess plateau. Both study sites have slightly varying relief characteristics. One is situated in the western part of the loess plateau and has a strongly dissected relief with small valleys and steeply rising hills. The second study area has a flatter relief with some deeply incised valleys and is located in the eastern part of the plateau. To evaluate the results of the conducted landform classifications, geo-located pictures taken on a field campaign in this area were used. The accuracy of the DEMs themselves are compared to measurements of DGPS profiling. However, the precision and accuracy of the DEMs is not considered here, due to the accessibility of the area and only relative heights are used in the selected approaches.

6.2 Study area

The Iranian loess plateau is a unique landscape covered by mineral dust, up to at least 70 m thick (Frechen et al., 2009). Recent sedimentological and geochronological investigations show that these loess deposits have high value as records of Quaternary landscape evolution and climate change. These deposits provide a link between the loess deposits in Southeastern Europe and Central Asia (Frechen et al., 2009; Kehl, 2010; Khormali and Ajami, 2011; Lauer et al., 2017). However, little information is available on its soil, plant cover and the geomorphological evolution of the plateau as well as on potentials and problems in land use.

The loess plateau covers an area of about 2250 km^2 in the Turkmen steppe of northern Iran (Figure 6-1). It is located at altitudes between about 45 m and 300 m above mean sea level. The base of the loess plateau belongs to the western part of the Kopeh Dagh Mountains. It is dissected in several fault blocks (Bretis et al., 2012). Differential tectonic uplift is expressed in several escarpments and in the sudden altitudinal rise at the boundary of the plateau. Tectonic uplift triggered deep erosion and valley incision into the loess and underlying strata, causing the pronounced relief of the loess plateau. It is characterized by steep slopes frequently dissected by deeply incised v-shaped side-valleys opening to larger valleys with broad floors. Both types are dry valleys with episodic runoff. The ridges in

between the valleys rise to about 80 m above the valley floors and mostly consist of loess. Frequent loess wells, sinkholes, pipes and gullies reflect intense erosion processes at the land surface and below. Small scarp faces and hummocky toes indicate local slumping. In addition, the slope surfaces are covered by dense networks of sheep and goat tracks related to severe overgrazing in the area (Kehl, 2010).

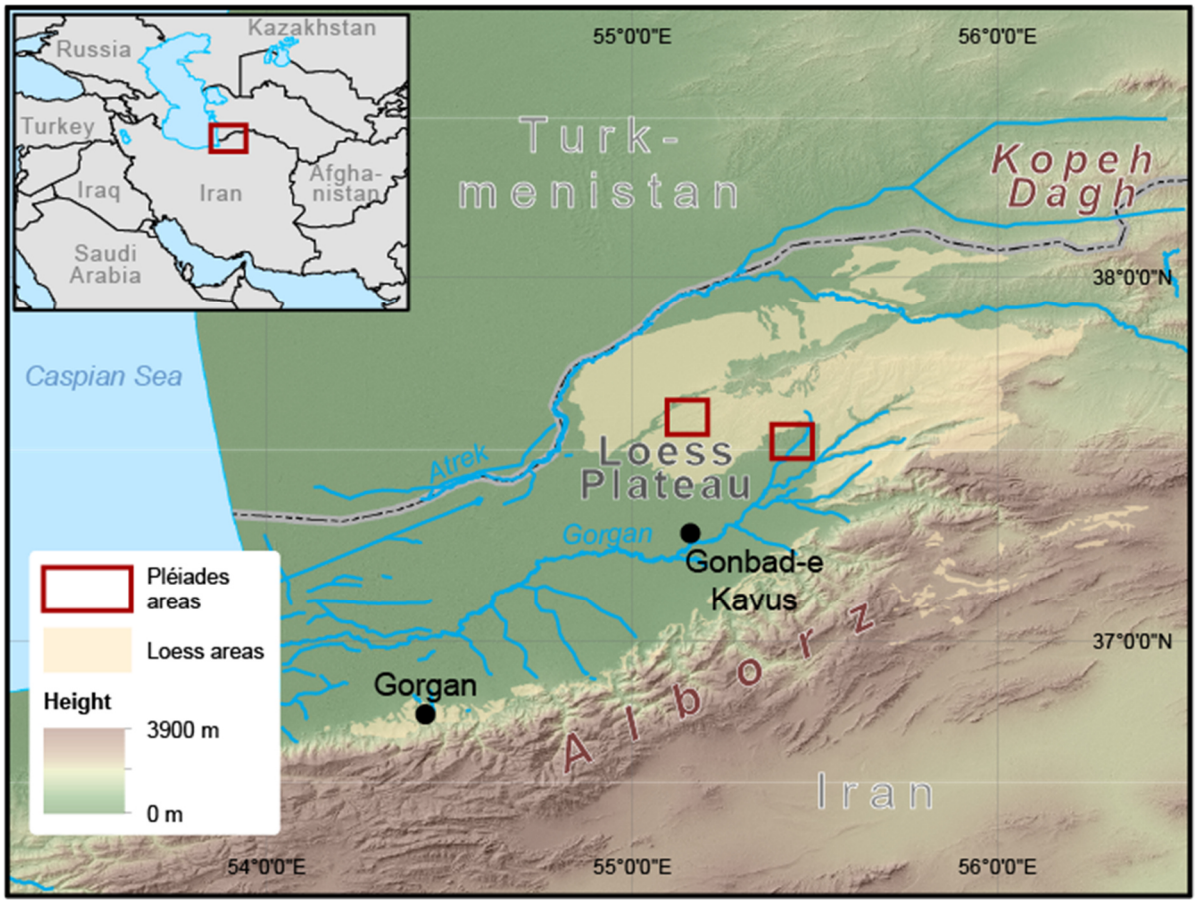

Figure 6-1: Overview of the study area in northeast Iran with the two different Pléiades satellite imagery extents. Data provided by Golestan Natural Resources and Watershed Management Central Office (loess areas), ASTER-GDEM2 and ArcWorld Supplement.

6.3 Materials and methods

6.3.1 Low resolution digital elevation models

For the comparison of the different landform classifications, the two global digital elevation models (GDEM) in a resolution of 30 m were used. The ASTER sensor is a multispectral imaging system that is on board NASA's ERA (Earth Observing System) TERRA satellite. The mission was launched in 1999 and was primarily used to collect multispectral data of the Earth (Abrams, 2000). In addition to the multispectral bands, the ASTER sensor has an additional near infrared sensor, which is inclined by 27.6°. These sensors enable a stereoscopic recording according to the 'as-track' principle (Hirano et al., 2003). In 2009, NASA and the Japanese Ministry of International Trade and Industry published a global digital terrain model for the first time. This ASTER global digital elevation model (GDEM) was generated from all collected stereo images. It has a geometric resolution of one arc second, which

corresponds to a pixel resolution of about 30 m (Abrams et al., 2015; Tachikawa et al., 2011). In 2011, the second version of the ASTER GDEM was released. For the ASTER GDEM 2 used in this contribution, further recordings and enhancements were made available (Tachikawa et al., 2011). The accuracy of the ASTER GDEM2 was assessed by the ASTER GDEM Validation Team (Tachikawa et al., 2011) with an average vertical root mean square error (RMSE) of 8.86 m. Additionally, they reported a RMSE of 6.1 m in flatter areas and of 15.1 m in mountainous regions. The horizontal average error was conducted by a shift of 0.13 arc-seconds to west and 0.19 arc-seconds to north.

In contrast to the previously described passive DEM derivation of the Earth's surface, it was actively recorded in February 2000 by the SRTM with the aid of RADAR systems by the InSAR principle (Farr et al., 2007). A DEM from the C-band data was first made available by the USGS in 2003 in a one arc second geometric resolution for the US and a three arc second resolution for the whole Earth. In the course of the year 2015, SRTM data with a geometric resolution of one arc second were made available for the rest of the Earth's surface. Thus, SRTM data for the region of northern Iran with a geometric resolution of 30 m was also available for the analysis in this contribution. According to Farr et al. (2007), the accuracy of the SRTM DEM is determined by an absolute vertical height error of 6.2 m and a relative height error of less than 8.7 m for Eurasia. The horizontal positional accuracy was assessed with a circular absolute geolocation error of 8.8 m.

6.3.2 High resolution digital elevation models

In contrast to the previously presented low resolution models, different models in a higher spatial resolution from Pléiades satellite imagery were derived. Pléiades is a satellite system operated by the French Space Center (CNES). The first of the two satellites (Pléiades 1A) was brought into a sun-synchronous orbit on 16 December 2011. One year later, Pléiades 1B followed as the second satellite on 2 December 2012, which completed the system (Astrium GEO-Information Services, 2012). This system is equipped with optoelectronic CCD scanners, which scan the Earth's surface transversely to the direction of flight and convert the measured radiation into a measurable electrical signal. It is recorded in a panchromatic channel and four multispectral channels each with five line sensors (de Lussy et al., 2006; Gleyzes et al., 2012). The line sensors of the panchromatic sensor have a width of more than 6000 pixels and the multispectral sensors have a resolution of 1500 pixels. Thus, the geometric resolution of the satellite is 50 cm in the panchromatic channel and 2 m in the multi-spectral channels (Astrium GEO-Information Services, 2012). The Pléiades satellites thus belong to the satellite systems with a very high spatial resolution. The panchromatic channel operates in a wavelength range between 480 nm and 830 nm. The positional accuracy is indicated with 8.5 m at nadir and 10.5 m within an angle of 30° (Astrium GEO-Information Services, 2012). The Pléiades data used in this study are two stereoscopic images, which were recorded over the investigation areas on 28 March 2015, each representing an area of about 10 by 10 km. From these stereo image pairs, the digital terrain models with a pixel resolution of 50 cm were established with the ENVI software. The generation of the Pléiades DEMs was conducted with 25 tie-points for relative orientation. No georeferenced ground control points (GCPs) were used, due to the accessibility. Therefore, only a DEM with relative heights was used in the classification process. From the high resolution dataset, two datasets with lower pixel resolution (5 m and 10 m) were resampled by the 'nearest neighbour' sampling method, which served as the basis for the compilation of the landform classifications.

6.3.3 Applied landform classifications

6.3.3.1 The approach of Dikau

Following the approach of Dikau in the 1990s, a stepwise classification was conducted, subdivided into the derivation of slope, local relief and profile type classifications. The whole procedure is computed in ArcMap 10.3 (ESRI) as an automatic tool, implemented with the model builder. Major functions used in ArcMap are slope, focal statistics and map algebra. The first step of this approach is to derive slope classes for each pixel by an adjustable number of neighbouring pixels building a rectangle containing a slope of less than 8 %. Class breaks are 20 %, 50 % and 80 %, resulting in four classes. The number of neighbouring pixels is adjusted to the spatial resolution of the input data, as assigned in Table 6-1.

Table 6-1: Parameters of the moving window sizes in pixels (px) for Dikau used in this approach for the three different pixel resolutions. Cell size in meters are shown in parentheses.

Moving window	**5 m**	**10 m**	**30 m**
Slope gradient (rectangle)	3 × 3 (15 m)	3 × 3 (30 m)	3 × 3 (90 m)
Local relief window (circle radius)	15 (75 m)	10 (100 m)	5 (150 m)
Profile type (rectangle)	10 × 10 (50 m)	10 × 10 (100 m)	10 × 10 (300 m)

The calculation of the local relief is conducted by building height differences for each pixel and the previously mentioned neighbouring pixels (Table 6-1). In this case, the neighbouring pixels are determined by a circle. Classes are built upon the height differences in six classes with class breaks at 30 m, 60 m, 100 m, 150 m and 300 m. Likewise, the profile type is calculated by assigning pixels to upland or lowland and further using classes of flatness, as described before. The assignment to upland or lowland is depending on the position of the pixel in relation to the overall height range of surrounding pixels. A pixel with a height higher than half of the height range of all pixels is in upland class, a pixel with a height smaller than half of the height range of all pixels is in the lowland class. Four classes are built by the combination of these calculations, where low- or upland pixels with a number of slope pixels smaller or higher than 75 % are used.

All possible classes of each classification were serially numbered from one to four for the slope and profile type classification and from one to six for the local relief classification. Consequently, each pixel became three numbers depending on their assigned class. A combination of these results in 96 possible combinations for each pixel (Table 6-2), in which the first digit represents the slope classification, the second one the local relief and the third one the profile type. Finally, these sub classes are remapped here to five major landform classes (plains, plateau, irregular plains, low hills and moderate hills) that fit the results of the other classification approaches.

Table 6-2: Reclassification scheme of the derived landform subclasses to final landform classes.

Landform sub-classes code	Landform type
111, 112, 121, 122, 131, 132, 141, 142, 151, 152, 161, 162, 211, 212, 221, 222	Plains
113, 114, 123, 124, 133, 134, 143, 144, 153, 154, 163, 164, 213, 214, 223, 224	Plateau
231, 232, 233, 234, 241, 242, 243, 244, 251, 252, 253, 254, 261, 262, 263, 264, 311, 312, 313, 314, 321, 322, 323, 324, 331, 332, 333, 334, 341, 342, 343, 344, 351, 352, 353, 354, 361, 362, 363, 364	Irregular Plains
411, 412, 413, 414, 421, 422, 423, 424	Low Hills
431, 432, 433, 434, 441, 442, 443, 444, 451, 452, 453, 454, 461, 462, 463, 464	Moderate Hills

6.3.3.2 The Topographic Position Index

The topographic position index was implemented as a tool with ArcMap 10.3 model builder (ESRI) after the concept of Weiss (2001). The TPI uses two different scales in order to derive different landform classes. The standardized index is built on each scale by comparing the current cell value to the moving mean of the neighbouring cells. In this case, neighbouring cells are selected by an annulus with an inner and outer cell radius. As previously described, these sizes are selected based on the pixel resolution of the input data. As recommended by De Reu et al. (2013), the size of the radius for the inner annulus was oriented on the dimensions of the smaller landforms in the study area. The values are listed in Table 6-3. Positive index values are assigned as ridge, negative values are assigned as valley. In combination with a slope analysis, a differentiation in two classes with values smaller or bigger than 5 %, as well as the two different scales, this results in ten classes. In this contribution, the number of classes is reduced to seven classes by integrating ridges and drainage classes.

Table 6-3: Parameters of the moving window sizes in pixels (px) for the TPI used in this approach for the three different pixel resolutions. Cell sizes in meters are shown in parentheses.

	5 m		**10 m**		**30 m**	
	Inner radius	Outer radius	Inner radius	Outer radius	Inner radius	Outer radius
TPI 300 annulus	5 *(25 m)*	10 *(50 m)*	3 *(30 m)*	5 *(50 m)*	3 *(90 m)*	5 *(150 m)*
TPI 2000 annulus	62 *(310 m)*	67 *(335 m)*	30 *(300 m)*	33 *(330 m)*	10 *(300 m)*	12 *(360 m)*

6.3.3.3 The object-based approach

For the object-based approach, slope and curvature are first calculated as further input datasets for the segmentation. The segmentation is conducted in eCognition Developer 9.0 (Trimble) by the multiresolution segmentation tool. The weighting for each parameter is similar as well as smoothness and compactness in the segmentation process. The scale parameter is set to 20, 10 and 5 for the pixel resolution of 5 m, 10 m and 30 m. Classes are built by using the mean value of profile curvature (<−0.5, −0.5 to 0.5 and >0.5) and slope (<2°, >35°) of each derived object. In addition, a peak class is built for all segments higher than their surrounding segments and footslope segments are selected from valley segments with neighbouring plain segments. Thus, seven classes are derived by this approach: ridge, hillslope, valley, plains, steep slope, peak and footslope.

6.3.3.4 Geomorphons

The applied geomorphons approach was developed by Jasiewicz and Stepinski (2013) for the open source GIS Software GRASS GIS (GRASS Development Team). It is a pattern recognition approach that compares height values of cells in eight different directions to the regarding cell. The approach uses input parameters for an inner and outer search radius to set the distance, which is considered for the calculation of the height differences. These height differences were calculated after the 'line-of-sight' principle by Yokoyama et al. (2002). In addition, a parameter flatness threshold is necessary as a threshold for flat terrain. The used parameters in this contribution are displayed in Table 6-4. The original approach results in ten different landform classes. For a better comparability to the other approaches in this contribution, the classes spur, slope and hollow were combined into one class and all classes were renamed (Table 6-5).

Table 6-4: Parameters of the moving window sizes in pixels (px) for the object-based approach used in this approach for the three different pixel resolutions. Cell sizes in meters are shown in parentheses.

Parameters	5 m	10 m	30 m
Outer search radius (px)	20 *(100 m)*	10 *(100 m)*	10 *(300 m)*
Inner search radius (px)	10 *(50 m)*	5 *(50 m)*	5 *(150 m)*
Flatness threshold (degrees)	3	3	3

Table 6-5: Reclassification scheme of the derived landforms to final landform classes used in this contribution for comparison of the approaches.

Geomorphons class names	Used class names
flat	plains
peak	peak
ridge	ridge
shoulder	plateau
spur, slope, hollow	hillslope
pit	gully
valley	valley
footslope	footslope

6.3.4 Methodology of accuracy assessment

For an accuracy assessment of the derived landform classes as well as for a determination of DEM error in the selected areas, a field campaign for ground-truth capture was conducted in September 2015. Therefore, a Trimble R3 DGPS was used for measuring some trenches inside the coverage of the Pléiades imagery. Due to the rougher relief of the western coverage area, the DGPS profiles were measured at steeper slopes at this location and contain height differences up to 60 m. In contrast, the measured points in the eastern area depict flatter terrain by only containing height differences of less than 20 m. Likewise, 66 geolocations based on the classification results were chosen and measured with a handheld GPS. At these locations, pictures were taken with the according orientation. Thus, approximately 150 landforms could be identified. As an example, Figure 6-2 shows the picture location 193 with the according pictures to the North and South.

Figure 6-2: Example location for the accuracy assessment: (A) location and viewing direction in the Pléiades scene (©CNES (2015), Distribution Airbus DS); and (B, C) pictures of the two viewing directions of this picture point.

6.4 Results

6.4.1 DEM accuracy

To evaluate the accuracy of the utilized DEMs, 314 DGPS points were measured during the field campaign at six locations (western part: 281 points; eastern part: 33 points). For each point, the altitudes of the datasets were compared to the DGPS heights. Hence, a root mean square error value was calculated for each dataset. For the Pléiades dataset, the originally achieved version with a pixel resolution of 0.5 m was used. The results are listed in Table 6-6. Generally, they show much higher deviations for the western than for the eastern study area. For the ASTER GDEM, the highest RMSE values were determined in both sites. In contrast, the altitude differences of the SRTM dataset were the lowest compared to the others.

Table 6-6: Calculated root mean square error (RMSE) of DGPS and digital elevation model (DEM) heights for both areas.

	West [m]	East [m]
Pléiades	11.7	3.2
ASTER	13.3	4.5
SRTM	9	2.9

6.4.2 Classification results

Figure 6-3 presents the percentage of the classified area for each landform class. All approaches indicate significant differences between the western and eastern study areas. Generally, they show more flat terrain in the eastern area, whereas the western area is dominated by landform classes that represent hilly landforms. Therefore, in the eastern site, the flat landscape representing the classes plains and plateau have the highest percentages and more than half of the pixels were classified by these classes. However, considerable differences between all approaches exist. While the proportion of the class plains with approximately 30 % is relatively low for Dikau's scheme, up to three-fourths of the pixels were classified as plains by the object-based approach. In contrast, in the western study area less than 20 % were classified as flat areas in high geometric resolution datasets. There, only 15 % were classified as plains by the object-based approach and less than 6 % by the others. The proportion of this class is largely stable in all spatial resolutions for Dikau's approach, whereby it is strongly increasing for all other approaches in low resolution.

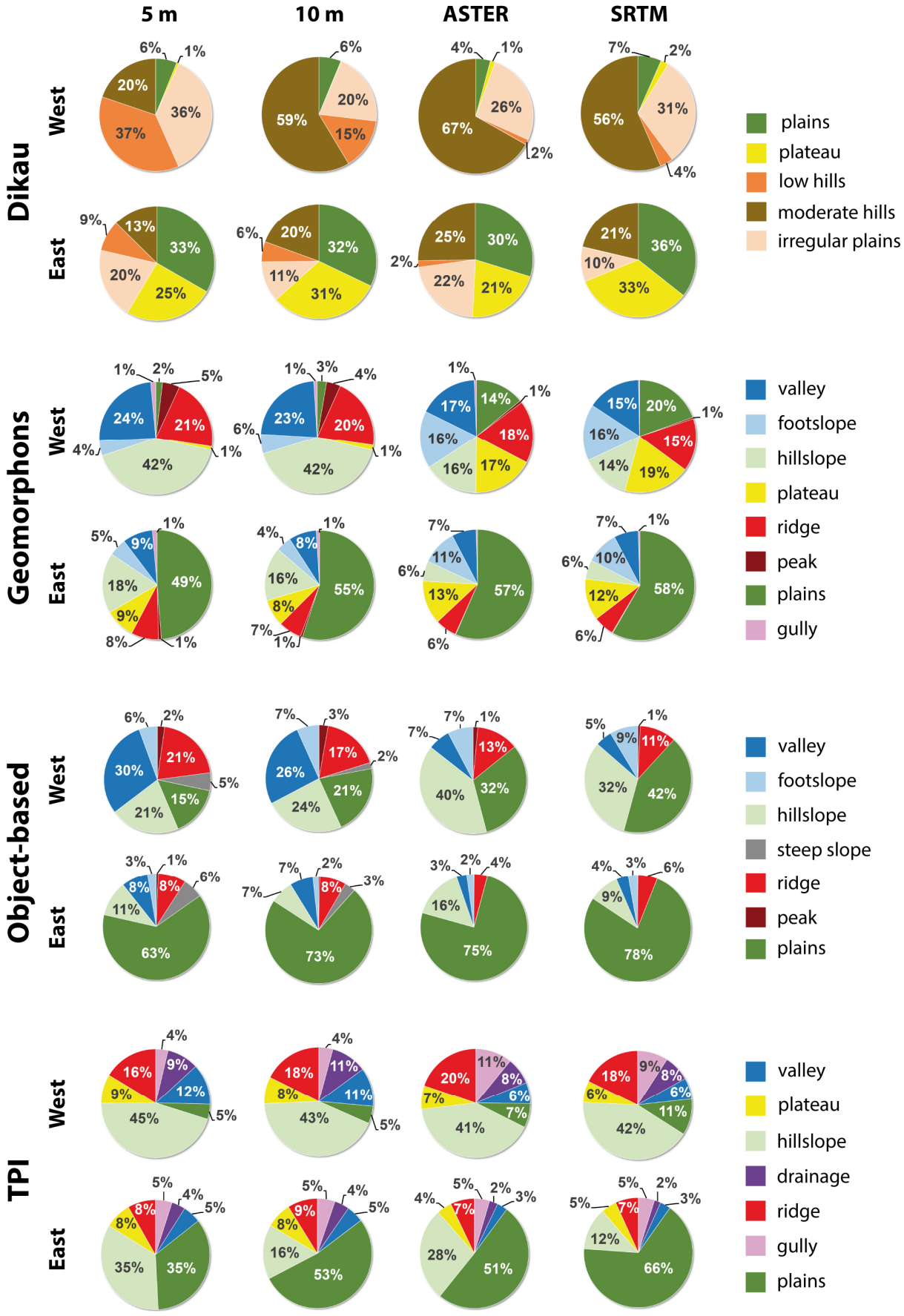

Figure 6-3: Percentage distribution of landform classes for each approach, area and pixel resolution.

In the western study area, the majority of pixels were classified into landform classes that represent hilly areas or incised valley landforms. Over one-fourth of the pixels were classified as valleys, gullies or drainage by all approaches in high spatial resolution datasets. In Dikau's approach, the class irregular plains is the best suitable class for valleys. By this approach, 36 % were classified as irregular plains, which is the highest rate for incised landforms compared to the other approaches. The results in low pixel resolution reveal a strong decrease of classified valleys for the object-based approach. Only 5 % and 7 % were classified as valleys with ASTER and SRTM DEM, respectively. For all other approaches, there is only a minor decrease of percentages. In the eastern study area, the percentages of valleys are slightly lower than in the western site. Apart from that, the results show the same properties in both sites.

Hills are the predominant landforms of the western study area. Therefore, all approaches classified the majority of pixels correctly into landforms, which represent hilly landforms. The percentage of these landforms with around 73 % is the highest for geomorphons with a high geometric resolution DEM. The other approaches classify between 55 % and 61 % as hills. Most of these areas were classified as low and moderate hills by Dikau's scheme and as hillslopes by the others. The percentage of hillslope with around 42 – 45 % is relatively high for geomorphons and TPI, whereas only an area of just over 20 % was classified with this landform class by the object-based approach in high spatial resolution. However, in low spatial resolution, the percentage of hillslope pixels is strongly increasing for the object-based approach, whereas it decreases for the geomorphons approach. By Dikau's approach, the majority was classified with the class low hills in the western area with a pixel resolution of 5 m. With low pixel resolutions, a significant increase in the percentage of the class moderate hills can be observed, whereas the class low hills is almost completely missing. The percentage of uprising landforms is significantly lower in the eastern study area. There, only 20 – 30 % were classified as hilly landforms. Only the TPI shows for the results of 5 m and ASTER a higher proportion of 43 % and 35 %, respectively. This is mainly due to a disproportionately high rate of hillslope landforms.

In Figure 6-4, an exemplary section of the classified landform maps of the eastern classification result is illustrated. It compares the results of the four approaches with the different DEMs. Some differences in the relief subdivision are noticeable. Generally, the approach after Dikau shows the least relief differentiation. All other approaches have more classes to subdivide the relief, whereby a more detailed classification result can be achieved. In particular, the TPI and the geomorphons classify the landscape in a line-like way, which accents the structure of the landscape best. For the object-based approach, the results reveal for the strongly fragmented parts of the landscape some weaknesses of the segmentation technique. Some segments seem to be too big, which leads to a less accurately classification of the landforms in some areas.

A comparison of the different geometric resolutions reveals for all approaches the weakest results for both 30 m classifications. Compared to the results with high pixel resolution, it is apparent that the landforms are classified spatially less accurate and small structures of the landscape were not detected. In contrast, the classification results with a pixel resolution of 5 m and 10 m show a much more differentiated subdivision of the landscape. Besides, they are less different from each other for three of the four approaches. Only for Dikau's approach, significant changes in the results can be observed between all spatial resolution levels.

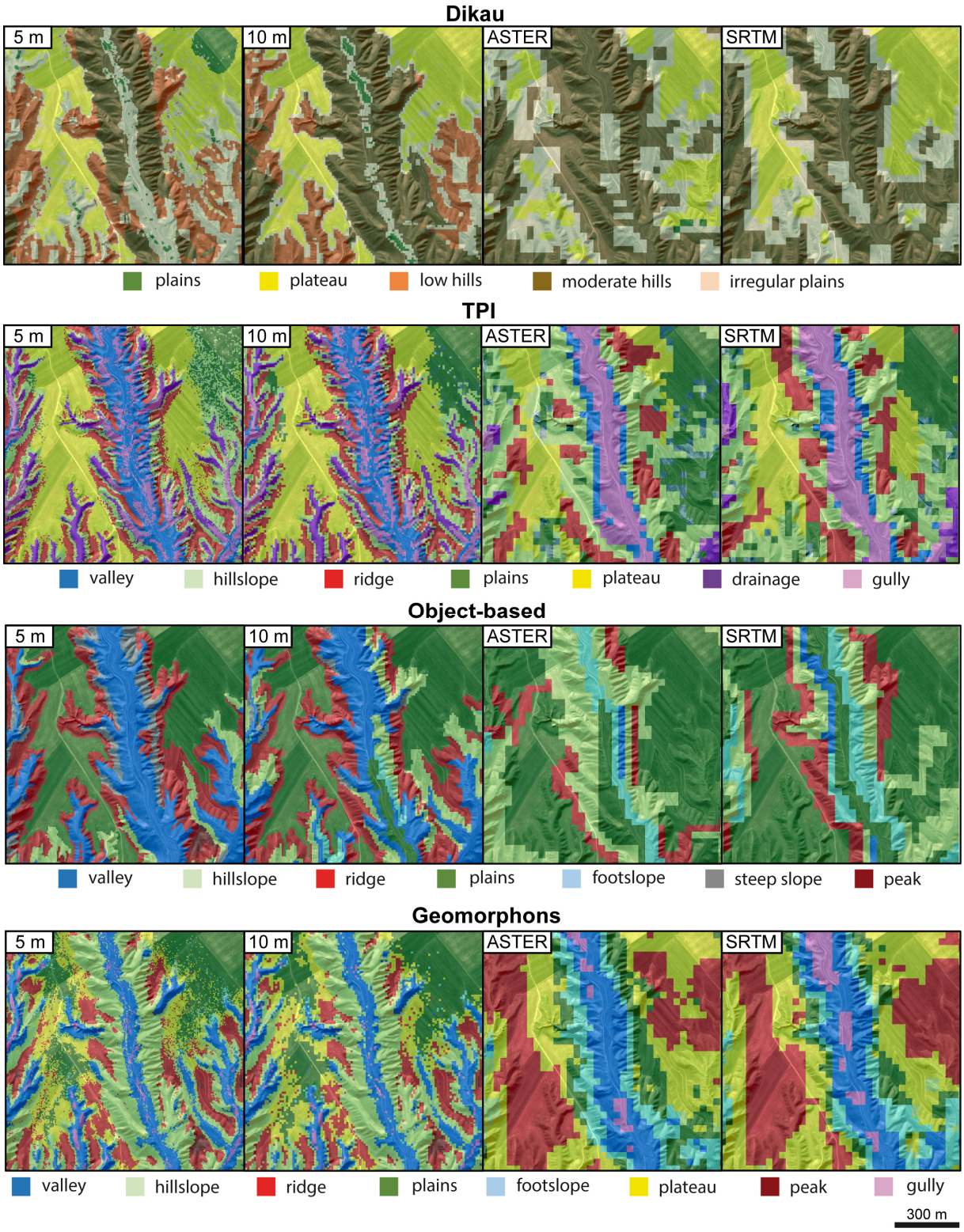

Figure 6-4: Comparison of a selected area, similar to Figure 6-2, for all approaches and different pixel resolutions. Background image: Pléiades satellite imagery © CNES (2015), Distribution Airbus DS.

The classified landscape can be divided into three general landform elements: flat areas, valleys and hills. The results of all approaches are compared in the following in detail for these areas.

- **Flat areas:** with the highest spatial resolution DEM, the TPI approach yielded the weakest results for flat areas in both regions due to a very inhomogeneous classification with the

classes plains and hillslope. The best results here can be observed by the object-based approach. Especially the segmentation technique leads to a very homogeneous classification in wider areas. The geomorphons approach also produces relatively homogeneous results, but only in very large flat areas as they exist in the eastern study area. If the flat area is relatively small, the results demonstrate many misclassifications with the class footslope. Contrary to that, Dikau's approach seems to be the best to classify small flat areas. Here the results of the Western study area show very homogeneous and spatially accurate results, whereas in wider areas many mixtures with the class plateau can be observed.

- **Valleys:** all results reveal that small valleys only were classified with spatially high resolution DEMs. With both 30 m terrain models, only the most distinct valleys were detected by all classification methods. The approach of Dikau classifies them barely even with a pixel resolution of 10 m. Only with a pixel resolution of 5 m this approach is able to classify valleys with the landform class irregular plains. With lower pixel resolutions, this approach is hardly able to detect them. Generally, the results of the TPI have the most diversification in the classification of valleys, caused by the largest variety of classes to divide these landform elements. Therefore, the TPI is the only approach that can distinguish different valley types and assign them to different classes. An observable weakness of this approach is that valleys were classified too broadly and some areas of the neighbouring hills were also classified as valleys (see Figure 6-4). It is also noticeable for this approach that both 30 m results classified the majority of valleys with the class gully, while they were assigned to the class valley in spatially high resolution results. The weakness of too wide classified areas of the class valley can also be observed in the results of the object-based approach. Furthermore, the built segments seem to be spatially inaccurate in some places. In contrast, the most accurate classification of valley widths was achieved by the geomorphons approach with a high pixel resolution DEM. Furthermore, small incisions can be shown separately with the class gully by this approach. However, the general subdivision of different incision types is less differentiated than by the TPI.
- **Hills:** a comparison of the classification results of hilly landforms indicates the least differentiation of the relief with Dikau's approach, caused by the fact that it just classifies these areas with the classes low hills and moderate hills. Furthermore, the results of Dikau's classification show a systematic change in the number of classified landforms with the class low hills. Whereas with a pixel resolution of 5 m the lower hills of the western part of the plateau were assigned correctly as low hills, with both 30 m DEMs almost all hills were classified as moderate hills. All other approaches produce much more diversity in their results, because their classification scheme is able to subdivide the hills into smaller sub elements. Figure 6-5 depicts the classification schemes of the four approaches in spatially high resolution on a typical range of hills in the western study area. In particular, the object-based approach has many suitable classes for a systematic classification of hills. However, the results reveal that the extremely fragmented structure of the hills is often not depicted accurately enough by the segments. Therefore, many classified landforms do not fit properly to the relief and overlap with areas, which should be better classified with another landform class. This leads to the effect that the classification result of the object-based approach seems to be coarser than the results of the TPI and geomorphons approach. A specific feature of the object-based approach is the differentiation between different slope gradients by the classes steep slope

and hillslope. The results demonstrate that the subdivision works properly only with a spatially high resolution DEM. It is observable that the amount of classified steep slope areas decreases strongly for lower pixel resolutions. With a geometric resolution of 30 m, almost no steep slope landforms were detected. The geomorphons approach generally classifies hills with the classes hillslope and the upper parts with the classes ridge and peak. Noticeable is that lower parts were not classified with the class footslope in the results with high pixel resolutions, although this class would be more suitable. A comparison of high- and low resolution results reveals a changed system in the classification of hillsides. Whereas the slopes were assigned to the class hillslope in spatially high resolution results, most areas were classified with the classes footslope and plateau with a low pixel resolution DEM. Furthermore, it is conspicuous that the classified landforms are much coarser with both 30 m DEMs.

The spatially high resolution results of the TPI generally point out a largely reasonable and accurate landform classification of hills. It has minor class diversity than the geomorphons and object-based approach, but especially the classification of hillslope and ridges is highly consistent and accurate. Only the classification of some upper parts of the hills with the class plateau in the western study area seems not meaningful. It seems that this class classifies different landform types in the eastern than in the western area. Therefore, the class name here is only suitable for the eastern part.

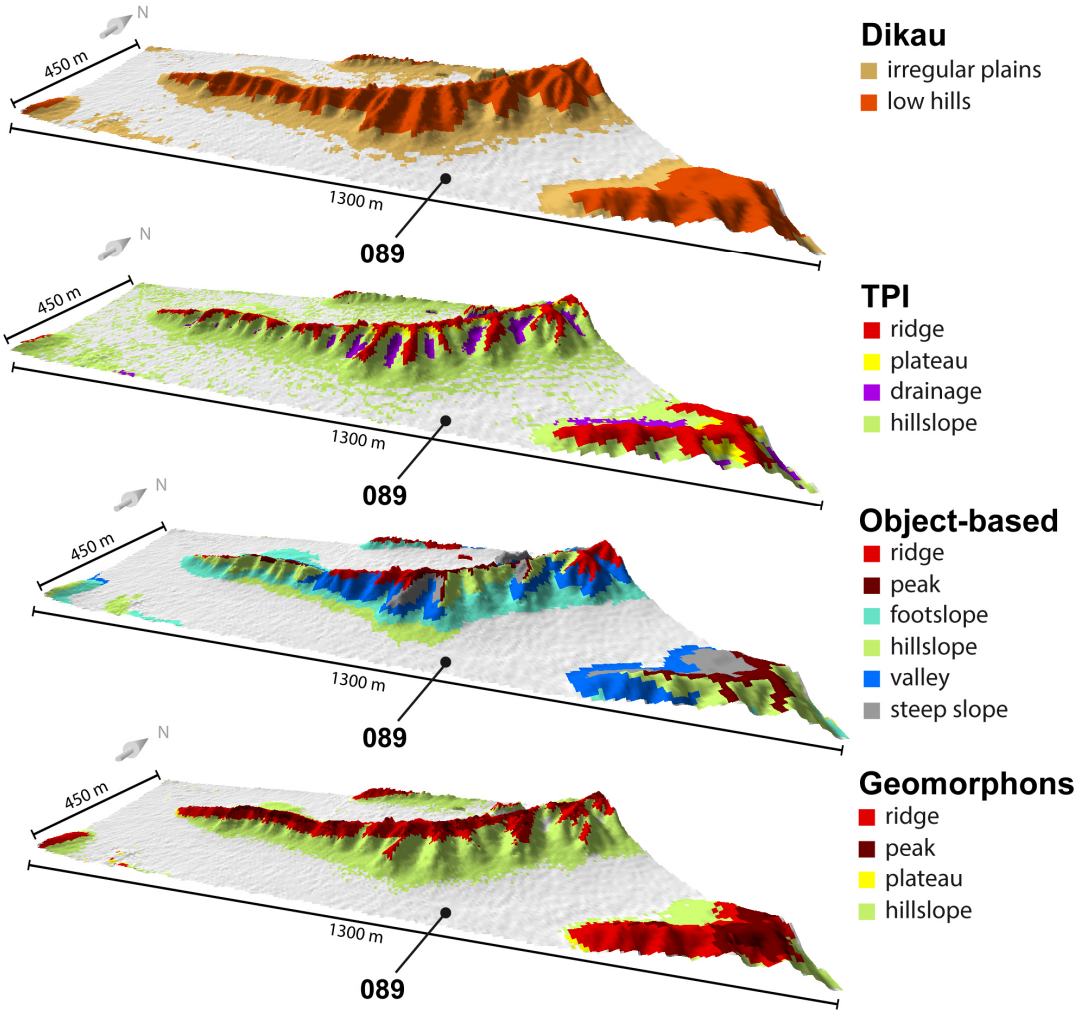

Figure 6-5: Perspective comparison for hilly classes of the different approaches in the highest pixel resolution of 5 m with the assigned picture position in the western study area. White areas represent flat surfaces.

6.4.3 Accuracy assessment

The final classification results were compared with landforms depicted in 66 pictures from both areas. Table 6-7 gives an overview of all achieved overall accuracies. The results show, as expected, a minor accuracy for the DEM with a pixel resolution of 30 m. The variation of the results is higher for the ASTER dataset than for the SRTM dataset. This is mainly due to the very low accuracy of Dikau's approach for this specific area. The higher pixel resolution of the Pléiades dataset results in an increase of 20 – 30 % in the classification accuracy. In addition, the differences in the accuracy between the 5 m and 10 m pixel resolution results are very low. Especially the TPI and the object-based approach achieve nearly the same accuracies in both spatial resolutions. Generally, the accuracy of the TPI approach is the best, followed by the geomorphons approach. The approach of Dikau generated the lowest accuracy, except for the SRTM dataset.

Table 6-7: Overall accuracy of the four approaches and the four different datasets derived as the relation of correctly classified to all classified elements from the confusion matrices (Tables 6-8 – A 6-11).

	5 m	10 m	Aster 30 m	SRTM 30 m
Dikau	63 %	58 %	33 %	42 %
TPI	72 %	71 %	44 %	41 %
Object-based	63 %	63 %	42 %	40 %
Geomorphons	70 %	65 %	39 %	39 %

The error matrices of the four approaches, as listed in Appendix Tables 6-8 – 6-11, generally underline the presented results. For the datasets with a lower spatial resolution, the accuracy decreases by about 20 % to 30 %. For Dikau's scheme (Appendix Table 6-8), the user's accuracy is decreasing on lower pixel resolutions and SRTM shows slightly better results than the ASTER based classification. Plains and low hills are best classified. Likewise, the producer's accuracy points out a decrease to lower pixel resolutions and the classes of irregular plains, low hills and moderate hills show the best fit. In particular, irregular plains and moderate hills are mixed.

For the TPI approach (Appendix Table 6-9), the results of the spatially high resolution Pléiades DEMs produced low user's accuracies for the class of valleys, due to their strong mixture with other flat areas. For the other classes, the majority of ground truth landforms were identified correctly by the TPI approach. Similar to the other approaches, the accuracies decrease strongly for both 30 m datasets for most classes.

The results of the object-based classification (Appendix Table 6-10) indicate generally more stable results over all geometric resolutions. In particular, plains were classified very well in the datasets with 5 m and 10 m pixel resolution. In contrast, in the classification results of the ASTER and SRTM datasets, all steep slope landforms were classified into other landforms and the class was not used at all. Similar results can be recognized for the class peak, which was also classified rarely for 30 m pixel resolution datasets. As the class was relatively often misclassified into the class ridge, the accuracies are generally low. Noticeable is also a strong increase of the number of classified landforms with the classes plains and hillslope in both 30 m datasets, due to misclassifications of other landforms into these classes.

The error matrix of the geomorphons approach in Appendix Table 6-11 shows a general decline of the user's accuracy with both 30 m datasets. The decline between 5 m and 10 m is very small. The

classification of the class footslope works less and was mostly mixed with classifications of plains and valleys. Interestingly, the accuracy rises for the classes of peaks and hillslopes.

6.5 Discussion

A comparison of the different landform classification results reveals strengths and weaknesses for all approaches. Overall, the TPI and the geomorphons approach achieved the highest accuracies. In addition, their classification results give the best visual feedback of the landscape structure of the Iranian loess plateau due to their spatially accurate classification of landforms. In particular, the TPI seems most suitable for a meaningful classification, as it has the highest class diversity for the classification of hills, hillslopes and valleys. However, it revealed some weaknesses in flat landscapes due to a very inhomogeneous classification of these areas with high pixel resolution datasets. In contrast, the geomorphons approach achieves higher accuracies in the classification of plains and valleys. However, it classified the structures of hilly landforms less detailed compared to the TPI, although the number of suitable classes is similar. Nonetheless, both approaches seem to have the highest suitability to classify such a distinct relief at this scale.

In this study, Dikau's approach achieved the lowest accuracies. Moreover, the classification results reveal the least relief differentiation compared to the other approaches. Overall, this approach seems to be least suitable for the classification of such a strongly dissected landscape. Due to its possible landform classes, it is probably more appropriate for the classification of landforms in other spatial scales. In addition, many authors demonstrated in their work a better suitability of the Dikau approach for landscapes on macroscales (Dikau et al., 1995; Gallant et al., 2005; Hrvatin and Perko, 2009; Martins et al., 2016).

The object-based classification produced ambivalent results. The advances of the segmentation technique can only be confirmed here for landforms, which extend over larger areas. Especially flat areas were classified best by this approach because of a high degree of homogeneity. In contrast, weaknesses in the classification of smaller landforms are recognizable in parts with rougher relief. This is mainly the result of a minor spatial accuracy of the built segments in these areas. As a result, the classified landform boundaries are spatially less accurate compared to the applied pixel-based approaches. A more complex segmentation process on different scales would probably avoid this problem. For example, a segmentation on different scale levels, as postulated by Dragut and Eisank (2012), accounts the issue of under-segmentation of small objects or over-segmentation of larger ones.

A comparison of the results in different spatial resolutions clearly demonstrates poor results for all approaches with both 30 m DEMs. Small landforms were not detected and the spatial accuracy of landform borders is less accurate. Only in extensive flat areas of the eastern part, a lower pixel resolution appears to result in a more homogeneous classification compared to the high resolution results. However, differences between the ASTER and the SRTM DEMs are recognizable. Generally, a higher suitability of the SRTM dataset for landform classifications was postulated by several authors (Libohova et al., 2016; Mashimbye et al., 2014; Rexer and Hirt, 2014). This can be confirmed here, as the use of the SRTM DEM results in a more homogeneous landform classification.

Nevertheless, both datasets are not able to achieve promising results in the majority of evaluated areas in this contribution. This is basically due to two main reasons. One reason lies in the DEM itself, as the

strongly dissected relief structure is already insufficiently contained in the input dataset. Generally, lower spatial resolutions lead to a smoother representation of the topography and the relief seems in the DEM much gentler and more rounded as it is in reality (Deng et al., 2007). Therefore, neither the ASTER GDEM nor the SRTM dataset include enough information to classify the very small landscape structures.

The second reason lies in the characteristic of the moving windows, which were used by most approaches in some way to classify landforms. The moving window defines the number of surrounding pixels that were included in the classification process to classify a certain pixel. A suitable definition is difficult due to different landscape characteristics and landform sizes. In the ideal case, it contains only landscape elements, which directly affect the landform of the considered pixel. Bigger window sizes result in too many considered pixels by the classification processes that have no influence on the considered landform. Thus, the choice of the best possible window size depends strongly on the scale of landforms and uneven landscapes mostly require smaller window sizes to represent small features (De Reu et al., 2013; Jasiewicz and Stepinski, 2013). Due to the very small landform elements in the study area, it was necessary for Dikau's approach to define a very small 3 × 3 pixel window already for the 5 m pixel resolution DEM. Thus, a further reduction of contemplated pixels was not possible for lower resolutions, which leads to an enlargement of the window size. The TPI and geomorphons approaches were affected by the same problem, as the minimum window size was reached with a 10 m DEM. As a result, the window size also gets too big with a 30 m pixel resolution DEM. In consequence, small landforms were not classified and bigger landforms were interpreted in false dimensions and assigned to incorrect classes. This effect is clearly recognizable in the results of the TPI where landforms, which were classified as valleys with a high-pixel resolution DEM, were assigned to class gully in lower resolutions. Hence, a differentiation between gullies and valleys was not possible. In addition, the number of classified peaks decreases significantly in lower resolutions in the results of the geomorphons approach.

The results clearly point out that a geometric resolution of at least 10 m is necessary for an accurate classification of such a strongly dissected relief. With both 30 m DEMs, no approaches are able to achieve sufficient results. A comparison of the classification results of the western and eastern study area indicate that flatter areas are less sensitive to resolution changes. Furthermore, low spatial resolutions lead to an increase of homogeneity. Thus, it can be confirmed here that the flatter the landscape is, the lower the spatial DEM resolution can be to achieve accurate classification results. In this contribution, the best results were achieved with a pixel resolution of 5 m. For such a strongly varying landscape, also a higher pixel resolution of around 3 m would probably effectuate results of similar quality, but higher pixel resolutions increase the risk of an over-classification of landforms. With a decreasing pixel size, too many micro-scaled landforms were identified, which were not necessary for further landscape interpretations (Libohova et al., 2016).

The accuracy assessment method conducted in this contribution provides reproducible results. However, a quantitative evaluation of landform classifications is still problematic. First, the acquisition of ground truth data is often time consuming and depends on the suitability of the terrain (Dragut and Blaschke, 2006; Saadat et al., 2008). Second, in this contribution, a relatively high number of photos were required to collect enough ground truth data for all classes to produce a statistically valid dataset. Furthermore, weaknesses still exist in the evaluation methodology itself. Several studies have shown that an accuracy assessment with ground truth based error matrices is able to produce suitable results

for geomorphometric classifications. However, a quantitative accuracy assessment of landform classifications is problematic as there still exists a lack of standardized applicable methods. Several authors have found different solutions to extract their ground truth data and compare them with their results. Some studies interpreted landforms from aerial or ground taken photos and generated ground truth samples to conduct an evaluation landform. Schneevoigt et al. (2008) defined test areas for each landform from photo material, but evaluated them pixel-based. Others generated a reference map from map data or field investigations and compared it pixel-wise to their results (Pedersen, 2016; Vannametee et al., 2014).

A pixel-wise comparison seemed unsuitable in this study, as this would have overrepresented some landforms due to their spatial extent. Landforms vary strongly in their extent, as there exist point-based, line-based and areal landforms (Evans, 2012). Consequently, in a pixel-wise evaluation, the class plains as an areal landform would have contained much more pixels in the error matrix than the class peak as a point-based landform. This would have led to a significant overrepresentation of some landforms in a pixel-wise evaluation process. Therefore, a landform-wise comparison method was applied here to avoid the influence of the spatial extent of landforms. In addition, the comparison is not biased by positional errors of the input datasets or the varying notation and detail of the applied approaches.

A major problem in geomorphometric analyses is that a clear delimitation of landforms is often not possible, as they do not have distinct boundaries (Dragut and Blaschke, 2006; Evans, 2012). Hence, the interpretation of these landforms is rather subjective. Moreover, a standardization of the classes between the different approaches was not completely possible in this contribution due to the diverse creation processes of the different approaches. Landform classes with the same name potentially do not exactly represent the same real landform, what makes them not completely comparable. In consequence, a high effort and dependency on the knowledge of the interpreter are still necessary for the interpretation and delineation of landforms. Furthermore, some influence of subjectivity on the evaluation process cannot be prevented.

6.6 Conclusions

Landform classifications can be derived by a high diversity of possible input data, different approaches and result in a multiplicity of landform classes. In this contribution, a comparison of four prominent approaches was conducted with four input datasets with different spatial resolutions and different measurement methods. The results show for the selected areas of the Iranian loess plateau, which is highly dissected, that higher resolution datasets are necessary to achieve satisfying overall accuracies. With the 5 m Pléiades DEM, the TPI and geomorphons approach achieved accuracies of greater than 70 % and the two other approaches reached overall accuracies of greater than 60 %. SRTM data worked generally better than ASTER GDEM data, but both elevation models are not able to generate accurate classification results here and only achieved accuracies of about 40 %. Thus, a decrease of 20 – 30 % for the lower spatial resolution datasets is detected. This variety in accuracy needs to be regarded before applying the derived landforms for further calculations. We expect that the applied methodological approach will lead to similar results concerning the accuracy of landform classifications if applied to other areas with similar landform characteristics. As shown here, the differences between the approaches and resolutions are smaller for areas with more flat terrain. All selected approaches

show weaknesses; in this case, the TPI and geomorphons approach revealed the best results and are more detailed in terms of derivable landform types. The approach of Dikau is generally less suitable for these areas and the approach based on the object segmentation is less accurate for areas with a rougher relief. However, the selection of moving window size and the accurate derivation of objects influences the results. The accuracy assessment of these classifications and the delineation between different landforms are influenced by the user.

Acknowledgments: The authors gratefully acknowledge the funding by the German Research Foundation (DFG) that allowed this study: 'Remote sensing methods as a base for landform and soil maps of the Iranian loess plateau' (HO-5515/2-1). We thank our Iranian partners for the warm welcome and support during the field campaign.

Author contributions: Tanja Kramm carried out the remote sensing and GIS analysis of the contribution and extensively helped to write the manuscript. Dirk Hoffmeister designed the study, drafted and wrote the manuscript. Constanze Curdt, Sedigheh Maleki, Dirk Hoffmeister, Farhad Khormali and Martin Kehl conducted the fieldwork. Constanze Curdt and Martin Kehl participated in the design of the study and helped to improve the manuscript. All authors read and approved the final version.

Conflicts of interest: The authors declare no conflict of interest.

6.7 Appendix

Table 6-8: Error matrix based on classified landform units for Dikau's approach for the four different DEMs (5 = 5 m, 10 = 10 m, A = Aster 30 m, S = SRTM 30 m) with producer's accuracy (PA) and user's accuracy (UA).

		Reference data																											
	landform class	**plains**				**plateau**				**irregular plains**				**low hills**				**moderate hills**				**Total**				**UA (%)**			
		5	**10**	**A**	**S**	**5**	**10**	**A**	**S**	**5**	**10**	**A**	**S**	**5**	**10**	**A**	**S**	**5**	**10**	**A**	**S**	**5**	**10**	**A**	**S**	**5**	**10**	**A**	**S**
Classification	**plains**	11	11	5	9	1	2	3	3	2	3	5	7	0	0	0	2	0	0	0	0	14	16	13	21	79	69	38	43
	plateau	3	3	0	0	4	3	2	2	0	1	0	0	0	0	0	1	0	0	0	1	7	7	2	4	57	43	100	50
	irregular plains	9	6	8	6	2	1	2	2	18	13	9	13	3	4	4	6	0	0	7	8	32	24	30	35	56	54	30	37
	low hills	0	0	0	0	0	0	0	0	0	0	0	0	15	11	0	1	9	1	0	0	24	12	0	1	63	92	-	100
	moderate hills	1	1	5	2	0	2	2	1	3	9	12	5	4	8	16	13	16	18	16	16	24	38	51	37	67	47	31	43
	Total	24	21	18	17	7	8	9	8	23	26	26	25	22	23	20	23	25	19	23	25	101	97	96	98				
	PA (%)	46	52	28	53	57	38	22	25	78	50	35	52	68	48	0	4	64	95	70	64								

Table 6-9: Error matrix based on classified landform units for the TPI approach for the four different DEMs (5 = 5 m, 10 = 10 m, A = Aster 30 m, S = SRTM 30 m) with producer's accuracy (PA) and user's accuracy (UA).

		Reference data																																	
	landform class	**gully**				**drainage**				**valley**				**plains**				**hillslope**				**plateau**				**ridge**				**Total**				**UA (%)**			
		5	**10**	**A**	**S**	**5**	**10**	**A**	**S**	**5**	**10**	**A**	**S**	**5**	**10**	**A**	**S**	**5**	**10**	**A**	**S**	**5**	**10**	**A**	**S**	**5**	**10**	**A**	**S**	**5**	**10**	**A**	**S**	**5**	**10**	**A**	**S**
Classification	**gully**	13	12	9	9	2	1	2	2	4	3	12	12	0	1	5	3	3	1	5	4	0	0	1	1	0	0	3	1	22	18	37	32	59	67	24	28
	drainage	1	1	1	1	9	8	1	1	1	0	2	1	1	0	2	3	4	3	2	1	0	0	0	0	0	0	0	0	16	12	8	7	56	67	13	14
	valley	3	2	2	2	0	0	0	0	13	12	2	2	10	8	2	6	6	8	3	3	0	0	0	0	2	1	3	4	34	31	12	17	38	39	17	12
	plains	0	0	1	1	0	0	0	0	2	1	1	1	11	12	8	8	1	1	1	3	0	0	0	0	0	0	1	3	14	14	12	16	79	86	67	50
	hillslope	0	0	1	0	0	0	3	4	1	0	0	0	3	4	3	2	24	18	15	14	2	2	2	2	0	3	10	10	30	27	34	32	80	67	44	44
	plateau	0	0	0	0	0	0	1	2	0	0	0	0	0	0	0	0	1	2	2	3	7	5	3	3	0	0	1	4	8	7	7	12	88	71	43	25
	ridge	0	0	0	0	0	0	3	2	0	0	0	0	0	0	1	0	1	0	2	2	0	1	1	1	47	38	23	21	48	39	30	26	98	97	77	81
	Total	17	15	14	13	11	9	10	11	21	16	17	16	25	25	21	22	40	33	30	30	9	8	7	7	49	42	41	43	172	148	140	142				
	PA (%)	76	80	64	69	82	89	10	9	62	75	12	13	44	48	38	36	60	55	50	47	78	63	43	43	96	90	56	49								

Table 6-10: Error matrix based on classified landform units for the object-based approach for the four different DEMs (5 = 5 m, 10 = 10 m, A = Aster 30 m, S = SRTM 30 m) with producer's accuracy (PA) and user's accuracy (UA).

		Reference data																															
	landform class	**peak**				**ridge**				**steep slope**				**plains**				**hillslope**				**valley**				**footslope**				**Total**				**UA (%)**			
		5	**10**	**A**	**S**	**5**	**10**	**A**	**S**	**5**	**10**	**A**	**S**	**5**	**10**	**A**	**S**	**5**	**10**	**A**	**S**	**5**	**10**	**A**	**S**	**5**	**10**	**A**	**S**	**5**	**10**	**A**	**S**	**5**	**10**	**A**	**S**
Classification	**peak**	5	6	4	0	5	4	0	0	0	0	0	0	0	0	0	0	0	0	1	0	0	0	0	0	0	0	0	0	10	10	5	0	50	60	80	-
	ridge	7	6	8	8	21	21	13	10	0	1	1	4	0	0	0	0	3	4	3	1	0	0	2	0	0	0	1	0	31	32	28	23	68	66	46	43
	steep slope	0	0	0	0	0	0	0	0	6	5	0	0	0	0	0	0	4	3	0	0	0	0	0	0	0	0	0	0	10	8	0	0	60	63	-	-
	plains	0	0	0	1	0	0	7	8	0	0	0	0	22	23	17	25	0	0	5	11	2	4	2	12	0	0	2	3	24	27	33	60	92	85	52	42
	hillslope	0	0	0	1	3	2	8	10	3	3	7	3	2	0	10	1	11	13	12	12	3	0	8	2	0	1	2	3	22	19	47	32	50	68	26	38
	valley	0	0	0	0	2	1	0	0	0	0	0	3	2	1	3	1	10	12	2	3	18	18	12	7	3	3	1	0	35	35	18	14	51	51	67	50
	footslope	0	0	0	0	1	1	1	0	0	1	1	1	2	3	2	1	1	0	5	3	2	4	4	4	9	7	4	3	15	16	17	12	60	44	24	25
	Total	12	12	12	10	32	29	29	28	9	10	9	11	28	27	32	28	29	32	28	30	25	26	28	25	12	11	10	9	147	147	148	141				
	PA (%)	42	50	33	0	66	72	45	36	67	50	0	0	79	85	53	89	38	41	43	40	72	69	43	28	75	64	40	33								

Table 6-11: Error matrix based on classified landform units for the geomorphons approach for the four different DEMs (5 = 5 m, 10 = 10 m, A = Aster 30 m, S = SRTM 30 m) with producer's accuracy (PA) and user's accuracy (UA).

		Reference data																																			
	landform	**plains**				**peak**				**ridge**				**plateau**				**hillslope**				**footslope**				**valley**				**gully**				**Total**				**UA (%)**			
	class	**5**	**10**	**A**	**S**	**5**	**10**	**A**	**S**	**5**	**10**	**A**	**S**	**5**	**10**	**A**	**S**	**5**	**10**	**A**	**S**	**5**	**10**	**A**	**S**	**5**	**10**	**A**	**S**	**5**	**10**	**A**	**S**	**5**	**10**	**A**	**S**	**5**	**10**	**A**	**S**
Classification	**plains**	9	7	4	5	0	0	0	0	0	0	1	1	0	0	0	1	0	0	2	3	0	0	0	0	0	0	0	1	0	0	0	0	9	7	7	11	100	100	57	45
	peak	0	0	0	0	8	8	1	1	6	7	0	0	0	0	0	0	0	0	1	0	0	0	0	0	0	0	0	0	0	0	0	0	14	15	2	1	57	53	50	100
	ridge	1	1	0	0	2	1	4	6	24	19	13	9	0	1	1	1	4	6	3	2	0	0	0	0	0	0	2	0	0	0	0	0	31	28	23	18	77	68	57	50
	plateau	0	0	0	0	0	0	1	0	0	0	3	8	3	2	3	1	0	0	6	6	0	0	0	0	0	0	2	1	0	0	0	0	3	2	15	16	100	100	20	6
	hillslope	4	3	1	0	0	0	0	0	3	3	3	2	2	0	0	1	23	20	5	9	2	3	1	0	0	1	0	0	0	0	0	0	34	30	10	12	68	67	50	75
	footslope	6	5	7	7	0	0	1	1	0	0	3	2	0	0	1	1	0	2	6	5	5	2	6	6	2	0	7	8	0	0	0	0	13	9	31	30	38	22	19	20
	valley	3	8	8	8	0	0	2	1	1	1	2	5	0	1	2	0	5	1	5	4	0	0	0	0	30	31	24	24	3	5	8	8	42	47	51	50	71	66	47	48
	gully	0	0	0	1	0	0	0	0	0	0	1	0	0	0	0	0	0	0	1	0	0	0	0	0	6	3	4	3	12	9	1	0	18	12	7	4	67	75	14	0
	Total	23	24	20	21	10	9	9	9	34	30	26	27	5	4	7	5	32	29	29	29	7	5	7	6	38	35	39	37	15	14	9	8	164	150	146	142				
	PA (%)	39	29	20	24	80	89	11	11	71	63	50	33	60	50	43	20	72	69	17	31	71	40	86	100	79	89	62	65	80	64	11	0								

6.8 References

Abrams, M., 2000. The Advanced Spaceborne Thermal Emission and Reflection Radiometer (ASTER): data products for the high spatial resolution imager on NASA's Terra platform. International Journal of Remote Sensing, 21 (5), 847-859. doi: 10.1080/014311600210326.

Abrams, M., Tsu, H., Hulley, G., Iwao, K., Pieri, D., Cudahy, T., Kargel, J., 2015. The Advanced Spaceborne Thermal Emission and Reflection Radiometer (ASTER) after fifteen years: Review of global products. International Journal of Applied Earth Observation and Geoinformation, 38, 292-301. doi: 10.1016/j.jag.2015.01.013.

Armstrong, R.N., Martz, L.W., 2003. Topographic parameterization in continental hydrology: a study in scale. Hydrological Processes, 17 (18), 3763-3781. doi: 10.1002/hyp.1352.

Astrium GEO-Information Services, 2012. Pléiades Imagery User Guide V 2.0. Astrium Services.

Barka, I., Vladovic, J., Malis, F., 2011. Landform Classification and Its Application in Predictive Mapping of Soil and Forest Units. In Proceedings of the GIS Ostrava, Ostrava, Czech Republic, 24–26 January 2011, p. 11.

Behrens, T., Schmidt, K., Ramirez-Lopez, L., Gallant, J., Zhu, A.X., Scholten, T., 2014. Hyper-scale digital soil mapping and soil formation analysis. Geoderma, 213, 578-588. doi: 10.1016/j.geoderma.2013.07.031.

Behrens, T., Zhu, A.X., Schmidt, K., Scholten, T., 2010. Multi-scale digital terrain analysis and feature selection for digital soil mapping. Geoderma, 155 (3-4), 175-185. doi: 10.1016/j.geoderma.2009.07.010.

Bishop, M.P., James, L.A., Shroder, J.F., Walsh, S.J., 2012. Geospatial technologies and digital geomorphological mapping: Concepts, issues and research. Geomorphology, 137 (1), 5-26. doi: 10.1016/j.geomorph.2011.06.027.

Brabyn, L., 1998. GIS Analysis of Macro Landform, 10th Colloquium of the Spatial Information Research Centre. Proceedings of the Spatial Information Research Centre's 10th Colloquium, University of Otago, New Zealand, 16–19 November 1998, 35–48.

Bretis, B., Grasemann, B., Conradi, F., 2012. An Active Fault Zone in the Western Kopeh Dagh (Iran). Austrian Journal of Earth Sciences, 105 (3), 95-107.

Burrough, P.A., van Gaans, P.F.M., MacMillan, R.A., 2000. High-resolution landform classification using fuzzy k-means. Fuzzy Sets and Systems, 113 (1), 37-52. doi: 10.1016/S0165-0114(99)00011-1.

Camiz, S., Poscolieri, M., Roverato, M., 2017. Geomorphometric comparative analysis of Latin-American volcanoes. Journal of South American Earth Sciences, 76, 47-62. doi: 10.1016/j.jsames.2017.02.011.

D'Oleire-Oltmanns, S., Eisank, C., Dragut, L., Blaschke, T., 2013. An Object-Based Workflow to Extract Landforms at Multiple Scales From Two Distinct Data Types. IEEE Geoscience and Remote Sensing Letters, 10 (4), 947-951. doi: 10.1109/Lgrs.2013.2254465.

De Lussy, F., Kubik, P., Greslou, D., Pascal, V., Gigord, P., P., C.J., 2006. Pleiades-HR Image System Products and Quality. Pleiades-HR Image System Products and Geometric Accuracy. Proceedings of the ISPRS Hannover Workshop, Hannover, Germany.

De Reu, J., Bourgeois, J., Bats, M., Zwertvaegher, A., Gelorini, V., De Smedt, P., Chu, W., Antrop, M., De Maeyer, P., Finke, P., Van Meirvenne, M., Verniers, J., Crombe, P., 2013. Application of the topographic position index to heterogeneous landscapes. Geomorphology, 186, 39-49. doi: 10.1016/j.geomorph.2012.12.015.

Dekavalla, M., Argialas, D., 2017. Object-based classification of global undersea topography and geomorphological features from the SRTM30_PLUS data. Geomorphology, 288, 66-82. doi: 10.1016/j.geomorph.2017.03.026.

Deng, Y., Wilson, J.P., Bauer, B.O., 2007. DEM resolution dependencies of terrain attributes across a landscape. International Journal of Geographical Information Science, 21 (1-2), 187-213. doi: 10.1080/13658810600894364.

Dikau, R., Brabb, E.E., Mark, R.M., Pike, R.J., 1995. Morphometric Landform Analysis of New Mexico. Zeitschrift für Geomorphologie, 101, 109-126.

Dragut, L., Blaschke, T., 2006. Automated classification of landform elements using object-based image analysis. Geomorphology, 81 (3-4), 330-344. doi: 10.1016/j.geomorph.2006.04.013.

Dragut, L., Eisank, C., 2012. Automated object-based classification of topography from SRTM data. Geomorphology, 141, 21-33. doi: 10.1016/j.geomorph.2011.12.001.

Evans, I.S., 2012. Geomorphometry and landform mapping: What is a landform? Geomorphology, 137 (1), 94-106. doi: 10.1016/j.geomorph.2010.09.029

Farr, T.G., Rosen, P.A., Caro, E., Crippen, R., Duren, R., Hensley, S., Kobrick, M., Paller, M., Rodríguez, E., Roth, L., Seal, D., Shaffer, S., Shimada, J., Umland, J., Werner, M., Oskin, M., Burbank, D., Alsdorf, D., 2007. The shuttle radar topography mission. Reviews of Geophysics, 45 (2). doi: 10.1029/2005rg000183.

Florinsky, I.V., 2012. Digital terrain analysis in soil science and geology. Elsevier/Academic Press, Amsterdam, The Netherlands.

Frechen, M., Kehl, M., Rolf, C., Sarvati, R., Skowronek, A., 2009. Loess chronology of the Caspian Lowland in Northern Iran. Quaternary International, 198, 220-233. doi: 10.1016/j.quaint.2008.12.012.

Gallant, A.L., Brown, D.D., Hoffer, R.M., 2005. Automated mapping of Hammond's landforms. IEEE Geoscience and Remote Sensing Letters, 2 (4), 384-388. doi: 10.1109/Lgrs.2005.848529.

Gleyzes, M.A., Perret, L., Kubik, P., 2012. Pleiades System Architecture and Main Performances, International Archives of the Photogrammetry, Remote Sensing and Spatial Information Sciences. XXII ISPRS Congress, Australia, Melbourne, 537-542. doi: 10.5194/isprsarchives-XXXIX-B1-537-2012.

Hammond, E.H., 1954. Small-Scale Continental Landform Maps. Annals of the Association of American Geographers, 44 (1), 33-42. doi: 10.1080/00045605409352120.

Hammond, E.H., 1964. Aanalysis of Properties in Land and Geography: An Application to Broad-Scale Land Form Mapping. Annals of the Association of American Geographers, 54 (1), 11-19. doi: 10.1111/j.1467-8306.1964.tb00470.x.

Hirano, A., Welch, R., Lang, H., 2003. Mapping from ASTER stereo image data: DEM validation and accuracy assessment. ISPRS Journal of Photogrammetry and Remote Sensing, 57 (5-6), 356-370. doi: 10.1016/S0924-2716(02)00164-8.

Hrvatin, M., Perko, D., 2009. Suitability of Hammond's method for determining landform units in Slovenia. Acta geographica Slovenica, 42 (2), 343-366. doi: 10.3986/AGS49204.

Iwahashi, J., Pike, R.J., 2007. Automated classifications of topography from DEMs by an unsupervised nested-means algorithm and a three-part geometric signature. Geomorphology, 86 (3-4), 409-440. doi: 10.1016/j.geomorph.2006.09.012.

Jasiewicz, J., Stepinski, T.F., 2013. Geomorphons - a pattern recognition approach to classification and mapping of landforms. Geomorphology, 182, 147-156. doi: 10.1016/j.geomorph.2012.11.005.

Kehl, M., 2010. Quaternary loesses, loess-like sediments, soils and climate change in Iran. Relief, Boden, Paläoklima. Gebrüder Borntraeger, Stuttgart, Germany.

Khormali, F., Ajami, M., 2011. Pedogenetic investigation of soil degradation on a deforested loess hillslope of Golestan Province, Northern Iran. Geoderma, 167-68, 274-283. doi: 10.1016/j.geoderma.2011.07.030.

Kienzle, S., 2004. The Effect of DEM Raster Resolution on First Order, Second Order and Compound Terrain Derivatives Transactions in GIS, 8 (1), 83-111. doi: 10.1111/j.1467-9671.2004.00169.x.

Klingseisen, B., Metternicht, G., Paulus, G., 2008. Geomorphometric landscape analysis using a semi-automated GIS-approach. Environmental Modelling & Software, 23 (1), 109-121. doi: 10.1016/j.envsoft.2007.05.007.

Lauer, T., Vlaminck, S., Frechen, M., Rolf, C., Kehl, M., Sharifi, J., Lehndorff, E., Khormali, F., 2017. The Agh Band loess-palaeosol sequence - A terrestrial archive for climatic shifts during the last and

penultimate glacialeinterglacial cycles in a semiarid region in northern Iran. Quaternary International, 429, 13-30. doi: 10.1016/j.quaint.2016.01.062.

Libohova, Z., Winzeler, H.E., Lee, B., Schoeneberger, P.J., Datta, J., Owens, P.R., 2016. Geomorphons: Landform and property predictions in a glacial moraine in Indiana landscapes. Catena, 142, 66-76. doi: 10.1016/j.catena.2016.01.002.

MacMillan, R.A., Pettapiece, W.W., Nolan, S.C., Goddard, T.W., 2000. A generic procedure for automatically segmenting landforms into landform elements using DEMs, heuristic rules and fuzzy logic. Fuzzy Sets and Systems, 113 (1), 81-109. Doi: 10.1016/S0165-0114(99)00014-7.

Martins, F.M.G., Fernandez, H.M., Isidoro, J.M.G.P., Jordan, A., Zavala, L., 2016. Classification of landforms in Southern Portugal (Ria Formosa Basin). Journal of Maps, 12 (3), 422-430. doi: 10.1080/17445647.2015.1035346.

Mashimbye, Z.E., de Clercq, W.P., Van Niekerk, A., 2014. An evaluation of digital elevation models (DEMs) for delineating land components. Geoderma, 213, 312-319. doi: 10.1016/j.geoderma.2013.08.023.

Pedersen, G.B.M., 2016. Semi-automatic classification of glaciovolcanic landforms: An object-based mapping approach based on geomorphometry. Journal of Volcanology and Geothermal Research, 311, 29-40. doi: 10.1016/j.jvolgeores.2015.12.015.

Pennock, D.J., Zebarth, B.J., Dejong, E., 1987. Landform Classification and Soil Distribution in Hummocky Terrain, Saskatchewan, Canada. Geoderma, 40 (3-4), 297-315. doi: 10.1016/0016-7061(87)90040-1.

Pike, R.J., Park, M., 1995. Geomorphometry—Progress, practice and prospect. Zeitschrift für Geomorphologie, 101, 221-235.

Rexer, M., Hirt, C., 2014. Comparison of free high resolution digital elevation data sets (ASTER GDEM2, SRTM v2.1/v4.1) and validation against accurate heights from the Australian National Gravity Database. Australian Journal of Earth Sciences, 61 (2), 213-226. doi: 10.1080/08120099.2014.884983.

Saadat, H., Bonnell, R., Sharifi, F., Mehuys, G., Namdar, M., Ale-Ebrahim, S., 2008. Landform classification from a digital elevation model and satellite imagery. Geomorphology, 100 (3-4), 453-464. doi: 10.1016/j.geomorph.2008.01.011.

Schmidt, J., Hewitt, A., 2004. Fuzzy land element classification from DTMs based on geometry and terrain position. Geoderma, 121 (3-4), 243-256. doi: 10.1016/j.geoderma.2003.10.008.

Schneevoigt, N.J., van der Linden, S., Thamm, H.P., Schrott, L., 2008. Detecting Alpine landforms from remotely sensed imagery. A pilot study in the Bavarian Alps. Geomorphology, 93 (1-2), 104-119. doi: 10.1016/j.geomorph.2006.12.034.

Schwanghart, W., Groom, G., Kuhn, N.J., Heckrath, G., 2013. Flow network derivation from a high resolution DEM in a low relief, agrarian landscape. Earth Surface Processes and Landforms, 38 (13), 1576-1586. doi: 10.1002/esp.3452.

Tachikawa, T., Kaku, M., Iwasaki, A., Gesch, D.B., Oimoen, M.J., Zhang, Z., Danielson, J.J., Krieger, T., Curtis, B., Haase, J., Abrams, M., Carabajal, C., 2011. ASTER Global Digital Elevation Model Version 2 - summary of validation results. NASA, Washington, DC, USA.

Van Asselen, S., Seijmonsbergen, A.C., 2006. Expert-driven semi-automated geomorphological mapping for a mountainous area using a laser DTM. Geomorphology, 78 (3-4), 309-320. doi: 10.1016/j.geomorph.2006.01.037.

Vannametee, E., Babel, L.V., Hendriks, M.R., Schuur, J., de Jong, S.M., Bierkens, M.F.P., Karssenberg, D., 2014. Semi-automated mapping of landforms using multiple point geostatistics. Geomorphology, 221, 298-319. doi: 10.1016/j.geomorph.2014.05.032.

Weiss, A.D., 2001. Topographic Position and Landforms Analysis, ESRI Users Conference, San Diego, CA, USA.

Wood, S.W., Murphy, B.P., Bowman, D.M.J.S., 2011. Firescape ecology how topography determines the contrasting distribution of fire and rain forest in the south-west of the Tasmanian

Wilderness World Heritage Area. Journal of Biogeography, 38 (9), 1807-1820. doi: 10.1111/j.1365-2699.2011.02524.x.

Yokoyama, R., Shirasawa, M., Pike, R.J., 2002. Visualizing topography by Openness: A new application of image processing to digital elevation models. Photogrammetric Engineering and Remote Sensing, 68 (3), 257-265.

Zhang, W.H., Montgomery, D.R., 1994. Digital Elevation Model Grid Size, Landscape Representation, and Hydrologic Simulations. Water Resources Research, 30 (4), 1019-1028. doi: 10.1029/93WR03553.

Zink, M., Bachmann, M., Brautigam, B., Fritz, T., Hajnsek, I., Krieger, G., Moreira, A., Wessel, B., 2014. TanDEM-X: The New Global DEM Takes Shape. IEEE Geoscience and Remote Sensing Magazine, 2 (2), 8-23. doi: 10.1109/Mgrs.2014.2318895.

7 Assessing the influence of environmental factors and datasets on soil type prediction with two machine learning algorithms in a heterogeneous area in the Rur catchment, Germany

TANJA KRAMM[1], DIRK HOFFMEISTER[1]

Published in: Geoderma Regional, 2020, **22**, e00316.

DOI: 10.1016/j.geodrs.2020.e00316

Formatting and orthography of the manuscript is adapted to the dissertation style.

[1]GIS and Remote Sensing, Institute of Geography, University of Cologne, Albertus Magnus Platz, 50923 Köln, Germany.

Abstract

Machine learning (ML) algorithms are a promising alternative to traditional acquisition methods for creating new or updating existing soil maps. This study analyses the suitability of two ML techniques for the prediction of 36 different soil types in the Rur catchment in North-Rhine Westphalia (Germany). For this purpose, the performance of random forest (RF) and artificial neural network (ANN) classifiers have been investigated for three different scenarios with varying environmental co-variables for prediction and two varying training datasets with different sampling strategies. It has been analysed how the accuracy of classified digital soil map products is affected by the diversity of available soil types within different landscapes of the catchment, by varying topography as well as different spatial resolutions of the co-variables and the distribution of training points. Co-variables derived from a digital elevation model (DEM) were once generated with a high resolution DEM from airborne laser scanning data in a spatial resolution of 15 m and once with the 90 m TanDEM-X WorldDEM™. Results generally show the best performance for the RF classification with overall accuracies (OA) over 70 % with a spatially homogenized training dataset. The ANN classifier performed on average about 5 % lower compared to RF. Furthermore, it could be shown for both algorithms that the OA is about 15 % – 25 % lower for areas in the northernmost and central part of the study area with a very diverse distribution of soil types, compared to other regions with only a few dominating soil types. Particularly for the ANN classifier with spatially homogenized training samples, the observed drop in accuracy was considerably high for heterogeneous regions. A comparison of different predictor variables from different DEM sources with greatly varying spatial resolutions showed similar results for both datasets and an increase of accuracy with higher spatial resolutions could not be detected here. Overall, the classification accuracy is mainly affected by the sampling strategy of training samples, the diversity of distributed soil types and the availability of predictive environmental co-variables. In contrast, the influence of topography and spatial resolution of the DEM for the generation of predictor variables was only minor.

Keywords: digital soil mapping; random forest; decision tree; artificial neural networks; soil classification; digital elevation model

7.1 Introduction

Detailed knowledge about the spatial distribution of different soil attributes and types is necessary for many environmental applications. Soil maps provide helpful information for agriculture (Iticha and Takele, 2019; Silva et al., 2013), sustainable forest management (Falk and Mellert, 2011), land use planning and management (Rossiter, 2004) and soil erosion risks (Le Bissonnais et al., 2002; Lu et al., 2004). Mostly, this soil information is provided by soil maps from conventional soil surveys on different scales. As these traditional soil mapping techniques are very expensive and many field observations are required to gain sufficient material for mapping, digital mapping technologies based on remote sensing data became more and more popular in the last decades, especially for larger extents (Ma et al., 2019; Minasny and McBratney, 2016).

For an (semi-) automatized prediction of digital soil maps, several machine learning techniques have been used. Machine learning is a type of artificial intelligence that provides computers with the ability to automatically learn from multi-source data sets and make predictions according to discovered patterns in a training dataset (Witten et al., 2011). As the formation of soils is mainly a product of the interaction of five environmental factors, namely parental material, time, climate, relief and organisms, a key component for soil type prediction is the definition of relationships between different soils and environmental co-variates describing these factors (Jenny, 1941). Thus, the selection of sufficient environmental covariates is crucial to achieve a comprehensive description of all influencing factors for soil genesis.

There are numerous machine learning algorithms available, which have been successfully applied to digital soil mapping on varying scales from large scales to nationwide small-scale predictions of soil types. Most common are tree-based learners, such as decision tree or random forest classifiers, which have been used by many studies in soil science for the prediction of different soil types (Adhikari et al., 2014; Barthold et al., 2013; Dornik et al., 2018; Grimm et al., 2008; Gruber et al., 2019; Häring et al., 2012; Hengl et al., 2017; Hengl et al., 2015; Hounkpatin et al., 2018; Leenaars et al., 2020; Pahlavan-Rad et al., 2014; Roecker et al., 2010; Stum et al., 2010). Additional algorithms are artificial neural networks (Bagheri Bodaghabadi et al., 2015; Behrens et al., 2005; Silveira et al., 2013), support vector machines (Kovacevic et al., 2010), k-nearest neighbour (Mansuy et al., 2014) multinomial logistic regressions (Kempen et al., 2009; Vasques et al., 2014) and fuzzy classification methods (Qi et al., 2006; Yang et al., 2011; Zhu et al., 2010). Furthermore, the predictive power of several combinations of these algorithms for the prediction of soils has been compared by several authors (Assami and Hamdi-Aissa, 2019; Brungard et al., 2015; Heung et al., 2016; Heung et al., 2017; Pahlavan-Rad et al., 2016; Pasztor et al., 2018; Taghizadeh-Mehrjardi et al., 2019a; Taghizadeh-Mehrjardi et al., 2019b).

There is a long tradition of creating soil maps in Germany. Since the end of World War II, the generation of soil data is influenced by the federal structure of the country (Behrens and Scholten, 2006). The creation and maintenance of large scaled soil maps is in the responsibility of the individual federal states of Germany for their territory. For example, large-scale soil maps of the federal state of this study area (North-Rhine Westphalia) were provided in two scales of 1:5000 and 1:50,000 by the Geological Service of North-Rhine Westphalia. But only the second one is available for the entire area of the federal state. These soil maps are still mainly based on data derived from traditional field observation methods and additional not ubiquitously available historical large-scale maps with soil information (Schrey, 2014). However, existing soil maps need to be updated and improved to gain

more detailed and accurate soil information. Although soil surveys are expensive, in particular on larger scales, machine learning techniques have hardly been investigated so far for soil type prediction in Germany. Häring et al. (2012) did a decision-tree based spatial disaggregation of a 1:25,000 soil map for Bavaria and several investigations on co-variables for prediction with neural networks have been done for a small area in Rhineland-Palatinate (Behrens et al., 2005; Behrens et al., 2018a; Behrens et al., 2018b; Behrens et al., 2010a; Behrens et al., 2010b).

Most of all previously named studies only differentiated less than 20 different soil classes in their study area and there is a lack of investigations of these algorithms for areas with a very diverse distribution of soil types. A comprehensive analysis on the performance of several machine learning algorithms to distinguish such a high number of different soil types on a catchment scale is still missing. Additionally, there is no study yet that directly compares the influence of different areas with varying complexity of soil occurrence on the classification result. One objective of this study is to evaluate this influence of varying soil heterogeneity in different areas on the prediction performance of random forest (RF) and artificial neural network (ANN). Therefore, soil types in a very heterogeneous landscape with 36 different soil type units on a scale of 1:50,000 were predicted and compared for different areas of the catchment with varying complexities of the occurring soil types.

Several studies revealed that different sampling strategies for training data can significantly influence the classification results. Heung et al. (2016) showed that an area-weighted sampling strategy achieved higher overall accuracies in digital soil mapping than class-weighted sampling approaches, where the number of sampling points was balanced for all soil classes. However, the focus on spatially weighted sampling points generally assigns little weight to rare soil classes with small coverages. This leads to an underrepresentation of these soil types by ML algorithms (He and Garcia, 2009). Further studies showed that sampling and resampling approaches to reduce these imbalances could also improve the classification results (Liu et al., 2020; Sharififar et al., 2019; Taghizadeh-Mehrjardi et al., 2019b). However, there is still a need for research on the optimization of sampling strategies for ML algorithms in digital soil mapping to solve the conflict between spatial homogeneity and class-balancing within the training data. To address this issue, two different training datasets were compared in this study: one only spatially weighted and one class-balanced training dataset. For these sampling strategies, the effect on the results of both ML algorithms in different regions was evaluated.

Another aim of this study is to investigate how the accuracy of predicted soil types is influenced by different sets of environmental co-variables. It should be highlighted to which degree derived relief variables are sufficient for soil type prediction or additional variables from other environmental factors have an advantageous effect. Furthermore, varying topography of the landscape and the influence of environmental co-variables derived from digital elevation models (DEMs) with different spatial resolutions are investigated. There is hardly any study yet using the publicly available 90 m TanDEM-X WorldDEM™ (TDX) for the derivation of environmental co-variables for soil type prediction and comparing it with results based on co-variables derived from a high resolution DEM. This leads to another purpose of this study, to evaluate the suitability of DEMs with a coarser spatial resolution for the delineation of co-variables for prediction in comparison with a very high resolution DEM from airborne laser scanning (ALS) data source. As the accuracy of DEMs is highly influenced by topography, an accuracy assessment has been done here for different landscapes with varying topography and soil types.

7.2 Study area

The Rur catchment is mainly located in North-Rhine Westphalia (Germany) with additional small parts in Belgium and the Netherlands (Figure 7-1). In this study, only the German part of the Rur catchment is considered, which covers an area of about 2000 km^2. It consists of an elevation decline from about 750 m to 30 m above sea level from south to north. The landscape can be subdivided into two major units. The northern part lies in the fertile Germany-Belgium loess belt and has a predominantly flat landscape with an average altitude of 100 m. It is mainly covered by Tertiary Pleistocene terrace deposits at the terraces of rivers Maas and Rur and aeolian deposits of loess and dune sands (Bogena et al., 2018). According to the FAO soil classification, major soils of this area are Haplic Luvisols as well as Cumulic Anthosols near drainage lines and Gleysols and Fluvisols nearby the Rur river (Korres et al., 2015). As these soils are highly productive for agriculture, the area is dominated by arable land, which is intensively used for crop growing. The cultivated crops are mainly winter wheat, winter barley, winter rapeseed, sugar beet, potato and maize (IT. NRW, 2012; Waldhoff et al., 2017). The southern part of the catchment area covers the upland parts with a low mountain range. Geologically, it consists of Paleozoic to Mesozoic solid rocks of the Rhenish Massif, with alternating sequences of silt- and mudstones as well as sandstones and greywackes (Bogena et al., 2018). The hilly landscape is mainly dominated by deciduous forest areas and grass land. Major soil types are Eutric Cambisols and Stagnic Gleysols as well as Fluvisols and Gleysols along the Rur river (Korres et al., 2015). Mean annual precipitation is about 1400 mm in the southern part and about 700 mm in the northern part of the catchment (Korres et al., 2015).

7.3 Material and methods

7.3.1 Soil map data

As reference data for soil type prediction in this contribution, the digital version of the official soil map of North-Rhine Westphalia, the Bodenkarte 50 (BK50), with a scale of 1:50,000 was used (Geologischer Dienst NRW, 2019a). The soil map is created and distributed by the Geological Service of North-Rhine Westphalia according to the official German guideline for soil mapping (Ad-hoc-AG Boden, 2005; Schrey, 2014). These guidelines base on a morphogenetic approach with regard to soil-forming processes and morphologic features. Thus, the BK50 describes the soil structure up to a depth of 2 m in a consistent manner. Its digital version is based on the originally produced analogue set of soil maps, which were digitised, standardised in nomenclature and systematics and irregularly updated (Schrey, 2014). For the area of this study, the map consists of 36 different soil type units according to the German soil classification system (Ad-hoc-AG Boden, 2005) (Figure 7-1). A complete list of these soil types is provided in Appendix Table 7-4. Anthropogenic landscapes with artificially deposited soils (e.g. backfilled areas of an opencast mine) were excluded from the study and not considered for prediction.

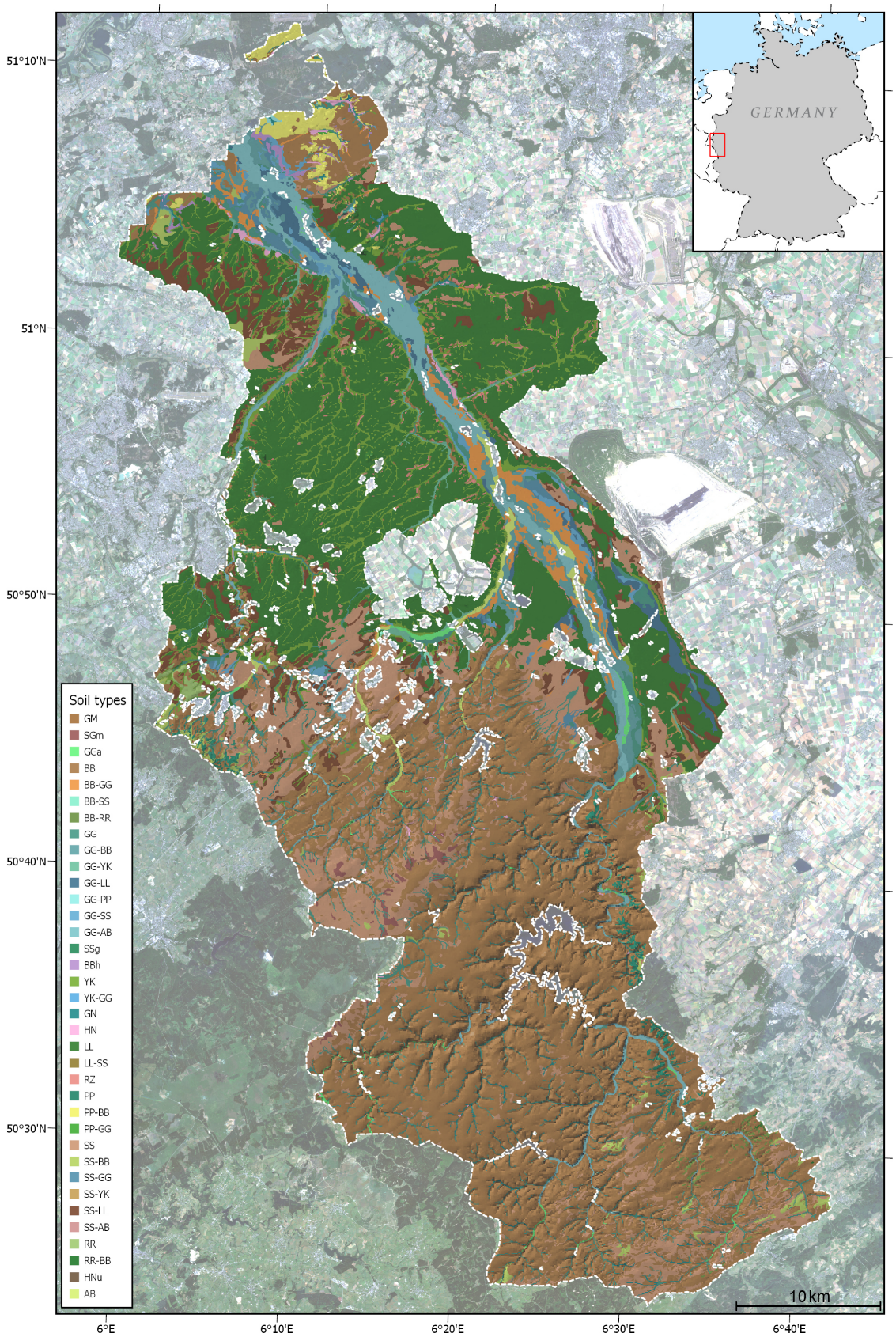

Figure 7-1: Hill-shaded overview of the study area and spatial distribution of BK50 soil type units. Abbreviations of soil types are according to the nomenclature of the German soil classification units and further explained in Appendix Table 7-4 (Ad-hoc AG Boden 2005). Background image: cloud-free mosaic of Sentinel-2 images from 2017 to 2019 derived by Google Earth Engine.

For soil type prediction and validation, two different point datasets for training and one for evaluation were created with Esri's ArcGIS Pro Software. A training dataset with randomly set points was created with ArcGIS 'Create Random Points' function. For each soil type unit, a set of 1000 points maximum with a minimum circular distance of 50 m was generated. This sampling strategy should provide a sufficiently large number of training samples for each soil class, but also consider the large differences in the occurrence of soil classes. Complex areas with many different soil types should be regarded with a higher point density than less heterogeneous areas. For most soil type units, this resulted in a considerably smaller amount of prediction points, as these areas are too small to generate such a high number of points with a minimal gap of 50 m. The final training dataset for classification with a class-based sampling strategy (CBS) contained 7211 points (Figure 7-2). Additionally, a second training dataset was created with a spatially homogenized sampling strategy (SHS) to maximize areal homogeneity in the derived point samples over the whole area. 7211 points were created with the ArcGIS 'Create Spatially Balanced Points' tool.

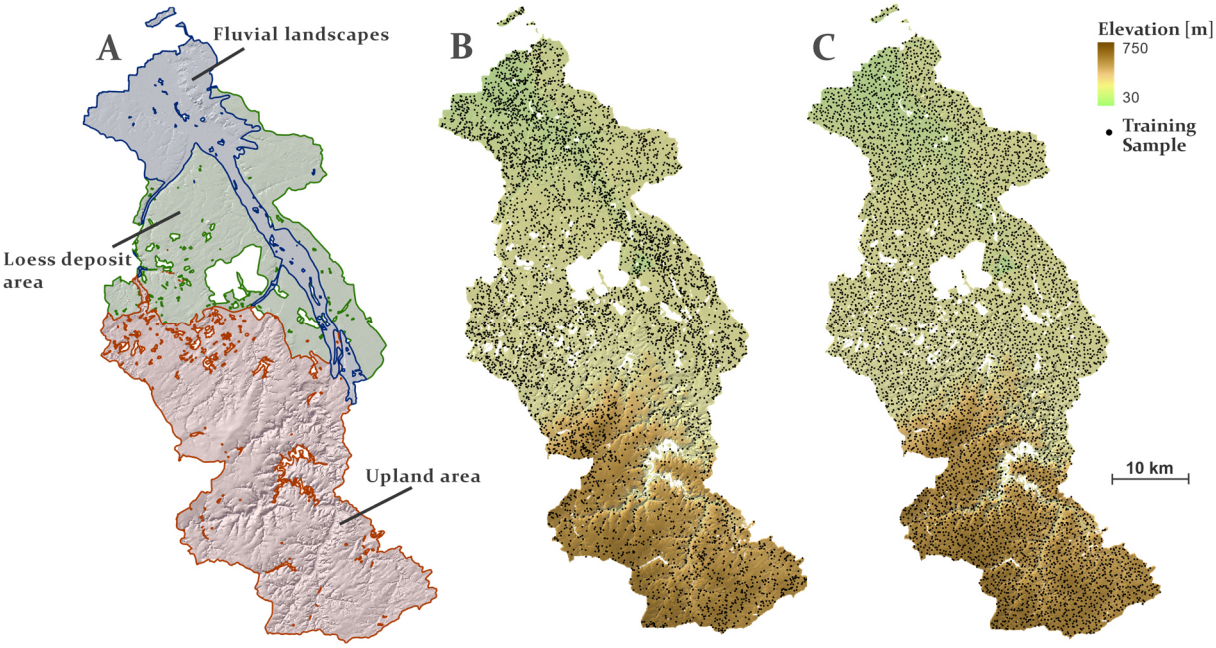

Figure 7-2: Location of subareas and training samples. A: location of the three subareas considered in this study. B: elevation gradient of the Rur catchment area and location of the 7,211 randomly generated training samples with the class-based sampling strategy (CBS). C: elevation gradient of the Rur catchment area and location of the 7,211 randomly generated training samples with the spatially homogenizes sampling strategy (SHS). The relief is indicated by a hillshade in all three images.

As the evaluation dataset, a homogeneous raster of points with a regular spacing distance of 50 m was created for the entire area. About 770,000 points were classified and evaluated. The evaluation was conducted once for the entire area and for three subareas with widely varying landscapes and soil types. These areas are the medium elevated upland area in the southern part of the catchment, which is mainly dominated by soil type units Braunerde (BB), Pseudogley (SS) and Gley (GG), according to the nomenclature of the German soil taxonomy, which is further explained in Appendix Table 7-4 (Figures 7-2 and 7-3). The relatively flat loess deposit area is mainly covered by soil types Parabraunerde (LL) and Kolluvisol (YK) and the fluvial area in the North has a highly heterogeneous distribution of different soil types.

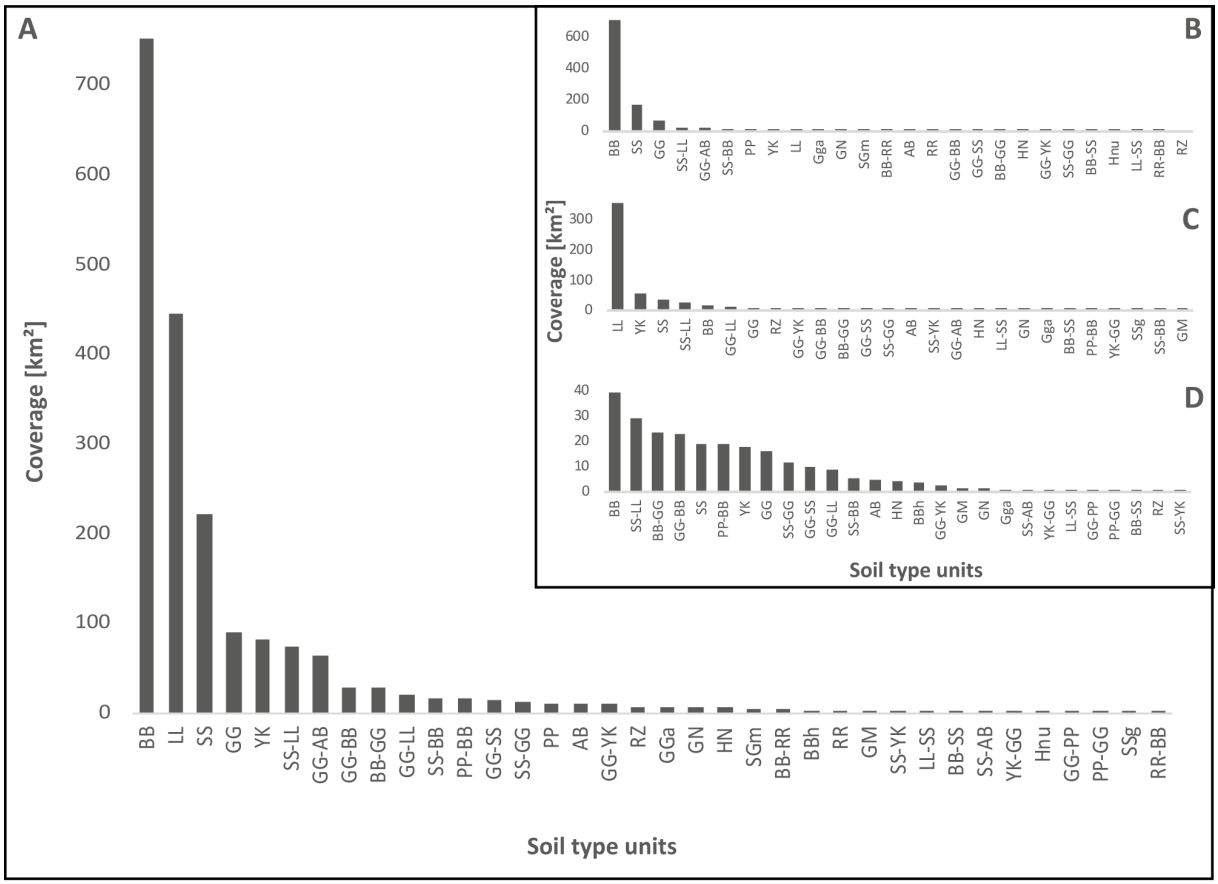

Figure 7-3: Coverage of soil type units in the Rur catchment area and different sub areas. A: entire area; B: upland area; C: loess deposit area; D: fluvial area. Abbreviations of soil types are according to the nomenclature of the German soil classification units and further explained in Appendix Table 7-4 (Ad-hoc AG Boden 2005).

7.3.2 Digital Elevation Models

Two digital elevation models with different spatial resolutions were used in this study to generate the majority of utilized relief based environmental co-variables. Thus, these variables were calculated with a 15 m high resolution digital elevation model (DGM1) and a 90 m TanDEM WorldDEM™. Both DEMs are described in detail in the following.

7.3.2.1 High resolution digital elevation model (DGM1)

The high resolution DGM1 is provided by the Regional Government of Cologne (Bezirksregierung Köln, 2017). The elevation model consists of 3D measurement data from airborne laser scanning. It has a point density of at least four points per square meter and includes only the Earth's surface without vegetation and buildings. The DGM1 is originally provided in a regular point grid with a point spacing density of 1 m. It is updated frequently, for this contribution a version of 2017 was used. The expectable vertical accuracy of the DGM1 is about 15 cm in flat to medium elevated landscapes and up to 30 cm in steep terrain (Arbeitsgemeinschaft der Vermessungsverwaltungen der Länder der Bundesrepublik Deutschland, 2019). The provided point cloud was converted to a raster dataset and resampled to a spatial resolution of 15 m.

7.3.2.2 TanDEM-X WorldDEM™

The TanDEM-X mission was launched as a public private effort between the German Aerospace Center (DLR) and Airbus Defence and Space with the aim to produce a highly accurate DEM for nearly the entire globe. Thus, the Earth was measured from 2010 to 2015 by two satellites (TerraSAR-X and TanDEM-X) in a controlled orbit with a baseline of 250 – 500 m with X-band RADAR interferometry (InSAR) (Rizzoli et al., 2017; Wessel, 2016). The TanDEM-X WorldDEM™ was originally generated with 0.4 arc-seconds (≈ 12 m) ground sampling distance (GSD). Additionally, a resampled version of 1 arc-second (≈ 30 m) and a freely available 3 arc-seconds (≈ 90 m) version have been released by the DLR in recent years. In this study, the TDX DEM in the spatial resolution of 90 m was used to generate a set of geomorphometric co-variables for model predictions. Several studies reveal that this DEM has a higher accuracy than the comparable 90 m SRTM DEM and shows a good performance, especially in flat landscapes (Altunel, 2019; Keys and Baade, 2019; Kramm and Hoffmeister, 2019).

7.3.3 Environmental co-variables

The genesis of soil mainly depends on a set of several environmental factors. To consider these factors, the environmental variables for the prediction of soil types were selected according to the 'SCORPAN' principle of McBratney et al. (2003), which is an enhancement of Jenny's (1941) equation. Thus, the soil class (S) is a function of climate (C), organisms (O), relief (R), parent material (P), age (A) and the spatial position (N). A total number of 28 environmental co-variables were used in this study (Table 7-1).

To represent climatic conditions (C) of the study area, the mean annual temperature and precipitation between 1971 and 2000, both provided via the geoserver of the German Weather Service (DWD), were used. Both datasets were originally provided with a spatial resolution of 1 km and up-sampled to 15 m resolution for this contribution. Furthermore, the solar radiation was calculated by using the 'Area Solar Radiation' function of ArcGIS Pro (Fu and Rich, 2002). For the factor organism (O), which also contains land use and land cover information, two different land use classifications were used. First one is the land use classification of the Rur catchment for the year 2015 (Waldhoff and Lussem, 2016). The classification is provided in a spatial resolution of 15 m. The second land use dataset is the CORINE Land Cover (CLC) classification of 2012, which contains a consistent classification of land cover and land use for entire Europe with a spatial resolution of 10 ha (European Environment Agency, 2017). This dataset was also resampled to a spatial resolution of 15 m for this contribution.

To describe the relief conditions (R) of the Rur catchment, a large set of topographical variables were derived. With both DEMs, the primary terrain parameters of elevation, slope, a combination of profile and plan curvature and aspect were calculated in ArcGIS Pro (Olaya, 2009; Wilson and Gallant, 2000). The terrain ruggedness index (Riley et al., 1999), as a measure for topographical heterogeneity, was calculated with two different window sizes (10 and 100 pixels). The dissection was calculated for a 9 × 9 pixels window for each DEM (Evans, 1972). Additionally, three different landform classification approaches were conducted with the topographic position index after Weiss (2001), the geomorphons approach (Jasiewicz and Stepinski, 2013) and the hillslope position after Marques et al. (2018). The topographic wetness index was calculated after Beven and Kirkby (1979), which describes the tendency of water accumulation for each cell (Gruber and Peckham, 2009). The terrain classification index for lowlands (Bock et al., 2007) and the valley depth were calculated with the open source GIS software

SAGA (System for Automated Geoscientific Analysis). In addition, a geomorphometric map was used, which combines three different categories of derived morphometric relief parameters based on digital elevation models (Scilands GmbH, 2010). Category one consists of bottom areas, summit areas and slopes, category two includes convergent and divergent areas and category three distinguishes between flat and sloped areas. Moreover, the three terrain parameters soil moisture index, relative height and a relative slope position, processed for the Rur catchment by the Scilands GmbH (2010), were used as co-variables for prediction.

Table 7-1: Environmental co-variables used for soil type prediction. Listed is their abbreviation code, if they are numerical (n) or categorical (c) and if they were derived both from the DGM1 and TDX.

Variable	Code	n/c	DGM1/TDX	Reference
Climate (C)				
Mean annual precipitation	PREC	n		German Weather Service (DWD)
Mean annual temperature	TEMP	n		German Weather Service (DWD)
Solar radiation	SOL_RAD	n		Fu and Rich (2002)
Organism (O)				
Land use classification 2015	LU2015	c		Waldhoff and Lussem (2016)
CORINE Land Cover 2012	CLC2012	c		European Environment Agency (2017)
Relief (R)				
Elevation	ELEV	n	x	
Slope	SLO	n	x	
Aspect	ASP	n	x	
Terrain ruggedness index 10	TRI10	n	x	Riley et al. (1999)
Terrain ruggedness index 100	TRI100	n	x	Riley et al. (1999)
Topographic position index	TPI	c	x	Weiss (2001)
Geomorphons	GEOM	c	x	Jasiewicz and Stepinski (2013)
Topographic wetness index	TWI	n	x	Beven and Kirkby (1979)
Terrain classification index lowlands	TCL	n	x	Bock et al. (2007)
Soil moisture index	SMI	n		Scilands GmbH (2010)
Relative height	RH	n		Scilands GmbH (2010)
Relative slope position	RSP	n		Scilands GmbH (2010)
Valley depth	VD	n	x	
Crest area index	CAI	n		Scilands GmbH (2010)
Dissection	DIS	n	x	Evans (1972)
Curvature	CURV	n	x	
Hillslope position	HP	c	x	Marques et al. (2018)
Geomorphometric map	GMK	c		Scilands GmbH (2010)
Parent material (P)				
Geological main units	GMU	c		Geologischer Dienst NRW (2019b)
Lithology	LIT	c		Geologischer Dienst NRW (2019b)
Permeability	PERM	c		Geologischer Dienst NRW (2019c)
Geochemical composition	GC	c		Geologischer Dienst NRW (2019c)
Age (A)				
Geological age	AGE	c		Geologischer Dienst NRW (2019b)

Four environmental variables were derived to represent the parental material (P) of the study area. From the geological map of North-Rhine Westphalia (GK100), the geological main units and lithology were used as predictor variables (Geologischer Dienst NRW, 2019b). Furthermore, from the hydrogeological map of North-Rhine Westphalia (HK100) the permeability of parent material and the geochemical composition were extracted (Geologischer Dienst NRW, 2019c). Both maps were provided with a scale of 1:100,000 by the Geological Service of North-Rhine Westphalia. Finally, for the factor of age (A), the stratigraphy of the geological data was extracted from the GK100.

7.3.4 Machine learning algorithms

The prediction of different soil type units was conducted with two different classifiers, namely the random forest and the artificial neural network classifier. Both algorithms belong to the category of machine learning classifiers and are described in detail in the following paragraphs. In this study, the prediction of soil types was conducted by a Python script with machine learning algorithms implemented in the Scikit-learn library. All predicted point datasets were finally exported to ArcGIS for further evaluation.

7.3.4.1 Random forest (RF)

The random forest classification was introduced by Breiman (2001) and consists of an ensemble of built decision trees to predict features. The construction of a decision tree is a top down procedure, which starts with a single root node, followed by binary questions to split the data at each level by forming new nodes. The objective is to find for each decision node of the tree the best test attribute, which allows to differentiate the mixture of classes between each subset. The resulting tree consists of many nodes connected by branches. Nodes at the end of the tree are called leaves and represent the unique classes. The RF algorithm uses only a limited number of randomly chosen predictor variables for each tree. Thus, it creates many weak independent trees that are due to the large number of single trees able to discern a pattern, which possibly would be unrecognized by a few strong trees. The number of built trees for the classification in this contribution was set to 500, as experimentations with higher numbers of trees did not lead to better results. The feature importance was calculated by the algorithm with ‘Gini importance‘ (Breiman, 1984).

7.3.4.2 Artificial neural networks (ANN)

Artificial neural networks are computational networks, which are initially inspired by biological processes of the nervous system in a human brain (McCulloch and Pitts, 1943). The structure of an ANN consists of a set of interconnected units called ‘neurons’ with the aim to estimate non-linear correlations between a set of variables. A neural network consists of an input and an output layer, which are (generally) connected by a set of hidden layers. All neurons from one layer are fully weighted and connected to neurons in the adjacent layers. The classification was conducted with the multilayer perceptron (MLP) classifier, which is a deep multilayer feed forward neural network. For soil type prediction, one hidden layer was used with 150 neurons.

7.3.5 Classification schema

With both machine learning algorithms and both training datasets, three different scenarios with different combinations of environmental co-variables were calculated for soil type prediction (Table 7-2). In the first scenario ('ALL'), all available variables were used. For the second scenario ('SCORPAN'), only the most important and not correlating variables of each SCORPAN factor were used. Due to the high number of variables for relief, two variables were chosen for the factor (R) and one each for the other SCORPAN factors. To exclude strongly correlating features, the Pearson correlation coefficient was calculated for all numerical co-variables and the Cramer's V coefficient was calculated for all categorical variables. Only numerical variables with a Pearson correlation between -0.5 and 0.5 were regarded. Categorical variables were only considered when they have a small correlation coefficient of less than 0.3 (Cohen, 1988; Ellis, 2010). The third scenario ('DEM') was set up to evaluate the predictive power of geomorphometric variables only. It contains only 19 variables, which were mainly calculated by a digital elevation model.

Table 7-2: Overview of all co-variables and their utilization in the three different scenarios 'ALL', 'SCORPAN' and 'DEM'.

Variable	ALL	SCORPAN	DEM
ELEV	x	x	x
TCL	x		x
SMI	x		x
VD	x	x	x
RH	x		x
TRI100	x		x
RSP	x		x
TRI10	x		x
GMU	x	x	
PREC	x	x	
CAI	x		x
DIS	x		x
SLO	x		x
LIT	x		
SOL_RAD	x		x
TWI	x		x
CURV	x		x
AGE	x	x	
CLC2012	x	x	
LU2015	x		
PERM	x		
TEMP	x		
GMK	x		x
GEOM	x		x
ASP	x		x
HP	x		x
TPI	x		x
GC	x		

7.3.6 Accuracy assessment

The accuracy assessment was conducted by counting the number of correctly classified points in comparison to the reference soil map BK50. The general accuracy of the predicted soil type units was assessed by calculating the overall accuracy (OA). OA is defined as the ratio of the number of correctly classified cases to the total number of cases (Congalton, 1991). Additionally, the individual classification accuracy of each soil type unit was assessed by calculating the user's accuracy (UA) and producer's accuracy (PA). The PA is the accuracy from the perspective of the producer and is defined as the ratio of correctly classified cases of one category to the total number of cases belonging to that specific category (Congalton, 1991). The UA is the accuracy of each predicted class from the perspective of a person who wants to use the predicted map. It is defined as the ratio between the number of correctly classified cases and the total number of classified cases for a certain category (Congalton, 1991).

7.4 Results

7.4.1 Comparison of classification accuracies

OA results of the entire Rur catchment and the three subareas for each scenario are depicted in Figure 7-4. It shows a slightly higher accuracy for the training dataset with a spatially homogenized sampling strategy compared to the class-based collection method. For the entire area, the scenario with RF and all environmental predictor variables has the highest OA with 71.9 % for variables based on DGM1 and 72.9 % for the TDX variables with SHS training dataset. The same scenarios with the CBS training dataset achieved an accuracy of 68.0 % (DGM1) and 69.1 % (TDX). A comparison of both ML algorithms reveals in most cases lower accuracies for ANN. The highest ANN OAs are 69.4 % (DGM1) and 69.7 % (TDX) for the scenario with SHS training dataset and all environmental variables. In comparison, the first scenario (‘ALL’) with the CBS dataset and ANN achieved an OA of 63.7 % with the DGM1 and 62.6 % with TDX variables. The observable differences in accuracy between both ML-algorithms are generally higher for the CBS training dataset.

The lowest prediction accuracies could be observed for the ‘SCOPRAN’ scenario with 56.8 % (DGM1) and the ‘DEM’ scenario with 55.7 % (TDX) calculated with ANN and the CBS training dataset. For both ML-algorithms and training datasets, the scenario ’ALL’ showed the highest accuracies, followed by the ‘DEM’ scenario. The ‘SCORPAN’ scenario generally performed worse. On average for all scenarios, the RF algorithm has a 4.2 % higher accuracy with the SHS dataset compared to the CBS dataset. This difference is even higher for the ANN algorithm, which has a 7.8 % higher accuracy with the SHS dataset on average. The observable differences in accuracy of the results between DGM1 and TDX are rather low. On average, the TDX DEM achieved 1.9 % higher OAs with RF and 1.3 % with ANN compared to the DGM1 results.

Considering only the southern upland parts of the Rur catchment (Figure 7-4), the OAs are higher for all algorithms and rise up to 76.6 % with RF and the SHS training dataset and 71.7 % with the CBS dataset. The ANN achieved an OA of 75.4 % (SHS) and 68.8 % (CBS) in this area. The OA of predicted soil type units with RF increased by 3.5 % on average for all scenarios with CBS dataset and 5.2 % with SHS training dataset, in comparison to the results of the entire study area. For ANN, the increase is slightly higher with 3.5 % on average with CBS and 5.8% with SHS dataset. For the loess deposit area

in the northern lowland area of the Rur catchment (Figure 7-4), similar accuracy results could be achieved for both ML algorithms. These are about 3 % (RF) and 5 % (ANN) higher on average compared to the accuracies of the entire catchment area. The average increase is slightly lower for the SHS training dataset with about 2 % (RF) and 3 % (ANN) in comparison to the entire area.

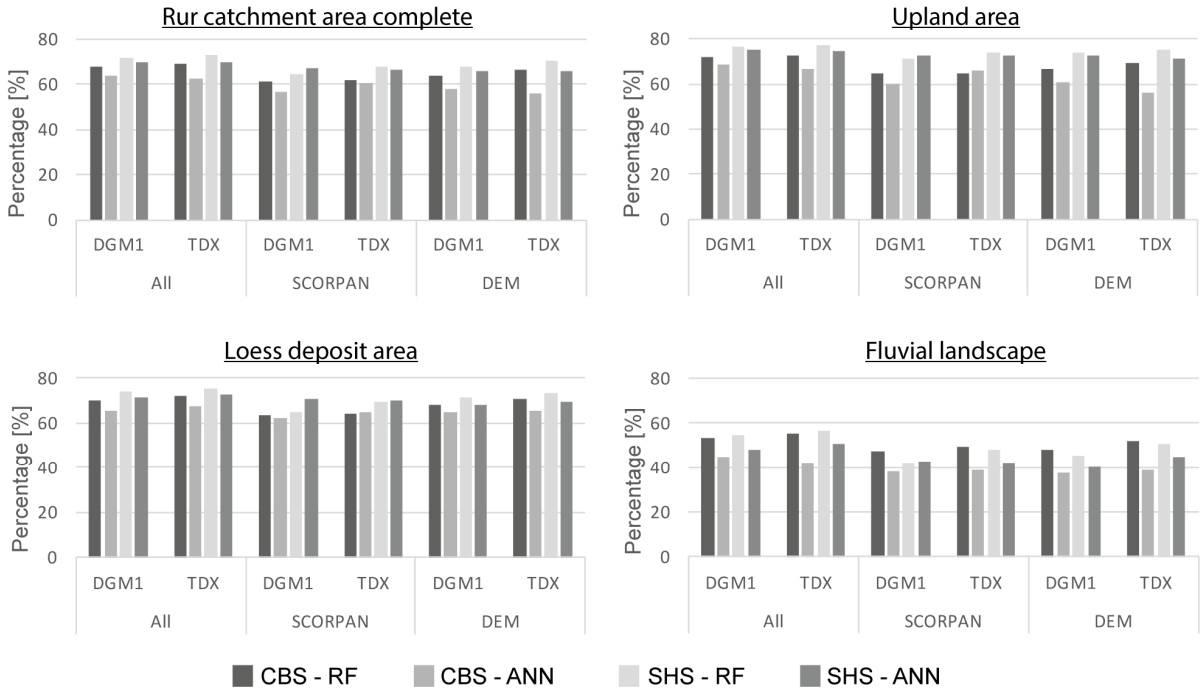

Figure 7-4: Calculated classification accuracies for each scenario, for the entire Rur catchment area and each subarea.

In the fluvial landscape area, all results show a strong decrease in accuracy and both training datasets achieved similar results here which are up to 20 % lower compared to the entire area. The highest achieved accuracies are 56.8 % (TDX) for the 'ALL' scenario with RF and the SHS dataset and 55.1 % with the CBS dataset. The observed accuracies for the ANN algorithm are about 10 % lower compared to the RF results with the CBS dataset and about 5 % for the SHS dataset. Comparing the results of both training datasets shows the highest differences in accuracy for the upland area. The accuracies are on average 6.3 % (RF) and 10.1 % (ANN) higher with the SHS dataset in comparison to the CBS dataset. In contrast, the accuracy of SHS is only 2.2 % (RF) and 4.7 % (ANN) higher in the fluvial area.

The importance for prediction ranking of all environmental variables used by the RF algorithm for both training datasets is listed in Table 7-3. Only the DGM1 scenarios are considered here, as observed differences between DGM1 and TDX variables were only minor. The results reveal that the DEM height plays by far the most important role for prediction here. Generally, many variables from the 'SCORPAN' factor (R) are of major importance for prediction. Particularly with the CBS scenario, the eight most important predictors were relief-based parameters. With the SHS training dataset, parent material features (P), such as lithology, geological main units and age are also important predictors. In contrast, the importance of land use and landform classifications is low for all scenarios. The importance of the climatic factor mean annual precipitation differs between both training datasets. While it is relatively unimportant with the SHS dataset (rank 24), it is on rank 10 with the CBS dataset. Mean annual temperature and the geochemical composition play almost no role for prediction.

Table 7-3: Overview of the importance for prediction (IMP) of the environmental variables based on the first scenario calculation for both training datasets.

	CBS		SHS	
Rank	**Variable**	**IMP**	**Variable**	**IMP**
1	ELEV	0.088	ELEV	0.106
2	TCL	0.062	TCL	0.070
3	SMI	0.061	TRI100	0.061
4	VD	0.054	LIT	0.055
5	RH	0.053	SMI	0.052
6	TRI100	0.053	RH	0.051
7	RSP	0.050	GMU	0.050
8	TRI10	0.043	RSP	0.049
9	GMU	0.041	AGE	0.047
10	PREC	0.040	GMK	0.043
11	CAI	0.039	TRI10	0.041
12	DIS	0.039	VD	0.040
13	SLO	0.037	SLO	0.035
14	LIT	0.036	SOL_RAD	0.034
15	SOL_RAD	0.036	CAI	0.032
16	TWI	0.033	DIS	0.032
17	CURV	0.033	TWI	0.030
18	AGE	0.031	CURV	0.029
19	CLC2012	0.026	CLC2012	0.029
20	LU2015	0.023	LU2015	0.021
21	PERM	0.021	GEOM	0.019
22	TEMP	0.021	PERM	0.017
23	GMK	0.020	ASP	0.016
24	GEOM	0.018	PREC	0.013
25	ASP	0.017	HP	0.010
26	HP	0.011	TPI	0.009
27	TPI	0.009	TEMP	0.005
28	GC	0.004	GC	0.004

Figure 7-5 shows the distribution of correctly and erroneous classified areas for all results of scenario ‘ALL’ in comparison to the BK50 reference soil map. In general, the RF results show the highest concordance rate of classified areas over the whole catchment. The spatial pattern of these classified areas is very similar for all results and detectable differences are only minor. Between the results of DGM1 and TDX almost no observable differences are recognizable. Correctly classified areas are mostly regions that are dominated by the soil types LL in the northern part and BB in the southern part. Areas with diverse soils in the northernmost and central part of the catchment generally show the highest rates of misclassification, particularly for ANN with more erroneous classified areas in the northernmost and central part of the catchment compared to the RF results.

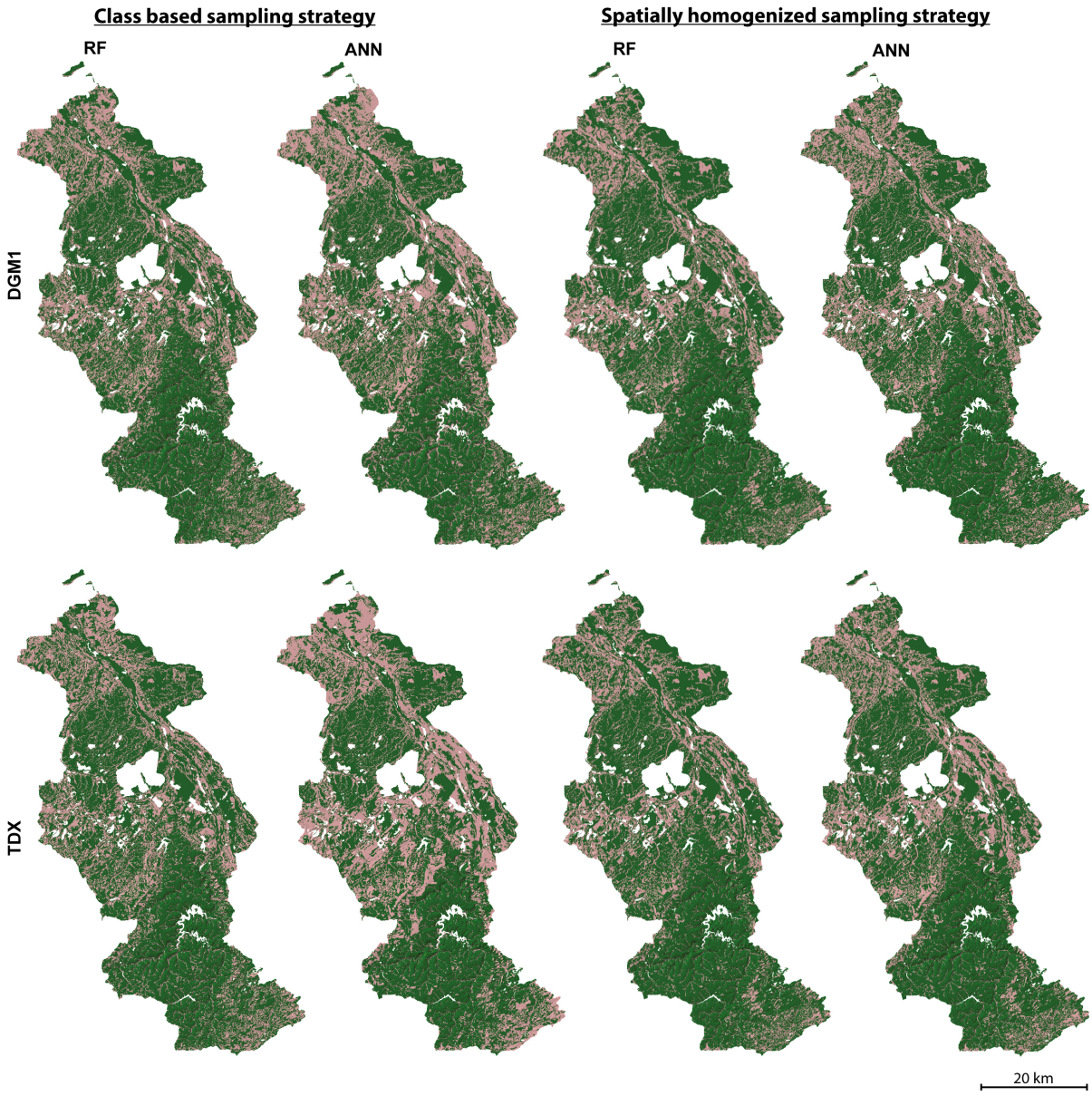

Figure 7-5: Conforming (green) and not conforming (red) classified areas in comparison with the reference soil map BK50. Regarded are the results of scenario 'ALL' for both algorithms, random forest (RF) and Artificial Neural Networks (ANN), with both training datasets in the Rur catchment. The relief is indicated by a hillshade in all images.

7.4.2 Derived user's accuracy (UA) and producer's accuracies (PA) for each soil type unit

The Appendix Tables 7-5 and 7-6 list all calculated user's accuracies and producer's accuracies for each soil type unit. Differences in accuracies between the scenarios with different environmental variables and both digital elevation models are minor. Only for rare soil types greater variations in accuracies between the different scenarios and different prediction algorithms are detectable. Both accuracy values generally decrease for rare soil types compared to the most frequent soil type units of the catchment area. Particularly with the ANN classifier, almost none of the rare soils were classified in agreement with the reference soil map and the number of completely omitted classes is higher than for RF. However, the decline varies between both training datasets. For the two most prevalent soil types BB and LL, the PA is about 20 % higher for all scenarios with the spatial homogenized training dataset compared to the class-based sampling point dataset. For the remaining more infrequently occurring soil type units, the PA values drop significantly and are lower with the SHS training dataset than for the CBS dataset. For the UA, an inversed ratio in the achieved accuracy values is detectable. While the two most dominant soil types achieved an about 10 % higher UA with the CBS dataset, the calculated UA values for the other soil type units are lower for the CBS dataset than for the SHS.

Comparing the variation of distribution of soil types between classification and reference data in Figure 7-6 shows that for the CBS training dataset, the most predominant soil types BB and LL are classified less frequently for all scenarios as they occur in the ground truth data. In contrast, the medium-frequent soil types SS, GG, YK, SS-LL, PP-BB have a strong positive ratio between classified areas of each soil type and ground truth data. Soil types GG-BB, BB-GG and GG-LL mostly show only minor differences in their appearance between classification and reference data. The rare soil types are mostly classified less often than they occur in the BK50 reference soil map and very rare soil types are almost not classified at all. For the SHS training dataset, the distribution of class occurrence differs significantly for the more frequently occurring soil types. With this dataset, the two most dominant soil types BB and LL are classified more often than they occur in the reference soil map and all other soil classes were classified less often compared to the results of the training dataset with a class-based sampling strategy.

A comparison of the different scenarios with various predictor variables shows mostly similar results, especially for the scenarios 'ALL' and 'DEM' with both DEMs. Only some rare soil types in the 'SCORPAN' scenario (BB-RR, BBh, RR) show a higher occurrence with the CBS training dataset than for the other scenarios. The observable differences in the results between both DEMs are only minor.

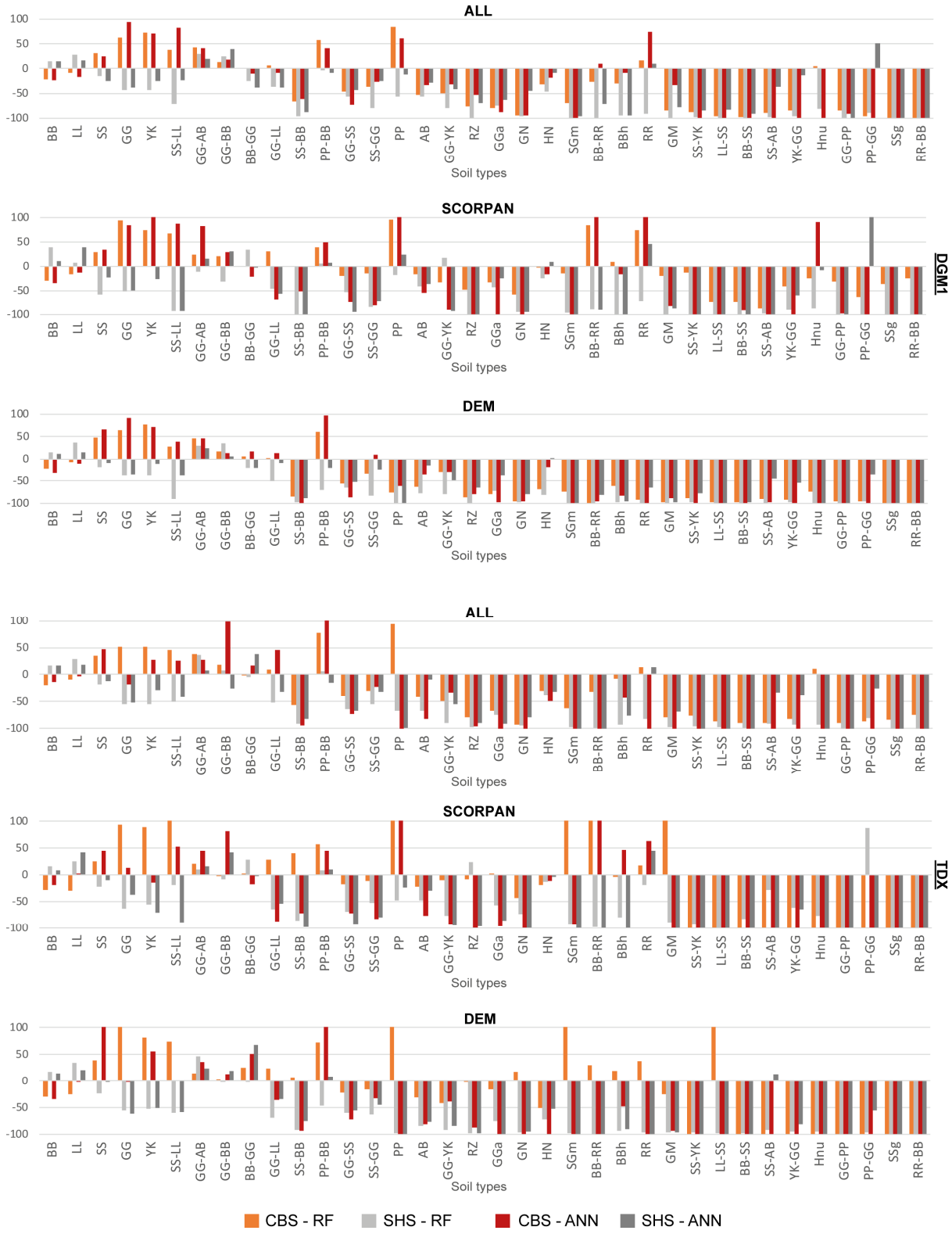

Figure 7-6: Distribution change (in percent) of all classified soil types compared to the reference soil map BK50. Soil classes are ordered from the most common soil class (BB) to the rarest soil class (RR-BB) of the study area.

7.4.3 Evaluation of the upland area results

Figure 7-7 shows a close-up comparison of the classification results for a small area in the upland part of the Rur catchment. The dominating soil type BB of this area was mainly correctly classified by all scenarios. The results created with the spatially homogenized sampling points tend to overestimate this soil type, which makes the results less diverse in contrast to the other sampling dataset.

It is recognizable that the scenarios 'ALL' and 'SCORPAN' with the CBS dataset tend to overestimate the appearance of PP on the upper crest areas. In contrast, this soil type was not classified at all in the 'DEM' scenario. The overestimation of this soil type is generally higher with the CBS training dataset. A similar pattern is also observable for the BB-RR soil type, which is also mainly situated in crest areas, in the southern part of the catchment area. Comparing the results regarding the influence of DGM1 and TDX derived variables, only minor differences could be detected. Only the ANN classification scenarios 'ALL' and 'SCORPAN' with the SHS training dataset vary considerably from the same scenarios with DGM1 predictor variables, as there is almost no classification of the soil type PP.

The incised areas are mainly dominated by gleyic soil types (GG and GG-AB). It can be observed that the classifications of these intersected areas are much more distinct with the CBS training data. Furthermore, they are slightly broader for the TDX classifications than for the DGM1 classifications. In particular, with the ANN classifier and the SHS dataset, there is almost no classification of small incisions with a gleyic soil type. The soil type predictions with RF show for most scenarios with the CBS dataset an overestimation of the soil type GG, whereas there is hardly any classification of the soil type GN in all scenarios over the whole upland area. Only the 'SCORPAN' scenario classified some sparse areas with this soil type. The classification of soil type GG-AB shows a high accordance compared to the BK50. For the ANN classification, only dominating soil types are classified. Thus, there is almost no classification of soil types GGa and GN detectable.

7.4.4 Evaluation of the loess deposit area results

Major soil types of the loess deposit area are LL and YK (Figure 7-8). All results show that these two soil types were mainly classified in accordance with the BK50 reference map by the different scenarios. Similar to the upland area, it is observable that the classification results are less diverse for the scenarios with the SHS training dataset. Particularly, soil type YK was classified more sparsely with the SHS training dataset than with the CBS training points. Less distributed soil types of this area, such as BB and RZ, were hardly detected by both ML-algorithms. Only the RF 'SCORPAN' scenario with the SHS training data classified these soil types considerably often. For the ANN 'SCORPAN' results with TDX data and the CBS training dataset, a relatively high number of misclassifications with soil type SS-LL are detectable. Soil type GG-YK was mainly classified correctly by all scenarios, except the 'SCOPRAN' one.

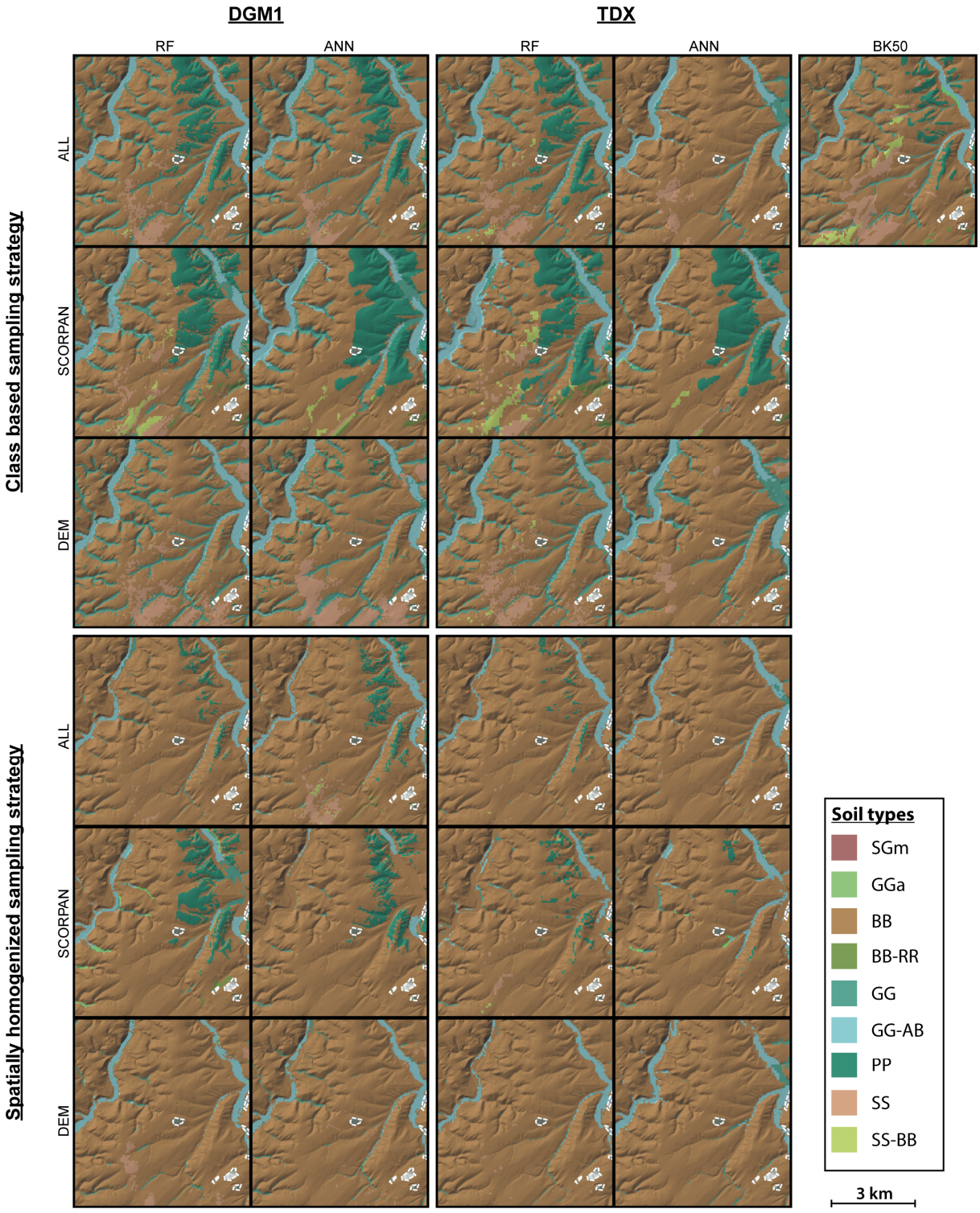

Figure 7-7: Comparison of predicted soil types for all scenarios for a small area in the upland part of the Rur catchment. The relief is indicated by a hillshade in all images and areas within white dashed lines are not considered for classification.

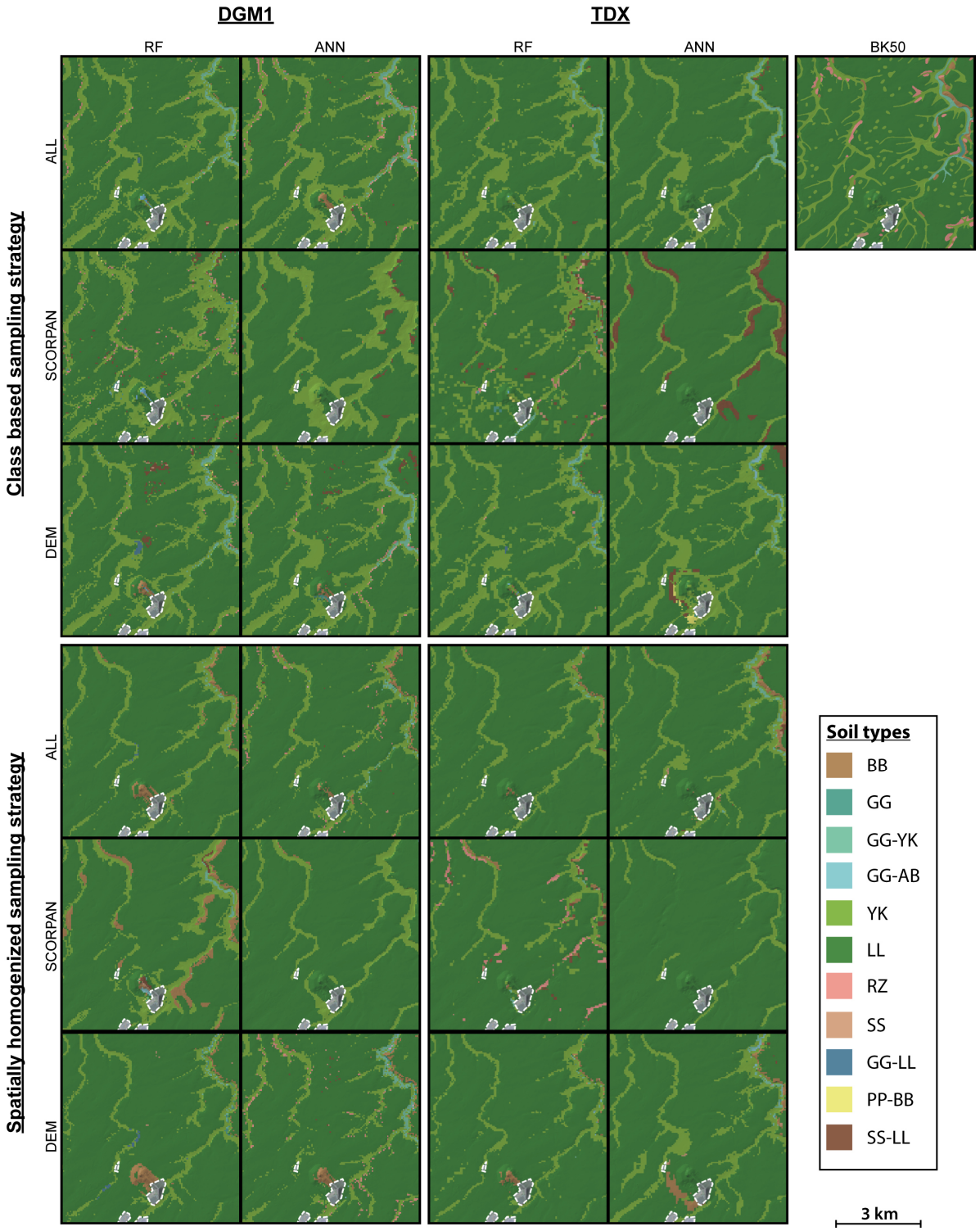

Figure 7-8: Comparison of predicted soil types for all scenarios for a small area in the loess deposit part of the Rur catchment. The relief is indicated by a hillshade in all images and areas within white dashed lines are not considered for classification.

7.4.5 Evaluation of the fluvial landscapes results

Figure 7-9 shows the classification results of a small area with fluvial topography and a very diverse distribution of soil types. The results depict an overestimation of the soil type SS-LL in the southern

part of the fluvial area for all scenarios with the CBS training dataset. This soil type was considerably less often classified with the SHS training dataset, especially in the 'SCORPAN' scenario. Likewise, soil type PP-BB is also overclassified with the CBS training dataset, particularly by the ANN classification for the 'DEM' scenario. Differences between DGM1 and TDX are only minor. The 'ALL' and 'SCORPAN' scenarios show the best agreement in classifying the gleyic soil types. Nevertheless, both ML algorithms tend to overestimate the distribution of soil type GG-AB.

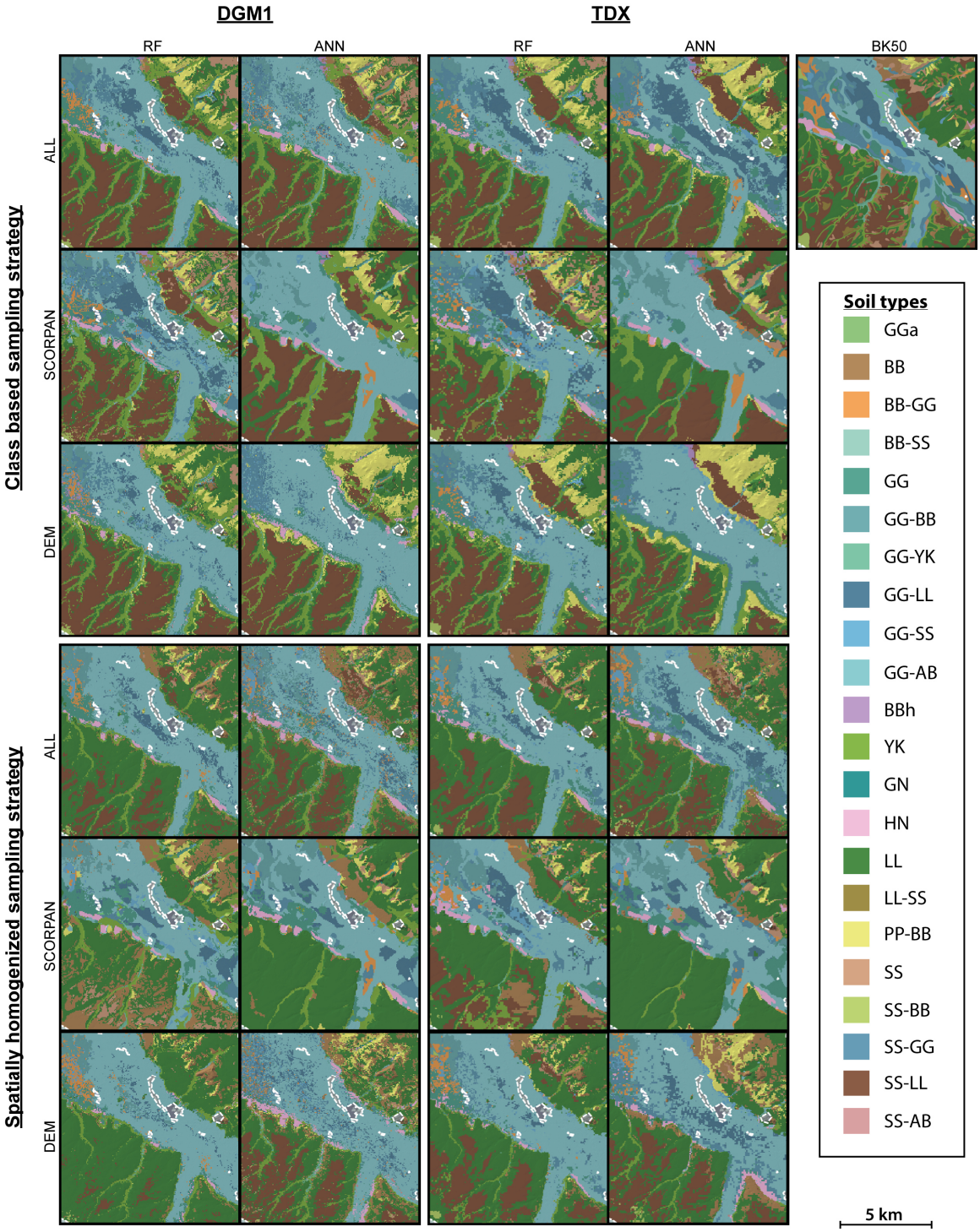

Figure 7-9: Comparison of predicted soil types for all scenarios for a small area in the fluvial part of the Rur catchment. The relief is indicated by a hillshade in all images and areas within white dashed lines are not considered for classification.

7.5 Discussion

The results reveal the highest prediction accuracies for the RF algorithm, which are on average 5 % superior compared to ANN. This is in accordance with findings from other studies, which also detected generally higher accuracies for predictions with random forest (Assami and Hamdi-Aissa, 2019; Brungard et al., 2015; Heung et al., 2016). The achieved accuracies here are significantly higher for areas with only a few dominating soil types and strongly decrease for regions with a very heterogeneous soil type structure. Therefore, areas with a particularly large distribution of LL in the northern part and BB in the southern part achieved high accuracies, whereas the classification of parts with a diverse soil type structure is problematic. In particular, the performance of the ANN classifier drops significantly in heterogeneous areas, whereas it has only a slightly worse performance than RF in the other areas. ANN tends to disregard minor soil types with smaller coverage and mainly classified only prevalent soil types. Thus, ANN results are generally more homogeneous than RF and a greater variation in classification accuracy could be detected here. It can be concluded that the classifier has more weaknesses in classifying very diverse soil structures than RF.

Classification accuracies from other studies widely range between average OAs of 40 % and 70 %. Barthold et al. (2013) achieved an OA of 71.1 % delineating 9 soil classes with RF and also using additional geological and land-use data besides DEM-derived variables for prediction. An OA of 64 % could be achieved by Assami and Hamdi-Aissa (2019) delineating 13 soil classes with RF. Pinheiro et al. (2017) used predictor variables for the soil-forming factors organisms, relief and parental material and achieved an OA of 68 % with RF distinguishing between 9 soil classes. These results mostly fit well with the results of this study from the upland and loess deposit areas with a less heterogeneous soil structure for the scenario ‘ALL’ including a large number of different input variables. Nevertheless, the training samples of this study were created from the same soil map as the evaluation data was assessed with. This possibly leads to some correlation and higher OA values than with a completely independent dataset. It should also be considered that the reference soil map does not necessarily reflect reality and contains uncertainties in soil type occurrence.

For heterogeneous landscapes with an increased number of different soil classes, the achieved results are significantly lower. For example, for the northern part with a fluvial landscape and a very disordered soil structure with 27 different soil types on a relatively small area, only accuracies of 50 – 55 % were achieved. Other studies with higher numbers of different soil classes achieved considerably lower OAs. For instance, Grinand et al. (2008) reached an OA of 44 % with a decision tree classification distinguishing between 31 soil classes. Stum et al. (2010) achieved an OA of 44.8 % for a classification of 24 different soil types with RF. Only Pasztor et al. (2018) got higher accuracies of 70 % for delineating 41 classes by combining the predicted results of different machine learning algorithms.

Observed differences between the results with predictor variables derived from DGM1 and TDX elevation models are only minor in this study and results with TDX co-variables are slightly superior to the results with DGM1 variables. Even in medium rugged landscapes with relatively small incisions and hillside slopes up to 40°, the performance of the high resolution DEM is not superior to the 90 m elevation model. This is in accordance with other findings, which also indicated that higher spatial resolutions of DEMs generally did not lead to higher prediction accuracies (Cavazzi et al., 2013; Massawe et al., 2018; Smith et al., 2006). Hence, it can be concluded that the availability of a very high resolution DEM is not essential for the prediction of different soil types and the globally freely available

TDX 90 m should be appropriate for relief variable delineation in most regions. This might be different in extremely rugged terrain with very steep slopes, but for most landscapes a medium to low resolution DEMs for co-variable generation should be sufficient.

Larger differences between the classification results are affected by the selection of different environmental co-variables for prediction. Scenario 'SCORPAN' generally achieved the lowest accuracies in this study, possibly due to the relatively low amount of used co-variables, which seems not enough to properly distinguish the soil type units of this catchment area. It is well-known that relief is one of the most important factors for soil genesis (Jenny, 1941). Thus, many relief dependent variables have a high influence on the classification results here. The features with the highest prediction importance are mainly terrain-based attributes derived from elevation models, in particular with the CBS training dataset (Table 7-3). In particular, the elevation itself seems to play an important role for the prediction of soil types and has by far the highest importance for the RF classification. In contrast, geomorphometric features only have minor influence as the importance of geomorphons, hillslope position, TPI and the geomorphometric map is relatively low. Contradicting to the findings of Barthold et al. (2013), also land use and land cover information seem to have a relatively low impact on the results here. Nevertheless, comparing the results of the 'DEM' scenario with scenario 'ALL' shows, that the use of DEM variables only is not sufficient for soil type prediction and further environmental predictors, such as geological or meteorological datasets, can significantly improve the accuracy. This is also indicated by other studies, which only used relief-based variables for prediction. Their results are also considerably lower than those from studies with further predictor variables. For instance, Dornik et al. (2018) achieved an OA of 56 % with an object-based approach and 48 % with a pixel-based approach by delineating 10 soil type classes only by RF with DEM derived variables. Taghizadeh-Mehrjardi et al. (2019a) achieved accuracies of 52 % (RF) and 51 % (ANN) with five soil type classes and 41 % (RF) and 39 % (ANN) with nine classes.

Comparing the results of both training datasets shows some significant differences. On a soil type level, a spatially homogenized sampling strategy without any class-based weighting led to an overestimation of the two dominating soil types and all other soils were underrepresented here. In contrast, the class-based sampling strategy with a less imbalanced training dataset overrepresented the medium occurring soils. The two very dominating and the remaining very rare soils were underrepresented with this sampling strategy. ANN seems more sensitive to different sampling strategies, as the achieved differences in accuracy were higher for this ML-algorithm than for RF. Whereas both algorithms performed almost on a similar level with a spatially homogenized sampling strategy, the results of the RF algorithm were superior to the class-based strategy.

The spatially homogeneous training dataset generally led to higher overall accuracies here. This is in accordance with the findings of other studies (Heung et al., 2016; Møller et al., 2019). They also found out that an area-weighted distribution of sampling points has a positive influence on the classification overall accuracy. This sampling strategy seems to be advantageous, especially for areas with a less complex soil structure. In the upland area with a less distributed soil class structure, the results here show a considerably higher accuracy for the SHS training dataset than for the CBS dataset. As the dominating soil types of this area got more points in the training dataset, this resulted in a higher classification accuracy for these soil types.

However, the results also show that a spatially homogeneous sampling strategy increases the inequalities between soil classes with different occurrences. For very rare soils, the probability rises that not enough training points were generated for these soils. In this study, for the three soil type units GG-PP, SSg and RR-BB no sampling points were generated at all with the SHS dataset and more than 70 % of the sampling points were located in the area of the three most frequent soils BB, LL and SS. In contrast, with the CBS dataset only about 40 % of the points were generated for these three major soil classes.

Complex areas with many soil classes are problematic for both training datasets and the achieved accuracy values are similar for all scenarios. Results on each soil type level show that it is difficult to classify rare soils with a sparse distribution. With the class-based sampling method, it was the aim to create for every soil type unit a sufficiently large training dataset for prediction. Although with the CBS method a 2 – 3 times higher point density could be reached for all soil types, except the three most dominating ones. For the rarest soils of the Rur catchment, the covered areas were too small to generate enough points for a sufficiently large training dataset. Nevertheless, increasing the number of samples for rare soils without increasing the absolute number of training points did not lead to a higher overall accuracy here. Probably a more efficient sampling strategy to select samples at more representative locations could improve the prediction performance of these soils (Liu et al., 2020). Results of Taghizadeh-Mehrjardi et al. (2019b) reveal that oversampling techniques that create additional synthetic interpolated samples could improve the overall accuracy. However, the prediction accuracy is also affected by the absolute number of training points (Sharififar et al., 2019). It is not entirely clear to which degree these resampling techniques benefit from the addition of interpolated points to rare classes or generally from an increased number of training samples. Creating a fully class-balanced dataset with an equal number of samples for all soil classes would probably decrease the prediction accuracy of the major soils and vastly underestimated them in the classification results.

Finding an optimal set of training samples for prediction is probably a compromise between several things. The minimum number of training points that are required to achieve even for rare soil classes a stable and representative description of their environmental properties. Also, a spatially-weighted location of these points and a consideration of the differences in the frequency of occurrence of the soil classes are important to reduce the over- and underrepresentation of distinct soil classes.

7.6 Conclusion

This study presents the accuracy of applying ML algorithms for the prediction of soil types with regard to several factors that influence the classification accuracy in a heterogeneous area with 36 different soil classes. Overall, the RF algorithm seems to be the most promising approach for soil type prediction in this study. Results showed that accuracies of around 75 % are possible for random forest in areas with less complex soil structures. ANN was able to reach similar OAs for these areas, but only with a spatially homogeneous training sample strategy. With the class-based sampling strategy, the results of ANN are considerably lower than for RF.

Areas with the lowest achieved accuracies for soil type prediction were the northernmost part of the catchment and the transition region from the mostly flat landscape of the loess deposit area to the upland area in the central part of the study area. In these areas with a diverse soil type distribution, a

significant drop in accuracy was detectable for both algorithms. The highest decrease of OA was detectable for ANN with accuracies of about 25 % lower than in less complex areas. For RF, a decrease in accuracy of about 20 % is detectable. Both training sample strategies were able to achieve similar accuracies here.

Comparing both training datasets showed that the selection of training samples is crucial for soil type prediction. On the one hand, a spatially balanced dataset leads to higher overall accuracies. On the other hand, this sampling strategy increases class imbalances by omitting rare soil classes and leads to a less diverse classification result. However, addressing these imbalances by adding more samples to rare soil classes without increasing the total number of training samples results in considerably lower overall accuracies.

A higher diversity of environmental co-variables for the prediction achieved better prediction results here. Thus, the set of predictor variables should be carefully chosen and ideally as versatile as possible. Results showed that using relief-based variables as the only source led to considerably lower OAs than using additional environmental parameters from the other 'SCORPAN' factors. In contrast, a significant influence of different elevation models for co-variable production could not be detected here and the 90 m TDX elevation model is as suitable as a highly accurate elevation model. It can be concluded that classification accuracy here seems mainly affected by the distribution and variation of existing soil types as well as the combination and availability of training samples and co-variables for prediction. In contrast, the accuracy was affected only minor by topography and spatial resolution of DEMs for the generation of predictor variables.

Acknowledgements

The authors gratefully acknowledge financial support by the CRC/TR32 'Patterns in Soil-Vegetation-Atmosphere Systems: Monitoring, Modelling, and Data Assimilation' funded by the German Research Foundation (DFG).

7.7 Appendix

Table 7-4: List of names for all soil type units of the BK50 from the Rur catchment area and their corresponding WRB soil classification group.

	Code	Name	Corresponding WRB Group
Terrestrial Soils	RR	Rendzina	Leptosol, Chernozem, Kastanozem, Phaeozem
	BB-RR	Braunerde-Rendzina *(Transition subtype of Rendzina)*	Leptosol, Phaeozem, Chernozem, Kastanozem
	RZ	Pararendzina	Leptosol, Regosol, Phaeozem, Chernozem, Kastanozem, Cambisol
	BB	Braunerde (Brown Earth)	Cambisol, Umbrisol, Arenosol
	BBh	Humusbraunerde *(Subtype of Braunerde)*	Umbrisol
	GG-BB	Gley-Braunerde *(Transition subtype of Braunerde)*	Cambisol, Gleysol
	PP-BB	Podsol-Braunerde *(Transition subtype of Braunerde)*	Podzol, Arenosol, Cambisol
	RR-BB	Rendzina-Braunerde *(Transition subtype of Braunerde)*	Cambisol
	SS-BB	Pseudogley-Braunerde *(Transition subtype of Braunerde)*	Cambisol, Planosol
	LL	Parabraunerde	Luvisol
	GG-LL	Gley-Parabraunerde *(Transition subtype of Parabraunerde)*	Luvisol
	SS-LL	Pseudogley-Parabraunerde *(Transition subtype of Parabraunerde)*	Luvisol
	PP	Podsol	Podzol
	GG-PP	Gley-Podsol *(Transition subtype of Podsol)*	Podzol, Gleysol
	SS	Pseudogley	Stagnosol, Albeluvisol, Planosol
	SSg	Hangpseudogley *(Subtype of Pseudogley)*	Planosol
	BB-SS	Braunerde-Pseudogley *(Transition subtype of Pseudogley)*	Planosol, Cambisol
	GG-SS	Gley-Pseudogley *(Transition subtype of Pseudogley)*	Gleysol, Planosol, Luvisol, Lixisol, Cambisol
	LL-SS	Parabraunerde-Pseudogley *(Transition subtype of Pseudogley)*	Planosol, Luvisol, Lixisol
	SGm	Anmoorstagnogley *(Subtype of Stagnogley)*	Planosol
	YK	Kolluvisol	Regosol, Phaeozem, Umbrisol, Anthrosol
	SS-YK	Pseudogley-Kolluvisol *(Transition subtype of Kolluvisol)*	Anthrosol
	GG-YK	Gley-Kolluvisol *(Transition subtype of Kolluvisol)*	Anthrosol
Semi-terrestrial Soils	AB	Vega (Brown Floodplain Soil)	Fluvisol, Cambisol
	SS-AB	Pseudogley-Vega *(Transition subtype of Vega)*	Cambisol, Fluvisol, Regosol
	GG-AB	Gley-Vega *(Transition subtype of Vega)*	Cambisol
	GG	Gley	Gleysol
	GGa	Auengley *(Subtype of Gley)*	Gleysol
	BB-GG	Braunerdegley *(Transition subtype of Gley)*	Gleysol
	PP-GG	Podsol-Gley *(Transition subtype of Gley)*	Podzol, Gleysol
	SS-GG	Pseudogley-Gley *(Transition subtype of Gley)*	Gleysol
	YK-GG	Kolluvisol-Gley *(Transition subtype of Gley)*	Anthrosol, Gleysol
	GN	Nassgley	Gleysol
	GM	Anmoorgley	Gleysol
Peat Soils	HN	Niedermoor	Histosol
	HNu	Übergangs(nieder)moor *(Subtype of Niedermoor)*	Histosol

Table 7-5: Calculated user's (UA) and producer's (PA) accuracies of all soil type units for all scenarios with the class-based training dataset.

	DGM1												TDX											
	RF						ANN						RF						ANN					
	ALL		SCORPAN		DEM		ALL		SCORPAN		DEM		ALL		SCORPAN		DEM		ALL		SCORPAN		DEM	
Soil type unit	**UA**	**PA**	**UA**	**PA**	**UA**	**PA**	**UA**	**PA**	**UA**	**PA**	**UA**	**PA**	**UA**	**PA**	**UA**	**PA**	**UA**	**PA**	**UA**	**PA**	**UA**	**PA**	**UA**	**PA**
BB	92	72	89	64	89	68	90	70	89	58	89	60	92	73	88	66	90	70	84	73	86	70	83	60
LL	82	74	80	67	79	74	83	69	78	68	78	70	83	75	80	69	81	75	79	76	74	77	79	54
SS	53	70	49	63	44	65	52	64	45	61	39	65	54	72	49	64	47	69	41	61	44	63	35	49
GG	36	59	25	49	34	56	28	54	20	37	27	52	36	54	24	38	35	52	30	25	23	26	24	46
YK	34	59	30	51	32	57	33	57	27	55	31	53	36	55	25	38	35	54	34	43	28	24	23	41
SS-LL	41	56	31	53	37	47	30	55	24	45	29	40	42	62	35	59	43	56	34	43	22	34	23	45
GG-AB	61	87	61	76	57	83	57	80	44	81	51	75	63	87	59	75	59	85	53	67	48	69	54	60
GG-BB	54	60	46	56	48	56	44	53	40	51	35	39	57	67	49	57	53	65	28	56	36	65	39	38
BB-GG	52	52	47	46	46	49	42	38	37	30	35	40	56	55	49	48	50	52	29	34	25	21	32	44
GG-LL	59	62	45	59	50	51	40	36	34	11	31	35	61	67	53	61	58	57	40	58	13	2	33	37
SS-BB	59	20	30	29	73	11	29	11	19	9	0	0	61	27	31	35	70	15	3	0	22	6	10	17
PP-BB	55	86	56	78	43	70	58	83	53	79	33	65	51	91	47	81	42	84	40	90	53	77	32	56
GG-SS	51	28	35	28	47	21	21	6	14	4	11	1	51	31	35	30	51	28	18	5	9	3	25	21
SS-GG	53	34	43	37	44	29	28	21	43	9	18	20	57	40	43	36	54	36	27	20	47	8	33	25
PP	42	77	36	71	34	8	41	66	31	85	18	7	41	79	35	76	48	14	57	0	31	82	7	19
AB	69	32	58	49	57	21	54	36	48	22	39	25	71	41	57	49	63	29	39	7	37	9	37	26
GG-YK	49	25	31	21	38	27	29	20	9	1	26	18	54	27	37	29	45	26	29	19	20	1	17	20
RZ	31	8	18	9	39	5	21	10	-	0	13	3	37	8	21	12	46	6	35	1	-	0	9	8
GGa	71	15	51	34	55	11	68	9	100	0	52	1	74	25	48	31	63	19	-	0	1	0	17	20
GN	65	4	20	8	58	3	28	2	0	0	15	1	58	4	16	10	58	3	-	0	-	0	7	6
HN	67	46	51	50	53	17	61	50	61	52	28	23	66	46	48	53	60	15	61	31	60	53	23	16
SGm	61	19	34	29	50	13	30	0	0	0	17	0	59	22	31	29	61	17	-	0	52	4	18	28
BB-RR	32	24	19	35	45	1	24	27	13	65	9	0	32	21	17	39	55	4	-	0	14	57	2	3
BBh	47	33	29	32	44	17	25	22	23	19	14	2	41	38	28	32	46	34	16	9	25	39	18	20
RR	59	68	44	76	62	5	47	81	40	88	29	0	63	72	49	76	62	36	-	0	51	84	15	19
GM	46	7	24	20	55	1	21	14	26	5	17	2	37	8	14	12	34	4	-	0	100	0	11	8
SS-YK	60	8	15	13	68	7	-	0	-	0	-	0	59	14	12	14	60	11	-	0	-	0	-	0
LL-SS	92	3	20	5	90	2	-	0	-	0	-	0	68	9	23	18	67	10	-	0	-	0	-	0
BB-SS	100	3	32	8	100	2	-	0	50	4	-	0	80	8	27	21	78	7	-	0	-	0	8	12
SS-AB	36	4	38	6	36	3	0	0	-	0	0	0	65	6	38	9	48	6	-	0	-	0	-	0
YK-GG	62	10	27	16	72	6	-	0	-	0	-	0	52	10	20	9	48	6	-	0	-	0	-	0
HNu	45	47	44	33	40	11	-	0	38	72	-	0	47	52	47	32	30	23	-	0	-	0	-	0
GG-PP	14	2	4	3	57	3	15	1	0	0	-	0	36	4	8	3	37	5	-	0	-	0	-	0
PP-GG	100	4	25	9	50	2	-	0	-	0	-	0	43	6	13	11	50	2	-	0	-	0	-	0
SSg	-	0	17	11	-	0	-	0	-	0	-	0	100	16	19	32	75	16	-	0	-	0	-	0
RR-BB	-	0	17	13	-	0	-	0	-	0	-	0	50	13	42	63	100	13	-	0	-	0	-	0

Table 7-6: Calculated user's (UA) and producer's (PA) accuracies of all soil type units for all scenarios with the spatially homogenized training dataset.

	DGM1												TDX											
	RF						ANN						RF						ANN					
	ALL		SCORPAN		DEM		ALL		SCORPAN		DEM		ALL		SCORPAN		DEM		ALL		SCORPAN		DEM	
Soil type unit	UA	PA	UA	PA	UA	PA	UA	PA	UA	PA	UA	PA	UA	PA	UA	PA	UA	PA	UA	PA	UA	PA	UA	PA
BB	80	92	67	94	78	90	79	90	78	87	78	87	80	93	77	90	78	92	78	92	80	87	77	88
LL	72	92	73	78	67	92	74	86	66	92	72	82	73	94	70	88	70	93	74	88	66	94	71	86
SS	64	54	56	24	54	43	64	48	56	44	50	46	66	54	60	47	60	46	58	51	54	48	47	47
GG	46	26	35	17	42	26	40	25	30	16	39	25	52	23	36	13	51	22	37	18	27	17	34	13
YK	46	26	30	30	39	24	40	30	33	25	36	32	49	22	29	13	43	21	40	29	38	11	46	23
SS-LL	63	19	26	2	61	6	40	31	32	2	37	23	61	31	39	32	60	24	47	27	32	4	46	20
GG-AB	61	79	61	54	58	76	59	70	55	64	55	68	59	81	58	64	54	79	61	65	51	59	51	64
GG-BB	50	62	50	34	43	58	42	58	39	51	37	39	56	59	46	42	52	52	49	36	36	51	33	39
BB-GG	50	37	38	51	44	35	40	25	40	38	37	29	48	45	41	52	42	42	37	52	34	33	25	42
GG-LL	60	38	49	26	52	26	36	22	46	20	31	28	71	34	67	23	74	23	54	36	43	20	50	33
SS-BB	83	3	41	0	87	2	26	3	-	0	14	2	84	7	43	6	81	7	47	8	60	2	35	9
PP-BB	68	66	62	66	61	18	68	62	63	67	42	33	67	71	61	66	71	38	76	65	61	67	52	57
GG-SS	42	18	23	11	38	13	25	14	15	1	19	9	38	14	26	8	34	14	22	7	20	2	18	8
SS-GG	62	13	66	11	54	9	30	22	41	12	19	15	53	24	38	18	55	21	29	20	37	7	25	14
PP	67	29	42	34	80	1	46	41	44	54	50	0	71	24	43	23	95	1	18	0	48	36	-	0
AB	50	22	48	28	46	10	44	32	44	29	27	23	64	21	40	21	57	9	31	28	35	25	14	3
GG-YK	43	9	15	17	43	9	25	15	0	0	20	11	66	6	15	3	65	5	29	13	12	1	29	5
RZ	100	1	14	0	100	0	22	7	-	0	18	6	57	1	9	12	83	1	39	4	2	0	76	1
GGa	54	14	41	23	40	11	41	15	24	18	20	12	64	16	48	21	58	15	50	5	5	1	33	0
GN	57	3	41	2	57	2	25	13	16	1	16	3	59	3	12	3	68	2	16	3	0	0	33	2
HN	66	35	56	42	43	8	53	48	52	57	28	28	60	37	46	40	47	13	58	40	55	53	33	16
SGm	100	1	57	3	100	0	7	0	-	0	-	0	94	2	29	2	92	1	-	0	-	0	-	0
BB-RR	100	1	14	2	56	1	27	8	2	0	10	2	100	1	22	0	100	1	-	0	-	0	-	0
BBh	85	5	100	0	77	2	39	2	-	0	23	1	65	4	30	6	49	3	18	4	-	0	15	2
RR	67	6	58	17	100	1	56	61	54	79	10	4	74	14	62	51	100	3	57	65	53	76	-	0
GM	80	1	100	0	100	0	39	9	24	3	38	1	46	1	53	6	48	2	27	8	0	0	19	1
SS-YK	78	1	-	0	50	1	16	2	-	0	8	2	76	3	7	1	79	3	-	0	-	0	-	0
LL-SS	100	1	-	0	100	0	30	5	-	0	-	0	38	1	50	1	44	1	-	0	-	0	-	0
BB-SS	100	1	-	0	100	1	29	3	-	0	56	2	100	2	15	3	100	2	-	0	-	0	-	0
SS-AB	75	1	60	1	100	1	32	21	-	0	8	4	68	6	38	27	72	6	36	24	-	0	25	28
YK-GG	78	3	78	8	100	2	21	19	41	16	11	5	56	4	24	9	73	4	17	11	14	5	48	9
HNu	43	8	61	9	100	1	40	40	42	39	-	0	42	3	35	8	50	3	-	0	-	0	-	0
GG-PP	-	0	-	0	-	0	-	0	-	0	-	0	-	0	-	0	-	0	-	0	-	0	-	0
PP-GG	50	6	-	0	100	4	11	17	5	15	9	6	20	4	7	13	100	4	15	11	-	0	8	4
SSg	-	0	-	0	-	0	-	0	-	0	-	0	-	0	-	0	-	0	-	0	-	0	-	0
RR-BB	-	0	-	0	-	0	-	0	-	0	-	0	-	0	-	0	-	0	-	0	-	0	-	0

7.8 References

Ad-hoc-AG Boden, 2005. Bodenkundliche Kartieranleitung. Schweizerbart'sche Verlagsbuchhandlung, Stuttgart, Germany.

Adhikari, K., Minasny, B., Greve, M.B., Greve, M.H., 2014. Constructing a soil class map of Denmark based on the FAO legend using digital techniques. Geoderma, 214, 101-113. Doi: 10.1016/j.geoderma.2013.09.023.

Altunel, A.O., 2019. Evaluation of TanDEM-X 90 m Digital Elevation Model. International Journal of Remote Sensing, 40 (7), 2841-2854. doi: 10.1080/01431161.2019.1585593.

Arbeitsgemeinschaft der Vermessungsverwaltungen der Länder der Bundesrepublik Deutschland (AdV), 2019. Produkt- und Qualitätsstandard für Digitale Geländemodelle - Version 3.0.

Assami, T., Hamdi-Aissa, B., 2019. Digital mapping of soil classes in Algeria - A comparison of methods. Geoderma Regional, 16, e00215. doi: 10.1016/j.geodrs.2019.e00215.

Bagheri Bodaghabadi, M., Martinez-Casasnovas, J.A., Salehi, M.H., Mohammadi, J., Esfandiarpoor Borujeni, I., Toomanian, N., Gandomkar, A., 2015. Digital Soil Mapping Using Artificial Neural Networks and Terrain-Related Attributes. Pedosphere, 25 (4), 580-591. doi: 10.1016/S1002-0160(15)30038-2.

Barthold, F.K., Wiesmeier, M., Breuer, L., Frede, H.G., Wu, J., Blank, F.B., 2013. Land use and climate control the spatial distribution of soil types in the grasslands of Inner Mongolia. Journal of Arid Environments, 88, 194-205. doi: 10.1016/j.jaridenv.2012.08.004.

Behrens, T., Förster, H., Scholten, T., Steinrücken, U., Spies, E.D., Goldschmitt, M., 2005. Digital soil mapping using artificial neural networks. Journal of Plant Nutrition and Soil Science, 168 (1), 21-33. Doi: 10.1002/jpin.200421414.

Behrens, T., Schmidt, K., MacMillan, R.A., Rossel, R.A.V., 2018a. Multi-scale digital soil mapping with deep learning. Scientific Reports, 8, 15244. doi: 10.1038/s41598-018-33516-6.

Behrens, T., Schmidt, K., MacMillan, R.A., Rossel, R.A.V., 2018b. Multiscale contextual spatial modelling with the Gaussian scale space. Geoderma, 310, 128-137. doi: 10.1016/ j.geoderma.2017.09.015.

Behrens, T., Schmidt, K., Zhu, A.X., Scholten, T., 2010a. The ConMap approach for terrain-based digital soil mapping. European Journal of Soil Science, 61 (1), 133-143. doi: 10.1111/j.1365-2389.2009.01205.x.

Behrens, T., Scholten, T., 2006. Digital soil mapping in Germany - a review. Journal of Plant Nutrition and Soil Science, 169 (3), 434-443. doi: 10.1002/jpln.200521962.

Behrens, T., Zhu, A.X., Schmidt, K., Scholten, T., 2010b. Multi-scale digital terrain analysis and feature selection for digital soil mapping. Geoderma, 155 (3-4), 175-185. doi: 10.1016/j.geoderma.2009.07.010.

Beven, K.J., Kirkby, M.J., 1979. A physically based, variable contributing area model of basin hydrology / Un modèle à base physique de zone d'appel variable de l'hydrologie du bassin versant. Hydrological Sciences Bulletin, 24 (1), 43-69. doi: 10.1080/02626667909491834.

Bezirksregierung Köln, 2017. Digital Elevation Model (DGM1) of the Rur Catchment, based on data from Bezirksregierung Köln [dataset]. CRC/TR32 Database (TR32DB). https://www.tr32db.uni-koeln.de/data.php?dataID=1690. 26.02.2020.

Bock, M., Böhner, J., Conrad, O., Köthe, R., Ringeler, A., 2007. Methods for creating Functional Soil Databases and applying Digital Soil Mapping with SAGA GIS. In T. Hengl, P. Panagos, A. Jones, G. Toth (Eds.), Status and prospect of soil information in southeastern Europe: soil databases, projects and applications. Office for Official Publications of the European Communities, Luxembourg, 149-163.

Bogena, H.R., Montzka, C., Huisman, J.A., Graf, A., Schmidt, M., Stockinger, M., von Hebel, C., Hendricks-Franssen, H.J., van der Kruk, J., Tappe, W., Baatz, R., Lucke, A., Bol, R., Groh, J., Putz, T., Jakobi, J., Kunkel, R., Sorg, J., Vereecken, H., 2018. The TERENO-Rur Hydrological

Observatory: A Multiscale Multi-Compartment Research Platform for the Advancement of Hydrological Science. Vadose Zone Journal, 17 (1), 1-22. doi: 10.2136/vzj2018.03.0055.

Breiman, L., 1984. Classification and regression trees. The Wadsworth statistics/probability series. Wadsworth International Group, Belmont, California, USA.

Breiman, L., 2001. Random forests. Machine Learning, 45 (1), 5-32. doi: 10.1023/ A:1010933404324.

Brungard, C.W., Boettinger, J.L., Duniway, M.C., Wills, S.A., Edwards, T.C., 2015. Machine learning for predicting soil classes in three semi-arid landscapes. Geoderma, 239, 68-83. doi: 10.1016/j.geoderma.2014.09.019.

Cavazzi, S., Corstanje, R., Mayr, T., Hannam, J., Fealy, R., 2013. Are fine resolution digital elevation models always the best choice in digital soil mapping? Geoderma, 195, 111-121. doi: 10.1016/j.geoderma.2012.11.020.

Cohen, J., 1988. Statistical power analysis for the behavioral sciences. L. Erlbaum Associates, Hillsdale, N.J, USA. doi: 10.4324/9780203771587.

Congalton, R.G., 1991. A Review of Assessing the Accuracy of Classifications of Remotely Sensed Data. Remote Sensing of Environment, 37 (1), 35-46. Doi: 10.1016/0034-4257(91)90048-B.

Dornik, A., Dragut, L., Urdea, P., 2018. Classification of Soil Types Using Geographic Object-Based Image Analysis and Random Forests. Pedosphere, 28 (6), 913-925. doi: 10.1016/S1002-0160(17)60377-1.

Ellis, P.D., 2010. The essential guide to effect sizes statistical power, meta-analysis, and the interpretation of research results. Cambridge University Press, UK.

European Environment Agency, 2017. CORINE Land Cover (CLC) 2012, Version 18.5.1 of the Rur Catchment [dataset]. CRC/TR32 Database (TR32DB). https://www.tr32db.uni-koeln.de/data.php?dataID=1697. 26.02.2020.

Evans, I.S., 1972. General Geomorphometry, Derivatives of Altitude, and Descriptive Statistics. Defense Technical Information Center, Ft. Belvoir, USA.

Falk, W., Mellert, K.H., 2011. Species distribution models as a tool for forest management planning under climate change: risk evaluation of Abies alba in Bavaria. Journal of Vegetation Science, 22 (4), 621-634. Doi: 10.1111/j.1654-1103.2011.01294.x.

Fu, P.D., Rich, P.M., 2002. A geometric solar radiation model with applications in agriculture and forestry. Computers and Electronics in Agriculture, 37 (1-3), 25-35. doi: 10.1016/S0168-1699(02)00115-1.

Geologischer Dienst NRW, 2019a. IS BK 50 Bodenkarte von NRW 1:50.000 – Datensatz [dataset]. Geoportal.NRW. https://open.nrw/dataset/ab0f265c-dabe-4bcd-869a-d97dc328c141. 26.02.2020.

Geologischer Dienst NRW, 2019b. IS GK 100 DS - Informationssystem Geologische Karte von Nordrhein-Westfalen 1:100.000 – Datensatz [dataset]. Geoportal.NRW. https://open.nrw/dataset/11ed9860-d540-4f77-8af8-97cee14ce91f. 26.02.2020.

Geologischer Dienst NRW, 2019c. IS HK 100 DS - Informationssystem Hydrogeologische Karte von Nordrhein-Westfalen 1:100.000 -Datensatz [dataset]. Geoportal.NRW. https://open.nrw/dataset/9fbf9f0a-5d86-4691-8873-d3fc0099bdc6. 26.02.2020.

Grimm, R., Behrens, T., Marker, M., Elsenbeer, H., 2008. Soil organic carbon concentrations and stocks on Barro Colorado Island - Digital soil mapping using Random Forests analysis. Geoderma, 146 (1-2), 102-113. doi: 10.1016/j.geoderma.2008.05.008.

Grinand, C., Arrouays, D., Laroche, B., Martin, M.P., 2008. Extrapolating regional soil landscapes from an existing soil map: Sampling intensity, validation procedures, and integration of spatial context. Geoderma, 143 (1-2), 180-190. doi: 10.1016/j.geoderma.2007.11.004.

Gruber, F.E., Baruck, J., Mair, V., Geitner, C., 2019. From geological to soil parent material maps - A random forest-supported analysis of geological map units and topography to support soil survey in South Tyrol. Geoderma, 354, 113884. doi: 10.1016/j.geoderma.2019.113884.

Gruber, S., Peckham, S., 2009. Chapter 7 Land-Surface Parameters and Objects in Hydrology. In T. Hengl, H.I. Reuter (Eds.), Geomorphometry Concepts, Software, Applications. Elsevier, Amsterdam, The Netherlands, 171-194. doi: 10.1016/S0166-2481(08)00007-X.

Häring, T., Dietz, E., Osenstetter, S., Koschitzki, T., Schroder, B., 2012. Spatial disaggregation of complex soil map units: A decision-tree based approach in Bavarian forest soils. Geoderma, 185, 37-47. doi: 10.1016/j.geoderma.2012.04.001.

He, H.B., Garcia, E.A., 2009. Learning from Imbalanced Data. IEEE Transactions on Knowledge and Data Engineerin, 21 (9), 1263-1284. doi: 10.1109/Tkde.2008.239.

Hengl, T., de Jesus, J.M., Heuvelink, G.B.M., Gonzalez, M.R., Kilibarda, M., Blagotic, A., Shangguan, W., Wright, M.N., Geng, X.Y., Bauer-Marschallinger, B., Guevara, M.A., Vargas, R., MacMillan, R.A., Batjes, N.H., Leenaars, J.G.B., Ribeiro, E., Wheeler, I., Mantel, S., Kempen, B., 2017. SoilGrids250m: Global gridded soil information based on machine learning. Plos One, 12 (2), e0169748. doi: 10.1371/journal.pone.0169748.

Hengl, T., Heuvelink, G.B.M., Kempen, B., Leenaars, J.G.B., Walsh, M.G., Shepherd, K.D., Sila, A., MacMillan, R.A., de Jesus, J.M., Tamene, L., Tondoh, J.E., 2015. Mapping Soil Properties of Africa at 250 m Resolution: Random Forests Significantly Improve Current Predictions. Plos One, 10 (6), e0125814. doi: 10.1371/journal.pone.0125814.

Heung, B., Ho, H.C., Zhang, J., Knudby, A., Bulmer, C.E., Schmidt, M.G., 2016. An overview and comparison of machine-learning techniques for classification purposes in digital soil mapping. Geoderma, 265, 62-77. doi: 10.1016/j.geoderma.2015.11.014.

Heung, B., Hodul, M., Schmidt, M.G., 2017. Comparing the use of training data derived from legacy soil pits and soil survey polygons for mapping soil classes. Geoderma, 290, 51-68. doi: 10.1016/j.geoderma.2016.12.001.

Hounkpatin, K.O.L., Schmidt, K., Stumpf, F., Forkuor, G., Behrens, T., Scholten, T., Amelung, W., Welp, G., 2018. Predicting reference soil groups using legacy data: A data pruning and Random Forest approach for tropical environment (Dano catchment, Burkina Faso). Scientific Reports, 8 (1), 9959. doi: 10.1038/s41598-018-28244-w.

IT.NRW, 2012. Landwirtschaftszählung in Nordrhein-Westfalen 2010 – Gemeinde- und Kreisstatistik der landwirtschaftlichen Betriebe Betriebsgrößen, Bodennutzung, Viehhaltung, sozialökonomische Betriebstypen, betriebswirtschaftliche Ausrichtung, Arbeitskräfte. Information und Technik Nordrhein-Westfalen (Geschäftsbereich Statistik). Düsseldorf, Germany.

Iticha, B., Takele, C., 2019. Digital soil mapping for site-specific management of soils. Geoderma, 351, 85-91. doi: 10.1016/j.geoderma.2019.05.026.

Jasiewicz, J., Stepinski, T.F., 2013. Geomorphons - a pattern recognition approach to classification and mapping of landforms. Geomorphology, 182, 147-156. doi: 10.1016/j.geomorph.2012.11.005.

Jenny, H., 1941. Factors of soil formation a system of quantitative pedology. McGraw-Hill publications in the agricultural sciences.

Kempen, B., Brus, D.J., Heuvelink, G.B.M., Stoorvogel, J.J., 2009. Updating the 1:50,000 Dutch soil map using legacy soil data: A multinomial logistic regression approach. Geoderma, 151 (3-4), 311-326. doi: 10.1016/j.geoderma.2009.04.023.

Keys, L., Baade, J., 2019. Uncertainty in Catchment Delineations as a Result of Digital Elevation Model Choice. Hydrology, 6 (1), 13. doi: 10.3390/hydrology6010013.

Korres, W., Reichenau, T.G., Fiener, P., Koyama, C.N., Bogena, H.R., Comelissen, T., Baatz, R., Herbst, M., Diekkruger, B., Vereecken, H., Schneider, K., 2015. Spatio-temporal soil moisture patterns - A meta-analysis using plot to catchment scale data. Journal of Hydrology, 520, 326-341. doi: 10.1016/j.jhydrol.2014.11.042.

Kovacevic, M., Bajat, B., Gajic, B., 2010. Soil type classification and estimation of soil properties using support vector machines. Geoderma, 154 (3-4), 340-347. doi: 10.1016/ j.geoderma.2009.11.005.

Kramm, T., Hoffmeister, D., 2019. A Relief Dependent Evaluation of Digital Elevation Models on Different Scales for Northern Chile. ISPRS International Journal of Geo-Information, 8 (10), 430. doi: 10.3390/ijgi8100430.

Le Bissonnais, Y., Montier, C., Jamagne, M., Daroussin, J., King, D., 2002. Mapping erosion risk for cultivated soil in France. Catena, 46 (2-3), 207-220. doi: 10.1016/S0341-8162(01)00167-9.

Leenaars, J.G.B., Elias, E., Wosten, J.H.M., Ruiperez-Gonzalez, M., Kempen, B., 2020. Mapping the major soil-landscape resources of the Ethiopian Highlands using random forest. Geoderma, 361, 114067. doi: 10.1016/j.geoderma.2019.114067.

Liu, X.Q., Zhu, A.X., Yang, L., Pei, T., Liu, J.Z., Zeng, C.Y., Wang, D.S., 2020. A graded proportion method of training sample selection for updating conventional soil maps. Geoderma, 357, 113939. doi: 10.1016/j.geoderma.2019.113939.

Lu, D., Li, G., Valladares, G.S., Batistella, M., 2004. Mapping soil erosion risk in Rondonia, Brazilian Amazonia: Using RULSE, remote sensing and GIS. Land Degradation & Development, 15 (5), 499-512. doi: 10.1002/ldr.634.

Ma, Y., Minasny, B., Malone, B.P., McBratney, A.B., 2019. Pedology and digital soil mapping (DSM). European Journal of Soil Science, 70 (2), 216-235. Doi: 10.1111/ejss.12790.

Mansuy, N., Thiffault, E., Pare, D., Bernier, P., Guindon, L., Villemaire, P., Poirier, V., Beaudoin, A., 2014. Digital mapping of soil properties in Canadian managed forests at 250 m of resolution using the k-nearest neighbor method. Geoderma, 235, 59-73. doi: 10.1016/ j.geoderma.2014.06.032.

Marques, K.P.P., Dematte, J.A.M., Miller, B.A., Lepsch, I.F., 2018. Geomorphometric segmentation of complex slope elements for detailed digital soil mapping in southeast Brazil. Geoderma Regional, 14, e00175. doi: 10.1016/j.geodrs.2018.e00175.

Massawe, B.H.J., Subburayalu, S.K., Kaaya, A.K., Winowiecki, L., Slater, B.K., 2018. Mapping numerically classified soil taxa in Kilombero Valley, Tanzania using machine learning. Geoderma, 311, 143-148. doi: 10.1016/j.geoderma.2016.11.020.

McBratney, A.B., Santos, M.L.M., Minasny, B., 2003. On digital soil mapping. Geoderma, 117 (1-2), 3-52. doi: 10.1016/S0016-7061(03)00223-4.

McCulloch, W.S., Pitts, W., 1943. A logical calculus of the ideas immanent in nervous activity. The Bulletin of Mathematical Biophysics, 5(4), 115-133. doi: 10.1007/BF02478259.

Minasny, B., McBratney, A.B., 2016. Digital soil mapping: A brief history and some lessons. Geoderma, 264, 301-311. doi: 10.1016/j.geoderma.2015.07.017.

Møller, A.B., Malone, B., Odgers, N.P., Beucher, A., Iversen, B.V., Greve, M.H., Minasny, B., 2019. Improved disaggregation of conventional soil maps. Geoderma, 341, 148-160. doi: 10.1016/j.geoderma.2019.01.038.

Olaya, V., 2009. Chapter 6 Basic Land-Surface Parameters. In T. Hengl, H.I. Reuter (Eds.), Geomorphometry Concepts, Software, Applications. Elsevier, Amsterdam, The Netherlands, 141-169. doi: 10.1016/S0166-2481(08)00006-8.

Pahlavan-Rad, M.R., Khormali, F., Toomanian, N., Brungard, C.W., Kiani, F., Komaki, C.B., Bogaert, P., 2016. Legacy soil maps as a covariate in digital soil mapping: A case study from Northern Iran. Geoderma, 279, 141-148. doi: 10.1016/j.geoderma.2016.05.014.

Pahlavan-Rad, M.R., Toomanian, N., Khormali, F., Brungard, C.W., Komaki, C.B., Bogaert, P., 2014. Updating soil survey maps using random forest and conditioned Latin hypercube sampling in the loess derived soils of northern Iran. Geoderma, 232, 97-106. doi: 10.1016/j.geoderma.2014.04.036.

Pasztor, L., Laborczi, A., Bakacsi, Z., Szabo, J., Illes, G., 2018. Compilation of a national soil-type map for Hungary by sequential classification methods. Geoderma, 311, 93-108. doi: 10.1016/j.geoderma.2017.04.018.

Pinheiro, H.S.K., Owens, P.R., Anjos, L.H.C., Carvalho, W., Chagas, C.S., 2017. Tree-based techniques to predict soil units. Soil Research, 55 (8), 788-798. doi: 10.1071/Sr16060.

Qi, F., Zhu, A.X., Harrower, M., Burt, J.E., 2006. Fuzzy soil mapping based on prototype category theory. Geoderma, 136 (3-4), 774-787. doi: 10.1016/j.geoderma.2006.06.001.

Riley, S.J., DeGloria, S.D., Elliot, R., 1999. A terrain ruggedness index that quantifies topographic heterogeneity. Intermountain Journal of Sciences., 5 (1-4), 23-27.

Rizzoli, P., Martone, M., Gonzalez, C., Wecklich, C., Tridon, D.B., Bräutigam, B., Bachmann, M., Schulze, D., Fritz, T., Huber, M., Wessel, B., Krieger, G., Zink, M., Moreira, A., 2017. Generation and performance assessment of the global TanDEM-X digital elevation model. ISPRS Journal of Photogrammetry and Remote Sensing, 132, 119-139. doi: 10.1016/j.isprsjprs.2017.08.008.

Roecker, S., Howell, D.W., Haydu-Houdeshell, C.A., Blinn, C., 2010. A Qualitative Comparison of Conventional Soil Survey and Digital Soil Mapping Approaches. In J.L. Boettinger, D.W. Howell, A.C. Moore, A.E. Hartemink, S. Kienast-Brown (Eds.), Digital Soil Mapping - Bridging Research, Environmental Application, and Operation, Springer, 369-384. doi: 10.1007/978-90-481-8863-5_29.

Rossiter, D.G., 2004. Digital soil resource inventories: status and prospects. Soil Use and Management, 20 (3), 296-301. doi: 10.1079/Sum2004258.

Schrey, H.P., 2014. Bodenkarte von Nordrhein-Westfalen 1:50000. Geologischer Dienst NRW, Krefeld, Germany.

Scilands GmbH, 2010. GMK10 Rur – Terrainfactors [dataset]. CRC/TR32 Database (TR32DB). https://www.tr32db.uni-koeln.de/data.php?dataID=196. 26.02.2020.

Sharififar, A., Sarmadian, F., Malone, B.P., Minasny, B., 2019. Addressing the issue of digital mapping of soil classes with imbalanced class observations. Geoderma, 350, 84-92. doi: 10.1016/j.geoderma.2019.05.016.

Silva, V.A., Curi, N., Marques, J.J.G., de Carvalho, L.M.T., dos Santos, W.R., 2013. Soil Maps, Field Knowledge, Forest Inventory and Ecological-Economic Zoning as a Basis for Agricultural Suitability of Lands in Minas Gerais Elaborated in Gis. Ciencia E Agrotecnologia, 37 (6), 538-549. doi: 10.1590/S1413-70542013000600007.

Silveira, C.T., Oka-Fiori, C., Santos, L.J.C., Sirtoli, A.E., Silva, C.R., Botelho, M.F., 2013. Soil prediction using artificial neural networks and topographic attributes. Geoderma, 195, 165-172. doi: 10.1016/j.geoderma.2012.11.016.

Smith, M.P., Zhu, A.X., Burt, J.E., Stiles, C., 2006. The effects of DEM resolution and neighborhood size on digital soil survey. Geoderma, 137 (1-2), 58-69. doi: 10.1016/j.geoderma.2006.07.002.

Stum, A.K., Boettinger, J., White, M.A., Ramsey, R., 2010. Random Forests Applied as a Soil Spatial Predictive Model in Arid Utah. In J.L. Boettinger, D.W. Howell, A.C. Moore, A.E. Hartemink, S. Kienast-Brown (Eds.), Digital Soil Mapping - Bridging Research, Environmental Application, and Operation, Springer, 179-190. doi: 10.1007/978-90-481-8863-5_15.

Taghizadeh-Mehrjardi, R., Minasny, B., Toomanian, N., Zeraatpisheh, M., Amirian-Chakan, A., Triantafilis, J., 2019a. Digital Mapping of Soil Classes Using Ensemble of Models in Isfahan Region, Iran. Soil Systems, 3 (2), 37. Doi: 10.3390/soilsystems3020037.

Taghizadeh-Mehrjardi, R., Schmidt, K., Eftekhari, K., Behrens, T., Jamshidi, M., Davatgar, N., Toomanian, N., Scholten, T., 2019b. Synthetic resampling strategies and machine learning for digital soil mapping in Iran. European Journal of Soil Science, 71 (3), 352-368. doi: 10.1111/ejss.12893.

Vasques, G.M., Dematte, J.A.M., Rossel, R.A.V., Ramirez-Lopez, L., Terra, F.S., 2014. Soil classification using visible/near-infrared diffuse reflectance spectra from multiple depths. Geoderma, 223, 73-78. doi: 10.1016/j.geoderma.2014.01.019.

Waldhoff, G., Lussem, U., 2016. Enhanced land use classification of 2015 for the Rur catchment – Update [dataset]. CRC/TR32 Database (TR32DB). doi: 10.5880/ TR32DB.19.

Waldhoff, G., Lussem, U., Bareth, G., 2017. Multi-Data Approach for remote sensing-based regional crop rotation mapping: A case study for the Rur catchment, Germany. International Journal of Applied Earth Observation and Geoinformation, 61, 55-69. doi: 10.1016/j.jag.2017.04.009.

Weiss, A.D., 2001. Topographic Position and Landforms Analysis, ESRI Users Conference, San Diego, CA, USA.

Wessel, B., 2016. TanDEM-X Ground Segment – DEM Products Specification Document. EOC, Munich, Germany, 2016.

Wilson, J., Gallant, J., 2000. Primary topographic attributes. In J.P. Wilson, J.C. Gallant (Eds.), Terrain Analysis: Principles and Applications. John Wiley & Sons, Inc, 51-85.

Witten, I.H., Frank, E., Hall, M.A., Pal, C.J., 2011. Data mining practical machine learning tools and techniques. Elsevier. doi: 10.1016/C2009-0-19715-5.

Yang, L., Jiao, Y., Fahmy, S., Zhu, A.X., Hann, S., Burt, J.E., Qi, F., 2011. Updating Conventional Soil Maps through Digital Soil Mapping. Soil Science Society of America Journal, 75 (3), 1044-1053. doi: /10.2136/sssaj2010.0002.

Zhu, A.X., Yang, L., Li, B.L., Qin, C.Z., Pei, T., Liu, B.Y., 2010. Construction of membership functions for predictive soil mapping under fuzzy logic. Geoderma, 155 (3-4), 164-174. doi: 10.1016/j.geoderma.2009.05.024.

8 Discussion

The first part of this contribution evaluated the accuracy of a large number of different DEMs with various resolutions and scales for very diverse landscapes. The accuracy assessment was conducted in the two landscapes of the Chilean Atacama Desert (chapters 3 and 4) and the mid-latitude Rur catchment in the western part of Germany (chapter 5). The achieved results enable a comprehensive comparison of the strengths and weaknesses of each DEM and provide detailed vertical accuracy measures for all tested DEMs in different topography and landscape. A summary as well as a discussion and interpretation of these results is presented in section 8.1. Furthermore, the results of both studies are combined and used to derive unbiased relief- and land cover adjusted error measures for each DEM.

In the second part of this contribution, it has been investigated in two different case studies to which degree the resolution and quality of a DEM have an influence on further applications. One case study was the classification of landforms with different approaches and DEMs (chapter 6). The accuracy of the different classification approaches and DEMs have been evaluated in this study. The second case study focused on the prediction of soil classes with machine learning algorithms, using elevations and further DEM derived land surface parameters for model prediction (chapter 7). The importance of these parameters was assessed and the results calculated with DEMs of two different spatial resolutions were compared. Section 8.2 discusses the strength of influence on these applications caused by the choice of a specific DEM. In addition, available studies from other applications that have examined the influence of different DEM sources and spatial resolutions on the outcome are discussed and summarized in this chapter.

8.1 Accuracy of DEMs

Eight medium resolution DEMs have been compared both for the Atacama Desert study area (chapters 3 and 4) and the Rur catchment in Germany (chapter 5). Additionally, the high resolution 12 m TanDEM-X and several DEMs from Pléiades and SPOT stereo imagery have been evaluated in chapter 3 and the EU-DEM in chapter 5. Certain patterns can be discovered here for DEMs of different generation sources and resolutions. Their achieved accuracies in flat and undulated landscapes as well as their mean overall accuracies over all used reference datasets are listed in Table 8-1. The results do not generally show a higher accuracy for the elevation models in one region compared to the other. Although both areas are completely different, the achieved overall accuracies are mostly in a similar range. This is partly surprising as the differences in the results between the southern and the northern part of the Rur catchment in chapter 5 showed that there could be significant differences in accuracies between different landscapes. It was expectable that the denser land cover with trees and houses above the surface in the Rur catchment would lead to more inaccuracies than in the Atacama Desert where the majority of the surface consists of bare ground. However, the overall steepness in the Atacama Desert region is higher with an average slope of 4.6° compared to the flat to medium elevated Rur catchment with an average slope of 2.1°. This may lead to some kind of balancing effect of the inaccuracies in both regions.

Table 8-1: Comparison of the achieved mean overall accuracies of all DEMs over all used reference datasets in chapters 3, 4 and 5 for the entire study areas and for only flat and moderately shaped landscapes of both areas. Listed are the calculated root mean square error (RMSE) and normalized median absolute deviation (NMAD) values. Flat landscapes are defined as areas with less than 5° slope. Moderate landscapes are areas with a slope steepness of 15°– 25°. The average slope of the entire Chilean study area is 4.6°, of the entire Rur catchment is 2.1°.

		flat (0° – 5°)				moderate (15° – 25°)				Entire study areas			
		Chile		**Rur**		**Chile**		**Rur**		**Chile**		**Rur**	
DEM	**Spatial resolution**	**RMSE [m]**	**NMAD [m]**	**RMSE [m]**	**NMAD [m]**	**RMSE [m]**	**NMAD [m]**	**RMSE [m]**	**NMAD [m]**	**RMSE [m]**	**NMAD [m]**	**RMSE [m]**	**NMAD [m]**
Pléiades	5 m	1.2	0.8	-	-	3.3	2.6	-	-	6.0	3.1	-	-
SPOT	5 m	1.9	1.8	-	-	5.3	3.7	-	-	5.0	3.1	-	-
TanDEM-X	12 m	1.2	0.5	-	-	3.4	2.3	-	-	3.3	1.3	-	-
EU-DEM	25 m	-	-	4.3	2.1	-	-	8.8	8.8	-	-	5.6	2.9
ASTER GDEM	30 m	7.6	6.0	6.9	5.5	10.7	10.1	10.0	9.9	8.7	7.0	6.8	6.8
ALOS W3D	30 m	2.5	1.9	5.6	2.8	5.0	4.6	7.5	8.3	4.3	2.8	5.9	3.2
SRTM	30 m	3.8	3.8	4.5	2.3	7.2	6.8	6.8	7.0	5.4	4.0	5.1	2.9
NASADEM	30 m	2.7	2.2	4.6	2.4	6.5	5.9	9.6	10.0	5.4	3.5	5.2	2.9
Copernicus DEM	30 m	1.9	1.5	5.6	1.7	5.5	5.2	9.0	9.8	4.6	2.2	6.0	3.1
SRTM	90 m	3.8	3.8	4.5	2.2	9.8	9.5	9.9	10.5	7.7	5.0	5.7	2.9
TanDEM-X	90 m	2.0	0.9	6.7	2.6	10.8	9.9	22.7	22.2	8.5	3.3	7.9	2.9
Copernicus DEM	90 m	2.6	2.0	5.5	2.0	12.6	11.5	11.7	11.8	6.8	3.5	7.6	3.1

Comparing the tested DEMs achieved overall accuracies in this contribution (Table 8-1) with average accuracies stated in the literature (Table 8-2) shows mostly results that are concordant with the current literature. Both SRTM DEMs lie within the range that has already been observed in literature with an average accuracy of 3 – 4 m in flat areas and about 7 m (30 m SRTM) and 10 m (90 m SRTM) in moderately steep landscapes. From the results shown in Table 8-1, it can be further observed that all DEMs from the C-band SRTM RADAR data are more accurate in the area of the Rur catchment than in Chile. Thus, except the ASTER GDEM, the SRTM DEMs are the only DEMs that are less accurate in the bare Earth region than in the region of dense land cover. The C-band RADAR is advantageous over X-band RADAR and photogrammetry in vegetation areas as it achieves a higher penetration depth (Schlund et al., 2019; Weydahl et al., 2007). This is also observable in vegetated areas of the Rur catchment where all DEMs from the X-band WorldDEM™ data were 3 – 6 m less accurate in forested areas than the C-band RADAR DEMs. Due to the acquisition time of the SRTM mission during the winter season in the northern hemisphere with less tree canopy, this effect might be stronger there than in the southern hemisphere. However, this assumption cannot be proven by this contribution.

For the NASADEM, only a few studies are available to date that have evaluated this DEM. Overall, the achieved results of this contribution in flat terrain are in accordance with the results of Carrera-Hernandez (2021) and are slightly better than those observed by Uuemaa et al. (2020) in a study area comparable to the Rur catchment. In undulated terrain, a relatively large difference in accuracy between the Rur catchment and the Atacama Desert can be observed here. An error of about 6 m in Chile is similar to findings of Carrera-Hernandez (2021), The error of about 10 m in the Rur catchment is slightly worse. The NASADEM as a successor of the SRTM DEM revealed an overall slightly higher performance than the SRTM DEM in this contribution. This was also confirmed by other studies that

state an improvement of this DEM over its predecessor (Carrera-Hernandez, 2021; Chen et al., 2022; Uuemaa et al., 2020).

Numerous studies have already stated the inferior performance of the ASTER GDEM in comparison to other global DEMs with a comparable spatial resolution (Alganci et al., 2018; Becek et al., 2016; Graf et al., 2018; Hu et al., 2017; Kumar et al., 2020; Liu et al., 2019; Liu et al., 2020b; Mouratidis and Ampatzidis, 2019; Pandey et al., 2017; Vassilaki and Stamos, 2020; Zhang et al., 2019b). These findings can be confirmed in all areas of this contribution. The achieved results of the ASTER GDEM in Table 8-1 are overall slightly worse in this contribution than in the literature (Table 8-2), but mostly in accordance with the findings of Carrera-Hernandez (2021), who found similar errors for flat and undulated terrain. With these results, the ASTER GDEM showed the by far overall lowest accuracies in almost all situations. It was in many situations even less accurate than DEMs with a lower spatial resolution of 90 m. Overall, the difference in accuracy between the ASTER GDEM and the other DEMs was larger in Chile than in the Rur catchment. Nevertheless, it cannot be recommended to use this DEM in any situation considering that there is a wide range of more accurate alternatives freely available in the same spatial resolution.

Table 8-2: Current state of findings from literature about achieved average RMSE accuracies of the global DEMs in flat and steep landscapes.

DEM	Spatial resolution	Average RMSE Flat [m]	Steep [m]	Reference
TanDEM-X	12 m	1 – 2	5 – 7	Baade and Schmullius (2016); Becek et al. (2016); Dobre et al. (2021); Gdulová et al. (2020); Zhang et al. (2019a)
EU-DEM	25 m	4	n/a	Mouratidis and Ampatzidis (2019)
ASTER GDEM	30 m	4 – 6	7 – 10	Alganci et al. (2018); Becek et al. (2016); Carrera-Hernandez (2021); Dobre et al. (2021); Graf et al. (2018); Hu et al. (2017); Karlson et al. (2021); Kumar et al. (2020); Liu et al. (2019); Mouratidis and Ampatzidis (2019); Pandey et al. (2017); Uuemaa et al. (2020); Vassilaki and Stamos (2020); Zhang et al. (2019b)
ALOS W3D	30 m	2 – 3	6 – 7	Alganci et al. (2018); Carrera-Hernandez (2021); Dobre et al. (2021); Karlson et al. (2021); Kumar et al. (2020); Liu et al. (2019); Uuemaa et al. (2020); Yahaya and El Azzab (2019)
SRTM	30 m	3 – 4	7 – 10	Carrera-Hernandez (2021); Dobre et al. (2021); Mukherjee et al. (2013); Rexer and Hirt (2014); Suwandana et al. (2012); Uuemaa et al. (2020); Zhao et al. (2011)
NASADEM	30 m	2 – 6	6 – 11	Carrera-Hernandez (2021); Marešová et al. (2021); Uuemaa et al. (2020)
Copernicus DEM	30 m	2 – 3	10	Karlson et al. (2021); Marešová et al. (2021)
SRTM	90 m	3 – 6	10 – 20	Becek et al. (2016); Dobre et al. (2021); Hu et al. (2017); Liu et al. (2019); Liu et al. (2020b); Nagaveni et al. (2019); Uuemaa et al. (2020); Yahaya and El Azzab (2019)
TanDEM-X	90 m	1 – 4	10 – 20	Altunel (2019); Dobre et al. (2021); Keys and Baade (2019); Kumar et al. (2020); Marešová et al. (2021)
Copernicus DEM	90 m	n/a	6 – 12	Marešová et al. (2021)

The EU-DEM was not available for the Chilean area and thus was only assessed for the Rur catchment area. As a combination of ASTER and SRTM data, it is clearly more accurate than the original ASTER GDEM and mostly showed a good performance, comparable to the other tested 30 m DEMs. Mouratidis and Ampatzidis (2019) recognized a superior performance of this DEM for vegetated areas compared to ASTER GDEM and SRTM. Their findings are comparable to the findings of this contribution in flat landscapes (Table 8-1). Here, it revealed a particularly high performance predominantly in flatter areas. However, the slightly higher spatial resolution of 25 m did not show any recognizable impact on the quality of this DEM.

The DEMs generated from X-band WorldDEM™ data revealed the biggest differences between the calculated RMSE and NMAD values in both areas (Table 8-1). Thus, it can be assumed that the overall accuracy of these DEMs is very high and very likely the highest of all tested DEMs. As the WorldDEM™ datasets still contain a relatively high number of outliers, it must be assumed that there is considerable room for improvements available for these DEMs. The accuracy of the 30 m Copernicus DEM was the overall highest of all tested 30 m DEMs in the Chilean study area with an error of less than 2 m (Table 8-1). In the Rur catchment, the observed accuracies were not significantly superior to other DEMs of this spatial resolution. This is mostly in agreement with findings from Karlson et al. (2021), who showed a similar vertical accuracy of the 30 m Copernicus DEM that is superior to the ALOS W3D. The achieved accuracies of 9 – 10 m in undulated terrain of the Rur catchment are in accordance with findings from Marešová et al. (2021) listed in Table 8-2. The achieved accuracies in the Chilean study area are significantly higher in this contribution with less than 6 m (Table 8-1). However, very few assessments on the accuracy of this DEM are available to date and more work needs to be done to further examine its quality.

The achieved results of the 90 m TanDEM-X are mostly in accordance with findings from the literature, except in undulated areas of the Rur catchment. There, an error of about 22 m is considerably higher than observed in most other studies (Table 8-1). Presumably, this is also caused by existing land cover and outliers in the DEM. Overall, both 90 m DEMs from WorldDEM™ data reveal a higher loss of accuracy than the 90 m SRTM DEM. In particular, the 90 m TanDEM-X consists of weaknesses in steep terrain and is considerably less accurate there. This has also been observed by other studies in very mountainous areas (Chen et al., 2022; Podgorski et al., 2019). The 90 m Copernicus DEM, created from the WorldDEM™ data of the TanDEM-X mission, overall performed slightly better than the 90 m TanDEM-X in most situations. This improvement of the Copernicus DEM has also been observed by Marešová et al. (2021) for three European mountainous areas. For the Rur catchment, a significantly higher accuracy of the 90 m Copernicus DEM over the TanDEM-X was also observable in this contribution, particularly in steeper areas. However, in the Chilean area it revealed in steeper areas even more uncertainties than the TanDEM-X DEM. This indicates that this accuracy improvement may not occur in all areas of the world. Nevertheless, more work is still necessary to investigate this. Overall, it must be stated from the results of this contribution that the WorldDEM™ is only in flat areas significantly more accurate than the SRTM DEM with the same pixel size. In steeper terrain, the 90 m SRTM is still the most accurate DEM of this spatial resolution. Probably the older 90 m SRTM benefits particularly in these areas from several improvements with other datasets, as it is contrary to the WorldDEM™ datasets already available in higher product versions.

The WorldDEM™ DEMs and the ALOS W3D mostly showed a slightly to considerable weaker performance in the Rur catchment than in the Atacama Desert. This leads to the conclusion that these DEMs are more affected by land cover than the SRTM DEMs. In particular, the ALOS W3D from stereo satellite imagery achieved considerably higher overall accuracies in the Chilean area than in the Rur catchment (Table 8-1). Thus, the ALOS W3D DEM seems to be strongly affected by land cover, which significantly lowers its accuracy, presumably due to the photogrammetric generation process that fully includes all objects on the Earth's surface. This DEM was only in the bare Earth region of Chile able to achieve similar results to DEMs from RADAR data. In areas with denser land cover, stereo imagery of this resolution shows disadvantages compared to other acquisition techniques. Overall, existing literature predominantly showed a superior accuracy of the ALOS W3D in comparison to SRTM (Alganci et al., 2018; Kumar et al., 2020; Liu et al., 2019; Yahaya and El Azzab, 2019) and a comparable accuracy to the newer NASADEM (Carrera-Hernandez, 2021; Chen et al., 2022). The results in Table 8-1 show for the ALOS W3D a higher accuracy in the Chilean area and a slightly inferior accuracy in the Rur catchment in comparison to the DEMs from SRTM data.

Considering the spatial resolution of the evaluated DEMs generally shows that a higher resolution potentially increases the vertical accuracy of DEMs. However, the accuracy depends on more factors and coarser datasets are not necessarily less accurate in every landscape. The spatial resolution is particularly important in steeper sections and leads to a 2 to 3 times higher accuracy decrease of 90 m DEM in steep areas compared to 30 m DEMs. Whereas the accuracy of a 30 m DEM decreased about 3 m to 5 m on average between flat (0° – 5° slope) and moderately shaped (15° – 25° slope) terrain, the accuracy of a 90 m DEM is more than 6 m and up to 15 m lower in undulated terrain than in flat landscapes.

Elevation models with a higher spatial resolution than 30 m were only evaluated for the Chilean study area in this contribution. Other studies already stated that the 12 m TanDEM-X provides a high level of detail and overall vertical accuracy (Gdulová et al., 2020; Pipaud et al., 2015; Vassilaki and Stamos, 2020; Wessel et al., 2018). The results of this contribution also show the 12 m TanDEM-X as the overall most accurate DEM that covered the entire Chilean study area. Overall, it achieved an accuracy of about 1 – 2 m in flat landscapes, which is about 1 – 2 m more accurate than the tested 30 m DEMs. In moderately shaped terrain, the 12 m TanDEM-X achieved a vertical error of less than 4 m (Table 8-1) which is slightly higher than observed in literature with 5 – 7 m on average (Table 8-2). This is probably caused by the absence of vegetation in the Chilean area, in contrast to other study areas in literature. The results of Dobre et al. (2021) show similar results for a predominantly non-vegetated area. Overall, the 12 m TanDEM-X is on average about 2 – 4 m more accurate than most other 30 m DEMs in steep landscapes but showed only a slightly better performance in less vegetated areas than the ALOS W3D DEM.

The very high resolution DEMs derived from stereo-satellite imagery of SPOT and Pléiades were also only evaluated for the Chilean study area. The results in Table 8-1 reveal an overall high accuracy, although the calculated mean overall error is higher than those of some other DEMs with a lower spatial resolution. Since these DEMs did not cover the entire area, it has to be considered that their overall accuracy values are not entirely comparable to the other global DEMs. Slope depending accuracy values showed comparable results to the 12 m TanDEM-X in both flat and undulated landscapes. In very steep terrain, the higher spatial resolution of Pléiades and SPOT imagery was advantageous over the 12 m TanDEM-X. Overall, the DEMs derived from Pléiades imagery are slightly

more accurate than DEMs from SPOT imagery. In particular, flat landscapes are depicted more smoothly in the Pléiades DEMs.

When interpreting the results of Pléiades and SPOT DEMs, it has to be considered that they were generated without the usage of GCPs. It is evident that GCPs can increase the accuracy of high resolution stereo DEMs (Barrand et al., 2009; Berthier et al., 2014). Overall, it can be stated that the increase of accuracy of the very high resolution DEMs over the global DEMs was relatively low here. However, due to the higher spatial resolution they are likely to be able to capture more details than DEMs of coarser resolution. As it has been shown in the study of chapter 6, this can be advantageous for certain large-scale applications. However, as these high resolution satellite stereo images are usually expensive, it's a matter of weighing up whether the price is worth it over entirely freely available DEMs with a coarser spatial resolution.

By the interpretation and comparison of the achieved vertical accuracy results, it has to be generally considered that different reference datasets have been used in both areas. While in the Rur catchment an area-wide dataset of very high accuracy was available, the distribution of reference points in the Atacama Desert was overall more sparsely. It was therefore not possible to evaluate the entire Chilean area and compare every height value of the DEMs with a reference dataset. Although a large number of reference points have been used, this can have a slight misbalancing effect on the achieved vertical accuracies. Moreover, it must be considered that DEMs and reference data were captured at different times. Thus, it is unavoidable that a timespan of more than ten years exists between the acquisition dates of some DEMs and the utilized reference data. Areas with significant human-made terrain changes during this time period, such as open cast mining areas, were excluded from the studies. Nevertheless, relief is not a static surface and other areas may also be affected by natural or human changes over time. These effects could not be quantified here, but may also have an impact on the validation results.

Additionally, the DEMs in this contribution have been evaluated mainly as they were provided by the distributor without any significant corrections or improvements prior to the evaluation process. Thus, it must be considered that individual quality improvements of the DEMs can also have positive effects on accuracy. Knowledge about the accuracy of a DEM in a certain area is also important as it can help to improve the quality of the DEM in the future. For example, the height of tree values can be used to remove them in the DEM and to model the ground surface in forested areas (Gallant et al., 2012). Zhao et al. (2018) created a corrected SRTM product for vegetated areas by the usage of average canopy heights of different vegetation types. With the knowledge of the error behaviour of a DEM, this could be extended to other land cover types in future work. Knowledge about the error of a DEM in a particular relief could be used for general corrections in these areas.

Besides internal error sources, such as horizontal georectification, spatial resolution, downsides of acquisition techniques or interpolation algorithms, the accuracy of a DEM is mainly influenced by the type of landscape that is covered by the DEM (American Society for Photogrammetry and Remote Sensing (ASPRS), 2004; American Society for Photogrammetry and Remote Sensing (ASPRS), 2015; Mesa-Mingorance and Ariza-Lopez, 2020). The results of both evaluations clearly show that the steepness and roughness as well as objects above the surface (land cover) are mainly responsible for elevation deviations. It has to be stated, that it is not completely identifiable in the presented results to which degree the accuracy of a DEM is influenced by relief and by land cover. Both factors are mutually dependent and influence each other. Since there is predominantly no land cover in the

Atacama Desert, it can be assumed that the factor relief is the dominating factor affecting the vertical accuracy there. In the Rur catchment, the interpretation of both factors is more complex as land cover is always influenced by relief and vice versa.

It was the aim of this contribution to extend the common knowledge of general DEM accuracies regarding relief, landform and land cover. To overcome this dependence of error, relief- and land use adjusted accuracy measures are derived from the formerly presented slope dependent results of chapters 3 to 5. From the achieved RMSE and NMAD values presented in Figures 3-7, 4-1 and 5-8, general values for the loss of accuracy per 10° slope were calculated for each DEM. The accuracy assessments of chapters 3 to 5 revealed that the slope dependent loss of accuracy was mostly linear from flat to moderately shaped terrain. Whether this linearity is also given for very steep relief (>35° slope) could not be proven by this contribution, since there were not enough reference points available in such steep slopes. Assuming a linear error increase from the achieved slope dependent accuracies of chapters 3 to 5, the average gradient of the curves in Figures 3-7, 4-1 and 5-8 is calculated for each DEM. The results are presented in Table 8-3 and show the average loss of accuracy per 10° slope for each DEM. The values of this table can be interpreted as the expectable loss of accuracy depending on the relief up to a steepness of 35° for both study areas individually and a combined value from both sites. Although, the derived values for the Rur catchment could be slightly influenced by land use, these average accuracies change rates can be stated as an approximate conversion factor between terrains of different steepness. Further accuracy values achieved from other areas without land cover could be helpful here in the future to consolidate these change rates. However, this was not feasible within the framework of this contribution.

Table 8-3: The calculated average loss of accuracy per 10° slope steepness for all tested DEMs. Listed are the average loss values (root mean square error (RMSE) and normalized median absolute deviation (NMAD)) for each study area individually and a combined value from both areas together.

		Chile		**Rur**		**Both areas**	
DEM	**Spatial resolution**	**RMSE [m]**	**NMAD [m]**	**RMSE [m]**	**NMAD [m]**	**RMSE [m]**	**NMAD [m]**
Pléiades	5 m	1.0	0,7	-	-	1.0	0,7
SPOT	5 m	1.2	0,9	-	-	1.2	0,9
TanDEM-X	12 m	1.3	1,0	-	-	1.3	1,0
EU-DEM	25 m	-	-	1.8	1,9	1.8	1,9
ASTER GDEM 30 m	30 m	2.1	2,4	1.9	1,9	2.0	2,2
ALOS W3D 30 m	30 m	1.6	1,6	0.7	1,3	1.2	1,5
SRTM 30 m	30 m	2.3	2,0	1.0	1,3	1.6	1,7
NASADEM 30 m	30 m	2.4	2,1	2.7	2,8	2.5	2,5
Copernicus DEM 30 m	30 m	2.2	2,2	1.4	2,0	1.8	2,1
SRTM 90 m	90 m	3.5	0,9	2.5	2,7	3.0	1,8
TanDEM-X 90 m	90 m	4.7	4,8	7.6	7,3	6.1	6,1
Copernicus DEM 90 m	90 m	5,6	5,4	3,2	3,3	4,4	4,4

Overall, Table 8-3 shows a significantly greater decrease in accuracy for the 90 m DEMs than for the others. In particular, the TanDEM-X and the Copernicus DEM have the largest slope related loss of accuracies of all DEMs in their 90 m versions. However, this table also reveals that the decrease depends on the acquisition source. These results underline that these DEMs from WorldDEM™ data are overall more negatively affected by relief and show the strongest decrease of accuracy in steeper slopes, which has also been observed by other studies (Gdulová et al., 2020; Uuemaa et al., 2020). In

contrast, the accuracy of DEMs generated by stereo imagery seems less affected by slope changes. In particular, the error of the ALOS W3D DEM rises only about 1 m per 10° slope. This is also supported by results of other studies that have shown a lower sensitivity of this DEM against steeper relief compared to a C-band RADAR SRTM DEM (Mukul and Mukul, 2021; Uuemaa et al., 2020). A reason could be the disrupted backscatter ability of interferometric RADAR in steeper relief that causes a higher number of larger errors (Liu et al., 2019). Furthermore, SAR acquisition has often larger viewing angle geometries than optical stereo imagery which can cause larger relief distortions (Yocky and Jakowatz, 2007). This effect is also partly visible in the slope curves of Figures 3-7, 4-1 and 5-8 where in extreme slopes the differences between achieved RMSE and NMAD values are often larger for the RADAR DEMs, than for others.

Considering the presented relief dependent changes in accuracy for each DEM in Table 8-3, this enables the possibility to additionally adjust the calculated land use dependent accuracy values of chapter 5.4.2 (Figure 5-7). The mean slope steepness of the eight land use classes is presented in Table 8-4. This shows that these classes are topographically biased and it must be assumed that the measured error values in Figure 5-7 are not only induced by land cover. Rather, differences in the relief steepness of each class have additionally influenced the measured error values. Correcting these values with the overall achieved slope dependent rates of accuracy change in Table 8-3 provides land use uncertainties that are homogenized on a hypothetical flat surface for all classes. This allows the calculation of a possible DEM error for any point on Earth with comparable land cover, regardless of slope.

Table 8-4: Mean overall slope angles of each land use class considered in the Rur catchment analysis in chapter 5.

Land use class	Mean slope angle [°]
Bare ground/Grassland	9.3
Coniferous Trees	7.9
Deciduous Trees	10.6
Agriculture	1.8
Residential Area	3.8
Urban Public/Commercial Area	2.6
Streets/Railways	5.0
Water	2.2

A calculation of such relief independent error values is presented in Figure 8-1. Based on these results, it can be stated that both tree classes and the water areas produce the by far largest errors in DEMs of about 6 – 7 m. The error caused by other land cover objects is significantly lower with less than 2 m on average for most DEMs. The land use class ‘Bare ground/Grassland’ had relatively large error values in the analysis of chapter 5 due to their occurrence in predominantly steeper relief than other classes. The unbiased results of Figure 8-1 now show that the error induced by this land cover class is not significantly higher than of classes ‘Agriculture’ or both urban classes. Overall, the achieved values of Table 8-3 and Figure 8-1 enable the calculation of a possible error for any point on Earth regardless of slope and land cover.

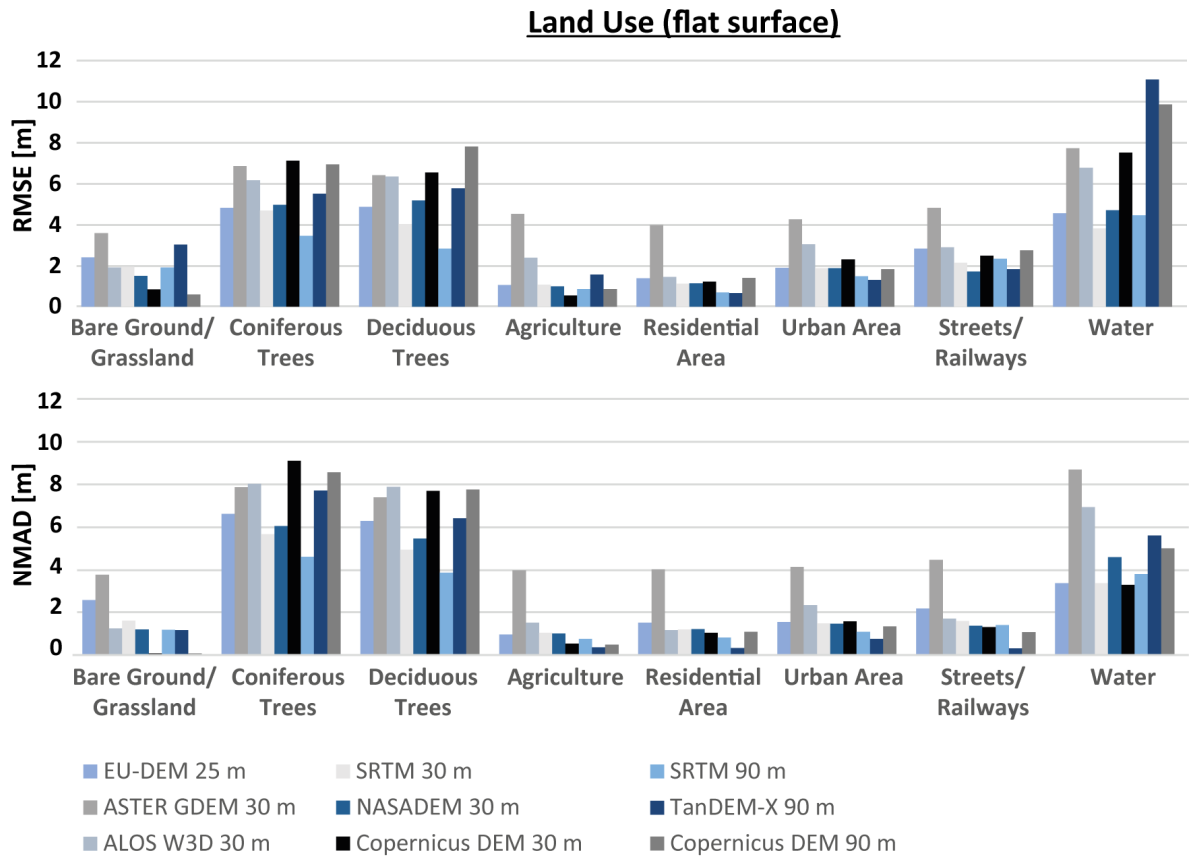

Figure 8-1: Calculated relief independent error values (RMSE and NMAD) for all tested land use classes. All error values are calculated for a homogenized hypothetical flat surface of 0° slope for each land use class to remove the topographical bias in the results of Figure 5-7.

To summarize all evaluation results gained in this contribution, Table 8-5 provides an assessment of how much the accuracy of DEMs from different sources is affected by relief and land cover. It can be stated that the DEMs acquired by RADAR technique are overall more affected by relief than DEMs from stereo photogrammetry. In contrast, these stereo photogrammetry DEMs are more sensitive to land cover and are more negatively affected in regions with dense land cover. However, also the X-band RADAR DEMs derived from the WorldDEM™ are significantly more affected by land cover than DEMs from the SRTM mission.

Table 8-5: Estimation, based on the results of this contribution, about the strength of influence of relief and land cover on the accuracy of DEMs depending on their acquisition source (= low influence; ** = medium influence; *** = strong influence).*

DEM data source	Acquisition technique	Relief	Land cover
SRTM	C-band RADAR	**	*
WorldDEM™	X-band RADAR	***	***
ALOS W3D	Stereo-photogrammetry	*	***
ASTER GDEM	Stereo-photogrammetry	**	**

8.2 Influence of different DEMs on applications

Digital elevation models are used in a countless variety of different disciplines and applications. In this contribution, the influence of using different DEMs was examined for two different applications. (I) the classification of landforms with different DEMs in chapter 6 and (II) the prediction of soil types with, among other data, relief parameters extracted from elevation models of different spatial resolutions in chapter 7. The investigated applications of this contribution show ambivalent results when it comes to the question of how accurate a DEM must be to provide sufficient results. It could be shown that a careful selection of an appropriate DEM is more crucial for certain applications than for others.

The classification of landforms at a local scale in chapter 6 showed that the results are strongly influenced by different DEMs. For the very complex Iranian loess plateau area, only high resolution DEMs derived from stereo imagery were capable to achieve sufficient classification results. Both 30 m medium resolution DEMs were not able to detect small landforms in the highly dissected areas and achieved overall accuracies that were up to 30 % lower than that of the high resolution DEMs. The difference in accuracy was observable for all classification approaches and in both flat and undulated areas. A comparison of two different DEMs with the same spatial resolution showed slightly superior results for the SRTM DEM than for the ASTER GDEM. This leads to the conclusion that DEMs from different acquisition sources may impact the results up to a certain point, but overall the spatial resolution of the DEM has much more impact on the classification of landforms. In other words, a DEM with an inappropriate spatial resolution produces far less accurate and detailed landforms than a DEM of higher resolution.

The general utilization of a DEM and its derived parameters to predict different soil types at a regional scale in chapter 7 showed that the input of elevation information as an environmental parameter was the most important factor for the prediction of soil types. Furthermore, many other derived terrain parameters, such as terrain classification index lowlands, terrain ruggedness index or valley depth, revealed great importance for model prediction. However, the results showed a relatively strong robustness of the results to the selection of different DEMs and other factors of the study design had a greater impact on the results. The results of the study in chapter 7 showed an accuracy difference of only less than 2 % between the very high resolution DGM1 and the 90 m TanDEM-X DEM in all tested scenarios. The choice of machine learning algorithm and the sampling strategy of training data resulted in greater accuracy differences than the choice of a different DEM. Using different machine learning algorithms as well as the selection of different sample strategies resulted in an average accuracy difference of about 6 %. Furthermore, the choice of prediction parameters is critical and different sets of environmental variables led to significant differences in the prediction power and accuracy differences of up to 9 %.

For the application of digital soil type prediction, the spatial resolution of the DEM and the derived input parameters shows a low influence on the results. The classification of soil types in chapter 7 produced similar results for a 90 m DEM as with a high resolution 15 m DEM. This is consistent with the findings of Cavazzi et al. (2013), who also found that a higher resolution does not automatically result in a higher accuracy in the prediction of different soil types. They state that a finer spatial resolution could be beneficial in areas with a heterogeneous soil type structure, but a coarser resolution leads to overall better results in flat and homogeneous areas. Furthermore, very detailed environmental parameters can produce too much noise, which can be disadvantageous for soil type

prediction algorithms. It can be assumed that more detailed relief parameters will improve the prediction accuracy only if there is a strong relationship between the environmental variables and the soil type classes being classified (Samuel-Rosa et al., 2015). A study of Costa et al. (2018) also showed little effect of the spatial resolution on digital soil mapping prediction results at a local scale. They also state that the occurrence of inherent noise and the overall smoothness of a DEM have a greater influence on soil type predictions than the spatial resolution of a DEM. If too many artefacts and very small features are included in the DEM, this can lead to discontinuous predictions of soil types.

In addition to the two applications that have been conducted in this contribution, several papers have been published that have also investigated the importance of an appropriate DEM selection for specific applications. A review of this literature also reveals a diverse image of the influence that the spatial resolution of a DEM and its acquisition source has on modelled or classified results in different scientific disciplines. A lot of work l has been carried out in the field of hydrology. Several authors stated that the resolution of a DEM is critical for delineating stream networks (Ariza-Villaverde et al., 2015; Gautam et al., 2019; Mukherjee et al., 2013; Nagaveni et al., 2019; Vaze et al., 2010). They found out that the length of predicted stream networks decreases significantly and the shape tends to be more abstract with DEMs of coarser resolutions for both local and regional watersheds. Additionally, Lidberg et al. (2017) noted that the selection of the preprocessing method for filling sinks in the DEM prior to the analysis can also have an impact on the resulting stream networks. Only Wu et al. (2017) recognized a minor effect of DEM resolution on their results on a national scale of entire China. Thus, it can be concluded, that the influence probably decreases with smaller scales. DEMs from different sources can also have a considerable influence on the delineation of stream networks. Several authors state that not only the spatial resolution impacts stream network models, also DEMs from different acquisition sources can produce different results (Drisya and Kumar, 2016; Mukherjee et al., 2013; Vaze et al., 2010). Overall, the selection of DEMs seems to play a very important role in applications that require an accurate drainage network.

In contrast, the delineation of watersheds seems to be more robust against DEMs of different spatial resolutions. Various authors state that by using different DEMs, fewer differences in the area and shape of watersheds can be detected (Keys and Baade, 2019; Nagaveni et al., 2019; Vaze et al., 2010). However, different DEMs with the same spatial resolution can also lead to noticeable differences in watershed boundaries (Keys and Baade, 2019; Rana and Suryanarayana, 2019). Thus, it can be concluded that the selection of DEMs is less critical for watershed delineation than for stream network delineation, but may also affect the results.

Coveney and Fotheringham (2011) conducted a large-scale analysis to examine how the selection of different high resolution DEMs has an impact on the prediction of coastal flood and erosion risks. Their results show that the quality of results depends less on the spatial resolution than on the overall accuracy of the DEMs. In particular, DEMs derived by photogrammetric techniques showed weaknesses compared to other generation sources. For the modelling of flood areas in urban environments, Muthusamy et al. (2021) used a DEM resampled to different spatial resolutions for their modelling and compared the achieved results. They found a considerable relationship between the spatial resolution of a DEM and the predicted flood depth and extent. In their study, the flooded extent was 30 % larger with a 1 m DEM than with a 50 m DEM. The calculation of inundation areas of six rivers by Saksena and Merwade (2015) also revealed a significant influence of spatial resolution on the results. They state that coarser DEM resolutions increase the predicted areas of inundation, in

particular for urban and steeply sloped areas. However, to which degree different DEM sources might influence these results was not investigated by these studies. Nevertheless, it can be concluded from these results that the selection of an appropriate DEM and resolution is crucial for flood risk modelling and high resolution DEMs are required to achieve reliable results.

In the field of geomorphometry, only relatively few studies are available that have investigated the influence of DEMs on certain applications. Dobre et al. (2021) found that the source of DEMs had only little effect on the detection of peaks. Also, the impact of spatial resolution was only minor and all investigated DEMs seemed to be suitable for this application. In contrast, for the mapping of gullies at a very local scale, Dai et al. (2019b) observed a strong influence of spatial resolution on the detection of gullies. However, they state that a very high resolution can lead to an overinterpretation and a coarse resolution to an underestimation of gully landforms. Brosens et al. (2022) state for the calculation of gully volumes that the spatial resolution of a DEM is critical for this purpose. In their work, a 30 m Copernicus DEM did not provide sufficient results and resulted in a strong underestimation of these features. However, they also found no significant differences between a 12 m TanDEM-X and a 0.2 m DEM from UAV data. It can be assumed that a higher resolution has an influence on the accuracy only up to a certain point. For the application of ice thickness modelling, Chen et al. (2022) showed that a higher resolution moderately improves the model outcome. The influence of DEMs from different sources on the model results varied depending on the model that has been chosen.

Much work has already been done in the field of landslide hazard modelling, both at a local and a regional scale. Many of them observed that the highest spatial resolution is not always beneficial for landslide prediction (Chen et al., 2020; Tian et al., 2008) and could lead to an overinterpretation of landslide risks (Keijsers et al., 2011). Tian et al. (2008) stated that the optimal resolution likely depends on the size of the study area. A review of existing literature on landslide modelling by Kakavas and Nikolakopoulos (2021) indicates that for local scale areas a very high spatial resolution of less than 5 m is required to achieve optimal results. In contrast, they state that DEMs with an average resolution of 20 – 30 m are generally adequate for landslide predictions at a regional scale. DEMs with a pixel size of less than 90 m are generally not recommended for this type of application. Therefore, spatial resolution is crucial, but the assumption that a finer resolution is always better does not apply to all scales in landslide hazard modelling. However, not only the spatial resolution but also the source of the DEM seems to be critical. Results from Kaminski (2020), who compared two DEMs of equal spatial resolution in terms of their suitability for landslide risk modelling, showed considerable differences between DEMs from different sources. In their study, a 20 m DEM derived from LiDAR data showed better results than a DEM with the same spatial resolution derived from stereo imagery. For the application of landslide risk mapping, it can therefore be assumed that the overall quality of the DEM is important for the outcome, at least at a local scale. This has not yet been investigated at a regional scale, but it can be assumed that the behavior is similar at this scale.

In the context of archaeology, Becker et al. (2017) investigated the influence of six DEMs from different sources and with different spatial resolutions on the results of cost distance modelling to calculate isochrones for prehistoric site catchments. They found out that the calculated size of the catchments varies significantly for different DEMs and the choice of an appropriate DEM is of great importance for this task. It could be shown in their study that both spatial resolution and overall quality, induced by different acquisition and processing techniques, have a major influence on the results.

In the field of ecology, some research has been conducted on the effects of different DEMs on plant species distribution. However, they mostly show only little influence of DEM resolution and source on modelling results, for both local and regional areas (Lassueur et al., 2006; Moudry et al., 2018). Minor differences between different DEM sources could be observed for very high resolution DEMs (Guillaume et al., 2021; Leempoel et al., 2015) as well as for low resolution DEMs (Moudry et al., 2018). Leempoel et al. (2015) suggest the use of multiple resolutions to achieve the best results on a local scale. However, the application of plant species distribution seems to be generally more robust to the choice of an appropriate DEM and coarser or less accurate DEMs could also provide promising results.

Another application where the selection of suitable DEMs seems crucial is the orthorectification of stereo satellite imagery. The study of Ortiz et al. (2012) reveals that for orthorectification at a local level, the spatial resolution is of great importance and a high resolution DEM leads to better results. In contrast, Ressl and Pfeifer (2018) observed a low relevance of spatial resolution for nationwide coverage in their study. Rather, the overall quality of the DEM had a higher impact on the orthorectification accuracy than the spatial resolution.

An overall summary of all presented findings on the influence of different DEMs on specific applications is listed in Table 8-6. The table serves as an indication of how important the choice of a particular DEM is for the quality of the outcome results. An estimation is given there concerning the importance of spatial resolution and the acquisition source of the DEM for specific applications. After reviewing the results of both studies in chapters 6 and 7 as well as several further published studies in different applications, it can be stated that the effects of DEM selection on the results of these respective applications are very diverse. The choice of an appropriate DEM of high quality and spatial resolution is more important for some applications than for others. Users usually tend to select the DEM with the highest available spatial resolution for their analysis (Mesa-Mingorance et al., 2017). This is reasonable as these DEMs mostly promise a higher accuracy than coarser DEMs. However, analysis results of soil type classification in this contribution have shown that the highest resolution is not always necessary for all applications. Some studies have even shown that a high resolution can be counterproductive in some scenarios (Cavazzi et al., 2013; Penizek et al., 2016). Others showed that the acquisition source and how the landscape is overall represented in the DEM has a higher influence on further study results than the spatial resolution of a DEM (Coveney and Fotheringham, 2011; Guillaume et al., 2021; Rana and Suryanarayana, 2019; Ressl and Pfeifer, 2018). Overall, the selection of a specific DEM seems to be less critical for applications that mainly use DEM derived land surface parameters for their further analysis. Although it is well known that spatial resolution significantly impacts the accuracy of derived land surface parameters (Deng et al., 2007; Grohmann, 2015; Kienzle, 2004; Vaze et al., 2010; Zhang and Montgomery, 1994), it is of little importance for many predictive modelling tasks. The results of other applications, which mainly derive their results directly from the DEM are more affected by the use of different DEMs.

Another aspect that has to be considered is that DEMs are static datasets. This means, they represent the landscape as it was at the time of data acquisition. However, topography and in particular areas such as river morphology and floodplains as well as urban areas are dynamic and can change rapidly over time. Thus, the date of acquisition may also be an important factor for some applications and an up-to-date DEM may be necessary to achieve reliable results (White et al., 2022). For example, up-to-date DEMs are required for the assessment of flow hazards in areas of active volcanoes (Deng et al.,

2019). However, actual on-demand acquired DEMs are usually expensive and often only available for study areas of limited size.

Furthermore, for many (but not all) applications, the scale of the study area additionally influences the impact of different DEMs on the results. Therefore, the spatial resolution of the DEM must be chosen according to the required level of detail of the analysis. Many studies listed in Table 8-6 showed that analyses at a local scale require higher spatial resolutions than analyses at a regional or national scale because of the size of objects that need to be represented within the DEM. In particular, for the delineation of hydrologic stream networks and landslide hazard modelling, it can be stated that the scale of the analysis is a very important factor and a study on a national scale is by far less affected by the selection of a specific DEM than studies on a local or regional scale (Table 8-6). In contrast, the summarized results show that for digital soil mapping and various ecological applications the selection of different DEMs had only small effects on the results, both at a local and national scale. Nevertheless, in many scientific fields, few studies are available to date that have investigated the impact of the choice of a particular DEM on the study outcome. Therefore, more work is necessary to prove existing results and widen the knowledge for more applications that have not been investigated to date. For most regions of the world, only DEMs with a spatial resolution of 30 m or lower are available free of charge. It is therefore also an economic question of whether a particular application needs an expensive high resolution DEM to achieve reliable results.

Table 8-6: Estimation about the influence of spatial resolution and source of a DEM on the results of certain applications (= low influence; ** = medium influence; *** = strong influence).*

Topic	Application	Scale	Importance of DEM		Reference
			Resolution	Source	
Hydrology	Stream network	Local & regional	***	**	Ariza-Villaverde et al. (2015); Drisya and Kumar (2016); Gautam et al. (2019); Lidberg et al. (2017); Mukherjee et al. (2013); Nagaveni et al. (2019); Vaze et al. (2010)
	Stream network	National	*	n/a	Wu et al. (2017)
	Watershed		**	**	Keys and Baade (2019); Nagaveni et al. (2019); Rana and Suryanarayana (2019); Vaze et al. (2010)
	SWAT water flow simulation	Regional & national	*	*	Gautam et al. (2019)
Risk hazard modelling	Coastal flood mapping	Local	**	***	Coveney and Fotheringham (2011)
	Urban flood modelling	Local	***	n/a	Muthusamy et al. (2021)
	River inundation modelling	Local & regional	***	n/a	Saksena and Merwade (2015)
	Landslide	Local	***	***	Kaminski (2020); Keijsers et al. (2011)
	Landslide	Regional	**	n/a	Chen et al. (2020); Tian et al. (2008)
Digital soil mapping	Soil type prediction	Regional	*	n/a	Chapter 7; Cavazzi et al. (2013)
	Soil type prediction	Local	*	**	Costa et al. (2018)
	Soil organic carbon modelling	Local	**	n/a	Gibson et al. (2021)
	Soil organic carbon modelling	Regional	*	n/a	Gibson et al. (2021)
Geomorphology	Landform classification	Local	***	**	Chapter 6
	Gully mapping	Local	***	n/a	Dai et al. (2019b)
	Peak detection	Regional	**	*	Dobre et al. (2021)
	Gully volumes	Local	***	*	Brosens et al. (2022)
Archaeology	Cost distance modelling	Regional	**	***	Becker et al. (2017)
Ecology	Plant species distribution modelling	Local	**	**	Guillaume et al. (2021); Leempoel et al. (2015)
	Plant species distribution modelling	Regional	*	**	Lassueur et al. (2006); Moudry et al. (2018)
Glaciology	Ice thickness modelling	National	**	** – *** (1)	Chen et al. (2022)
Image processing	Orthorectification	Local & national	**	***	Ortiz et al. (2012); Ressl and Pfeifer (2018)

(1) Observed influence depends on the used model.

9 Conclusion and outlook

This contribution provides a comprehensive vertical accuracy analysis of a multitude of different DEMs. It could be shown that DEMs of identical spatial resolution have significant differences in their accuracies depending on relief and land cover. Relief dependent accuracy values were calculated for each DEM, which may help users in the future to better estimate the accuracy of each tested DEM in a given landscape. For rising slopes, it can be summarized that the loss of accuracy is two to three times higher for a 90 m DEM than for DEMs of higher spatial resolution. Furthermore, these measures were used in this contribution to derive the uncertainties of different land cover classes for an unbiased relief to reduce the influence of topography on these values. Based on these results it can be stated that particularly forested and water areas cause uncertainties in DEMs of about 6 m on average. In contrast, the other land cover classes, e.g. urban areas, produced minor errors in DEMs of about 1 – 2 m on average.

Nevertheless, the results of this contribution reveal that there is no universal solution to the question of which DEM is the most accurate one. Not only the spatial resolution, but also the acquisition source has a valuable impact on the error behaviour of a DEM. Although the new DEMs from WorldDEM™ data have a high overall accuracy, they reveal weaknesses in steeper terrain. In contrast, photogrammetric DEMs from stereo-imagery remained with more stable accuracies in terrain of varying steepness levels. These DEMs were more affected by land cover and are likely to be less advisable in areas of dense land cover. The DEMs from SRTM data contain the oldest elevation data of all tested DEMs, which is perhaps problematic in areas of rapid surface changes. However, the dataset was improved over the years and is still a valuable alternative in certain situations, as it has been shown in the Rur catchment.

Overall, the assessment of DEMs and the impact of their quality on further analyses is a complex task that still needs much attention in the future. It can be assumed that more and more DEM products with higher resolutions will be launched in the future, which will have to be evaluated and compared with the existing products. Furthermore, there is still a need to find more standardised evaluation methods that consider relief and landscape. These should provide quality measures that are transferable to a broader region and increase the knowledge on the presence and behaviour of uncertainties in DEMs. This contribution provides a first attempt to establish individual error values for each DEM that are independent of slope and land cover by determining the individual error caused by both factors. In the future, it should be the aim to determine accuracies that are transferable to every point on Earth. Furthermore, the knowledge about the average error behaviour of a DEM for a certain land cover type can help to improve it for these areas.

In the second part of this contribution, the results prove that the spatial resolution and acquisition source of a DEM can have completely different effects on the results of certain applications. Most applications generally benefit from more accurate digital elevation models, but some are more affected by differences between the DEMs than others. In the context of this contribution, it has been shown in two studies that for digital soil mapping tasks the choice of DEMs was by far less critical than for the delineation of landforms. Furthermore, scale often influences the importance of DEM selection. Especially for large-scale analyses, spatial resolution often plays a greater role than for applications conducted in larger study areas. In summary, the selection of an appropriate DEM highly depends on the topic and the level of detail of the study area. Overall, a summarization of the current knowledge

on the consequences of DEM choice in different applications was established in the previous section 8.2. This addresses the increasing need for knowledge about the impact that different error behavior of DEMs has on different applications (Ariza-Lopez et al., 2018; Polidori and El Hage, 2020). However, the provided list in Table 8-6 is by far not complete and still many applications exist where only a few or no studies are available on this topic to date. Therefore, this table can be seen as a basis, but still more work is necessary in the future to extend the knowledge with more experiences of these and other applications.

References

Includes only references of chapters 1,2,4,8 and 9

Abolins, M., Ogden, A., 2021. Application of the global SRTM and AW3D30 digital elevation models to mapping folds at cave sites. International Journal of Speleology, 50 (1), 75-89. doi: 10.5038/1827-806x.50.1.2338.

Abrams, M., Bailey, B., Tsu, H., Hato, M., 2010. The ASTER Global DEM. Photogrammetric Engineering and Remote Sensing, 76 (4), 344-348.

Abrams, M., Crippen, R., 2019. ASTER GDEM V3 (ASTER Global DEM).

Adhikari, K., Minasny, B., Greve, M.B., Greve, M.H., 2014. Constructing a soil class map of Denmark based on the FAO legend using digital techniques. Geoderma, 214, 101-113. doi: 10.1016/j.geoderma.2013.09.023.

Aguilar, M.A., Aguilar, F.J., Negreiros, J., 2009. Off-the-shelf laser scanning and close-range digital photogrammetry for measuring agricultural soils microrelief. Biosystems Engineering, 103 (4), 504-517. doi: 10.1016/j.biosystemseng.2009.02.010.

Aguilar, M.A., Saldana, M.D., Aguilar, F.J., 2013. Assessing geometric accuracy of the orthorectification process from GeoEye-1 and WorldView-2 panchromatic images. International Journal of Applied Earth Observation and Geoinformation, 21, 427-435. doi: 10.1016/j.jag.2012.06.004.

Ahmad, F., Goparaju, L., Qayum, A., 2018a. Wild life habitat suitability and conservation hotspot mapping: Remote Sensing and GIS based decision support system. Aims Geosciences, 4 (1), 66-87. doi: 10.3934/geosci.2018.1.66.

Ahmad, F., Goparaju, L., Qayum, A., 2019. FAO guidelines and geospatial application for agroforestry suitability mapping: case study of Ranchi, Jharkhand state of India. Agroforestry Systems, 93 (2), 531-544. doi: 10.1007/s10457-017-0145-y.

Ahmad, F., Uddin, M.M., Goparaju, L., 2018b. Assessment of remote sensing and GIS application in identification of land suitability for agroforestry: A case study of Samastipur, Bihar, India. Contemporary Trends in Geoscience, 7 (2), 214-227. doi: 10.2478/ctg-2018-0015.

Aini, S., Sood, A.M., Saaban, S., 2015. Analysing Elephant Habitat Parameters using GIS, Remote Sensing and Analytic Hierarchy Process in Peninsular Malaysia. Pertanika Journal of Science and Technology, 23 (1), 37-50.

Airbus Defence and Space, 2020a. Copernicus Digital Elevation Model - Product Handbook. Airbus Defense & Space. https://spacedata.copernicus.eu/documents/20126/0/GEO1988-CopernicusDEM-SPE-002_ProductHandbook_I1.00.pdf. 12.04.2021.

Airbus Defence and Space, 2020b. Copernicus Digital Elevation Model - Validation Report. Airbus Defense & Space. https://spacedata.copernicus.eu/documents/20126/0/GEO1988-CopernicusDEM-RP-001_ValidationReport_V1.0.pdf. 12.04.2021.

Ajayi, O.G., Ajulo, J., 2021. Investigating the Applicability of Unmanned Aerial Vehicles (Uav) Photogrammetry for the Estimation of the Volume of Stockpiles. Quaestiones Geographicae, 40 (1), 25-38. doi: 10.2478/quageo-2021-0002.

Albertz, J., 2009. Grundlagen der Interpretation von Luft- und Satellitenbildern : eine Einführung in die Fernerkundung. Wissenschaftliche Buchgesellschaft, Darmstadt, Germany.

Alganci, U., Besol, B., Sertel, E., 2018. Accuracy Assessment of Different Digital Surface Models. ISPRS International Journal of Geo-Information, 7 (3), 114. doi: 10.3390/ijgi7030114.

Altunel, A.O., 2019. Evaluation of TanDEM-X 90 m Digital Elevation Model. International Journal of Remote Sensing, 40 (7), 2841-2854. doi: 10.1080/01431161.2019.1585593.

Amatulli, G., Domisch, S., Tuanmu, M.N., Parmentier, B., Ranipeta, A., Malczyk, J., Jetz, W., 2018. A suite of global, cross-scale topographic variables for environmental and biodiversity modeling. Scientific Data, 5, 180040. doi: 10.1038/sdata.2018.40.

American Society for Photogrammetry and Remote Sensing (ASPRS), 2004. ASPRS Guidelines: Vertical Accuracy Reporting for Lidar Data.

American Society for Photogrammetry and Remote Sensing (ASPRS), 2015. ASPRS Positional Accuracy Standards for Digital Geospatial Data. Photogrammetric Engineering & Remote Sensing, 81 (3). doi: 10.14358/PERS.81.3.A1-A26.

Ardakani, A.H.H., Shojaei, S., Siasar, H., Ekhtesasi, M.R., 2020. Heuristic Evaluation of Groundwater in Arid Zones Using Remote Sensing and Geographic Information System. International Journal of Environmental Science and Technology, 17 (2), 633-644. doi: 10.1007/s13762-018-2104-1.

Ariza-Lopez, F.J., Mora, E.G.C., Mingorance, J.L.M., Cai, J.H., Gordo, J.F.R., 2018. DEMs: An Approach to Users and Uses from the Quality Perspective. International Journal of Spatial Data Infrastructures Research, 13, 131-171. doi: 10.2902/1725-0463.2018.13.art12.

Ariza-Villaverde, A.B., Jimenez-Hornero, F.J., de Rave, E.G., 2015. Influence of DEM resolution on drainage network extraction: A multifractal analysis. Geomorphology, 241, 243-254. doi: 10.1016/j.geomorph.2015.03.040.

Arrell, K., Wise, S., Wood, J., Donoghue, D., 2008. Spectral filtering as a method of visualising and removing striped artefacts in digital elevation data. Earth Surface Processes and Landforms, 33 (6), 943-961. doi: 10.1002/esp.1597.

Arya, S., Subramani, T., Vennila, G., Roy, P.D., 2020. Groundwater vulnerability to pollution in the semi-arid Vattamalaikarai River Basin of south India thorough DRASTIC index evaluation. Geochemistry, 80 (4), 125635. doi: 10.1016/j.chemer.2020.125635.

Aspinall, R., Veitch, N., 1993. Habitat Mapping from Satellite Imagery and Wildlife Survey Data Using a Bayesian Modeling Procedure in a Gis. Photogrammetric Engineering and Remote Sensing, 59 (4), 537-543.

Baade, J., Schmullius, C., 2016. TanDEM-X IDEM precision and accuracy assessment based on a large assembly of differential GNSS measurements in Kruger National Park, South Africa. ISPRS Journal of Photogrammetry and Remote Sensing, 119, 496-508. doi: 10.1016/j.isprsjprs.2016.05.005.

Baharvand, S., Rahnamarad, J., Soori, S., Saadatkhah, N., 2020. Landslide susceptibility zoning in a catchment of Zagros Mountains using fuzzy logic and GIS. Environmental Earth Sciences, 79 (10), 204. doi: 10.1007/s12665-020-08957-w.

Baize, S., Audin, L., Alvarado, A., Jomard, H., Bablon, M., Champenois, J., Espin, P., Samaniego, P., Quidelleur, X., Le Pennec, J.L., 2020. Active Tectonics and Earthquake Geology Along the Pallatanga Fault, Central Andes of Ecuador. Frontiers in Earth Science, 8, 193. doi: 10.3389/feart.2020.00193.

Bajabaa, S., Masoud, M., Al-Amri, N., 2014. Flash flood hazard mapping based on quantitative hydrology, geomorphology and GIS techniques (case study of Wadi Al Lith, Saudi Arabia). Arabian Journal of Geosciences, 7 (6), 2469-2481. doi: 10.1007/s12517-013-0941-2.

Bamler, R., 1999. The SRTM-Mission: A world-wide 30 m resolution DEM from SAR interferometry in 11 days. In D. Fritsch, R. Spiller (Eds.), Photogrammetrische Woche 1999. Wiechmann Verlag, Heidelberg, Germany, 145-154.

Bamler, R., Eineder, M., 2017. Grenzen der Vermessung der Erde aus dem All mit Synthetischem Apertur Radar. In C. Heipke (Ed.), Photogrammetrie und Fernerkundung: Handbuch der Geodäsie, herausgegeben von Willi Freeden und Reiner Rummel. Springer Berlin, Heidelberg, Germany, 483-524.

Bareth, G., Bendig, J., Tilly, N., Hoffmeister, D., Aasen, H., Bolten, A., 2016. A Comparison of UAV- and TLS-derived Plant Height for Crop Monitoring: Using Polygon Grids for the Analysis of Crop Surface Models (CSMs). Photogrammetrie Fernerkundung Geoinformation, 2016 (2), 85-94. doi: 10.1127/pfg/2016/0289.

Barrand, N.E., Murray, T., James, T.D., Barr, S.L., Mills, J.P., 2009. Optimizing photogrammetric DEMs for glacier volume change assessment using laser-scanning derived ground-control points. Journal of Glaciology, 55 (189), 106-116. doi: 10.3189/002214309788609001.

Becek, K., 2014. Assessing Global Digital Elevation Models Using the Runway Method: The Advanced Spaceborne Thermal Emission and Reflection Radiometer Versus the Shuttle Radar

Topography Mission Case. IEEE Transactions on Geoscience and Remote Sensing, 52 (8), 4823-4831. doi: 10.1109/Tgrs.2013.2285187.

Becek, K., Koppe, W., Kutoglu, S.H., 2016. Evaluation of Vertical Accuracy of the WorldDEM (TM) Using the Runway Method. Remote Sensing, 8 (11), 934. doi: 10.3390/rs8110934.

Becker, D., de Andres-Herrero, M., Willmes, C., Weniger, G.C., Bareth, G., 2017. Investigating the Influence of Different DEMs on GIS-Based Cost Distance Modeling for Site Catchment Analysis of Prehistoric Sites in Andalusia. ISPRS International Journal of Geo-Information, 6 (2), 36. doi: 10.3390/ijgi6020036.

Beraldin, J.A., Blais, F., Lohr, U., 2010. Laser Scanning Technology. In G. Vosselman, H.-G. Maas (Eds.), Airborne and Terrestrial Laser Scanning. Whittles Publishing, Dunbeath, UK, 1-42.

Berry, P., Hilton, R., Johnson, C., 2002. Ace: First Full Release of The New 30" Gdem Incoporating Satellite Altimeter Derived Heights, EGS XXVII General Assembly, Nice, France, p. 4405.

Berthier, E., Vincent, C., Magnusson, E., Gunnlaugsson, A.T., Pitte, P., Le Meur, E., Masiokas, M., Ruiz, L., Palsson, F., Belart, J.M.C., Wagnon, P., 2014. Glacier topography and elevation changes derived from Pleiades sub-meter stereo images. Cryosphere, 8 (6), 2275-2291. doi: 10.5194/tc-8-2275-2014.

Beven, K.J., Kirkby, M.J., 1979. A physically based, variable contributing area model of basin hydrology / Un modèle à base physique de zone d'appel variable de l'hydrologie du bassin versant. Hydrological Sciences Bulletin, 24 (1), 43-69. doi: 10.1080/02626667909491834.

Bianchi, E., Villalba, R., Viale, M., Couvreux, F., Marticorena, R., 2016. New Precipitation and Temperature Grids for Northern Patagonia: Advances in Relation to Global Climate Grids. Journal of Meteorological Research, 30 (1), 38-52. doi: 10.1007/s13351-015-5058-y.

Bishop, M.P., Schroder, J.F., Colby, J.D., 2003. Remote sensing and geomorphometry for studying relief production in high mountains. Geomorphology, 55 (1-4), 345-361. doi: 10.1016/S0169-555x(03)00149-1.

Brenner, A.C., DiMarzio, J.P., Zwally, H.J., 2007. Precision and Accuracy of Satellite Radar and Laser Altimeter Data Over the Continental Ice Sheets. IEEE Transactions on Geoscience and Remote Sensing, 45 (2), 321-331. doi: 10.1109/TGRS.2006.887172.

Brosens, L., Campforts, B., Govers, G., Aldana-Jague, E., Razanamahandry, V.F., Razafimbelo, T., Rafolisy, T., Jacobs, L., 2022. Comparative analysis of the Copernicus, TanDEM-X, and UAV-SfM digital elevation models to estimate lavaka (gully) volumes and mobilization rates in the Lake Alaotra region (Madagascar). Earth Surface Dynamics, 10 (2), 209-227. doi: 10.5194/esurf-10-209-2022.

Brown, D.R.N., Jorgenson, M.T., Kielland, K., Verbyla, D.L., Prakash, A., Koch, J.C., 2016. Landscape Effects of Wildfire on Permafrost Distribution in Interior Alaska Derived from Remote Sensing. Remote Sensing, 8 (8), 654. doi: 10.3390/rs8080654.

Brungard, C.W., Boettinger, J.L., Duniway, M.C., Wills, S.A., Edwards, T.C., 2015. Machine learning for predicting soil classes in three semi-arid landscapes. Geoderma, 239, 68-83. doi: 10.1016/j.geoderma.2014.09.019.

Bürgmann, R., Rosen, P.A., Fielding, E.J., 2000. Synthetic aperture radar interferometry to measure Earth's surface topography and its deformation. Annual Review of Earth and Planetary Sciences, 28, 169-209. doi: 10.1146/annurev.earth.28.1.169.

Callaghan, K.L., Wickert, A.D., 2019. Computing water flow through complex landscapes - Part 1: Incorporating depressions in flow routing using FlowFill. Earth Surface Dynamics, 7 (3), 737-753. doi: 10.5194/esurf-7-737-2019.

Carrara, A., Bitelli, G., Carla, R., 1997. Comparison of techniques for generating digital terrain models from contour lines. International Journal of Geographical Information Science, 11 (5), 451-473. doi: 10.1080/136588197242257.

Carrera-Hernandez, J.J., 2021. Not all DEMs are equal: An evaluation of six globally available 30 m resolution DEMs with geodetic benchmarks and LiDAR in Mexico. Remote Sensing of Environment, 261, 112474. doi: 10.1016/j.rse.2021.112474.

Casana, J., Cothren, J., 2008. Stereo analysis, DEM extraction and orthorectification of CORONA satellite imagery: archaeological applications from the Near East. Antiquity, 82 (317), 732-749. doi: 10.1017/S0003598x00097349.

Cavazzi, S., Corstanje, R., Mayr, T., Hannam, J., Fealy, R., 2013. Are fine resolution digital elevation models always the best choice in digital soil mapping? Geoderma, 195, 111-121. doi: 10.1016/j.geoderma.2012.11.020.

Chaves, P.P., Ruokolainen, K., Tuomisto, H., 2018. Using remote sensing to model tree species distribution in Peruvian lowland Amazonia. Biotropica, 50 (5), 758-767. doi: 10.1111/btp.12597.

Chen, W.F., Yao, T.D., Zhang, G.Q., Li, F., Zheng, G.X., Zhou, Y.S., Xu, F.L., 2022. Towards ice-thickness inversion: an evaluation of global digital elevation models (DEMs) in the glacierized Tibetan Plateau. Cryosphere, 16 (1), 197-218. doi: 10.5194/tc-16-197-2022.

Chen, Z., Ye, F., Fu, W.X., Ke, Y.T., Hong, H.Y., 2020. The influence of DEM spatial resolution on landslide susceptibility mapping in the Baxie River basin, NW China. Natural Hazards, 101 (3), 853-877. doi: 10.1007/s11069-020-03899-9.

Chias, P., Abad, T., 2013. Wind farms: GIS-based visual impact assessment and visualization tools. Cartography and Geographic Information Science, 40 (3), 229-237. doi: 10.1080/15230406.2013.809231.

Chudy, F., Slamova, M., Tomastik, J., Prokesova, R., Mokros, M., 2019. Identification of Micro-Scale Landforms of Landslides Using Precise Digital Elevation Models. Geosciences, 9 (3), 117. doi: 10.3390/geosciences9030117.

Clubb, F.J., Mudd, S.M., Milodowski, D.T., Hurst, M.D., Slater, L.J., 2014. Objective extraction of channel heads from high-resolution topographic data. Water Resources Research, 50 (5), 4283-4304. doi: 10.1002/2013wr015167.

Costa, E.M., Samuel-Rosa, A., dos Anjos, L.H.C., 2018. Digital elevation model quality on digital soil mapping prediction accuracy. Ciencia E Agrotecnologia, 42 (6), 608-622. doi: 10.1590/1413-70542018426027418.

Coveney, S., Fotheringham, A.S., 2011. The impact of DEM data source on prediction of flooding and erosion risk due to sea-level rise. International Journal of Geographical Information Science, 25 (7), 1191-1211. doi: 10.1080/13658816.2010.545064.

Coveney, S., Roberts, K., 2017. Lightweight UAV digital elevation models and orthoimagery for environmental applications: data accuracy evaluation and potential for river flood risk modelling. International Journal of Remote Sensing, 38 (8-10), 3159-3180. doi: 10.1080/01431161.2017.1292074.

Crippen, R., Buckley, S., Agram, P., Belz, E., Gurrola, E., Hensley, S., Kobrick, M., Lavalle, M., Martin, J., Neumann, M. Nguyen, Q., Rosen, P., Shimada, J., Simard, M., Tung, W., 2016. NASADEM Global Elevation Model: Methods and Progress. ISPRS - International Archives of the Photogrammetry, Remote Sensing and Spatial Information Sciences, XLI-B4, 125-128. doi: 10.5194/isprs-archives-XLI-B4-125-2016.

Cruzan, M.B., Weinstein, B.G., Grasty, M.R., Kohrn, B.F., Hendrickson, E.C., Arredondo, T.M., Thompson, P.G., 2016. Small Unmanned Aerial Vehicles (Micro-Uavs, Drones) in Plant Ecology. Applications in Plant Sciences, 4 (9), 1600041. doi: 10.3732/apps.1600041.

Cuthbertson, P., Ullmann, T., Budel, C., Varis, A., Namen, A., Seltmann, R., Reed, D., Taimagambetov, Z., Iovita, R., 2021. Finding karstic caves and rockshelters in the Inner Asian mountain corridor using predictive modelling and field survey. Plos One, 16 (1), e0245170. doi: 10.1371/journal.pone.0245170.

D'Oleire-Oltmanns, S., Eisank, C., Dragut, L., Blaschke, T., 2013. An Object-Based Workflow to Extract Landforms at Multiple Scales From Two Distinct Data Types. IEEE Geoscience and Remote Sensing Letters, 10 (4), 947-951. doi: 10.1109/Lgrs.2013.2254465.

Dai, W., Hu, G.H., Huang, N., Zhang, P., Yang, X., Tang, G.A., 2019a. A Contour-Directional Detection for Deriving Terrace Ridge From Open Source Images and Digital Elevation Models. IEEE Access, 7, 129215-129224. doi: 10.1109/Access.2019.2940437.

Dai, W., Yang, X., Na, J.M., Li, J.W., Brus, D., Xiong, L.Y., Tang, G.A., Huang, X.L., 2019b. Effects of DEM resolution on the accuracy of gully maps in loess hilly areas. Catena, 177, 114-125. doi: 10.1016/j.catena.2019.02.010.

Danson, F.M., Hetherington, D., Morsdorf, F., Koetz, B., Allgower, B., 2007. Forest canopy gap fraction from terrestrial laser scanning. IEEE Geoscience and Remote Sensing Letters, 4 (1), 157-160. doi: 10.1109/Lgrs.2006.887064.

Day, S.S., Gran, K.B., Belmont, P., Wawrzyniec, T., 2013. Measuring bluff erosion part 1: terrestrial laser scanning methods for change detection. Earth Surface Processes and Landforms, 38 (10), 1055-1067. doi: 10.1002/esp.3353.

De Clercq, M., Chademenos, V., Van Lancker, V., Missiaen, T., 2016. A high-resolution DEM for the Top-Palaeogene surface of the Belgian Continental Shelf. Journal of Maps, 12 (5), 1047-1054. doi: 10.1080/17445647.2015.1117992.

Dekavalla, M., Argialas, D., 2017. Object-based classification of global undersea topography and geomorphological features from the SRTM30_PLUS data. Geomorphology, 288, 66-82. doi: 10.1016/j.geomorph.2017.03.026.

Deng, F.H., Rodgers, M., Xie, S.R., Dixon, T.H., Charbonnier, S., Gallant, E.A., Velez, C.M.L., Ordonez, M., Malservisi, R., Voss, N.K., Richardson, J.A., 2019. High-resolution DEM generation from spaceborne and terrestrial remote sensing data for improved volcano hazard assessment - A case study at Nevado del Ruiz, Colombia. Remote Sensing of Environment, 233, 111348. doi: 10.1016/j.rse.2019.111348.

Deng, Y., Wilson, J.P., Bauer, B.O., 2007. DEM resolution dependencies of terrain attributes across a landscape. International Journal of Geographical Information Science, 21 (1-2), 187-213. doi: 10.1080/13658810600894364.

Devine, S.M., O'Geen, A.T., Liu, H., Jin, Y.F., Dahlke, H.E., Larsen, R.E., Dahlgren, R.A., 2020. Terrain attributes and forage productivity predict catchment-scale soil organic carbon stocks. Geoderma, 368, 114286. doi: 10.1016/j.geoderma.2020.114286.

Dietrich, M., 2021. Koordinatensysteme in ArcGIS Pro. Praxis der Transformationen und Projektionen. Wichmann Verlag, Berlin, Germany.

Dikau, R., 1989. The application of a digital relief model to landform analysis. In J. Raper (Ed.), Three dimensional applications in Geographical Information Systems. Taylor and Francis, London, UK, 51-77.

Dikau, R., Brabb, E.E., Mark, R.M., Pike, R.J., 1995. Morphometric Landform Analysis of New Mexico. Zeitschrift für Geomorphologie, 101, 109-126.

Dikau, R., Schmidt, J., 1999. Georeliefklassifikation. In R. Schneider-Sliwa, D. Schaub, G. Gerold (Eds.), Angewandte Landschaftökologie: Grundlagen und Methoden. Springer, Berlin, Heidelberg, Germany, 217-244.

Dingle, E.H., Creed, M.J., Sinclair, H.D., Gautam, D., Gourmelen, N., Borthwick, A.G.L., Attal, M., 2020. Dynamic flood topographies in the Terai region of Nepal. Earth Surface Processes and Landforms, 45 (13), 3092-3102. doi: 10.1002/esp.4953.

Dirscherl, M., Rossi, C., 2018. Geomorphometric analysis of the 2014-2015 Baroarbunga volcanic eruption, Iceland. Remote Sensing of Environment, 204, 244-259. doi: 10.1016/j.rse.2017.10.027.

Dobre, B., Kovacs, I.P., Bugya, T., 2021. Comparison of digital elevation models through the analysis of geomorphic surface remnants in the Desatoya Mountains, Nevada. Transactions in Gis, 25 (5), 2262-2282. doi: 10.1111/tgis.12819.

Dornik, A., Dragut, L., Urdea, P., 2018. Classification of Soil Types Using Geographic Object-Based Image Analysis and Random Forests. Pedosphere, 28 (6), 913-925. doi: 10.1016/S1002-0160(17)60377-1.

Dragut, L., Blaschke, T., 2006. Automated classification of landform elements using object-based image analysis. Geomorphology, 81 (3-4), 330-344. doi: 10.1016/j.geomorph.2006.04.013.

Drisya, J., Kumar, D.S., 2016. Comparison of digitally delineated stream networks from different spaceborne digital elevation models: A case study based on two watersheds in South India. Arabian Journal of Geosciences, 9 (18), 710. doi: 10.1007/s12517-016-2726-x.

Drouin, A., Saint-Laurent, D., Lavoie, L., Ouellet, C., 2011. High-Precision Elevation Model to Evaluate the Spatial Distribution of Soil Organic Carbon in Active Floodplains. Wetlands, 31 (6), 1151-1164. doi: 10.1007/s13157-011-0226-z.

Duong, H., Lindenbergh, R., Pfeifer, N., Vosselman, G., 2009. ICESat Full-Waveform Altimetry Compared to Airborne Laser Scanning Altimetry Over The Netherlands. IEEE Transactions on Geoscience and Remote Sensing, 47 (10), 3365-3378. doi: 10.1109/Tgrs.2009.2021468.

Ehlers, E., 1980. Iran : Grundzüge e. geograph. Landeskunde. Wissenschaftliche Länderkunden. Wissenschaftliche Buchgesellschaft, Darmstadt, Germany.

Erdelyi, J., Kopacik, A., Kyrinovic, P., 2020. Spatial Data Analysis for Deformation Monitoring of Bridge Structures. Applied Sciences, 10 (23), 8731. doi: 10.3390/app10238731.

Evans, I.S., 1972. General Geomorphometry, Derivatives of Altitude, and Descriptive Statistics. Defense Technical Information Center, Ft. Belvoir, USA.

Farr, T.G., Rosen, P.A., Caro, E., Crippen, R., Duren, R., Hensley, S., Kobrick, M., Paller, M., Rodríguez, E., Roth, L., Seal, D., Shaffer, S., Shimada, J., Umland, J., Werner, M., Oskin, M., Burbank, D., Alsdorf, D., 2007. The shuttle radar topography mission. Reviews of Geophysics, 45 (2). doi: 10.1029/2005rg000183.

Fisher, P.E., Tate, N.J., 2006. Causes and consequences of error in digital elevation models. Progress in Physical Geography, 30 (4), 467-489. doi: 10.1191/0309133306pp492ra.

Fleischmann, A.S., Siqueira, V.A., Wongchuig-Correa, S., Collischonn, W., De Paiva, R.C.D., 2020. The great 1983 floods in South American large rivers: a continental hydrological modelling approach. Hydrological Sciences Journal-Journal Des Sciences Hydrologiques, 65 (8), 1358-1373. doi: 10.1080/02626667.2020.1747622.

Florinsky, I.V., 2012. Digital terrain analysis in soil science and geology. Elsevier/Academic Press, Amsterdam, The Netherlands.

Florinsky, I.V., 2016. Chapter 3 - Digital Elevation Models. In I.V. Florinsky (Ed.), Digital Terrain Analysis in Soil Science and Geology (Second Edition). Academic Press, 77-108. doi: 10.1016/B978-0-12-804632-6.00003-1.

Franklin, J., 1995. Predictive vegetation mapping: Geographic modelling of biospatial patterns in relation to environmental gradients. Progress in Physical Geography, 19 (4), 474-499. doi: 10.1177/030913339501900403.

Franklin, S.E., 2020. Interpretation and use of geomorphometry in remote sensing: a guide and review of integrated applications. International Journal of Remote Sensing, 41 (19), 7700-7733. doi: 10.1080/01431161.2020.1792577.

Frechen, M., Kehl, M., Rolf, C., Sarvati, R., Skowronek, A., 2009. Loess chronology of the Caspian Lowland in Northern Iran. Quaternary International, 198, 220-233. doi: 10.1016/j.quaint.2008.12.012.

Fricker, H.A., Borsa, A., Minster, B., Carabajal, C., Quinn, K., Bills, B., 2005. Assessment of ICESat performance at the Salar de Uyuni, Bolivia. Geophysical Research Letters, 32 (21), L21s06. doi: 10.1029/2005gl023423.

Gallant, J.C., Read, A.M., Dowling, T.I., 2012. Removal of Tree Offsets from SRTM and other Digital Surface Models. The International Archives of the Photogrammetry, Remote Sensing and Spatial Information Sciences, XXXIX-B4, 275-280. doi: 10.5194/isprsarchives-XXXIX-B4-275-2012.

Gardzinska, A., 2021. Application of Terrestrial Laser Scanning for the Inventory of Historical Buildings on the Example of Measuring the Elevations of the Buildings in the Old Market Square in

Jaroslaw. Civil and Environmental Engineering Reports, 31 (2), 293-309. doi: 10.2478/ceer-2021-0030.

Gautam, S., Dahal, V., Bhattarai, R., 2019. Impacts of Dem Source, Resolution and Area Threshold Values on SWAT Generated Stream Network and Streamflow in Two Distinct Nepalese Catchments. Environmental Processes, 6 (3), 597-617. doi: 10.1007/s40710-019-00379-6.

Gawrysiak, L., Kociuba, W., 2020. Application of geomorphons for analysing changes in the morphology of a proglacial valley (case study: The Scott River, SW Svalbard). Geomorphology, 371, 107449. doi: 10.1016/j.geomorph.2020.107449.

Gdulová, K., Marešová, J., Moudrý, V., 2020. Accuracy assessment of the global TanDEM-X digital elevation model in a mountain environment. Remote Sensing of Environment, 241, 111724. doi: https://doi.org/10.1016/j.rse.2020.111724.

German Aerospace Center (DLR), 2018. TanDEM-X - Digital Elevation Model (DEM) - Global, 90m [dataset]. doi: 10.15489/ju28hc7pui09.

Gesch, D., Oimoen , M., Zhang, Z., Meyer, D., Danielson, J., 2012. Validation of the ASTER GLOBAL Digital Elevation Model Version 2 Over the Conterminous United States, International Archives of the Photogrammetry, Remote Sensing and Spatial Information Sciences, Melbourne, Australia, XXXIX-B4, 281-286.

Gesch, D.B., Verdin, K.L., Greenlee, S.K., 1999. New land surface digital elevation model covers the Earth. Transactions American Geophysical Union, 80 (6), 69-70. doi: https://doi.org/10.1029/99EO00050.

Gharehchahi, S., James, W.H.M., Bhardwaj, A., Jensen, J.L.R., Sam, L., Ballinger, T.J., Butler, D.R., 2020. Glacier Ice Thickness Estimation and Future Lake Formation in Swiss Southwestern Alps-The Upper Rhone Catchment: A VOLTA Application. Remote Sensing, 12 (20), 3443. doi: 10.3390/rs12203443.

Ghilani, C.D., Wolf, P.R., 2015. Elementary surveying an introduction to geomatics. Always learning. Pearson Education Limited.

Gibson, A.J., Hancock, G.R., Bretreger, D., Cox, T., Hughes, J., Kunkel, V., 2021. Assessing digital elevation model resolution for soil organic carbon prediction. Geoderma, 398, 115106. doi: 10.1016/j.geoderma.2021.115106.

Gomez, C., 2018. Understanding volcanic geomorphology from derivatives and wavelet analysis: A case study at Miyakejima Volcano, Izu Islands, Japan. Journal of Volcanology and Geothermal Research, 354, 57-66. doi: 10.1016/j.jvolgeores.2018.02.007.

Gottfried, M., Pauli, H., Grabherr, G., 1998. Prediction of vegetation patterns at the limits of plant life: A new view of the alpine-nival ecotone. Arctic and Alpine Research, 30 (3), 207-221. doi: 10.2307/1551968.

Gottwald, M., Kenkmann, T., Reimold, W.U., Fritz, T., Breit, H., 2021. The TanDEM-X Digital Elevation Model and Terrestrial Impact Structures. Ieee Journal of Selected Topics in Applied Earth Observations and Remote Sensing, 14, 4128-4138. doi: 10.1109/Jstars.2021.3069640.

Graf, L., Moreno-de-las-Heras, M., Ruiz, M., Calsamiglia, A., Garcia-Comendador, J., Fortesa, J., Lopez-Tarazon, J.A., Estrany, J., 2018. Accuracy Assessment of Digital Terrain Model Dataset Sources for Hydrogeomorphological Modelling in Small Mediterranean Catchments. Remote Sensing, 10 (12), 2014. doi: 10.3390/rs10122014.

Grimm, R., Behrens, T., Marker, M., Elsenbeer, H., 2008. Soil organic carbon concentrations and stocks on Barro Colorado Island - Digital soil mapping using Random Forests analysis. Geoderma, 146 (1-2), 102-113. doi: 10.1016/j.geoderma.2008.05.008.

Grohmann, C.H., 2015. Effects of spatial resolution on slope and aspect derivation for regional-scale analysis. Computers & Geosciences, 77, 111-117. doi: 10.1016/j.cageo.2015.02.003.

Gruber, F.E., Baruck, J., Mair, V., Geitner, C., 2019. From geological to soil parent material maps - A random forest-supported analysis of geological map units and topography to support soil survey in South Tyrol. Geoderma, 354, 113884. doi: 10.1016/j.geoderma.2019.113884.

Guan, L.Y., Pan, H.B., Zou, S.Y., Hu, J., Zhu, X.Y., Zhou, P., 2020. The impact of horizontal errors on the accuracy of freely available Digital Elevation Models (DEMs). International Journal of Remote Sensing, 41 (19), 7367-7383. doi: 10.1080/01431161.2020.1759840.

Guillaume, A.S., Leempoel, K., Rochat, E., Rogivue, A., Kasser, M., Gugerli, F., Parisod, C., Joost, S., 2021. Multiscale Very High Resolution Topographic Models in Alpine Ecology: Pros and Cons of Airborne LiDAR and Drone-Based Stereo-Photogrammetry Technologies. Remote Sensing, 13 (8), 1588. doi: 10.3390/rs13081588.

Guo, L., Shi, T.Z., Linderman, M., Chen, Y.Y., Zhang, H.T., Fu, P., 2019. Exploring the Influence of Spatial Resolution on the Digital Mapping of Soil Organic Carbon by Airborne Hyperspectral VNIR Imaging. Remote Sensing, 11 (9), 1032. doi: 10.3390/rs11091032.

Guth, P.L., Van Niekerk, A., Grohmann, C.H., Muller, J.P., Hawker, L., Florinsky, I.V., Gesch, D., Reuter, H.I., Herrera-Cruz, V., Riazanoff, S., Lopez-Vazquez, C., Carabajal, C.C., Albinet, C., Strobl, P., 2021. Digital Elevation Models: Terminology and Definitions. Remote Sensing, 13 (18), 3581. doi: 10.3390/rs13183581.

Hancock, S., McGrath, C., Lowe, C., Davenport, I., Woodhouse, I., 2021. Requirements for a global lidar system: spaceborne lidar with wall-to-wall coverage. Royal Society Open Science, 8 (12), 211166. doi: 10.1098/rsos.211166.

Hanief, A., Laursen, A.E., 2019. Modeling the Natural Drainage Network of the Grand River in Southern Ontario: Agriculture May Increase Total Channel Length of Low-Order Streams. Geosciences, 9 (1), 46. doi: 10.3390/geosciences9010046.

Hawker, L., Bates, P., Neal, J., Rougier, J., 2018. Perspectives on Digital Elevation Model (DEM) Simulation for Flood Modeling in the Absence of a High-Accuracy Open Access Global DEM. Frontiers in Earth Science, 6, 233. doi: 10.3389/feart.2018.00233.

Hengl, T., Evans, I.S., 2009. Chapter 2 Mathematical and Digital Models of the Land Surface. In T. Hengl, H.I. Reuter (Eds.), Geomorphometry Concepts, Software, Applications. Elsevier, Amsterdam, The Netherlands, 31-63. Doi: 10.1016/S0166-2481(08)00002-0.

Heritage, G.L., Milan, D.J., 2009. Terrestrial Laser Scanning of grain roughness in a gravel-bed river. Geomorphology, 113 (1-2), 4-11. doi: 10.1016/j.geomorph.2009.03.021.

Hobi, M.L., Ginzler, C., 2012. Accuracy Assessment of Digital Surface Models Based on WorldView-2 and ADS80 Stereo Remote Sensing Data. Sensors, 12 (5), 6347-6368. doi: 10.3390/s120506347.

Hoch, J.M., Haag, A.V., van Dam, A., Winsemius, H.C., van Beek, L.P.H., Bierkens, M.F.P., 2017. Assessing the impact of hydrodynamics on large-scale flood wave propagation - a case study for the Amazon Basin. Hydrology and Earth System Sciences, 21 (1), 117-132. doi: 10.5194/hess-21-117-2017.

Hodgson, M.E., Bresnahan, P., 2004. Accuracy of airborne lidar-derived elevation: Empirical assessment and error budget. Photogrammetric Engineering and Remote Sensing, 70 (3), 331-339. doi: 10.14358/Pers.70.3.331.

Hoffmeister, D., Curdt, C., Bareth, G., 2020. Monitoring the sedimentary budget and dislocated boulders in western Greece - results since 2008. Sedimentology, 67 (3), 1411-1430. doi: 10.1111/sed.12723.

Hoffmeister, D., Waldhoff, G., Korres, W., Curdt, C., Bareth, G., 2016a. Crop height variability detection in a single field by multi-temporal terrestrial laser scanning. Precision Agriculture, 17 (3), 296-312. doi: 10.1007/s11119-015-9420-y.

Hoffmeister, D., Zellmann, S., Pastoors, A., Kehl, M., Cantalejo, P., Ramos, J., Weniger, G.-C., Bareth, G., 2016b. The Investigation of the Ardales Cave, Spain – 3D Documentation, Topographic Analyses, and Lighting Simulations based on Terrestrial Laser Scanning. Archaeological Prospection, 23 (2), 75-86. doi: 10.1002/arp.1519.

Höhle, J., Höhle, M., 2009. Accuracy assessment of digital elevation models by means of robust statistical methods. ISPRS Journal of Photogrammetry and Remote Sensing, 64 (4), 398-406. doi: 10.1016/j.isprsjprs.2009.02.003.

Hu, P., Liu, X.H., Hu, H., 2009. Accuracy Assessment of Digital Elevation Models based on Approximation Theory. Photogrammetric Engineering and Remote Sensing, 75 (1), 49-56. doi: 10.14358/Pers.75.1.49.

Hu, Z.H., Peng, J.W., Hou, Y.L., Shan, J., 2017. Evaluation of Recently Released Open Global Digital Elevation Models of Hubei, China. Remote Sensing, 9 (3), 262. doi: 10.3390/rs9030262.

Iwahashi, J., Yamazaki, D., Nakano, T., Endo, R., 2021. Classification of topography for ground vulnerability assessment of alluvial plains and mountains of Japan using 30 m DEM. Progress in Earth and Planetary Science, 8 (1), 3. doi: 10.1186/s40645-020-00398-0.

Jabbar, A., Othman, A.A., Merkel, B., Hasan, S.E., 2020. Change detection of glaciers and snow cover and temperature using remote sensing and GIS: A case study of the Upper Indus Basin, Pakistan. Remote Sensing Applications-Society and Environment, 18, 100308. doi: 10.1016/j.rsase.2020.100308.

Jacobsen, K., 2012. Airborne or Spaceborne Images for Topographic Mapping. In Perakis Konstantinos, M. Athanasios (Eds.), EARSeL Symposium.

Jacobsen, K., 2017. Satellitenphotogrammetrie. In C. Heipke (Ed.), Photogrammetrie und Fernerkundung: Handbuch der Geodäsie, Springer, Berlin, Heidelberg, Germany, 343-372.

Jarasiunas, G., 2016. Assessment of the agricultural land under steep slope in Lithuania. Journal of Central European Agriculture, 17 (1), 176-187. doi: 10.5513/JCEA01/17.1.1688.

Jaroslav, H., 2013. Topographic Solar Radiation Modeling for Environmental Applications. In C. Richter, D. Lincot, C.A. Gueymard (Eds.), Sol Energy. Springer New York, USA, 715-730.

Jarvis, A., Reuter, H., Nelsen, A., Guevara, E., 2008. Hole-filled seamless SRTM data V4 [dataset]. International Centre for Tropical Agriculture (CIAT). http://srtm.csi.cgiar.org. 12.04.2021.

Jasiewicz, J., Stepinski, T.F., 2013. Geomorphons - a pattern recognition approach to classification and mapping of landforms. Geomorphology, 182, 147-156. doi: 10.1016/j.geomorph.2012.11.005.

Jenny, H., 1941. Factors of soil formation a system of quantitative pedology. McGraw-Hill publications in the agricultural sciences.

Jensen, J.R., 1995. Issues involving the creation of digital elevation models and terrain corrected orthoimagery using soft-copy photogrammetry. Geocarto International, 10 (1), 5-21. doi: 10.1080/10106049509354475.

Jenson, S.K., 1991. Applications of Hydrologic Information Automatically Extracted from Digital Elevation Models. Hydrological Processes, 5 (1), 31-44. doi: 10.1002/hyp.3360050104.

Jenson, S.K., Domingue, J.O., 1988. Extracting Topographic Structure from Digital Elevation Data for Geographic Information-System Analysis. Photogrammetric Engineering and Remote Sensing, 54 (11), 1593-1600.

Jutzi, B., Meyer, F.J., Hinz, S., 2017. Aktive Fernerkundungssensorik – Technologische Grundlagen und Abbildungsgeometrie. In C. Heipke (Ed.), Photogrammetrie und Fernerkundung: Handbuch der Geodäsie, Springer, Berlin, Heidelberg, Germany, 65-103.

Kadhem, G.M., Zubari, W.K., 2020. Identifying Optimal Locations for Artificial Groundwater Recharge by Rainfall in the Kingdom of Bahrain. Earth Systems and Environment, 4 (3), 551-566. doi: 10.1007/s41748-020-00178-2.

Kahmen, H., 2006. Angewandte Geodäsie: Vermessungskunde. De Gruyter, Berlin, New York.

Kakavas, M.P., Nikolakopoulos, K.G., 2021. Digital Elevation Models of Rockfalls and Landslides: A Review and Meta-Analysis. Geosciences, 11 (6), 256. doi: 10.3390/geosciences11060256.

Kakembo, V., Rowntree, K., Palmer, A.R., 2007. Topographic controls on the invasion of Pteronia incana (Blue bush) onto hillslopes in Ngqushwa (formerly Peddie) district, Eastern Cape, South Africa. Catena, 70 (2), 185-199. doi: 10.1016/j.catena.2006.08.005.

Kaminski, M., 2020. The Impact of Quality of Digital Elevation Models on the Result of Landslide Susceptibility Modeling Using the Method of Weights of Evidence. Geosciences, 10 (12), 488. doi: 10.3390/geosciences10120488.

Karlson, M., Bastviken, D., Reese, H., 2021. Error Characteristics of Pan-Arctic Digital Elevation Models and Elevation Derivatives in Northern Sweden. Remote Sensing, 13 (22), 4653. doi: 10.3390/rs13224653.

Ke, C.Q., Lee, H., Han, Y.F., 2019. Glacier Change in the Yigong Zangbo Basin, Tibetan Plateau, China. Korean Journal of Remote Sensing, 35 (4), 491-502. doi: 10.7780/kjrs.2019.35.4.1.

Kehl, M., 2010. Quaternary loesses, loess-like sediments, soils and climate change in Iran. Relief, Boden, Paläoklima. Gebrüder Borntraeger, Stuttgart, Germany.

Keijsers, J.G.S., Schoorl, J.M., Chang, K.T., Chiang, S.H., Claessens, L., Veldkamp, A., 2011. Calibration and resolution effects on model performance for predicting shallow landslide locations in Taiwan. Geomorphology, 133 (3-4), 168-177. doi: 10.1016/j.geomorph.2011.03.020.

Keys, L., Baade, J., 2019. Uncertainty in Catchment Delineations as a Result of Digital Elevation Model Choice. Hydrology, 6 (1), 13. doi: 10.3390/hydrology6010013.

Khan, N., 2019. Tectonic geomorphology and structural architecture of eastern Sulaiman Fold Thrust Belt (SFTB) and adjacent Sulaiman Foredeep (SF), northwest Pakistan. Geomorphology, 343, 145-167. doi: 10.1016/j.geomorph.2019.06.015.

Kienzle, S., 2004. The Effect of DEM Raster Resolution on First Order, Second Order and Compound Terrain Derivatives Transactions in GIS, 8 (1), 83-111. doi: 10.1111/j.1467-9671.2004.00169.x.

Kim, S., Park, S., Han, J., Son, S., Lee, S., Han, K., Kim, J., Kim, J., 2019. Feasibility of UAV Photogrammetry for Coastal Monitoring: A Case Study in Imlang Beach, South Korea. Journal of Coastal Research, 386-392. doi: 10.2112/Si90-049.1.

Kirkby, M.J., Chorley, R.J., 1967. Throughflow, Overland Flow and Erosion. International Association of Scientific Hydrology, 12 (3), 5-21. doi: 10.1080/02626666709493533.

Koch, B., Heyder, U., Weinacker, H., 2006. Detection of individual tree crowns in airborne lidar data. Photogrammetric Engineering and Remote Sensing, 72 (4), 357-363. doi: 10.14358/Pers.72.4.357.

Kraus, K., 2004. Photogrammetrie, De Gruyter Lehrbuch. Band 1: Photogrammetrie Geometrische Informationen aus Photographien und Laserscanneraufnahmen, Berlin, Germany.

Krieger, G., Moreira, A., Fiedler, H., Hajnsek, I., Werner, M., Younis, M., Zink, M., 2007. TanDEM-X: A satellite formation for high-resolution SAR interferometry. IEEE Transactions on Geoscience and Remote Sensing, 45 (11), 3317-3341. doi: 10.1109/Tgrs.2007.900693.

Kuhni, A., Pfiffner, O.A., 2001. The relief of the Swiss Alps and adjacent areas and its relation to lithology and structure: topographic analysis from a 250-m DEM. Geomorphology, 41 (4), 285-307. doi: 10.1016/S0169-555x(01)00060-5.

Kumar, A., Negi, H.S., Kumar, K., Shekhar, C., 2020. Accuracy validation and bias assessment for various multi-sensor open-source DEMs in part of the Karakoram region. Remote Sensing Letters, 11 (10), 893-902. doi: 10.1080/2150704x.2020.1792001.

Kumar, L., Skidmore, A.K., Knowles, E., 1997. Modelling topographic variation in solar radiation in a GIS environment. International Journal of Geographical Information Science, 11 (5), 475-497. doi: 10.1080/136588197242266.

Kumler, M.P., 1994. An intensive comparison of triangulated irregular networks (TINs) and digital elevation models (DEMs). Cartographica, 31 (2), 1-99. doi: 10.3138/TM56-74K7-QH1T-8575.

Kushla, J.D., Ripple, W.J., 1997. The role of terrain in a fire mosaic of a temperate coniferous forest. Forest Ecology and Management, 95 (2), 97-107. doi: 10.1016/S0378-1127(97)82929-5.

Lamichhane, S., Kumar, L., Wilson, B., 2019. Digital soil mapping algorithms and covariates for soil organic carbon mapping and their implications: A review. Geoderma, 352, 395-413. doi: 10.1016/j.geoderma.2019.05.031.

Larsen, C.F., Motyka, R.J., Arendt, A.A., Echelmeyer, K.A., Geissler, P.E., 2007. Glacier changes in southeast Alaska and northwest British Columbia and contribution to sea level rise. Journal of Geophysical Research-Earth Surface, 112 (F1), F01007. doi: 10.1029/2006jf000586.

Lassueur, T., Joost, S., Randin, C.F., 2006. Very high resolution digital elevation models: Do they improve models of plant species distribution? Ecological Modelling, 198 (1-2), 139-153. doi: 10.1016/j.ecolmodel.2006.04.004.

Leempoel, K., Parisod, C., Geiser, C., Daprà, L., Vittoz, P., Joost, S., 2015. Very high-resolution digital elevation models: are multi-scale derived variables ecologically relevant? Methods in Ecology and Evolution, 6 (12), 1373-1383. doi: 10.1111/2041-210x.12427.

Leitao, J.P., de Vitry, M.M., Scheidegger, A., Rieckermann, J., 2016. Assessing the quality of digital elevation models obtained from mini unmanned aerial vehicles for overland flow modelling in urban areas. Hydrology and Earth System Sciences, 20 (4), 1637-1653. doi: 10.5194/hess-20-1637-2016.

Lenk, U., 2001. 2.5D-GIS und Geobasisdaten - Integration von Höheninformation und Digitalen Situationsmodellen. Dissertation, University of Hannover, Hannover, Germany.

Lenk, U., Heipke, C., 2002. Ein 2.5D-GIS-Datenmodell durch Integration von DGM und DSM mittels Triangulationen – theoretischer und praktischer Vergleich von Algorithmen und ihrer Ergebnisse. Photogrammetrie Fernerkundung Geoinformation (PFG), 2002 (3), 205-216.

Lewis, J., 2021. Probabilistic Modelling for Incorporating Uncertainty in Least Cost Path Results: a Postdictive Roman Road Case Study. Journal of Archaeological Method and Theory, 28 (3), 911-924. doi: 10.1007/s10816-021-09522-w.

Li, L.L., Yang, J.T., Wu, J., 2019. A Method of Watershed Delineation for Flat Terrain Using Sentinel-2A Imagery and DEM: A Case Study of the Taihu Basin. ISPRS International Journal of Geo-Information, 8(12), 528. doi: 10.3390/ijgi8120528.

Li, R.K., Li, Y.B., Li, B., Fu, D.A.J., 2021. Landscape change patterns at three stages of the construction and operation of the TGP. Scientific Reports, 11 (1), 9288. doi: 10.1038/s41598-021-87732-8.

Lidberg, W., Nilsson, M., Lundmark, T., Ågren, A.M., 2017. Evaluating preprocessing methods of digital elevation models for hydrological modelling. Hydrological Processes, 31 (26), 4660-4668. doi: 10.1002/hyp.11385.

Lillesand, T.M., Kiefer, R.W., Chipman, J.W., 2015. Remote sensing and image interpretation. John Wiley & Sons, Inc., Hoboken, N.J., USA.

Liu, F., Yao, X., Li, L.J., 2021. Applicability of Geomorphic Index for the Potential Slope Instability in the Three River Region, Eastern Tibetan Plateau. Sensors, 21(19), 6505. doi: 10.3390/s21196505.

Liu, J.P., Shen, J., Zhao, R., Xu, S.H., 2013. Extraction of individual tree crowns from airborne LiDAR data in human settlements. Mathematical and Computer Modelling, 58 (3-4), 524-535. doi: 10.1016/j.mcm.2011.10.071.

Liu, K., Song, C.Q., Ke, L.H., Jiang, L., Ma, R.H., 2020a. Automatic watershed delineation in the Tibetan endorheic basin: A lake-oriented approach based on digital elevation models. Geomorphology, 358, 107127. doi: 10.1016/j.geomorph.2020.107127.

Liu, K., Song, C.Q., Ke, L.H., Jiang, L., Pan, Y.Y., Ma, R.H., 2019. Global open-access DEM performances in Earth's most rugged region High Mountain Asia: A multi-level assessment. Geomorphology, 338, 16-26. doi: 10.1016/j.geomorph.2019.04.012.

Liu, X.Y., Zhang, Z.Y., 2011. Drainage network extraction using LiDAR-derived DEM in volcanic plains. Area, 43 (1), 42-52. doi: 10.1111/j.1475-4762.2010.00955.x.

Liu, X.Y., Zhang, Z.Y., Peterson, J., Chandra, S., 2007. LiDAR-derived high quality ground control information and DEM for image orthorectification. Geoinformatica, 11 (1), 37-53. doi: 10.1007/s10707-006-0005-9.

Liu, Z.W., Zhu, J.J., Fu, H.Q., Zhou, C., Zuo, T.Y., 2020b. Evaluation of the Vertical Accuracy of Open Global DEMs over Steep Terrain Regions Using ICESat Data: A Case Study over Hunan Province, China. Sensors, 20 (17), 4865. doi: 10.3390/s20174865.

Lloyd, C.D., 2005. Assessing the effect of integrating elevation data into the estimation of monthly precipitation in Great Britain. Journal of Hydrology, 308 (1-4), 128-150. doi: 10.1016/j.jhydrol.2004.10.026.

MacMillan, R.A., Pettapiece, W.W., Nolan, S.C., Goddard, T.W., 2000. A generic procedure for automatically segmenting landforms into landform elements using DEMs, heuristic rules and fuzzy logic. Fuzzy Sets and Systems, 113 (1), 81-109. Doi: 10.1016/S0165-0114(99)00014-7.

Maity, D.K., Mandal, S., 2019. Identification of groundwater potential zones of the Kumari river basin, India: an RS & GISbased semi-quantitative approach. Environment Development and Sustainability, 21 (2), 1013-1034. doi: 10.1007/s10668-017-0072-0.

Mansuy, N., Thiffault, E., Pare, D., Bernier, P., Guindon, L., Villemaire, P., Poirier, V., Beaudoin, A., 2014. Digital mapping of soil properties in Canadian managed forests at 250 m of resolution using the k-nearest neighbor method. Geoderma, 235, 59-73. doi: 10.1016/ j.geoderma.2014.06.032.

Marešová, J., Gdulová, K., Pracná, P., Moravec, D., Gábor, L., Prošek, J., Barták, V., Moudrý, V., 2021. Applicability of Data Acquisition Characteristics to the Identification of Local Artefacts in Global Digital Elevation Models: Comparison of the Copernicus and TanDEM-X DEMs. Remote Sensing, 13 (19), 3931. doi: 10.3390/rs13193931.

Marin-Buzon, C., Perez-Romero, A.M., Leon-Bonillo, M.J., Martinez-Alvarez, R., Mejias-Garcia, J.C., Manzano-Agugliaro, F., 2021. Photogrammetry (SfM) vs. Terrestrial Laser Scanning (TLS) for Archaeological Excavations: Mosaic of Cantillana (Spain) as a Case Study. Applied Sciences, 11 (24), 11994. doi: 10.3390/app112411994.

Marques, K.P.P., Dematte, J.A.M., Miller, B.A., Lepsch, I.F., 2018. Geomorphometric segmentation of complex slope elements for detailed digital soil mapping in southeast Brazil. Geoderma Regional, 14, e00175. doi: 10.1016/j.geodrs.2018.e00175.

Mashimbye, Z.E., De Clercq, W.P., Van Niekerk, A., 2019. Assessing the influence of DEM source on derived streamline and catchment boundary accuracy. Water Sa, 45 (4), 672-684. doi: 10.17159/wsa/2019.v45.i4.7549.

Massawe, B.H.J., Subburayalu, S.K., Kaaya, A.K., Winowiecki, L., Slater, B.K., 2018. Mapping numerically classified soil taxa in Kilombero Valley, Tanzania using machine learning. Geoderma, 311, 143-148. doi: 10.1016/j.geoderma.2016.11.020.

Maune, D.F., Nayegandhi, A., 2018. Digital elevation model technologies and applications: the DEM users manual. American Society for Photogrammetry and Remote Sensing, Bethesda, Md, USA.

McBratney, A.B., Santos, M.L.M., Minasny, B., 2003. On digital soil mapping. Geoderma, 117 (1-2), 3-52. doi: 10.1016/S0016-7061(03)00223-4.

Mesa-Mingorance, J.L., Ariza-Lopez, F.J., 2020. Accuracy Assessment of Digital Elevation Models (DEMs): A Critical Review of Practices of the Past Three Decades. Remote Sensing, 12 (16), 2630. doi: 10.3390/rs12162630.

Mesa-Mingorance, J.L., Chicaiza, E.G., Buenano, X., Cai, J.H., Rodríguez -Pascual, A.F., Ariza-Lopez, F.J., 2017. Analysis of Users and Uses of DEMs in Spain. ISPRS International Journal of Geo-Information, 6 (12), 406. doi: 10.3390/ijgi6120406.

Miller, C.L., Laflamme, R.A., 1958. The digital terrain model - theory & application. M.I.T. Photogrammetry Laboratory, Cambridge, Mass.

Mishra, D., Singh, B.N., 2019. Identification of Groundwater Prospect in Bara Region of Allahabad District Based on Hydro-Geomorphological Analysis Using Satellite Imagery. Journal of the Indian Society of Remote Sensing, 47 (7), 1257-1273. doi: 10.1007/s12524-019-00984-w.

Mitas, L., Mitasova, H., 1999. Spatial interpolation. In P. Longley, M.F. Goodchild, D.J. Maguire, D.W. Rhind (Eds.), Geographical Information Systems: Principles, Techniques, Management and Applications. Wiley, 481-492.

Mohtashamian, M., Attar, F., Kavousi, K., Masoudi-Nejad, A., 2017. Biogeography, distribution and conservation status of maples (Acer L.) in Iran. Trees-Structure and Function, 31 (5), 1583-1598. doi: 10.1007/s00468-017-1571-1.

Moore, I.D., Grayson, R.B., Ladson, A.R., 1991. Digital Terrain Modeling - a Review of Hydrological, Geomorphological, and Biological Applications. Hydrological Processes, 5 (1), 3-30. doi: 10.1002/hyp.3360050103.

Moore, I.D., Hutchinson, M.F., 1991. Spatial extension of hydrologic process modelling. International Hydrology and Water Resources Symposium, Australia, 91, 803-808.

Moudry, V., Lecours, V., Gdulova, K., Gabor, L., Moudra, L., Kropacek, J., Wild, J., 2018. On the use of global DEMs in ecological modelling and the accuracy of new bare-earth DEMs. Ecological Modelling, 383, 3-9. doi: 10.1016/j.ecolmodel.2018.05.006.

Mouratidis, A., Ampatzidis, D., 2019. European Digital Elevation Model Validation against Extensive Global Navigation Satellite Systems Data and Comparison with SRTM DEM and ASTER GDEM in Central Macedonia (Greece). ISPRS International Journal of Geo-Information, 8 (3), 108. doi: 10.3390/ijgi8030108.

Mukherjee, S., Joshi, P.K., Mukherjee, S., Ghosh, A., Garg, R.D., Mukhopadhyay, A., 2013. Evaluation of vertical accuracy of open source Digital Elevation Model (DEM). International Journal of Applied Earth Observation and Geoinformation, 21, 205-217. doi: 10.1016/j.jag.2012.09.004.

Mukul, M., Mukul, M., 2021. Uncertainties in Digital Elevation Models from Global Advanced Land Observing Satellite (ALOS) digital topography data in the Indian subcontinent Journal of Earth System Science, 130 (1), 51. doi: 10.1007/s12040-020-01523-9.

Murgatroyd, M., Bouten, W., Amar, A., 2021. A predictive model for improving placement of wind turbines to minimise collision risk potential for a large soaring raptor. Journal of Applied Ecology, 58 (4), 857-868. doi: 10.1111/1365-2664.13799.

Muthusamy, M., Casado, M.R., Butler, D., Leinster, P., 2021. Understanding the effects of Digital Elevation Model resolution in urban fluvial flood modelling. Journal of Hydrology, 596, 126088. doi: 10.1016/j.jhydrol.2021.126088.

Nagaveni, C., Kumar, K.P., Ravibabu, M.V., 2019. Evaluation of TanDEMx and SRTM DEM on watershed simulated runoff estimation. Journal of Earth System Science, 128 (1), 2. doi: 10.1007/s12040-018-1035-z.

NASA JPL, 2020. NASADEM Merged DEM Global 1 arc second V001 [dataset]. NASA EOSDIS Land Processes DAAC. doi: 10.5067/MEaSUREs/ NASADEM/NASADEM_HGT.001.

NASA Shuttle Radar Topography Mission (SRTM), 2013. Shuttle Radar Topography Mission (SRTM) Global [dataset]. OpenTopography. doi: 10.5069/ G9445JDF.

Naturwissenschaftliche Abtheilung, 1901. Bericht aus den naturwissenschaftlichen Abtheilungen der 73. Versammlungen deutscher Naturforscher und Aerzte in Hamburg, Naturwissenschaftliche Rundschau XVI.

Nelson, A., Reuter, H.I., Gessler, P., 2009. Chapter 3 DEM Production Methods and Sources. In T. Hengl, H.I. Reuter (Eds.), Geomorphometry Concepts, Software, Applications. Elsevier, Amsterdam, The Netherlands, 65-85. Doi: 10.1016/S0166-2481(08)00003-2.

Neuenschwander, A., Pitts, K., 2019. The ATL08 land and vegetation product for the ICESat-2 Mission. Remote Sensing of Environment, 221, 247-259. doi: 10.1016/j.rse.2018.11.005.

Neuenschwander, L.A., Magruder, A.L., 2019. Canopy and Terrain Height Retrievals with ICESat-2: A First Look. Remote Sensing, 11 (14), 1721. doi: 10.3390/rs11141721.

Ngunjiri, M.W., Libohova, Z., Minai, J.O., Serrem, C., Owens, P.R., Schulze, D.G., 2019. Predicting soil types and soil properties with limited data in the Uasin Gishu Plateau, Kenya. Geoderma Regional, 16, e00210. doi: 10.1016/j.geodrs.2019.e00210.

Niculita, M., 2016. Automatic landslide length and width estimation based on the geometric processing of the bounding box and the geomorphometric analysis of DEMs. Natural Hazards and Earth System Sciences, 16 (8), 2021-2030. doi: 10.5194/nhess-16-2021-2016.

Nilsen, L., Brossard, T., Joly, D., 1999. Mapping plant communities in a local Arctic landscape applying a scanned infrared aerial photograph in a geographical information system. International Journal of Remote Sensing, 20 (2), 463-480. doi: Doi 10.1080/014311699213541.

NOAA, 1988. Data Announcement 88-MGG-02, Digital relief of the Surface of the Earth. National Geophysical Data Center, Boulder, Colorado, USA.

Novak, A., Ostir, K., 2021. Towards Better Visualisation of Alpine Quaternary Landform Features on High-Resolution Digital Elevation Models. Remote Sensing, 13 (21), 4211. doi: 10.3390/rs13214211.

Nugraha, H., Wacano, D., Dipayana, G.A., Cahyadi, A., Mutaqin, B.W., Larasati, A., 2015. Geomorphometric Characteristics of Landslides in the Tinalah Watershed, Menoreh Mountains, Yogyakarta, Indonesia. Procedia Environmental Sciences, 28, 578-586. doi: https://doi.org/10.1016/j.proenv.2015.07.068.

Olaya, V., 2009. Chapter 6 Basic Land-Surface Parameters. In T. Hengl, H.I. Reuter (Eds.), Geomorphometry Concepts, Software, Applications. Elsevier, Amsterdam, The Netherlands, 141-169. doi: 10.1016/S0166-2481(08)00006-8.

Ortiz, S.M., Breidenbach, J., Knuth, R., Kandler, G., 2012. The Influence of DEM Quality on Mapping Accuracy of Coniferous- and Deciduous-Dominated Forest Using TerraSAR-X Images. Remote Sensing, 4 (3), 661-681. doi: 10.3390/rs4030661.

Otgonbayar, M., Atzberger, C., Mattiuzzi, M., Erdenedalai, A., 2019. Estimation of Climatologies of Average Monthly Air Temperature over Mongolia Using MODIS Land Surface Temperature (LST) Time Series and Machine Learning Techniques. Remote Sensing, 11 (21), 2588. doi: 10.3390/rs11212588.

Pandey, A., Himanshu, S.K., Mishra, S.K., Singh, V.P., 2016. Physically based soil erosion and sediment yield models revisited. Catena, 147, 595-620. doi: 10.1016/j.catena.2016.08.002.

Pandey, P., Manickam, S., Bhattacharya, A., Ramanathan, A.L., Singh, G., Venkataraman, G., 2017. Qualitative and quantitative assessment of TanDEM-X DEM over western Himalayan glaciated terrain. Geocarto International, 32 (4), 442-454. doi: 10.1080/10106049.2016.1155655.

Park, S., Park, H., Im, J., Yoo, C., Rhee, J., Lee, B., Kwon, C., 2019. Delineation of high resolution climate regions over the Korean Peninsula using machine learning approaches. Plos One, 14 (10), e0223362. doi: 10.1371/journal.pone.0223362.

Paul, F., Maisch, M., Rothenbuhler, C., Hoelzle, M., Haeberli, W., 2007. Calculation and visualisation of future glacier extent in the Swiss Alps by means of hypsographic modelling. Global Planet Change, 55 (4), 343-357. doi: 10.1016/j.gloplacha.2006.08.003.

Paul, F., Rastner, P., Azzoni, R.S., Diolaiuti, G., Fugazza, D., Le Bris, R., Nemec, J., Rabatel, A., Ramusovic, M., Schwaizer, G., Smiraglia, C., 2020. Glacier shrinkage in the Alps continues unabated as revealed by a new glacier inventory from Sentinel-2. Earth System Science Data, 12 (3), 1805-1821. doi: 10.5194/essd-12-1805-2020.

Pécsi, M., Richter, G., 1996. Löss: Herkunft-Gliederung-Landschaft. Zeitschrift für Geomorphologie, 98, Gebrüder Bornträger, Stuttgart, Germany.

Pelletier, J.D., 2013. A robust, two-parameter method for the extraction of drainage networks from high-resolution digital elevation models (DEMs): Evaluation using synthetic and real-world DEMs. Water Resources Research, 49 (1), 75-89. doi: 10.1029/2012wr012452.

Pena, F., Nardi, F., Melesse, A., Obeysekera, J., 2021. Assessing geomorphic floodplain models for large scale coarse resolution 2D flood modelling in data scarce regions. Geomorphology, 389, 107841. doi: 10.1016/j.geomorph.2021.107841.

Penizek, V., Zadorova, T., Kodesova, R., Vanek, A., 2016. Influence of Elevation Data Resolution on Spatial Prediction of Colluvial Soils in a Luvisol Region. Plos One, 11 (11), e0165699. doi: 10.1371/journal.pone.0165699.

Perez-Alvarez, R., de Luis-Ruiz, J.M., Pereda-Garcia, R., Fernandez-Maroto, G., Malagon-Picon, B., 2020. 3D Documentation with TLS of Caliphal Gate (Ceuta, Spain). Applied Sciences, 10 (15), 5377. doi: 10.3390/app10155377.

Piccini, C., Francaviglia, R., Marchetti, A., 2020. Predicted Maps for Soil Organic Matter Evaluation: The Case of Abruzzo Region (Italy). Land, 9 (10), 349. doi: 10.3390/land9100349.

Piccini, C., Marchetti, A., Francaviglia, R., 2014. Estimation of soil organic matter by geostatistical methods: Use of auxiliary information in agricultural and environmental assessment. Ecological Indicators, 36, 301-314. doi: 10.1016/j.ecolind.2013.08.009.

Pipaud, I., Loibl, D., Lehmkuhl, F., 2015. Evaluation of TanDEM-X elevation data for geomorphological mapping and interpretation in high mountain environments - A case study from SE Tibet, China. Geomorphology, 246, 232-254. doi: 10.1016/j.geomorph.2015.06.025.

Podgorski, J., Kinnard, C., Petlicki, M., Urrutia, R., 2019. Performance Assessment of TanDEM-X DEM for Mountain Glacier Elevation Change Detection. Remote Sensing, 11 (2), 187. doi: 10.3390/rs11020187.

Polidori, L., El Hage, M., 2020. Digital Elevation Model Quality Assessment Methods: A Critical Review. Remote Sensing, 12 (21), 3522. doi: 10.3390/rs12213522.

Polidori, L., Simonetto, E., 2014. Effect of Scale on the Correlation Between Topography and Canopy Elevations in an Airborne InSAR Product Over AMAZONIA. Procedia Technology, 16, 180-185. doi: 10.1016/j.protcy.2014.10.081.

Pradervand, J.N., Dubuis, A., Pellissier, L., Guisan, A., Randin, C., 2014. Very high resolution environmental predictors in species distribution models: Moving beyond topography? Progress in Physical Geography-Earth and Environment, 38 (1), 79-96. doi: 10.1177/0309133313512667.

Purinton, B., Bookhagen, B., 2021. Beyond Vertical Point Accuracy: Assessing Inter-pixel Consistency in 30 m Global DEMs for the Arid Central Andes. Frontiers in Earth Science, 9, 758606. doi: 10.3389/feart.2021.758606.

Qin, C.Z., Zhu, A.X., Qiu, W.L., Lu, Y.J., Li, B.L., Pei, T., 2012. Mapping soil organic matter in small low-relief catchments using fuzzy slope position information. Geoderma, 171, 64-74. doi: 10.1016/j.geoderma.2011.06.006.

Qiu, W., Cheng, Y.-J., 2017. High-Resolution DEM Generation of Railway Tunnel Surface Using Terrestrial Laser Scanning Data for Clearance Inspection. Journal of Computing in Civil Engineering, 31 (1), 04016045. doi: 10.1061/(ASCE)CP.1943-5487.0000611.

Rabus, B., Eineder, M., Roth, A., Bamler, R., 2003. The shuttle radar topography mission - a new class of digital elevation models acquired by spaceborne radar. ISPRS Journal of Photogrammetry and Remote Sensing, 57 (4), 241-262. doi: 10.1016/S0924-2716(02)00124-7.

Rana, V.K., Suryanarayana, T.M.V., 2019. Visual and statistical comparison of ASTER, SRTM, and Cartosat digital elevation models for watershed. Journal of Geovisualization and Spatial Analysis, 3 (2), 12. doi: 10.1007/s41651-019-0036-z.

Rashid, B., Iqbal, J., Su, L.J., 2020. Landslide susceptibility analysis of Karakoram highway using analytical hierarchy process and scoops 3D. Journal of Mountain Science, 17 (7), 1596-1612. doi: 10.1007/s11629-018-5195-8.

Renslow, M.S., 2012. Airborne Topographic Lidar Manual. American Society for Photogrammetry and Remote Sensing, Bethesda, USA.

Resop, J.P., Kozarek, J.L., Hession, W.C., 2012. Terrestrial Laser Scanning for Delineating In-stream Boulders and Quantifying Habitat Complexity Measures. Photogrammetric Engineering and Remote Sensing, 78 (4), 363-371. doi: 10.14358/Pers.78.4.363.

Ressl, C., Pfeifer, N., 2018. Evaluation of the elevation model influence on the orthorectification of Sentinel-2 satellite images over Austria. European Journal of Remote Sensing, 51 (1), 693-709. doi: 10.1080/22797254.2018.1478676.

Reuter, H.I., Hengl, T., Gessler, P., Soille, P., 2009. Chapter 4 Preparation of DEMs for Geomorphometric Analysis. In T. Hengl, H.I. Reuter (Eds.), Geomorphometry Concepts, Software, Applications. Elsevier, Amsterdam, The Netherlands, 87-120. doi: 10.1016/S0166-2481(08)00004-4.

Rexer, M., Hirt, C., 2014. Comparison of free high resolution digital elevation data sets (ASTER GDEM2, SRTM v2.1/v4.1) and validation against accurate heights from the Australian National Gravity Database. Australian Journal of Earth Sciences, 61 (2), 213-226. doi: 10.1080/08120099.2014.884983.

Rieg, L., Klug, C., Nicholson, L., Sailer, R., 2018. Pleiades Tri-Stereo Data for Glacier InvestigationsExamples from the European Alps and the Khumbu Himal. Remote Sensing, 10 (10), 1563. doi: 10.3390/rs10101563.

Riley, S.J., DeGloria, S.D., Elliot, R., 1999. A terrain ruggedness index that quantifies topographic heterogeneity. Intermountain Journal of Sciences., 5 (1-4), 23-27.

Rim, C.B., Om, K.C., Ren, G.Y., Kim, S.S., Kim, H.C., Kang-Chol, O., 2018. Establishment of a wildfire forecasting system based on coupled weather-Wildfire modeling. Applied Geography, 90, 224-228. doi: 10.1016/j.apgeog.2017.12.011.

Saksena, S., Merwade, V., 2015. Incorporating the effect of DEM resolution and accuracy for improved flood inundation mapping. Journal of Hydrology, 530, 180-194. doi: 10.1016/j.jhydrol.2015.09.069.

Saleem, N., Huq, M.E., Twumasi, N.Y.D., Javed, A., Sajjad, A., 2019. Parameters Derived from and/or Used with Digital Elevation Models (DEMs) for Landslide Susceptibility Mapping and Landslide Risk Assessment: A Review. ISPRS International Journal of Geo-Information, 8 (12), 545. doi: 10.3390/ijgi8120545.

Samuel-Rosa, A., Heuvelink, G.B.M., Vasques, G.M., Anjos, L.H.C., 2015. Do more detailed environmental covariates deliver more accurate soil maps? Geoderma, 243, 214-227. doi: 10.1016/j.geoderma.2014.12.017.

Schlund, M., Baron, D., Magdon, P., Erasmi, S., 2019. Canopy penetration depth estimation with TanDEM-X and its compensation in temperate forests. ISPRS Journal of Photogrammetry and Remote Sensing, 147, 232-241. doi: 10.1016/j.isprsjprs.2018.11.021.

Schneevoigt, N.J., van der Linden, S., Thamm, H.P., Schrott, L., 2008. Detecting Alpine landforms from remotely sensed imagery. A pilot study in the Bavarian Alps. Geomorphology, 93 (1-2), 104-119. doi: 10.1016/j.geomorph.2006.12.034.

Schutz, B.E., Zwally, H.J., Shuman, C.A., Hancock, D., DiMarzio, J.P., 2005. Overview of the ICESat Mission. Geophysical Research Letters, 32, L21S01. doi: 10.1029/2005gl024009.

Schwanghart, W., Groom, G., Kuhn, N.J., Heckrath, G., 2013. Flow network derivation from a high resolution DEM in a low relief, agrarian landscape. Earth Surface Processes and Landforms, 38 (13), 1576-1586. doi: 10.1002/esp.3452.

Semakova, E.R., Semakov, D.G., 2017. On a possibility to use the remote sensing techniques for glaciological analysis in mountain regions of Uzbekistan. Ice and Snow, 57 (2), 185-199. doi: 10.15356/2076-6734-2017-2-185-199.

Seyler, F., Muller, F., Cochonneau, G., Guimaraes, L., Guyot, J.L., 2009. Watershed delineation for the Amazon sub-basin system using GTOPO30 DEM and a drainage network extracted from JERS SAR images. Hydrological Processes, 23 (22), 3173-3185. doi: 10.1002/hyp.7397.

Shary, P.A., 1995. Land-Surface in Gravity Points Classification by a Complete System of Curvatures. Mathematical Geology, 27 (3), 373-390. doi: 10.1007/Bf02084608.

Shi, X., Xue, B.W., 2016. Deriving a minimum set of viewpoints for maximum coverage over any given digital elevation model data. International Journal of Digital Earth, 9 (12), 1153-1167. doi: 10.1080/17538947.2016.1207718.

Smith, B., Fricker, H.A., Holschuh, N., Gardner, A.S., Adusumilli, S., Brunt, K.M., Csatho, B., Harbeck, K., Huth, A., Neumann, T., Nilsson, J., Siegfried, M.R., 2019. Land ice height-retrieval algorithm for NASA's ICESat-2 photon-counting laser altimeter. Remote Sensing of Environment, 233, 111352. doi: 10.1016/j.rse.2019.111352.

Smith, M.J., Rose, J., Booth, S., 2006. Geomorphological mapping of glacial landforms from remotely sensed data: An evaluation of the principal data sources and an assessment of their quality. Geomorphology, 76 (1-2), 148-165. doi: 10.1016/j.geomorph.2005.11.001.

Sofia, G., 2020. Combining geomorphometry, feature extraction techniques and Earth-surface processes research: The way forward. Geomorphology, 355, 107055. doi: 10.1016/j.geomorph.2020.107055.

Stein, A., Kreft, H., 2015. Terminology and quantification of environmental heterogeneity in species-richness research. Biological Reviews, 90 (3), 815-836. doi: 10.1111/brv.12135.

Steven, S., Gastil-Buhl, M., Melack, J., 2007. Characterizing patterns of plant distribution in a southern California salt marsh using remotely sensed topographic and hyperspectral data and local tidal

fluctuations. Remote Sensing of Environment, 110 (2), 226-239. doi: 10.1016/j.rse.2007.02.024.

Stular, B., Lozic, E., Eichert, S., 2021. Airborne LiDAR-Derived Digital Elevation Model for Archaeology. Remote Sensing, 13 (9), 1855. doi: 10.3390/rs13091855.

Stumpf, A., Malet, J.P., Allemand, P., Ulrich, P., 2014. Surface reconstruction and landslide displacement measurements with Pleiades satellite images. ISPRS Journal of Photogrammetry and Remote Sensing, 95, 1-12. doi: 10.1016/j.isprsjprs.2014.05.008.

Sturzenegger, M., Holm, K., Lau, C.A., Jakob, M., 2021. Debris-Flow and Debris-Flood Susceptibility Mapping for Geohazard Risk Prioritization. Environmental & Engineering Geoscience, 27 (2), 179-194. doi: 10.2113/EEG-D-20-00006.

Suwandana, E., Kawamura, K., Sakuno, Y., Kustiyanto, E., Raharjo, B., 2012. Evaluation of ASTER GDEM2 in Comparison with GDEM1, SRTM DEM and Topographic-Map-Derived DEM Using Inundation Area Analysis and RTK-dGPS Data. Remote Sensing, 4 (8), 2419-2431. doi: 10.3390/rs4082419.

Tachikawa, T., Kaku, M., Iwasaki, A., Gesch, D.B., Oimoen, M.J., Zhang, Z., Danielson, J.J., Krieger, T., Curtis, B., Haase, J., Abrams, M., Carabajal, C., 2011. ASTER Global Digital Elevation Model Version 2 - summary of validation results. NASA, Washington, DC, USA.

Tadono, T., Shimada, M., Murakami, H., Takaku, J., 2009. Calibration of PRISM and AVNIR-2 Onboard ALOS "Daichi". IEEE Transactions on Geoscience and Remote Sensing, 47 (12), 4042-4050. doi: 10.1109/Tgrs.2009.2025270.

Taghizadeh-Mehrjardi, R., Minasny, B., Toomanian, N., Zeraatpisheh, M., Amirian-Chakan, A., Triantafilis, J., 2019. Digital Mapping of Soil Classes Using Ensemble of Models in Isfahan Region, Iran. Soil Systems, 3 (2), 37. Doi: 10.3390/soilsystems3020037.

Takaku, J., Tadono, T., Tsutsui, K., 2014. Generation of High Resolution Global DSM from ALOS PRISM. International Archives of the Photogrammetry, Remote Sensing and Spatial Information Sciences, XL-4, 243-248. doi: 10.5194/isprsarchives-XL-4-243-2014.

Takaku, J., Tadono, T., Tsutsui, K., Ichikawa, M., 2018. Quality Improvements of 'AW3D' Global Dsm Derived from Alos Prism, IGARSS 2018 - 2018 IEEE International Geoscience and Remote Sensing Symposium, 1612-1615.

Tarboton, D.G., Bras, R.L., Rodríguez -Iturbe, I., 1991. On the Extraction of Channel Networks from Digital Elevation Data. Hydrological Processes, 5 (1), 81-100. doi: 10.1002/hyp.3360050107.

Tarquini, S., Nannipieri, L., 2017. The 10 m-resolution TINITALY DEM as a trans-disciplinary basis for the analysis of the Italian territory: Current trends and new perspectives. Geomorphology, 281, 108-115. doi: 10.1016/j.geomorph.2016.12.022.

Thompson, J.A., Bell, J.C., Butler, C.A., 2001. Digital elevation model resolution: effects on terrain attribute calculation and quantitative soil-landscape modeling. Geoderma, 100 (1-2), 67-89. doi: 10.1016/S0016-7061(00)00081-1.

Thornton, P.E., Running, S.W., White, M.A., 1997. Generating surfaces of daily meteorological variables over large regions of complex terrain. Journal of Hydrology, 190 (3-4), 214-251. doi: 10.1016/S0022-1694(96)03128-9.

Tian, Y., Xiao, C.C., Liu, Y., Wu, L., 2008. Effects of raster resolution on landslide susceptibility mapping: A case study of Shenzhen. Science in China Series E-Technological Sciences, 51, 188-198. doi: 10.1007/s11431-008-6009-y.

Tilly, N., Hoffmeister, D., Cao, Q., Huang, S.Y., Lenz-Wiedemann, V., Miao, Y.X., Bareth, G., 2014. Multitemporal crop surface models: accurate plant height measurement and biomass estimation with terrestrial laser scanning in paddy rice. Journal of Applied Remote Sensing, 8, 083671. doi: 10.1117/1.Jrs.8.083671.

Tracz, W., Ciurzycki, W., Zaniewski, P., Kwasny, L., Marciszewska, K., Mozgawa, J., 2019. Identification of zones with high potential for biological diversity on dormant forested landslides. European Journal of Forest Research, 138 (3), 363-373. doi: 10.1007/s10342-019-01170-w.

Tsunetaka, H., Hotta, N., Hayakawa, Y.S., Imaizumi, F., 2020. Spatial accuracy assessment of unmanned aerial vehicle-based structures from motion multi-view stereo photogrammetry for

geomorphic observations in initiation zones of debris flows, Ohya landslide, Japan. Progress in Earth and Planetary Science, 7 (1), 24. doi: 10.1186/s40645-020-00336-0.

Tufekcioglu, M., Yavuz, M., Zaimes, G.N., Dinc, M., Koutalakis, P., Tufekcioglu, A., 2017. Application of Soil Water Assessment Tool (SWAT) to suppress wildfire at Bayam Forest, Turkey. Journal of Environmental Biology, 38 (5), 719-726. doi: 10.22438/jeb/38/5/MRN-331.

USGS, 1996. Digital Elevation - Global 30 Arc-Second Elevation (GTOPO30). USGS EROS Archive.

Uuemaa, E., Ahi, S., Montibeller, B., Muru, M., Kmoch, A., 2020. Vertical Accuracy of Freely Available Global Digital Elevation Models (ASTER, AW3D30, MERIT, TanDEM-X, SRTM, and NASADEM). Remote Sensing, 12 (21), 3482. doi: 10.3390/rs12213482.

Valentine, A., Kalnins, L., 2016. An introduction to learning algorithms and potential applications in geomorphometry and Earth surface dynamics. Earth Surface Dynamics, 4 (2), 445-460. doi: 10.5194/esurf-4-445-2016.

Vassilaki, D.I., Stamos, A.A., 2020. TanDEM-X DEM: Comparative performance review employing LIDAR data and DSMs. ISPRS Journal of Photogrammetry and Remote Sensing, 160, 33-50. doi: 10.1016/j.isprsjprs.2019.11.015.

Vaze, J., Teng, J., Spencer, G., 2010. Impact of DEM accuracy and resolution on topographic indices. Environmental Modelling & Software, 25 (10), 1086-1098. doi: 10.1016/j.envsoft.2010.03.014.

Weiss, A.D., 2001. Topographic Position and Landforms Analysis, ESRI Users Conference, San Diego, CA, USA.

Wessel, B., Huber, M., Wohlfart, C., Marschalk, U., Kosmann, D., Roth, A., 2018. Accuracy assessment of the global TanDEM-X Digital Elevation Model with GPS data. ISPRS Journal of Photogrammetry and Remote Sensing, 139, 171-182. doi: 10.1016/j.isprsjprs.2018.02.017.

Weydahl, D.J., Sagstuen, J., Dick, O.B., Ronning, H., 2007. SRTM DEM accuracy assessment over vegetated areas in Norway. International Journal of Remote Sensing, 28 (16), 3513-3527. doi: 10.1080/01431160600993447.

White, C.T., Reckling, W., Petrasova, A., Meentemeyer, R.K., Mitasova, H., 2022. Rapid-DEM: Rapid Topographic Updates through Satellite Change Detection and UAS Data Fusion. Remote Sensing , 14 (7), 1718. doi: 10.3390/rs14071718.

Wilson, J., Gallant, J., 2000a. Primary topographic attributes. In J.P. Wilson, J.C. Gallant (Eds.), Terrain Analysis: Principles and Applications. John Wiley & Sons, Inc, 51-85.

Wilson, J.P., 2018. Environmental applications of digital terrain modeling, Analytical methods in earth and environmental science. Wiley-Blackwell, Hoboken, NJ, USA.

Wilson, J.P., Gallant, J.C., 2000b. Digital Terrain Analysis. In J.P. Wilson, J.C. Gallant (Eds.), Terrain Analysis: Principles and Applications. John Wiley & Sons, Inc, 1-27.

Wise, S., 2000. Assessing the quality for hydrological applications of digital elevation models derived from contours. Hydrological Processes, 14 (11-12), 1909-1929. doi: Doi 10.1002/1099-1085(20000815/30)14:11/12<1909::Aid-Hyp45>3.0.Co;2-6.

Wu, C., Yuan, Y.B., Tang, Y., Tian, B.Q., 2022. Application of Terrestrial Laser Scanning (TLS) in the Architecture, Engineering and Construction (AEC) Industry. Sensors, 22 (1), 265. doi: 10.3390/s22010265.

Wu, M., Shi, P., Chen, A., Shen, C., Wang, P.Y., 2017. Impacts of DEM resolution and area threshold value uncertainty on the drainage network derived using SWAT. Water Sa, 43 (3), 450-462. doi: 10.4314/wsa.v43i3.10.

Wu, Q.S., Lane, C.R., 2017. Delineating wetland catchments and modeling hydrologic connectivity using lidar data and aerial imagery. Hydrology and Earth System Science, 21 (7), 3579-3595. doi: 10.5194/hess-21-3579-2017.

Xu, W.J., Wang, S., Bilal, M., 2020. LEM-DEM coupling for slope stability analysis. Science China-Technological Sciences, 63 (2), 329-340. doi: 10.1007/s11431-018-9387-2.

Yahaya, S.I., El Azzab, D., 2019. Vertical accuracy assessment of global digital elevation models and validation of gravity database heights in Niger. International Journal of Remote Sensing, 40 (20), 7966-7985. doi: 10.1080/01431161.2019.1607982.

Yamazaki, D., Ikeshima, D., Tawatari, R., Yamaguchi, T., O'Loughlin, F., Neal, J.C., Sampson, C.C., Kanae, S., Bates, P.D., 2017. A high-accuracy map of global terrain elevations. Geophysical Research Letters, 44 (11), 5844-5853. doi: 10.1002/2017gl072874.

Yocky, D.A., Jakowatz, C.V., 2007. Shift-scale complex correlation for wide-angle coherent cross-track SAR stereo processing. IEEE Transactions on Geoscience and Remote Sensing, 45 (3), 576-583. doi: 10.1109/Tgrs.2006.886193.

Yokoyama, R., Shirasawa, M., Pike, R.J., 2002. Visualizing topography by Openness: A new application of image processing to digital elevation models. Photogrammetric Engineering and Remote Sensing, 68 (3), 257-265.

Yue, L.W., Shen, H.F., Zhang, L.P., Zheng, X.W., Zhang, F., Yuan, Q.Q., 2017. High-quality seamless DEM generation blending SRTM-1, ASTER GDEM v2 and ICESat/GLAS observations. ISPRS Journal of Photogrammetry and Remote Sensing, 123, 20-34. doi: 10.1016/j.isprsjprs.2016.11.002.

Yurtseven, H., 2019. Comparison of GNSS-, TLS- and Different Altitude UAV-Generated Datasets on the Basis of Spatial Differences. ISPRS International Journal of Geo-Information, 8 (4), 175. doi: 10.3390/ijgi8040175.

Zevenbergen, L.W., Thorne, C.R., 1987. Quantitative-Analysis of Land Surface-Topography. Earth Surface Processes and Landforms, 12 (1), 47-56. doi: DOI 10.1002/esp.3290120107.

Zhang, K.Q., Gann, D., Ross, M., Biswas, H., Li, Y.P., Rhome, J., 2019a. Comparison of TanDEM-X DEM with LiDAR Data for Accuracy Assessment in a Coastal Urban Area. Remote Sensing, 11 (7), 876. doi: 10.3390/rs11070876.

Zhang, K.Q., Gann, D., Ross, M., Robertson, Q., Sarmiento, J., Santana, S., Rhome, J., Fritz, C., 2019b. Accuracy assessment of ASTER, SRTM, ALOS, and TDX DEMs for Hispaniola and implications for mapping vulnerability to coastal flooding. Remote Sensing of Environment ,225, 290-306. doi: 10.1016/j.rse.2019.02.028.

Zhang, S.W., Huang, Y.F., Shen, C.Y., Ye, H.C., Du, Y.C., 2012. Spatial prediction of soil organic matter using terrain indices and categorical variables as auxiliary information. Geoderma, 171, 35-43. doi: 10.1016/j.geoderma.2011.07.012.

Zhang, W.H., Montgomery, D.R., 1994. Digital Elevation Model Grid Size, Landscape Representation, and Hydrologic Simulations. Water Resources Research, 30 (4), 1019-1028. doi: 10.1029/93WR03553.

Zhang, Z., Du, Z.H., Liu, S.Y., Jiang, Z.L., Shangguan, D.H., Wei, J.F., Xu, J.L., Zhang, S.S., 2020a. Glacier mass changes over Duxueshan, Burog Kangri, and Zangser Kangri in the Inner Tibetan Plateau. Environmental Earth Sciences, 79 (12), 292. doi: 10.1007/s12665-020-09044-w.

Zhang, Z., Liu, S.Y., Jiang, Z.L., Shangguan, D.H., Wei, J.F., Guo, W.Q., Xu, J.L., Zhang, Y., Zhang, S.S., Huang, D.N., 2020b. Glacier Variations at Xinqingfeng and Malan Ice Caps in the Inner Tibetan Plateau Since 1970. Remote Sensing, 12 (3), 421. doi: 10.3390/rs12030421.

Zhang, Z., Liu, S.Y., Zhang, Y., Wei, J.F., Jiang, Z.L., Wu, K.P., 2018. Glacier variations at Aru Co in western Tibet from 1971 to 2016 derived from remote-sensing data. Journal of Glaciology, 64 (245), 397-406. doi: 10.1017/jog.2018.34.

Zhao, S.M., Cheng, W.M., Zhou, C.H., Chen, X., Zhang, S.F., Zhou, Z.P., Liu, H.J., Chai, H.X., 2011. Accuracy assessment of the ASTER GDEM and SRTM3 DEM: an example in the Loess Plateau and North China Plain of China. International Journal of Remote Sensing, 32 (23), 8081-8093. doi: 10.1080/01431161.2010.532176.

Zhao, W.F., Xiong, L.Y., Ding, H., Tang, G.A., 2017. Automatic recognition of loess landforms using Random Forest method. Journal of Mountain Science, 14 (5), 885-897. doi: 10.1007/s11629-016-4320-9.

Zhao, X.Q., Su, Y.J., Hu, T.Y., Chen, L.H., Gao, S., Wang, R., Jin, S.C., Guo, Q.H., 2018. A global corrected SRTM DEM product for vegetated areas. Remote Sensing Letters, 9 (4), 393-402. doi: 10.1080/2150704x.2018.1425560.

Zheng, W., Pritchard, M.E., Willis, M.J., Tepes, P., Gourmelen, N., Benham, T.J., Dowdeswell, J.A., 2018. Accelerating glacier mass loss on Franz Josef Land, Russian Arctic. Remote Sensing of Environment, 211, 357-375. doi: 10.1016/j.rse.2018.04.004.

Zhong, B., Xu, Y.J., 2009. Topographic Effects on Soil Organic Carbon in Louisiana Watersheds. Environmental Management, 43 (4), 662-672. doi: 10.1007/s00267-008-9182-7.

Zhong, C., Liu, Y., Gao, P., Chen, W.L., Li, H., Hou, Y., Nuremanguli, T., Ma, H.J., 2020. Landslide mapping with remote sensing: challenges and opportunities. International Journal of Remote Sensing, 41 (4), 1555-1581. doi: 10.1080/01431161.2019.1672904.

Zhu, H.C., Huang, W., Liu, H.Y., 2018. Loess terrain segmentation from digital elevation models based on the region growth method. Physical Geography, 39 (1), 51-66. doi: 10.1080/02723646.2017.1342215.

Zwally, H.J., Schutz, B., Abdalati, W., Abshire, J., Bentley, C., Brenner, A., Bufton, J., Dezio, J., Hancock, D., Harding, D., Herring, T., Minster, B., Quinn, K., Palm, S., Spinhirne, J., Thomas, R., 2002. ICESat's laser measurements of polar ice, atmosphere, ocean, and land. Journal of Geodynamics, 34 (3-4), 405-445. doi: 10.1016/S0264-3707(02)00042-X.

Appendix A: Eigenanteil

Kapitel 3

Titel	A Relief Dependent Evaluation of Digital Elevation Models on Different Scales for Northern Chile
Autoren	Tanja Kramm Dirk Hoffmeister
Status	Veröffentlicht
Journal	ISPRS International Journal of Geo-Information (MDPI)
Jahr	2019
Band, Ausgabe	8, 10
Artikelnummer	430
DOI	10.3390/ijgi8100430
Eigenanteil	• Beschaffung, Erstellung und Aufbereitung der Daten (Ausnahme: UAV und TLS Daten) • Datenanalyse und Auswertung • Verfassen des Manuskripts und Überarbeitungen

Kapitel 5

Titel	Comprehensive vertical accuracy analysis of freely available DEMs for different landscape types of the Rur catchment, Germany
Autoren	Tanja Kramm Dirk Hoffmeister
Status	Veröffentlicht (In Press)
Journal	Geocarto International (Taylor & Francis)
Jahr	2021
Band, Ausgabe	Noch nicht bekannt
DOI	10.1080/10106049.2021.1984588
Eigenanteil	• Beschaffung und Aufbereitung der Daten • Datenanalyse und Auswertung • Verfassen des Manuskripts und Überarbeitungen

Kapitel 6

Titel	Accuracy Assessment of Landform Classification Approaches on Different Spatial Scales for the Iranian Loess Plateau
Autoren	Tanja Kramm Dirk Hoffmeister Constanze Curdt Sedigheh Maleki Farhad Khormali Martin Kehl
Status	Veröffentlicht
Journal	ISPRS International Journal of Geo-Information (MDPI)
Jahr	2017
Band, Ausgabe	6, 11
Artikelnummer	366
DOI	10.3390/ijgi6110366
Eigenanteil	• Beschaffung, Erstellung und Aufbereitung der digitalen Geländemodelle • Datenanalyse und Auswertung (erfolgte im Rahmen meiner Masterarbeit) • Verfassen überwiegender Teile des Manuskripts und Überarbeitungen

Kapitel 7

Titel	Assessing the influence of environmental factors and datasets on soil type prediction with two machine learning algorithms in a heterogeneous area in the Rur catchment, Germany
Autoren	Tanja Kramm Dirk Hoffmeister
Status	Veröffentlicht
Journal	Geoderma Regional (Elsevier)
Jahr	2020
Band	22
Artikelnummer	e00316
DOI	10.1016/j.geodrs.2020.e00316
Eigenanteil	• Beschaffung und Aufbereitung der Daten • Datenanalyse und Auswertung • Verfassen des Manuskripts und Überarbeitungen

Appendix B: Erklärung

Ich versichere, dass ich die von mir vorgelegte Dissertation selbständig angefertigt, die benutzten Quellen und Hilfsmittel vollständig angegeben und die Stellen der Arbeit − einschließlich Tabellen, Karten und Abbildungen −, die anderen Werken im Wortlaut oder dem Sinn nach entnommen sind, in jedem Einzelfall als Entlehnung kenntlich gemacht habe; dass diese Dissertation noch keiner anderen Fakultät oder Universität zur Prüfung vorgelegen hat; dass sie − abgesehen von unten angegebenen Teilpublikationen − noch nicht veröffentlicht worden ist, sowie, dass ich eine solche Veröffentlichung vor Abschluss des Promotionsverfahrens nicht vornehmen werde. Die Bestimmungen der Promotionsordnung sind mir bekannt. Die von mir vorgelegte Dissertation ist von Prof. Dr. Georg Bareth betreut worden.

Köln, den 19.08.2022

Tanja Kramm

Teilpublikationen:

Kramm, T., Hoffmeister, D., Curdt, C., Maleki, S., Khormali, F., Kehl, M., 2017. Accuracy Assessment of Landform Classification Approaches on Different Spatial Scales for the Iranian Loess Plateau. ISPRS International Journal of Geo-Information, 6 (11), 366. doi: 10.3390/ijgi6110366.

Kramm, T., Hoffmeister, D., 2019. A Relief Dependent Evaluation of Digital Elevation Models on Different Scales for Northern Chile. ISPRS International Journal of Geo-Information, 8 (10), 430. doi: 10.3390/ijgi8100430.

Kramm, T., Hoffmeister, D., 2020. Assessing the influence of environmental factors and datasets on soil type prediction with two machine learning algorithms in a heterogeneous area in the Rur catchment, Germany. Geoderma Regional, 22, e00316. doi: 10.1016/j.geodrs.2020.e00316.

Kramm, T., Hoffmeister, D., 2021. Comprehensive vertical accuracy analysis of freely available DEMs for different landscape types of the Rur catchment, Germany. Geocarto International, In Press. doi: 10.1080/10106049.2021.1984588.